Structures Research Report 2010/72908/74039

University of Florida
Civil and Coastal Engineering

University of Florida
Civil and Coastal Engineering

Final Report **August 2010**

Vessel Crushing and Structural Collapse Relationships for Bridge Design

Principal investigator:
Gary R. Consolazio, Ph.D.

Research assistants:
Michael T. Davidson
Daniel J. Getter

Department of Civil and Coastal Engineering
University of Florida
P.O. Box 116580
Gainesville, Florida 32611

Sponsor:
Florida Department of Transportation (FDOT)
Sam Fallaha, P.E. – Project manager

Contract:
UF Project No. 00072908/00074039
FDOT Contract No. BDK75 977-02

DISCLAIMER

The opinions, findings, and conclusions expressed in this publication are those of the authors and not necessarily those of the State of Florida Department of Transportation.

Technical Report Documentation Page

1. Report No.	2. Government Accession No.	3. Recipient's Catalog No.

4. Title and Subtitle	5. Report Date
Vessel Crushing and Structural Collapse Relationships for Bridge Design	August 2010
	6. Performing Organization Code
	8. Performing Organization Report No.
7. Author(s) G. R. Consolazio, M. T. Davidson, D. J. Getter	2010/72908/74039
9. Performing Organization Name and Address University of Florida Department of Civil & Coastal Engineering P.O. Box 116580 Gainesville, FL 32611-6580	10. Work Unit No. (TRAIS)
	11. Contract or Grant No. BDK75 977-02
12. Sponsoring Agency Name and Address Florida Department of Transportation Research Management Center 605 Suwannee Street, MS 30 Tallahassee, FL 32301-8064	13. Type of Report and Period Covered Final Report
	14. Sponsoring Agency Code

15. Supplementary Notes

16. Abstract

Accounting for waterway vessel collision is an integral component of structural design for any bridge spanning a navigable waterway. Each time a vessel traverses a given waterway, there is an inherent risk that the vessel may become aberrant from the intended transit path, and once aberrant, may strike a nearby bridge structural component. During collision events, massive waterway vessel groups, such as barge flotillas, are capable of dynamically transmitting horizontal forces to impacted bridge components such as piers. Furthermore, such collision-induced forces can be sufficient to cause collapse of piers or roadway spans in the vicinity of the impact location. If collapse takes place, economic loss is suffered due to subsequent traffic rerouting and bridge replacement costs. Additionally, fatalities may occur if the roadway is occupied during or shortly after the collapse event.

The research presented in this report focuses on the development of improved probability of collapse expressions for bridge piers subject to barge impact loading, where such relationships are integral to current bridge design methodologies. Expression development is facilitated by employing probabilistic descriptions for a multitude of random variables related to barge traffic characteristics and bridge structures in conjunction with nonlinear dynamic finite element analyses of barge-bridge collisions. High levels of efficiency, achieved through use of advanced probabilistic simulation techniques, are necessarily incorporated into the barge-bridge collision analysis framework to allow feasible estimation of structural reliability parameters. Through joint use of efficient probabilistic simulation and vessel collision analysis techniques, the probability of collapse—and furthermore, the proximity to applicable structural limit states—is quantified for a representative set of bridges. The structural reliability parameters are then, in turn, used to form structural collapse relationships that aid in the design of bridges subject to barge collision. Finally, to facilitate use of the improved probability of collapse expressions in design applications, vessel crushing behavior is characterized for a wide range of potential design impact scenarios, and a design-oriented barge impact loading scheme is proposed that accounts for these scenarios.

17. Key Words	18. Distribution Statement
Barge, impact, collision, bridge pier, structural reliability, finite element analysis, dynamic analysis, probability of collapse, bridge design specifications	No restrictions.

19. Security Classif. (of this report)	20. Security Classif. (of this page)	21. No. of Pages	22. Price
Unclassified	Unclassified	231	

Form DOT F 1700.7 (8-72). Reproduction of completed page authorized

ACKNOWLEDGEMENTS

The authors would like to thank the Florida Department of Transportation (FDOT) for providing the funding that made this research project possible.

EXECUTIVE SUMMARY

Accounting for waterway vessel collision is an integral component of structural design for any bridge spanning a navigable waterway. Each time a vessel traverses a given waterway, there is an inherent risk that the vessel may become aberrant from the intended transit path, and once aberrant, may strike a nearby bridge structural component. During collision events, massive waterway vessel groups, such as barge flotillas, are capable of dynamically transmitting horizontal forces to impacted bridge components such as piers. Furthermore, such collision-induced forces can be sufficient to cause collapse of piers or roadway spans in the vicinity of the impact location. If collapse takes place, economic loss is suffered due to subsequent traffic rerouting and bridge replacement costs. Additionally, fatalities may occur if the roadway is occupied during or shortly after the collapse event.

The research presented in this report focuses on the development of improved probability of collapse expressions for bridge piers subject to barge impact loading, where such relationships are integral to current bridge design methodologies. Expression development is facilitated by employing probabilistic descriptions for a multitude of random variables related to barge traffic characteristics and bridge structures in conjunction with nonlinear dynamic finite element analyses of barge-bridge collisions. High levels of efficiency, achieved through use of advanced probabilistic simulation techniques, are necessarily incorporated into the barge-bridge collision analysis framework to allow feasible estimation of structural reliability parameters. Through joint use of efficient probabilistic simulation and vessel collision analysis techniques, the probability of collapse—and furthermore, the proximity to applicable structural limit states—is quantified for a representative set of bridges. The structural reliability parameters are then, in turn, used to form structural collapse relationships that aid in the design of bridges subject to barge collision. Finally, to facilitate use of the improved probability of collapse expressions in design applications, vessel crushing behavior is characterized for a wide range of potential design impact scenarios, and a design-oriented barge impact loading scheme is proposed that accounts for these scenarios.

TABLE OF CONTENTS

LIST OF FIGURES

LIST OF TABLES

CHAPTER 1
INTRODUCTION

1.1 Introduction

Navigable waterways in the U.S. are regularly transited by massive waterway vessels such as ships and barges. In the vicinity of bridges that span navigable waterways, pre-specified vessel transit paths are indicated by navigation lights and physical barriers (fender systems) to guide the in-transit waterway traffic under a designated portion of the bridge. For a given vessel in transit, however, there is a risk that the vessel will become aberrant (e.g., as a result of pilot error, poor navigational conditions) and stray from the intended vessel transit path. Aberrant vessels pose a significant risk to nearby bridge structures, in that an aberrant vessel may collide with a nearby bridge pier (or other bridge structural component). In the event of a vessel-bridge collision, large lateral forces can be transmitted to the impacted bridge structure. Furthermore, as an impacted bridge absorbs dynamic collision load, significant inertial forces may develop that, in turn, produce additional structural demands. Vessel-bridge collision forces can, therefore, lead to severe structural damage and even catastrophic failure of the impacted bridge.

Collapses of bridges spanning navigable waterways—such as the 1980 collapse of the Sunshine Skyway Bridge in Tampa, FL—prompted the American Association of State Highway and Transportation Officials (AASHTO) to develop a *Guide Specification and Commentary for Vessel Collision Design of Highway Bridges* (AASHTO 1991). The AASHTO provisions have been incorporated into, and remain a part of, the *AASHTO LRFD Bridge Design Specifications and Commentary* (2007). The AASHTO code language pertaining to design for waterway vessel collision consists of prescriptive analysis and design procedures that are intended to minimize susceptibility to catastrophic collapse for bridges that cross navigable waterways.

As part of the AASHTO design procedure, bridge designers are required to assess the risk of collapse (i.e., structural failure) associated with a given bridge design, with consideration of the bridge position in the waterway and the corresponding waterway traffic characteristics. Bridge collapse risk is expressed as an annual frequency of collapse, i.e., the percentage chance over a one-year period that the bridge will collapse as a result of being struck by a waterway vessel. The inverse of the annual frequency of collapse is defined as the return period (i.e., the expected number of years that will pass before collision-induced bridge collapse will occur). Per the AASHTO provisions, bridge designs are constrained by enforcing maximum values of the calculated return period (i.e., minimum values of the annual frequency of collapse). The annual frequency of collapse, as defined in the AASHTO provisions, is the product of several terms, including several conditional probability factors. These terms (and factors) are used to quantify the rate at which vessels transit a given waterway; vessel aberrancy rates; the probability that an aberrant vessel will strike a bridge structural component of interest; and, given that a collision occurs, the probability that the bridge structural component will undergo failure.

The final contributing factor described above, the probability of collapse in the event that a bridge structural component is impacted, is investigated in the current study for collisions between *barges* and bridges. Barges (as well as groups of barges, referred to as barge flotillas)

generally have smaller draft depths, relative to ships, thus enabling both inland waterway and coastal waterway transit. Additionally, numerous recent bridge collapse incidents involving barge collisions attest to the relatively higher collapse risk inherent to bridges that are susceptible to barge—as opposed to ship—impact.

In bridge design applications related to waterway vessel collision, the probability of collapse (PC) is typically calculated for each bridge pier in a waterway that is susceptible to collision—and in turn—for each type of vessel (or vessel group) that transits the waterway. Probability of collapse (PC) values, which are conditional upon imminent collision between vessel and bridge, are determined using an empirical expression that was developed by Cowiconsult (1987). The AASHTO PC expression requires two input parameters: static bridge structural capacity (typically this is taken as the bridge pier pushover capacity) and static impact load (determined using the AASHTO provisions). Using these two quantities, a capacity-demand ratio is then used to determine a corresponding PC value.

With regards to bridge design for barge collision, use of the existing AASHTO PC expression carries with it severe limitations. Specifically, the same PC expression is used for all impact scenarios regardless of the impacting vessel type (ship or barge). However, the empirical PC equation is based on a study of ship-ship collisions (Fujii and Shiobara 1978). Therefore, the expression may not be applicable to vessel-bridge collisions. Furthermore, the structural configurations of ship and barge structures differ substantially, and so, the applicability of the AASHTO PC expression to barge-bridge collisions is further diminished.

A second shortcoming in the AASHTO PC expression is found by considering that the expression relies on input parameters from a static analysis framework. Recent experimental and analytical studies (Consolazio et al. 2006, Consolazio et al. 2008, Davidson et al. 2010) have found that vessel-bridge collisions are fundamentally dynamic events, and further, that the incorporation of dynamic effects into the bridge design process (relating to waterway vessel collision) is strongly needed. However, the AASHTO PC expression is incompatible with dynamic input parameters of demand and capacity.

A third limitation arises from the use of a capacity-demand relationship (as opposed to a demand-capacity relationship) as the form of input for the AASHTO PC expression. As recognized in Gluver and Olsen (1998), the range of capacity-demand ratios applicable to the PC expression can lead to instances where, even though the impact load (structural demand) is substantially larger than the bridge capacity, the calculated PC value is small (i.e., the PC value is much closer to 0 than to 1).

Recent advances have been made toward the development of vessel-bridge collision analysis and modeling techniques (Consolazio and Cowan 2005, Consolazio and Davidson 2008). These simulation tools facilitate rapid assessment of barge impact force and bridge response where constitutive nonlinearity, kinematic nonlinearity, and dynamic effects are incorporated into the analytical framework. Additionally, an inventory of finite element (FE)

models of bridges from around the state of Florida was previously developed (Consolazio et al. 2008) from construction drawings. Bridge models from this inventory are selected that vary in age, size, and structural configuration and are intended to constitute a representative cross-section of Florida bridges that are currently in service. The efficacy of combining analytical techniques with the existing bridge model inventory makes feasible the task of assessing the probability of collapse rate for each of a representative set of bridges subject to barge impact.

1.2 Objectives

The primary objective of this study is the development of a revised probability of collapse (structural failure) relationship for bridges that are subject to barge impact. In contrast to the ship-ship collision data that were used to from the existing AASHTO PC expression, in the present study, probability of collapse expression development is facilitated, in part, by identifying probabilistic descriptions for a multitude of random variables related to barge and bridge structures (including pertinent structural limit state parameters). The random variable descriptions (taken from the literature and various government agencies) are then employed in barge collision simulations that are conducted for selected bridge cases from the pre-existing bridge FE model inventory. For each collision simulation conducted, the recently developed bridge modeling and collision analysis techniques are employed. Furthermore, both standard Monte Carlo (sMC) and Markov Chain Monte Carlo (MCMC) probabilistic simulation techniques are employed so that expected values of demand, capacity, and probability of failure can be estimated. Through joint use of statistical simulation (e.g., Monte Carlo methods) and nonlinear dynamic vessel collision analysis techniques, the probability of collapse—and furthermore, the proximity to applicable limit states—can be quantified for the selected, representative cross-section of bridge types. The structural reliability parameters of demand, capacity, and probability of collapse can then (in turn) be used to form a revised probability of collapse expression for the applicable structural limit states. The newly developed, rational probability of collapse expression is intended to replace the existing AASHTO PC expression as a component of bridge design for barge collision.

Given the revised PC expression, bridge designers are able to estimate the probability of a bridge pier failing under barge impact loading. However, barge impact loads can be highly sensitive to small changes in certain impact conditions. Specifically, it will be demonstrated in this report that the orientation of the barge relative to flat pier surfaces has a significant influence on forces generated during impact. Such variability is accounted for directly in the statistical simulations that have been used to form the revised PC expression. However, quantifying impact loads using statistical simulations is not practical within the context bridge design practice.

Consequently, a secondary objective of this study is to develop a deterministic (non-probabilistic) barge impact load-prediction framework that takes into account the sensitivity of impact loads to barge orientation. For this task, a parametric study of high-resolution finite element analyses of barge bow crushing is conducted. Using these data, the dependence between barge impact forces and barge orientation (impact obliquity angle) is quantified. Probabilistic

simulation tools are again employed to develop a load-prediction model for use in design that takes into consideration not only the sensitivity of impact loads to obliquity, but also the probability of impact occurring at particular orientation angles. This load-prediction model, when combined with the newly developed PC expression, allows designers to assess the risk of structural failure due to barge impact using non-probabilistic analysis tools while still accounting for uncertainties involved in barge collision loading and structural performance.

1.3 Scope of Work

- Conduct a literature review: A literature review is conducted in which studies are identified that focus on the improvement of, or the development of alternative frameworks to, the probability of collapse determination procedure given in the AASHTO provisions. Based on the studies identified, limitations of the existing AASHTO probability of collapse determination procedure are assessed. Additionally, as part of the literature review, statistical descriptions of pertinent bridge and barge random variables are identified.

- Develop a rational framework for assessing probability of bridge collapse (structural failure): By combining statistical descriptions of barge and bridge parameters; recently developed collision analysis and bridge modeling techniques; and, probabilistic simulation, a probabilistic framework is formed that can be used to assess the probability of collapse (structural failure) for a given bridge structure and limit state(s) of interest.

- Identify representative set of bridge cases and determine applicable structural limit states: Using the previously developed inventory of bridge FE models for bridges located throughout Florida, a representative cross-section of in-service bridges has been selected for study. The bridges selected are all publicly owned, and therefore, the vessel collision limit states defined by the Florida Department of Transportation (FDOT) are applicable in each case.

- Determine expected values of demand, capacity, and probability of collapse for each bridge case: Using the probabilistic framework, expected values are determined for the demand and capacity terms that comprise the limit states applicable to each bridge case. Additionally, limit state exceedance rates (i.e., probability of collapse values) are assessed for each FDOT limit state, and in turn, each bridge case.

- Form revised probability of collapse expression: For each FDOT limit state, a set of demand-capacity ratios and limit state exceedance rate values are paired, and then fit with a regression line that constitutes a probability of collapse expression. Bridge designers can then determine the probability of collapse for a limit state of interest simply by supplying a demand-capacity ratio as input to the applicable regression curve.

- Quantify barge force-deformation characteristics related to oblique impact with flat pier surfaces: A series of high-resolution finite element simulations is conducted that involves crushing a hopper barge bow model with flat-faced pier surfaces of various widths oriented over a range of oblique angles. Force data obtained from these simulations are used to quantify how peak crushing forces are influenced by the width of the impacted pier surface and barge orientation (impact obliquity).

- Develop a revised design-oriented barge force-deformation model that considers the influence of obliquity on impact forces: Empirical expressions relating barge forces to pier width and angle of obliquity are used in a probabilistic study for the purpose of forming estimates of peak barge collision forces that are based on an expected probability of exceedance. Computed forces are used to develop a revised force-deformation model that accounts for the probability of barge impact occurring at specific angles of obliquity and can be employed in a design setting using non-probabilistic barge-bridge collision analysis techniques.

CHAPTER 2
BACKGROUND

2.1 Motivation

From 1960–2002, a total of 31 major bridge collapses occurred worldwide as a result of ship or barge collision (AASHTO 2009). These events cost over 342 lives and generated substantial economic loss. Since 1991, the AASHTO provisions for waterway vessel collision (AASHTO 1991) have provided a means for bridge designers to assess the risk associated with a given waterway, waterway traffic characteristics, and planned bridge layout. As part of the risk assessment, the probability of collapse of each pier in the waterway of interest is determined under the conditional probability that impact is imminent. Due to a scarcity of bridge collapse data, the AASHTO probability of collapse expression was adapted from a study of ship-ship collisions, and furthermore, the expression has not been revised since inception of the AASHTO guide specification.

2.2 Incidents of Barge-Bridge Collision

The 1980 collapse of the Sunshine Skyway Bridge in Tampa, Florida (Fig. 2.1) is considered to be the galvanizing event that led to the development of the AASHTO guide specification. This catastrophic bridge collapse, which resulted in the loss of 35 lives, was the result of a collision between a large cargo ship named the Summit Venture and an anchor pier (Larsen 1993). Cargo ships such as the Summit Venture typically have large drafts, and consequently, can operate in deep waterways such as Tampa Bay, but not most inland waterways.

Figure 2.1 Collapse of the Sunshine Skyway Bridge in Tampa, FL (1980) due to ship collision

Bridge collapses caused by barge collisions are more pertinent to the research proposed here. Barge flotillas have smaller draft depths, enabling both inland waterway and coastal waterway transit. The locations of numerous recent bridge collapse incidents involving barge collisions attest to the relatively higher risk inherent to bridges spanning such waterways.

For example, in 1993, a barge struck the Big Bayou Canot railroad bridge near Mobile, Alabama (Fig. 2.2a). Although the bridge did not immediately collapse, a passenger train soon after crashed while crossing the bridge due to large collision-induced track displacements. Ultimately, the bridge collapsed and 47 people were killed (Knott and Prucz 2000). In 2001, an aberrant 4-barge tow near South Padre, Texas impacted a pier of the Queen Isabella Causeway Bridge (Fig. 2.2b), resulting in the collapse of several spans and numerous fatalities (Wilson 2003). In 2003, a barge tow struck a pier of the I-40 bridge near Webbers Falls, Oklahoma (Fig. 2.2c) In this case, a portion of the superstructure collapsed and 14 people were killed (NTSB 2004). Most recently, in 2009, the Popps Ferry Bridge near Biloxi, Mississippi was struck by an 8-barge flotilla, causing collapse of a span adjacent to the channel piers (Fig. 2.2d).

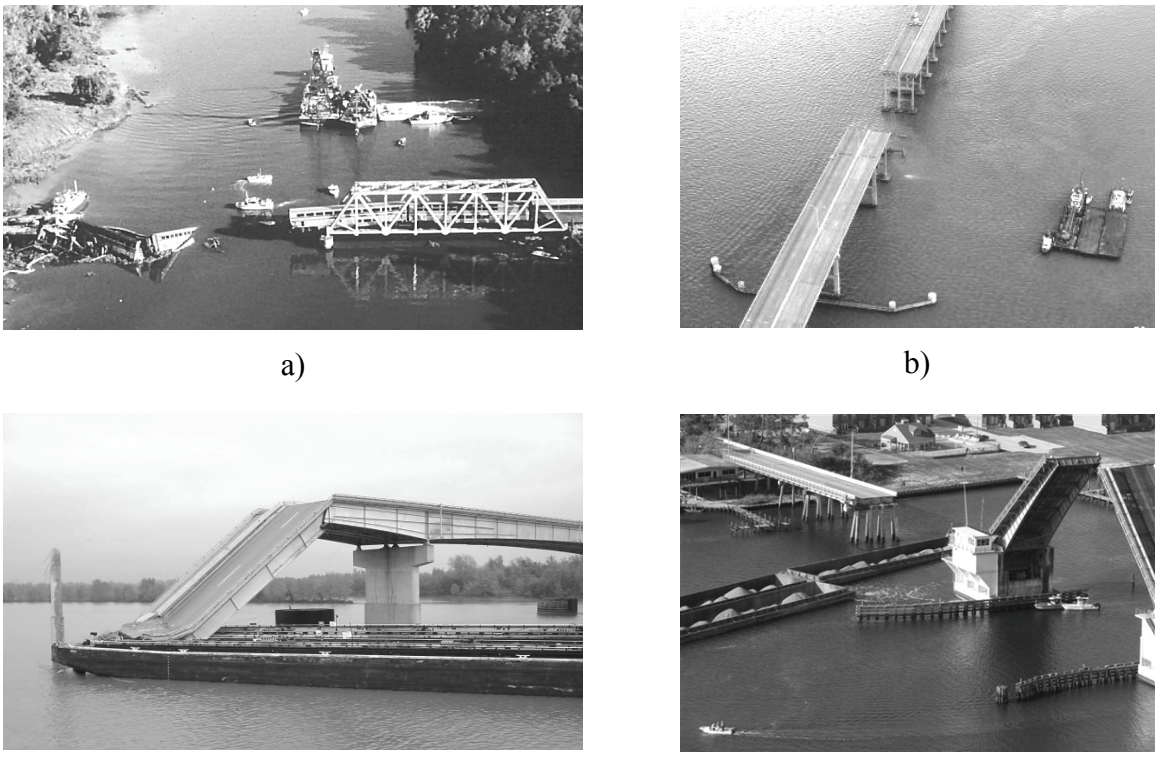

a) b)

c) d)

Figure 2.2 Bridge collapse due to barge collision. a) Big Bayou Canot Bridge, AL; b) Queen Isabella Causeway Bridge, TX; c) I-40 bridge, OK; d) Popps Ferry Bridge, MS. (Source: U.S. Coast Guard)

2.3 AASHTO Risk Assessment for Vessel Collision

The intent of the AASHTO guide specification is to establish analysis and design provisions to minimize susceptibility to catastrophic collapse for bridges that cross navigable waterways (AASHTO 2009). This intent is manifested through a risk assessment that culminates in an annual frequency of collapse expression for bridges:

$$AF = (N)(PA)(PG)(PC)(PF) \tag{2.1}$$

where AF is the annual frequency of collapse (number expected collapses per year) and the inverse of AF is the bridge collapse return period. Return periods of 1,000 and 10,000 years are used for regular and critical bridges, respectively. Vessel trip frequency (N) and dead weight tonnage (DWT) data for traffic on a given waterway may be determined from various government agency resources as listed in Section C3.4 of the AASHTO provisions. Vessels that traverse a given waterway are divided into groups based on type, length, DWT, etc. and each group is assigned a frequency value (N).

For each vessel group, the probability of vessel aberrancy (PA) is found by empirically combining factors such as vessel type; bridge location within the waterway (the bridge may be located in a straight or bend/turn region); waterway current data; and the historical collision rate in the vicinity. Also, for each vessel group, the geometric probability (PG)—the probability that a given pier or span for a bridge will be struck by an aberrant vessel—and the probability of collapse (PC) are determined for each pier and span. The PC term is discussed in greater detail below. The final coefficient in Eq. 2.1—the protection factor (PF)—is determined for each pier, and in turn, for each vessel group. The protection factor varies from 0.0 for piers that are entirely sheltered from impact (e.g., by land masses, dolphins) to 1.0 for piers that are not sheltered from impact.

As a result of grouping each risk coefficient by vessel group, the annual frequency of collapse expression may be given as the sum of the individual risk associated with each pier and span (j) within each vessel group (i):

$$AF = \sum_{i=1}^{N_{VG}} \sum_{j=1}^{N_{PS}} (N_i)(PA_{ij})(PG_{ij})(PC_{ij})(PF_{ij}) \tag{2.2}$$

where N_{VG} is the number of vessel groups and N_{PS} is the number of piers and spans. For barges, the exposed height (the height of the barge above the waterline) is generally small relative to the elevation of the superstructure bottom; hence barge collision with the superstructure spans is precluded. As a result, the annual frequency of collapse for barges may be expressed as:

$$AF = \sum_{i=1}^{N_{VG}} \sum_{j=1}^{N_P} (N_i)(PA_{ij})(PG_{ij})(PC_{ij})(PF_{ij}) \quad (2.3)$$

where N_P is the number of bridge piers in the waterway.

2.4 AASHTO Probability of Collapse Expression

An important component of the annual frequency of collapse expression for barges (Eq. 2.1) is the probability of bridge collapse (PC), which is calculated as conditional impact occurring. The AASHTO PC expression was derived from a study of ship-ship collision damage rates (AASHTO 2009, Fujii and Shiobara 1978). In this derivation, a correlation was made between the ship damage rate, x—the ratio between the estimated damage cost of a ship structure to the estimated ship value (excluding cargo)—and a capacity-to-demand ratio of bridge resistance to barge impact force.

In relating ship-ship collision damage rates to ship-bridge collisions, it was first assumed that impacted bridge piers can be considered as large collision objects relative to the impacting ship. Specifically, only those ship-ship collisions in which the gross registered tonnage (GRT) ratios, y, between the two ships were greater than 10 were considered. Consequently, relative cumulative frequency values for different damage rates were considered to be applicable only for collision incidents where the larger ship possessed at least an order of magnitude more tonnage than the smaller ship (Fig. 2.3a). Furthermore, it was assumed for bridge design that the damage rate, x, could be interpreted as being equal to the ratio of the actual force imparted during a ship-ship collision, p, to the maximum possible force that could be imparted during the same ship-ship collision, p_{max}, (Fig. 2.3b). In the AASHTO adaption of the ship-ship collision data, the damage rate and collision force ratio apply to the smaller ship while the larger ship represents the bridge pier.

From Fig. 2.3b, it was then assumed that ship-ship collision force ratios equal to or greater than 0.1 correspond to a 10% probability of occurrence with uniform distribution. By further assuming a uniform probability density function (PDF) over the remainder of the domain, 90% of the total probability was attributed to ship collision force ratios between 0.0 and 0.1 (Fig. 2.4a). A cumulative distribution function (CDF) for collision force ratios was then obtained by integrating the PDF from right-to-left (Fig. 2.4b).

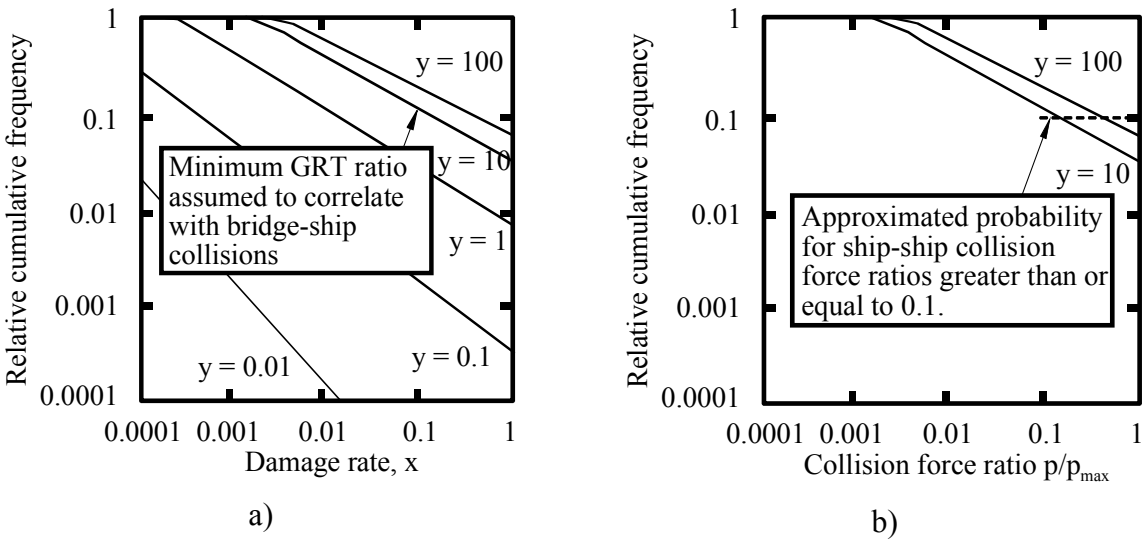

Figure 2.3 Relative cumulative frequency plots (after Fujii and Shiobara 1978). a) damage rates for ship-ship collisions; b) collision force ratio for ship-ship collisions

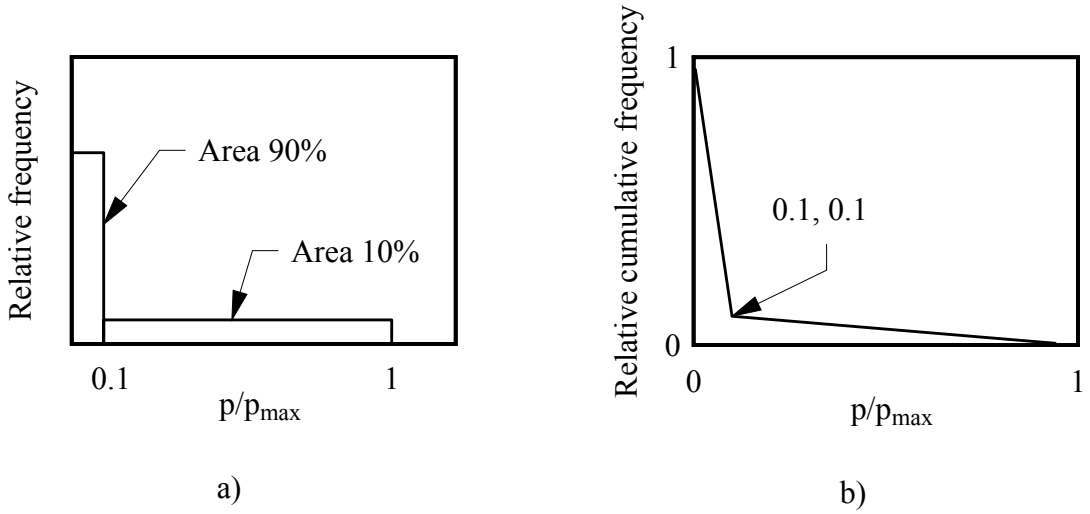

Figure 2.4 Statistical description of ship-ship collision force ratios (after Cowiconsult 1987). a) Probability distribution function; b) Cumulative distribution function

The ship-ship collision force ratio was assumed by AASHTO to be equal to the ratio of the capacity (H) of a given bridge element (e.g., pushover capacity of a pier) to the applied impact force (P_B). Furthermore, the relative cumulative frequency of ship-ship collision force ratios was assumed to possess a correlative relationship with probability of bridge collapse. Due to a lack of data for barge collisions, the probability of collapse curve (Fig. 2.5) was assumed to be applicable to both ship-bridge collisions and barge-bridge collisions.

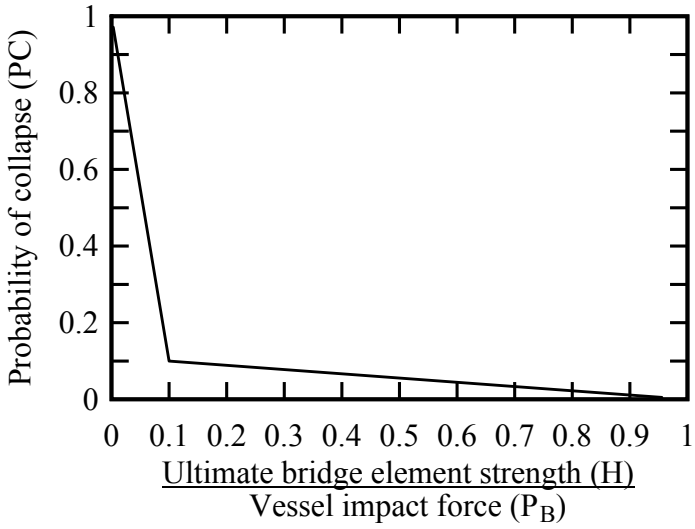

Figure 2.5 Probability of collapse for vessel-bridge collisions (AASHTO 2009)

The probability of collapse (PC) expression is given in AASHTO as:

$$PC=0.1+9\left(0.1-\frac{H}{P_B}\right),\ 0 \le H/P_B < 0.1 \tag{2.4}$$

$$PC=\left(1-\frac{H}{P_B}\right),\ 0.1 \le H/P_B \le 1 \tag{2.5}$$

Note that per AASHTO, for values of $H/P_B > 1$, there is a zero percent probability of bridge collapse.

2.5 Recent Probabilistic Studies of Collision-Induced Bridge Collapse

In 1998, a group of international experts (in the area of vessel-bridge collision) each contributed to a compilation of papers relating to the (then) state-of-the-art in ship-bridge collision analysis (Gluver and Olsen 1998). However, no comprehensive probabilistic framework pertaining to barge-bridge collision was detailed among the papers other than that given in the AASHTO provisions (1991). The AASHTO provisions constitute a means for bridge designers to assess the structural reliability of a given bridge in relation to the corresponding waterway vessel traffic. However, continued incidents of collision-induced bridge collapse have (since 1998) prompted a small number of studies to be undertaken, in which improved or alternate means of assessing bridge structural reliability (as it pertains to waterway vessel collision) are developed.

One pertinent reference is found in Manuel et al. (2006), where it is recognized that a probabilistic treatment of bridge and barge structural descriptors, combined with simulation, could lead to an alternative means of assessing bridge collapse rates. This approach was taken by Wang et al. (2009) as part of the development of a probabilistic framework (as an alternative to the AASHTO provisions) that utilizes the method of moments (of reliability theory) to assess bridge failure probabilities associated with ship collision. However, only a small number (less than five) random variables were included in the proposed framework. Geng et al. (2009) also developed a probabilistic framework for determining vessel-bridge collision forces for three bridges spanning the Yangtze River, China based on a small number of random variables (less than five).

In a study by Proske and Curbach (2005), a multitude of random variables (more than twenty) were used to characterize bridge structural resistance and vessel collision load parameters for multiple, historical bridges spanning German inland waterways. Using the bridge and vessel collision statistical descriptions, probabilistic simulations were carried out for the selected, historical bridges to obtain corresponding probability of failure estimates. Also, in this study, multiple stages of probabilistic simulation were carried out to refine the failure rate predictions (e.g., use of the first order reliability method, FORM, followed by use of the second order reliability method, SORM). Additional details pertaining to the structural reliability of historical bridges are given in Proske and Van Gelder (2009).

2.6 Observations

Previous studies aimed at quantifying bridge collapse (structural failure) rates have largely focused on the assessment of bridge collapse on a case-by-case basis, or alternatively, the development of probabilistic frameworks that are entirely independent of the existing AASHTO provisions. An approach that remains largely uninvestigated, however, is that of working within the existing AASHTO provisions to produce a revised probability of collapse expression, which can feasibly be implemented in the U.S. design provisions. This latter approach is facilitated through identification of the shortcomings present in the existing AASHTO provisions. One of these shortcomings has been recognized above: the AASHTO PC expression is used as part of barge-bridge collision design; however, the expression is based on a study of ship-ship collisions.

An additional, severe shortcoming of the existing AASHTO provisions has been identified as part of recently conducted barge collision analysis studies (Consolazio et al. 2008, Davidson et al. 2010), where dynamic collision analyses were conducted to assess bridge structural response for a representative set of bridges and barge impact conditions. Using the dynamic response data, comparisons were made to the computed design forces from respective static (collision) analyses. The dynamic-versus-static comparisons corroborated findings from previously conducted full-scale impact experiments (Consolazio et al. 2006)—namely, that dynamic effects need to be incorporated into the AASHTO vessel collision design provisions.

This assertion (pertaining to the incorporation of collision-related dynamic phenomena) has implications that extend beyond determination of impact load and bridge structural response. The current PC expression in AASHTO requires essentially two input parameters: the static pushover capacity of a pier (H) and the static impact load (P_B). However, no easily discernable process exists for obtaining these two parameters from analyses that incorporate dynamic effects.

Additionally, the form of the AASHTO PC expression (Eqs. 2.4–2.5) is such that a capacity-demand (H/P_B) ratio (rather than a demand-capacity ratio) is calculated for a given analysis case. Consequently, conspicuously small predictions of PC can be obtained given certain conditions. For example, for a bridge pier with pushover capacity H, if the applied impact load (P_B) is relatively larger by an order of magnitude such that $H/P_B = 0.1$, then Eq. 2.4 gives a PC value of only 0.1. Alternatively stated, even though (in the example) the applied impact load is ten times larger than the bridge pier capacity, the predicted probability of collapse (structural failure) is only 0.1.

Given the need to incorporate dynamic phenomena into bridge design for barge-bridge collision; the utilization of capacity-demand ratios in the current PC expression; and, perhaps most importantly, the fact that the current AASHTO PC expression is based on structural cost damage rates from a ship-ship collision study, the development of improved probability of collapse relationships is warranted. Determining bridge collapse rates directly from nonlinear dynamic barge-bridge collision analyses clearly constitutes a more rational basis for any newly developed PC expressions. Furthermore, analytical tools exist that greatly facilitate such an investigation: studies aimed at developing barge collision modeling and analysis techniques (discussed in Chapter 3) were previously undertaken to establish accurate and efficient means of dynamically obtaining impact-induced bridge internal forces. Using the recently developed collision analysis tools in conjunction with probabilistic simulation techniques (discussed in Chapter 4 and Chapter 5, respectively), revised probability of bridge collapse expressions can be developed and incorporated into the existing AASHTO provisions for bridges subject to barge collision.

CHAPTER 3
MODELING AND ANALYSIS OF BARGE-BRIDGE COLLISION

3.1 Introduction

Probabilistic investigation of barge-bridge collision in the current study involves conducting thousands of simulations for each bridge case of interest. Therefore, methods are employed that are not only capable of producing accurate impacted bridge response, but also, employ efficient response calculations. In this chapter, the structural modeling and analysis techniques used in the current study are presented (probabilistic simulation components are discussed in Chapter 5). Efficient, yet accurate structural modeling and analysis techniques provide an essential component in the development of probability of collapse relationships for barge-bridge collisions.

3.2 Barge Impact Force Determination Using Current Design Provisions

The AASHTO provisions contain a design barge force-deformation relationship that was developed from experimental test data obtained during an early 1980s study (Meier-Dörnberg 1983). In these experiments, several European (type IIa) barge bows were constructed at approximately 1:5 scale, placed upright on a fixed base, and crushed statically and dynamically using presses and impact hammers, respectively. Data collected from these tests were used to formulate an empirical barge force-deformation relationship (the AASHTO curve in Fig. 3.1). This relationship, as adopted in the AASHTO provisions, is currently used in bridge design for barge-bridge collision loading.

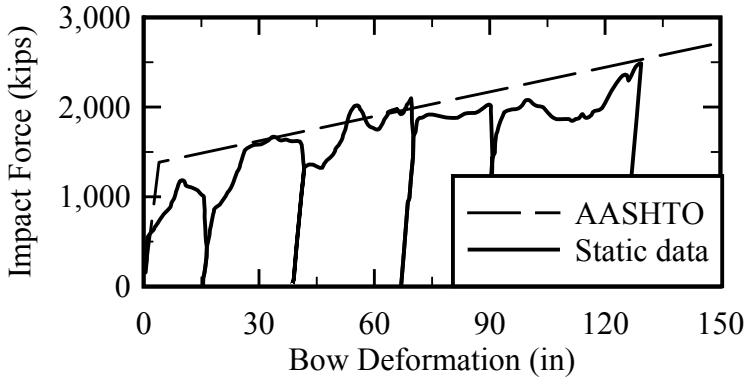

Figure 3.1 AASHTO crush-curve and sample test data (after Meier-Dörnberg 1983)

For a given colliding barge flotilla, or group of barges and tug (with a corresponding total weight and impact velocity), the AASHTO provisions can be used to determine a design impact load imparted to a bridge element (e.g., pier column). Using the barge flotilla weight and impact velocity, the kinetic energy of the barge is computed as:

$$KE = \frac{C_H W V^2}{29.2} \tag{3.1}$$

where KE is the kinetic energy of the impacting vessel (kip-ft), C_H is the hydrodynamic mass coefficient, W is the weight of the barge flotilla (tonnes), and V is the design velocity (or impact velocity) of the barge flotilla in (ft/sec). Using the calculated kinetic energy, the magnitude of barge crushing deformation is determined using the empirical relationship:

$$a_B = \left[\left(1+\frac{KE}{5672}\right)^{1/2} - 1\right]\frac{10.2}{R_B} \tag{3.2}$$

where a_B is the depth (ft) of barge crush deformation (depth of penetration of the bridge element into the bow of the impacting barge), KE is the barge kinetic energy (kip-ft), and $R_B = B_B/35$; where B_B is the barge width (ft). A static impact load is then determined using the empirical relationship:

$$P_{Bs} = \begin{cases} 4112 a_B R_B & \text{if } a_B < 0.34 \\ (1349 + 110 a_B) R_B & \text{if } a_B \geq 0.34 \end{cases} \tag{3.3}$$

where P_{Bs} is a static barge impact load (kips).

3.3 Limitations of the Existing Design Provisions for Barge Impact Loading

Recent studies have identified severe shortcomings associated with the use of the barge impact loading scheme that is present in the current design provisions:

- As identified in Consolazio et al. (2009a,) the Meier-Dörnberg (1983) tests, while extremely valuable, utilized rib-stiffened (largely hollow) internal barge structures that were common to European waterways. However, the barge structures that were subjected to crushing are not representative of common U.S. barge types, which are generally internally stiffened by a network of transverse and longitudinal trusses (Cameron et al. 1997).

- Full-scale barge-bridge collision tests conducted in 2004 (Consolazio et al. 2006) revealed that the mass of the superstructure overlying an impacted bridge pier can generate significant inertial forces during vessel collision events and that these inertial forces can amplify pier column demands. The barge impact loading approach given in the current

AASHTO design provisions does not account for the significant dynamic amplification effects.

Consequently, recently developed modeling and analysis techniques (discussed below) are employed in the current study.

3.4 Barge Bow Force-Deformation Relationships for Bridge Design

Given the limitations associated with the currently adopted AASHTO force-deformation relationship, barge-bow crushing behavior has recently been investigated numerically using high-resolution finite element (FE) simulations (Consolazio and Cowan 2003; Yuan et al. 2008). As part of the findings from both studies, it was determined that barge bow response is strongly dependent on the size and shape (i.e., the geometry) of the impacted surface. It was also found that impact forces do not necessarily increase monotonically with increasing crush deformation (as is the case for the curve shown in Fig. 3.1).

3.4.1 Barge bow force-deformation relationships for direct (head-on) impact

A recent study was carried out to analytically develop barge bow force-deformation relationships—as an update to the existing AASHTO force-deformation relationship—for use in bridge design (Consolazio et al. 2009a). Detailed structural barge plans were obtained from manufacturers and used to develop FE models of a jumbo hopper and oversize tanker barge (the two most common barge types in the US), for analysis using the nonlinear finite element analysis (FEA) code LS-DYNA (LSTC 2009). Each barge model consisted of three primary sections: a relatively short bow, a long hopper or tanker area, and a relatively short stern. In previously conducted crushing simulations, peak force levels generally occurred at low deformation levels (relative to overall barge length), therefore, only the bow section of each barge was modeled (Fig. 3.2).

3.4.2 Barge model components

Barge components were generally modeled using four-node shell elements (totaling more than 120,000 elements per barge). [The tanker model aft-most longitudinal truss members were modeled using cross-section-integrated beam elements.] Shell elements were used ubiquitously to allow for local and global member buckling. Individual steel members were joined through a combination of continuous and intermittent welds, where weld failures were represented through element deletion when shell element strains reached the defined material failure state. Steel (A36) material properties (Consolazio et al. 2009a) were specified for all barge components (most barges fabricated in the U.S. are constructed from A36 structural steel).

Analyses were conducted by fixing the rear section of each barge bow model and advancing a rigid impact surface (having the shape and size of a pier element) in a direct, head-on manner (Fig. 3.3) at a constant prescribed velocity (48 in/sec). Due to the quasi-static

nature of the simulations, strain-rate effects were not included in the barge bow models. Steel-to-concrete (barge to impacted surface) contact, and simultaneously, self-contact (steel-to-steel) definitions were employed between various components inside the barge bow. Additional details of the structural models are discussed in Consolazio et al. (2009a).

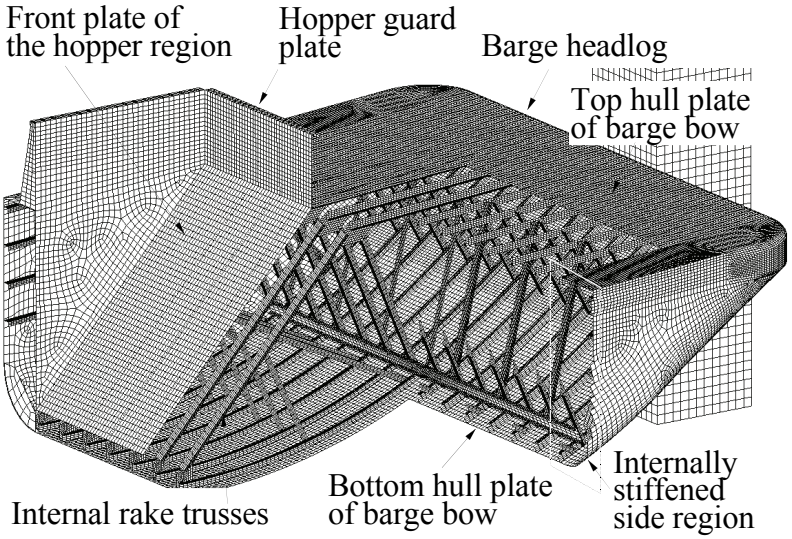

a)

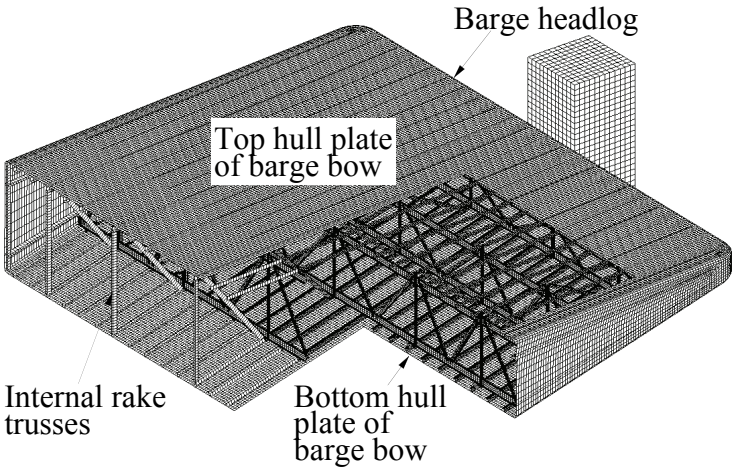

b)

Figure 3.2 Barge bow internal structures (not to relative scale, Consolazio et al. 2009a). a) Jumbo hopper; b) Oversize tanker

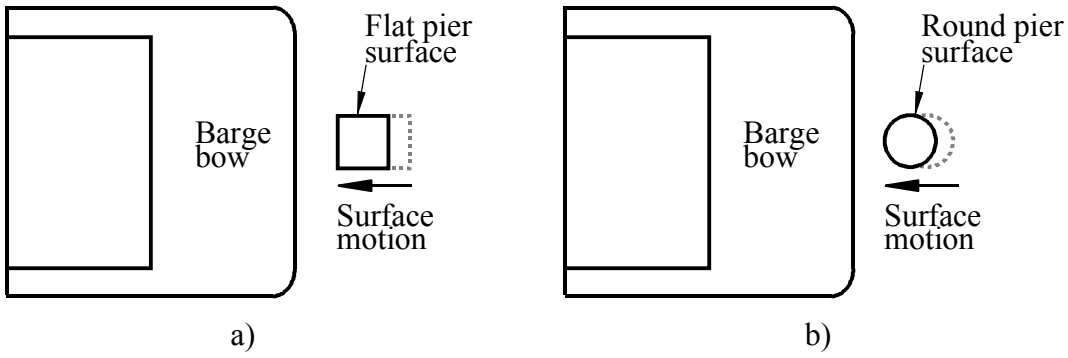

Figure 3.3 Head-on barge bow crushing simulation schematics.
a) Flat surface; b) Round surface.

3.4.3 Direct (head-on) barge bow crushing simulation findings

The following observations were made after simulating direct (head-on) bow crushing with various flat-faced (square) and round impact surfaces (with widths ranging from 1 ft to 35 ft) at both centerline and non-centerline locations:

- Comparisons between simulated force-deformation results and available full-scale data (Fig. 3.4) were found to be in agreement (Consolazio et al. 2009a);

- Crushing force magnitudes were not sensitive to barge type (despite differences in overall width) or impacted surface location (relative to the barge centerline);

- Plastic loads associated with barge bow yielding are reached at small bow deformations (approximately 2 in. for the cases considered)

- For the simulations conducted, barge forces do not increase monotonically with respect to deformation level, and so, elastic-perfectly-plastic force-deformation relationships can be used to envelope force-deformation data; and,

- Relationships between peak impact force and pier width were recognized as necessary components of the proposed design curves.

Crush data obtained for flat-faced piers indicated that one of two mechanisms determined peak impact force (Fig. 3.5a). For flat-faced piers with widths less than approximately 10 ft, the barge hull plate membrane yield or rupture capacity governed the global maximum impact force. For larger-width flat-faced piers, the yield capacity of the internal trusses in the barge governed the global maximum of impact force. In contrast, maximum force magnitudes for impact simulations corresponding to round (circular) piers (Fig. 3.5b) were limited by the gradual

progression of deformation across the barge bow width. This phenomenon precluded peak force generation due to the simultaneous yielding of multiple-trusses (as exhibited during large-width flat-faced impacts), and also resulted in a less pronounced dependence between impact force and impact surface diameter (width).

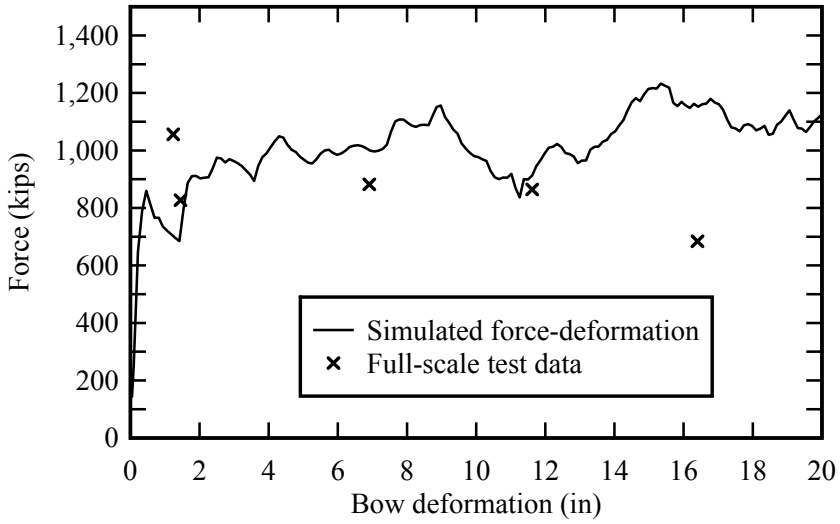

Figure 3.4 Analytical force-deformation data compared to data from tests conducted on the St. George Island Bridge (from Consolazio et al. 2009a)

Distinct linear trends associated with each behavioral mode were clearly identifiable over the respectively applicable ranges of impacted surface widths, and therefore, linear regression trend-lines were fit through the peak force data (Fig. 3.5). Each regression line was then scaled up by 1.33 to account for the possibility of higher steel strengths or thicker hull plates (scale factor derivation is detailed in Consolazio et al. 2009a). Subsequently, the scaled regression line coefficients were rounded to facilitate use in design applications. In Fig. 3.6, a flowchart is shown that summarizes the process for determining elastic-perfectly-plastic barge bow force-deformation relationships for flat-faced and round impact surfaces. In this process, a plastic (yield) crush force (P_{BY}) is first determined for a given surface type (flat-faced or round) and width (w_P) (Fig. 3.6, top and center). Then, a barge bow force-deformation model is formed (Fig. 3.6, bottom) by pairing P_{BY} with a yield crush depth of 2 in.

3.4.4 Barge bow force-deformation relationships for oblique impacts on flat surfaces

As discussed above, width-dependent barge bow force-deformation relationships have been developed for two common impact surface types (flat and round). For round impact surfaces—in which the entire width of the impact surface is engaged by the barge—the applicable barge bow force-deformation model is independent of impact angle (partial engagement of round impact surfaces is discussed in Appendix C). For flat impact surfaces, however, barge force-deformation relationships are only applicable to directly head-on impact scenarios (Fig. 3.7a). To increase applicability of the curves derived from flat impact surface

crushing simulations, additional simulations were carried out using previously developed barge bow models (Consolazio et al. 2009b) and obliquely oriented flat impact surfaces (Fig. 3.7b).

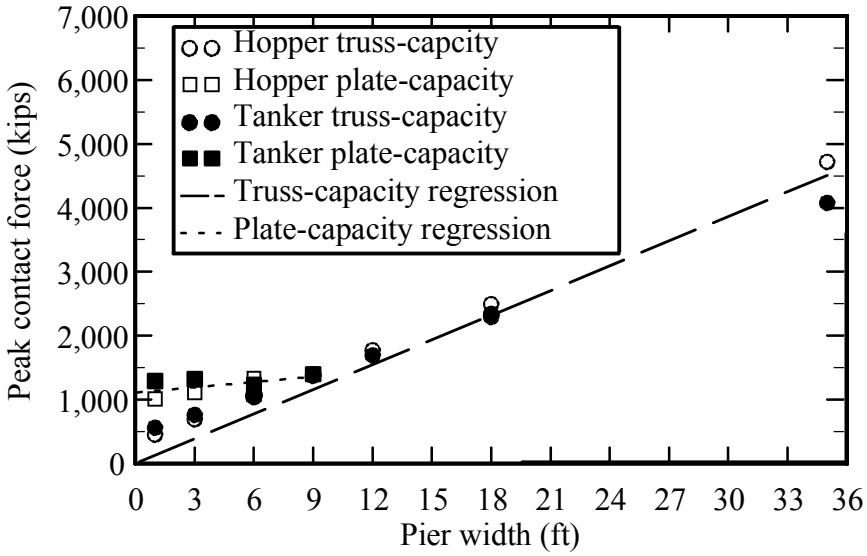

a)

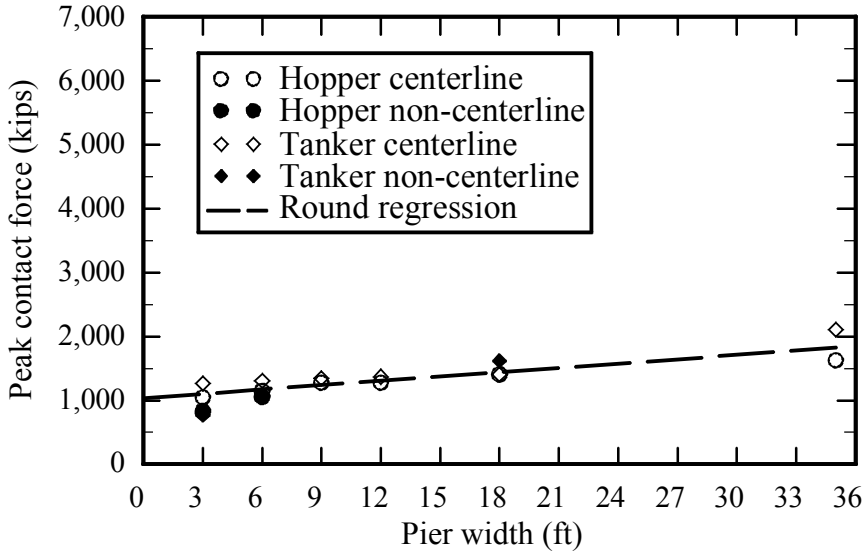

b)

Figure 3.5 Barge peak contact force versus impactor width regression curves (after Consolazio et al. 2009a). a) Flat data; b) Round data

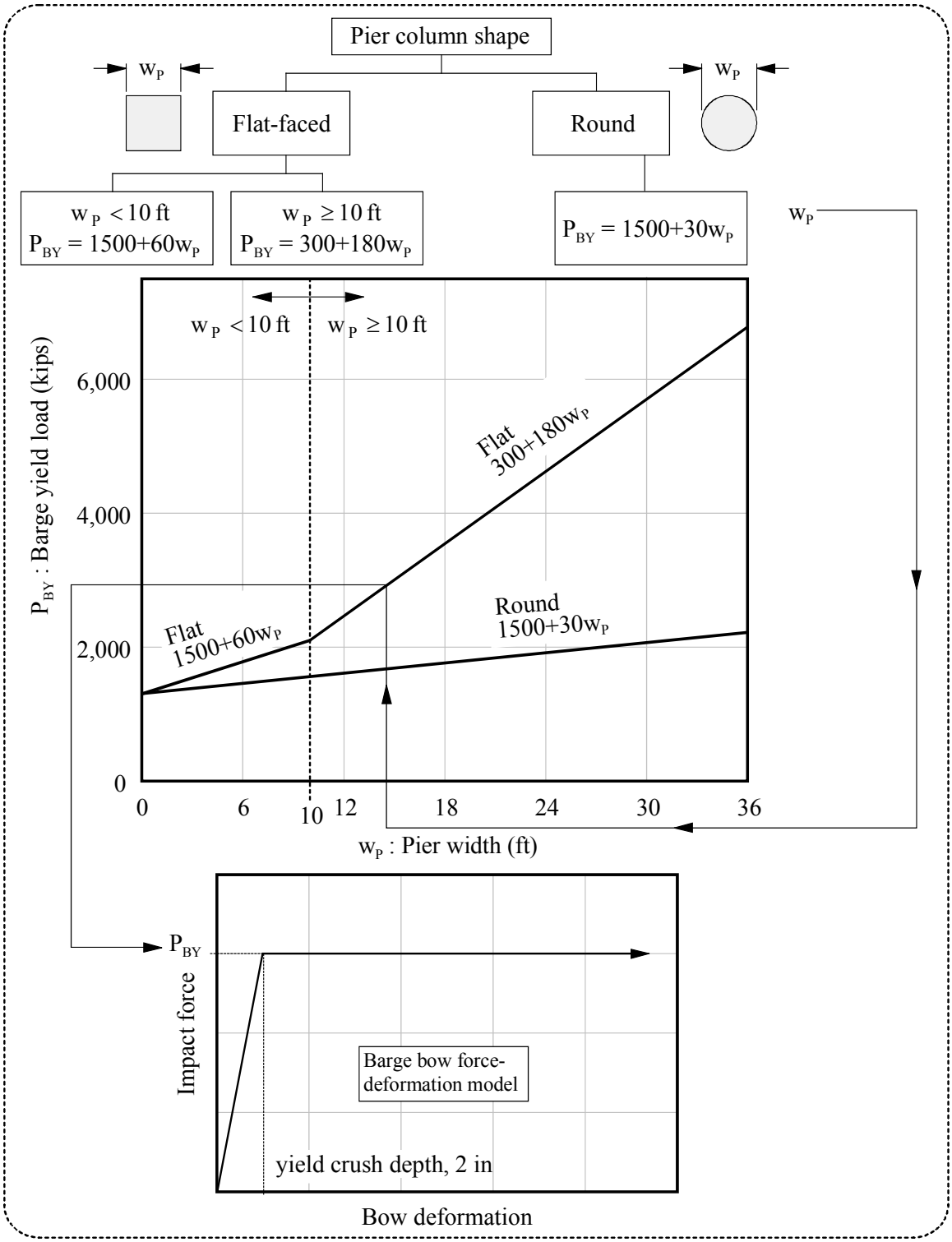

Figure 3.6. Barge bow force-deformation flowchart (after Consolazio et al. 2009a)

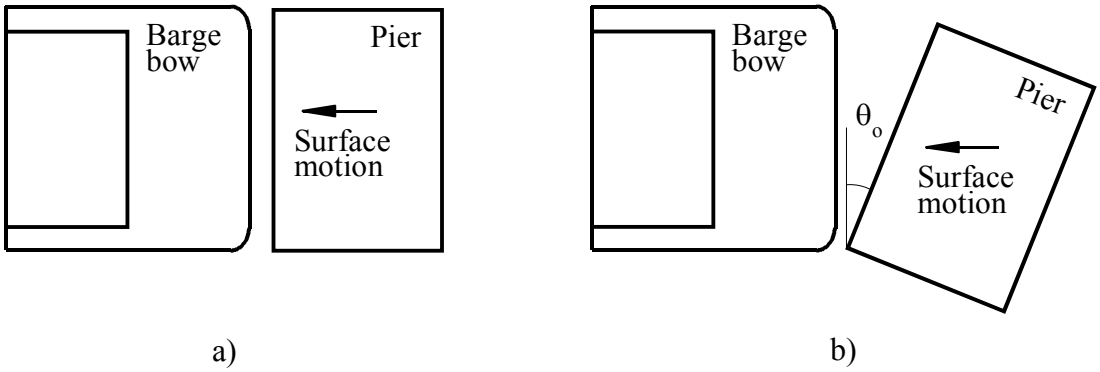

Figure 3.7 Barge bow crushing simulation schematics. a) Head-on; b) Oblique

The maximum forces associated with oblique simulations exhibit a 30% decrease (relative to maximum head-on forces) at an oblique angle of only 2° (Consolazio et al. 2009b). For simulations involving oblique angles greater than 2°, however, maximum force levels were found to be independent of impact surface obliquity (relative to the barge). Accordingly, an impact force reduction scheme was developed (Consolazio et al. 2009b) for obliquely oriented flat impact surfaces:

$$P_{BYO} = P_{BY} \cdot (1400e^{-1.6\theta_O} + 3000) / 4400 \tag{3.4}$$

where P_{BYO} is the maximum (plastic) oblique impact force (kips) and θ_O is the angle of obliquity in degrees. In the analyses used to develop the revised probability of collapse expression, discussed in Chapters 4-8 of this report, an explicit probabilistic treatment of impact angle is used in conjunction with the deterministic force reduction equation (Eq. 3.4) to compute impact angles and loads.

In addition to the findings documented in Consolazio et al. (2009b), additional oblique simulations have also been conducted as part of the present study. In Chapter 9, results from these additional simulations are used to develop a design-oriented force-deformation framework that implicitly accounts for both force reductions arising from obliquity *and* the probability of impacts occurring at particular oblique angles. It is important to note that the method presented in Chapter 9 is intended for use in typical bridge design calculations and is not suitable for use within the probabilistic analyses discussed in Chapters 4-8. This is due to the fact that the method presented Chapter 9 implicitly incorporates a probabilistic treatment of impact angle—making it simple to use in bridge design—but impact angles must be treated explicitly within the probabilistic analyses discussed in Chapters 4-8.

3.4.5 Barge bow force-deformation relationships for pointed impact scenarios

In contrast to oblique impacts, sharp-corner impacts (Fig. 3.8a) were not investigated as part of the previously conducted simulation studies. For the current study, therefore, previously developed barge bow models (from Consolazio et al. 2009a) have been employed in bow crushing simulations involving flat impact surfaces, where the impact surfaces are oriented such that a sharp corner first contacts the barge bow at the bow centerline. Specifically, these simulations have been carried out for both hopper and tanker barge types in 15° increments (Fig. 3.8b).

It is clear from the force-deformation data (Fig. 3.8b–c) that barge bow response for sharp-corner (pointed) impact conditions is generally independent of orientation angle (θ_P) and barge type. Additionally, increases in impact load are exhibited for most cases over the full range of simulated crush depths. This latter observation precludes the use of elastic-perfectly-plastic force-deformation relationships to represent barge bow response during sharp-corner impacts.

An expression governing barge bow force-deformation behavior for this type of impact has been developed by defining a bilinear envelope of the simulated data. The first linear segment of the envelope (Fig. 3.8b) was created using the maximum initial stiffness among the dataset. The second segment was formed using the minimum slope and intercept necessary to envelope the entire dataset (Fig. 3.8c). Consistent with that of the Consolazio et al. (2009a) study, coefficients of each envelope segment were then scaled up by a factor of 1.33 to account for barge material and plate thickness variability. To facilitate use in design applications, coefficients of the scaled expression have been rounded, resulting in:

$$P_{BP} = 1000 \cdot d,\ 0 \le d < 1;\quad P_{BP} = 16 \cdot d + 984,\ d \ge 1 \tag{3.5}$$

where P_{BP} is the impact force (kips) as a function of barge bow crushing deformation, d (in.).

3.5 Coupled Vessel Impact Analysis (CVIA)

The barge force-deformation relationships discussed above facilitate the modeling of barges as single-degree-of-freedom (SDF) systems for dynamic barge-bridge collision analysis, in which dynamic amplification effects are inherently incorporated into the analysis framework. Coupled vessel impact analysis (CVIA), developed previously (Consolazio and Cowan 2005), is one such dynamic analysis technique that employs a SDF vessel model. As part of the CVIA method, a shared contact force, P_B, is used to computationally link a SDF vessel model—with stiffness, mass, and initial velocity—to a multiple-degree-of-freedom (MDF) bridge model (Fig. 3.9). Upon impact, the vessel generates a time-varying impact force and the MDF bridge-soil model displaces and develops internal forces in reaction to the imparted load.

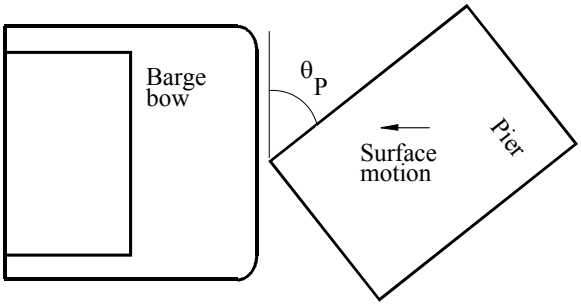

a)

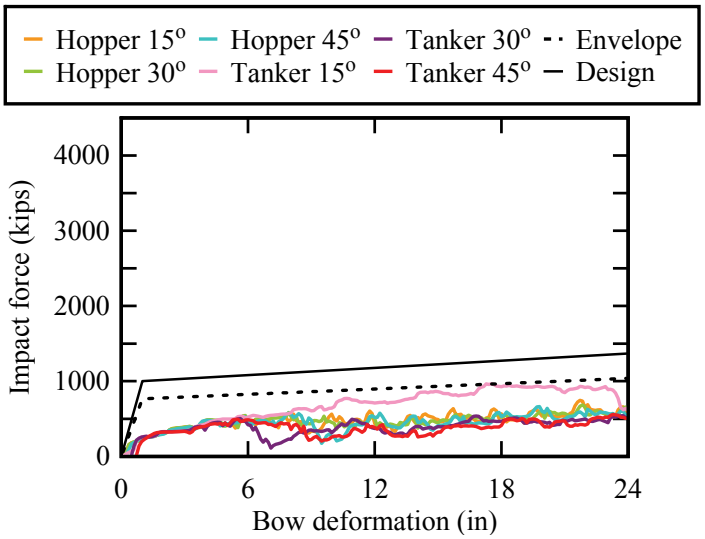

b)

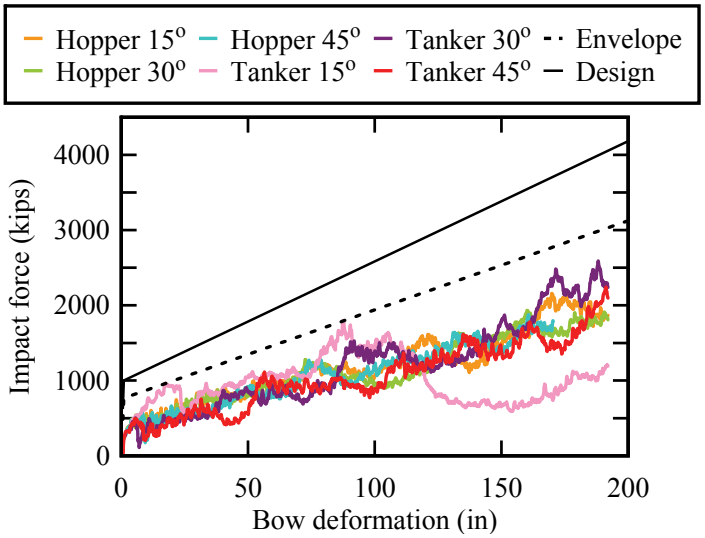

c)

Figure 3.8 Pointed crush simulations. a) Schematic; b) Simulated force-deformation data, initial slope; c) Simulated force-deformation data, full dataset

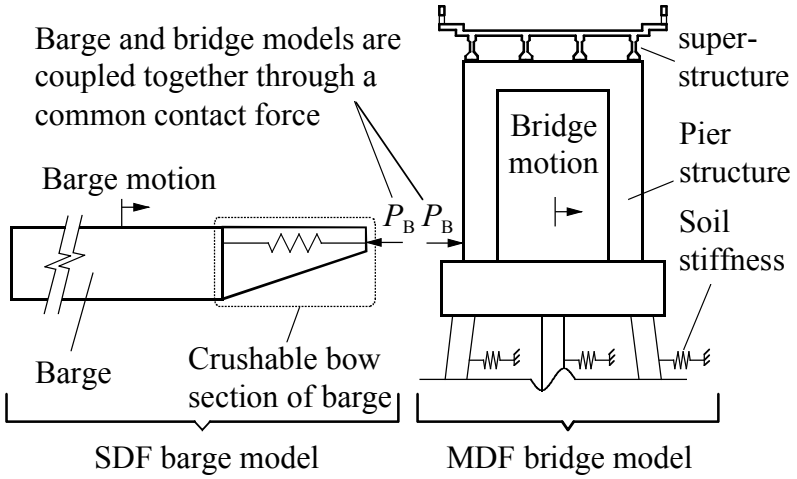

Figure 3.9 Coupling between barge and bridge (after Consolazio and Cowan 2005)

3.6 Validation of Coupled Vessel Impact Analysis (CVIA)

Using data from selected full-scale experimental impact tests on bridges, validation of CVIA was carried out (Consolazio and Davidson 2008). As part of the full-scale barge impact experiments, which were conducted at St. George Island, FL in 2004 (Consolazio et al. 2006), data were collected during tests conducted on an isolated channel pier, termed Pier 1-S (Fig. 3.10a). The fourth test conducted on Pier 1-S (referred to as test P1T4) generated the largest measured impact force, and therefore, data from this test were used for validation case V1. Similarly, data from the fourth test on a partial bridge structure, termed B3 (Fig. 3.10b), were selected for validation case V2; the largest force from the B3 test series was generated during the fourth test (referred to as test B3T4).

Structural models for cases V1 and V2 (Fig. 3.10) were developed from construction drawings and direct site measurements. Soil models for V1 and V2 were developed based on boring logs and dynamic soil properties obtained from a geotechnical investigation (McVay et al. 2005) conducted in parallel with the structural impact testing. The bridge FEA software FB-MultiPier (2009) was used for validation modeling and analysis.

For each case (V1 and V2), an analysis was conducted in which the experimentally measured load time-history was irectly applied at the impact point on the pier. The resulting displacement-history of the structure was compared to experimentally measured displacement data, then adjustments to the structure and soil models were made, and the process repeated. Once direct analytical application of the experimentally measured load produced a computed pier response in agreement with experimental data, validation of the CVIA method was undertaken by replacing the directly applied load with a SDF barge model in the analysis process.

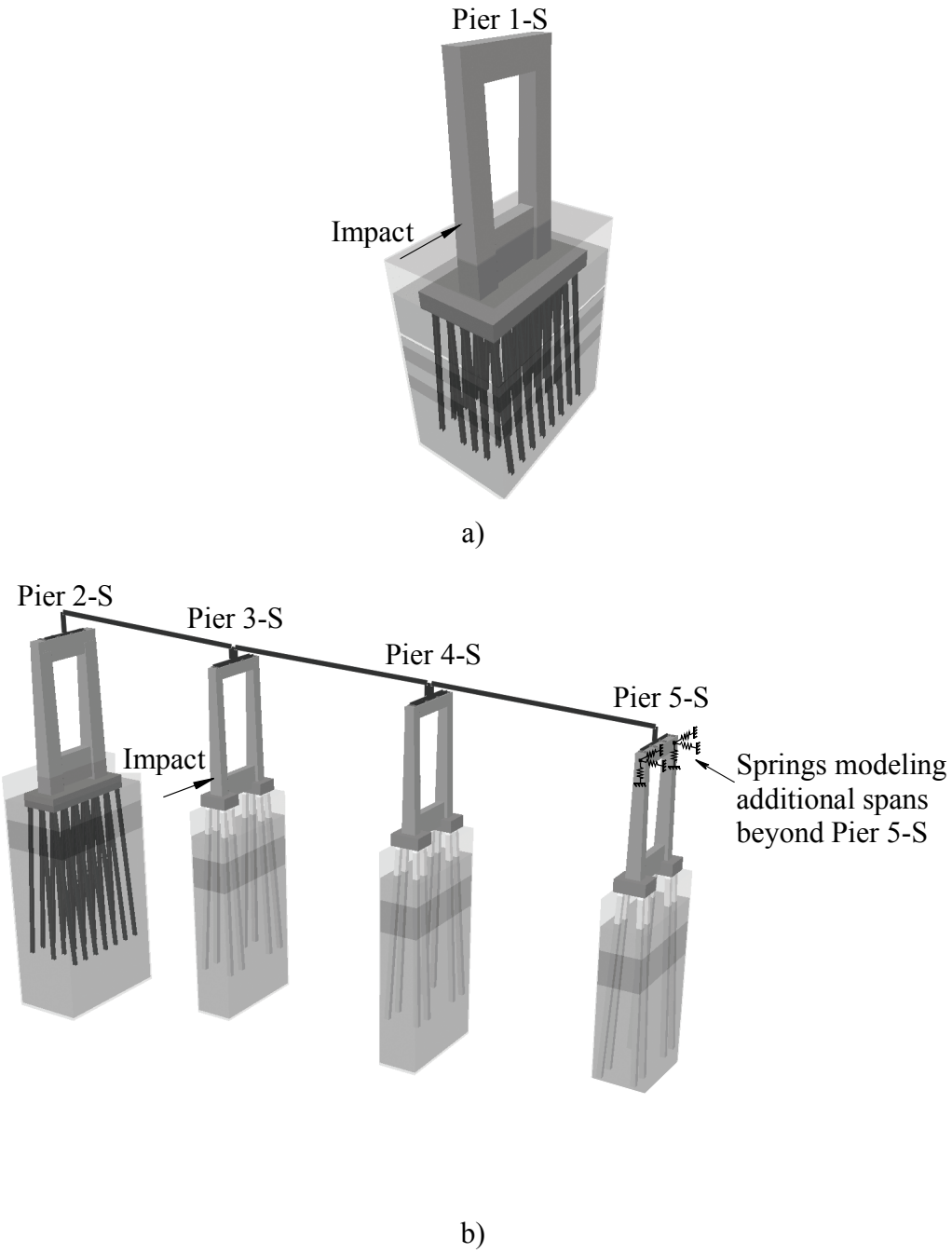

Figure 3.10 Validation models (Consolazio and Davidson 2008). a) V1; b) V2

In CVIA, the stiffness of the barge bow is modeled by a force-deformation relationship. For cases V1 and V2, the loading portion of the force-deformation relationship (Fig. 3.11) was derived from impact-point force and displacement data experimentally measured during test P1T4. Beyond the peak force point on the force-deformation relationship, experimental data were not available. Hence, barge bow crushing data from a previous study (Consolazio and Cowan 2003) were used to develop the remainder of the crush curve.

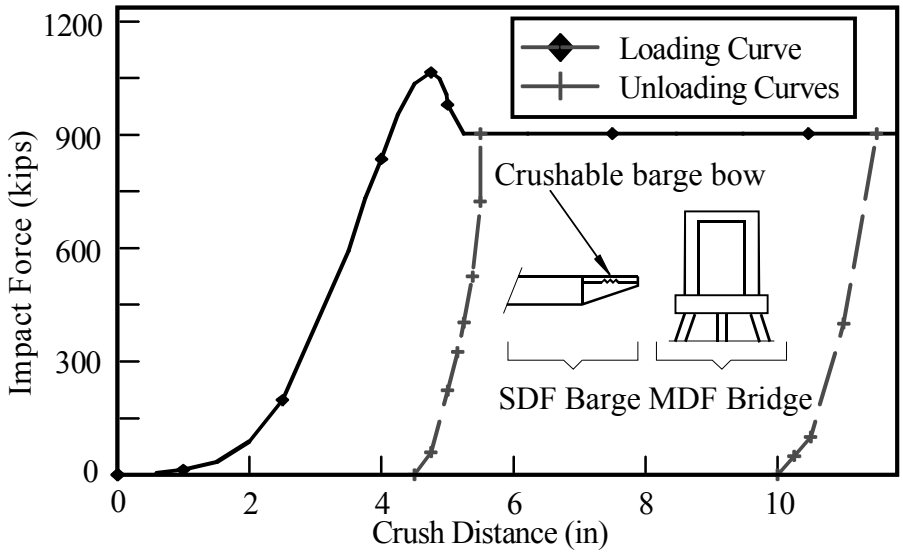

Figure 3.11 CVIA barge bow force-deformation curve features (Consolazio and Davidson 2008)

In Fig. 3.12, comparisons of CVIA and experimental data are shown for cases V1 and V2. Generally, the force and displacement time-histories, respectively show excellent agreement. Supplementary validations for additional impact conditions (Davidson 2007) on Pier 1-S and the B3 configuration exhibit similar or better levels of agreement. Consistent agreement in displacements demonstrates that coupled analysis is capable of predicting accurate pier response data, even when superstructure effects are present. Agreement between predicted and measured pier response is the most important outcome of the CVIA procedure since internal member forces ultimately govern structural design.

3.7 One-Pier Two-Span (OPTS) Bridge Modeling

When vessel-bridge collisions occur, stiffness and mass dependent superstructure restraint can result in a significant portion of the impact load being transferred from the impacted pier to the overlying superstructure. Hence, the influence of adjacent non-impacted piers and spans must be included in vessel-bridge collision analyses. However, employing the CVIA technique for multiple-pier, multiple-span bridge models can require substantial computing and post-processing resources. Alternatively, such structures can be analyzed in a numerically efficient manner using an equivalent one-pier two-span (OPTS) bridge model (Consolazio and Davidson 2008).

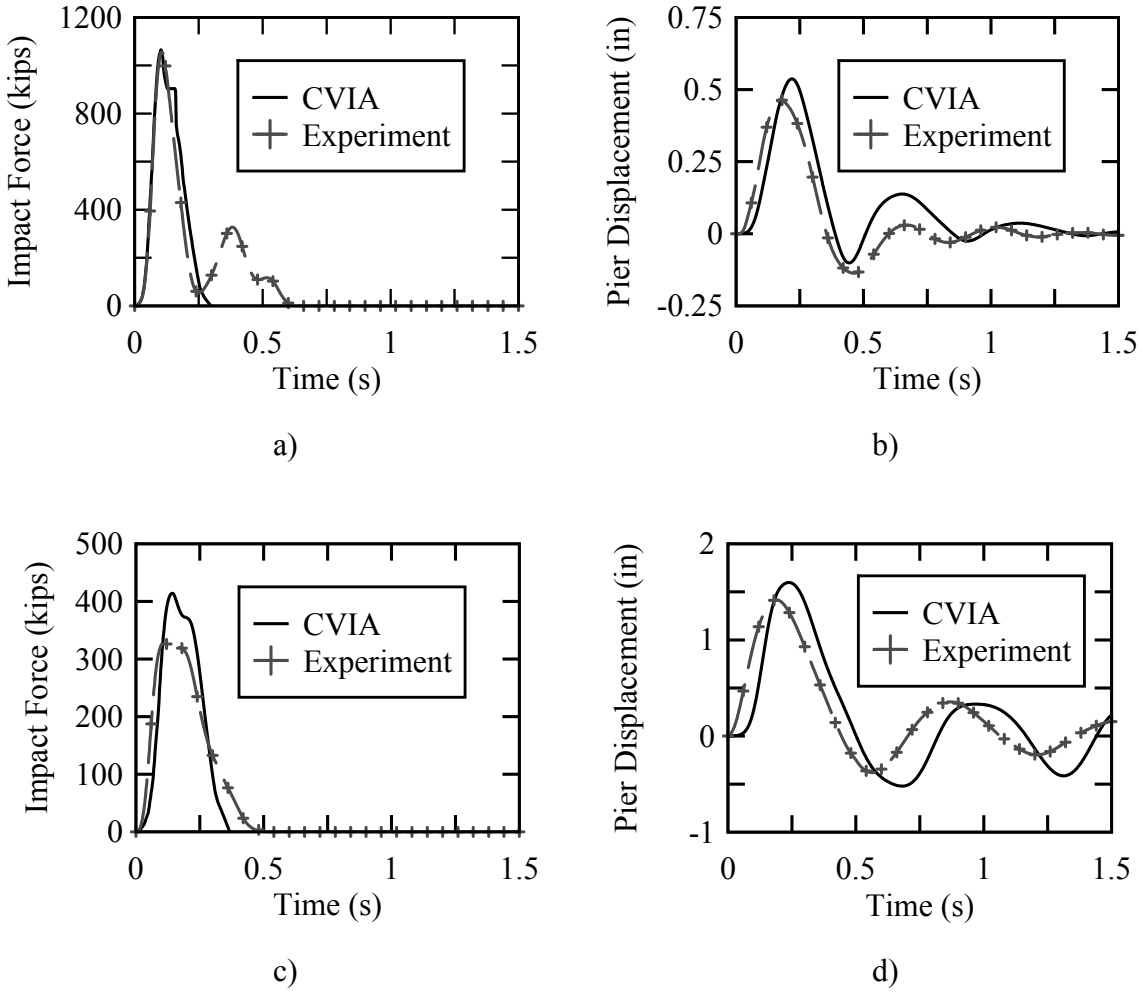

Figure 3.12 CVIA and experimental data (after Consolazio and Davidson 2008). a) V1 impact force; b) V1 pier displacement; c) V2 impact force; d) V2 pier displacement

The OPTS model simplification procedure involves reducing a multiple-pier, multiple-span bridge model to an equivalent model with concentrated stiffnesses and masses connected at the distant ends of each of two retained spans (Fig. 3.13). The concentrated stiffnesses are formed using stiffness condensation (e.g., flexibility matrix inversion) for each of the left and right flanking structures (Fig. 3.13a). The lumped masses are formed by simply lumping each of the half-span masses, as indicated in Fig. 3.13b, at the ends of the OPTS model. A further simplification is made by negating off-diagonal stiffness terms at each condensed stiffness location, resulting in a set of independent springs and lumped masses at each end of the OPTS model (Fig. 3.14).

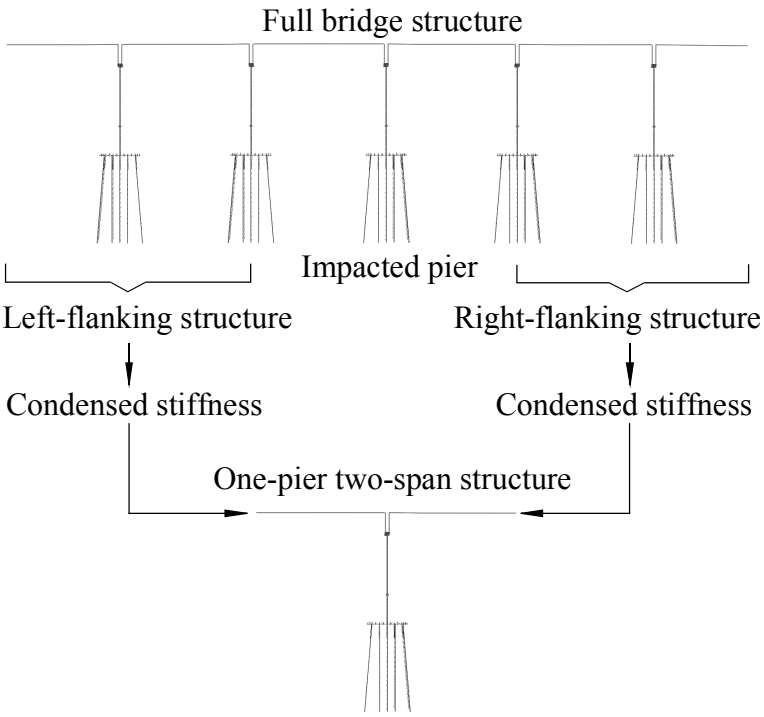

a)

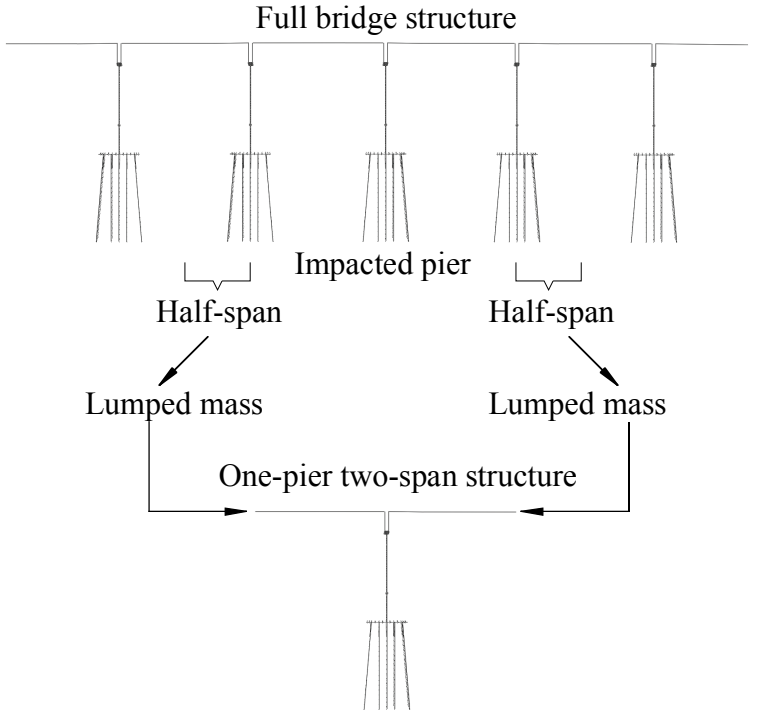

b)

Figure 3.13 Stiffness and mass condensation for OPTS model (after Davidson and Consolazio 2008). a) Condensed stiffness; b) Lumped mass

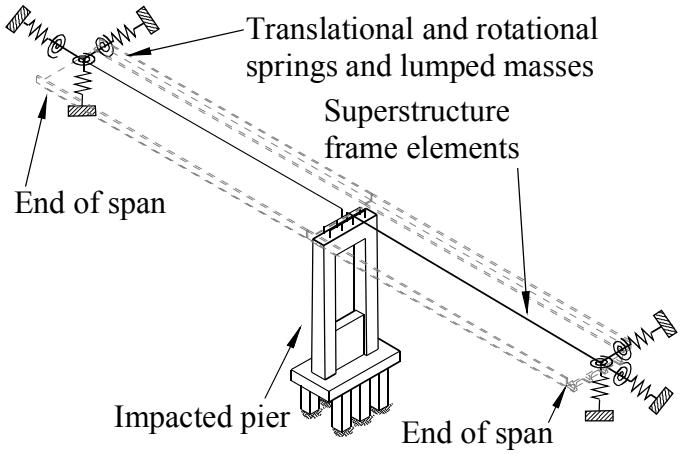

Figure 3.14 OPTS numerical model (Consolazio and Davidson 2008)

3.8 Verification of One-Pier Two-Span (OPTS) Bridge Modeling

From construction drawings, FB-MultiPier models of thirteen Florida bridge structures of varying age, size, and structural configuration were developed (Consolazio et al. 2008) to form a FE bridge model inventory. Once completed, four models (Table 3.1) with centrally located channel piers and four models with centrally located off-channel piers were selected for analysis. The central pier of each selected model was subjected to CVIA with various impact conditions to evaluate the level of agreement between full-bridge and OPTS models for a broad range of bridge and pier configurations. Structural configuration details and detailed analysis results for each of the OPTS verification cases are given in Consolazio et al. 2008.

Table 3.1 OPTS demonstration cases from bridge inventory (Consolazio et al. 2008)

Bridge Name	Verification case ID
SR-20 at Blountstown	BLT
New St. George Island Causeway	NSG
Old St. George Island Causeway	OSG
John Ringling Causeway	RNG

From the parametric study, maximum internal forces (e.g., column moments) predicted using OPTS models—normalized by the respective full-bridge values—are near or slightly greater than unity (Fig. 3.15). [The notation used in Fig. 3.15 is used to distinguish between channel (CHA) and off-channel (OFF) impacts for various impact energies: low (L); medium (M); high (H); or severe (S). The impact energies are quantified in Consolazio et al. 2008.] Required computation times for the OPTS models were generally reduced by an order of magnitude from those required to perform a full multiple-pier, multiple-span bridge analysis. In absolute terms, CVIA analysis combined with OPTS modeling typically enables accurate prediction of maximum dynamic internal forces in 15 minutes or less (Consolazio et al. 2008).

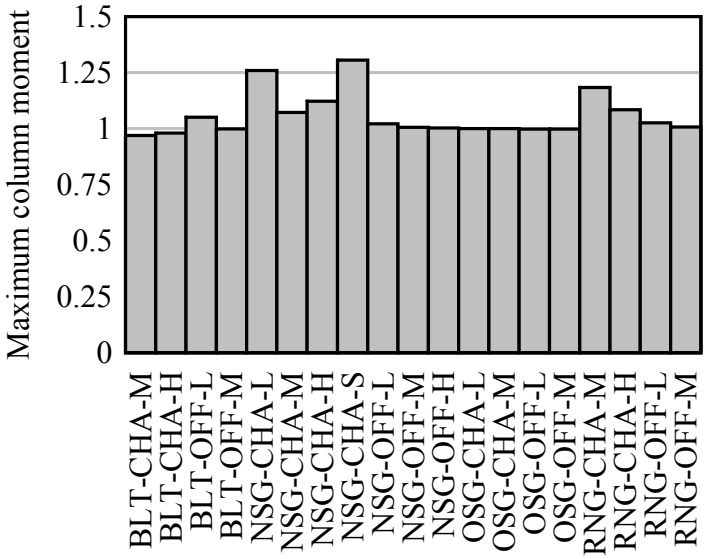

Figure 3.15 CVIA comparison for full-bridge and OPTS models (normalized by full-bridge results; after Consolazio et al. 2008).

3.9 Incorporation of Permanent Loads in Transient Dynamic Analysis

All dynamic vessel collision analyses conducted as part of the current study include structural member self-weight (dead) load due to gravity (with buoyancy effects included). When conducting a static (as opposed to dynamic) analysis, the application of permanent loads (e.g., gravity loading) is typically straight-forward. During static analysis, the structure achieves static equilibrium under the combination of self-weight and other sources of loading. However, to properly incorporate permanent loads into the structure as part of a dynamic analysis, careful consideration of non-transient loads, such as self-weight, is important.

Dynamically, abrupt application of self-weight loading is unrealistic, and furthermore, can lead to undesired dynamic pier response. The effect of sudden load application in a transient (i.e., time-history) dynamic analysis for an SDF system is illustrated in Fig. 3.16. Inertial forces caused by motion of the SDF mass (with weight, w) push the system far beyond the static displacement (u_{st}). By applying the load abruptly, the maximum dynamic displacement (u_{max}) is 100% larger than that predicted by a static analysis. Additionally, the excessive displacement (u) leads to amplified internal forces, which can in turn lead to inelastic deformations.

When a bridge structure is subjected to suddenly applied loads, vertical oscillations result in amplified axial forces in the pier columns and piles. Furthermore, if additional loads are applied (e.g., barge impact loads), vertical oscillations due to the suddenly applied self-weight can artificially amplify demands throughout the pier. The erroneous pier behavior caused by instantaneous self-weight application renders any assessment of structural response, such as load-moment interaction, unreliable.

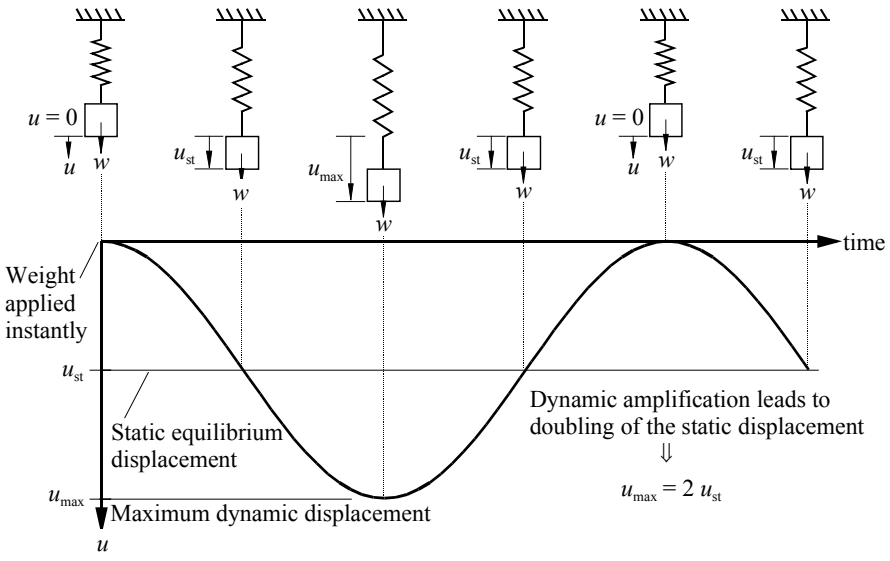

Figure 3.16 Dynamic amplification due to instantaneous load application (after Consolazio et al. 2009b).

In the current study, all dynamic collision analyses are initialized such that the dynamic system is in equilibrium with static loads (e.g., gravity loads). Specifically, for each collision scenario considered, two distinct analyses are conducted—one static analysis (with only gravity and buoyancy loading), and one dynamic analysis, including both the initialized gravity loading and vessel collision loading (Fig. 3.17). To perform static gravity pre-analysis, the bridge is analyzed (statically) with only the self-weight in place. Once the structure reaches static equilibrium, the static predictions of stiffness and displacement are stored. These quantities are then used to prescribe initial conditions for the transient-dynamic (CVIA) analysis, where the self-weight is applied in a sudden (instantaneous) manner. However, because the structure has been initialized in a pre-displaced state (with all corresponding internal forces), sudden application of the permanent loads does not produce additional displacements in the structure. Therefore, those dynamic oscillations that would be produced as a result of applying permanent loads in an instantaneous manner to an uninitialized model are eliminated.

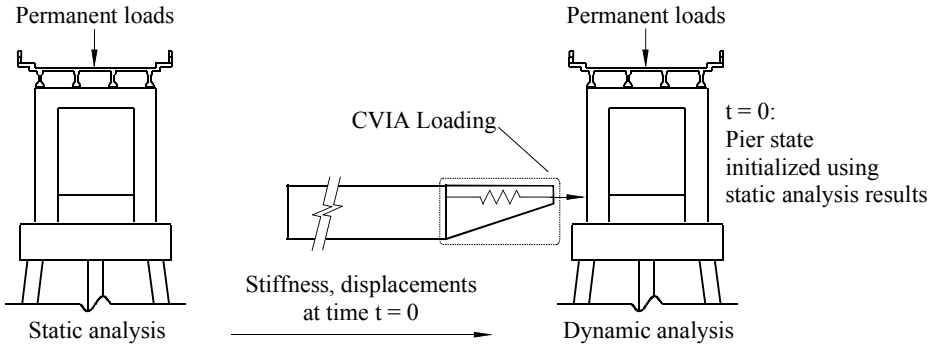

Figure 3.17 Incorporation of permanent loads into transient-dynamic (CVIA) analysis

A demonstration case is presented to illustrate the effectiveness of the static pre-load procedure as a means of conducting dynamic analysis with proper incorporation of permanent loading. The New St. George Island Causeway Bridge Pier 53 OPTS model shown in Fig. 3.18a was analyzed with self-weight loading (a permanent load) using three methods: static analysis, dynamic analysis with static pre-analysis, and dynamic analysis without static pre-analysis (the structural configuration for this model is discussed in Chapter 4). The predictions of vertical displacement for the central pile (at the pile head) are shown in Fig. 3.18b. Note that good agreement is shown between the vertical displacement-histories associated with the static and dynamic (with static pre-analysis) analyses. In contrast, the dynamic analysis (without static pre-analysis) predicts vertical displacements that contain high levels of oscillation relative to the dynamic analysis (with pre-static analysis) results.

3.10 Finite Element (FE) Software Employed for Barge-Bridge Collision Analysis

The validated and verified modeling and analysis techniques described above have been implemented in a research version of the bridge FEA software, FB-MultiPier (2009). The corresponding FB-MultiPier research code was employed for all barge-bridge collision analyses conducted in the current study.

FB-MultiPier employs fiber-based frame elements for piles, pier columns, and pier caps; flat shell elements for pile caps; frame elements, based on gross section properties, for superstructure spans; and, distributed nonlinear springs to represent soil stiffness. Transfer beams transmit load from bearings, for which the stiffness and location are user-specified, to the superstructure elements. FB-MultiPier permits the use of Rayleigh damping, which was applied to all structural elements in the models used for this study such that approximately 5% of critical damping was achieved over the first five natural modes of vibration.

Finally, given that the primary objective of the current study centers around the investigation of bridge collapse (structural failure), both kinematic and constitutive nonlinear analysis features (discussed in Consolazio et al. 2009b) were employed for all barge-bridge collision simulations conducted.

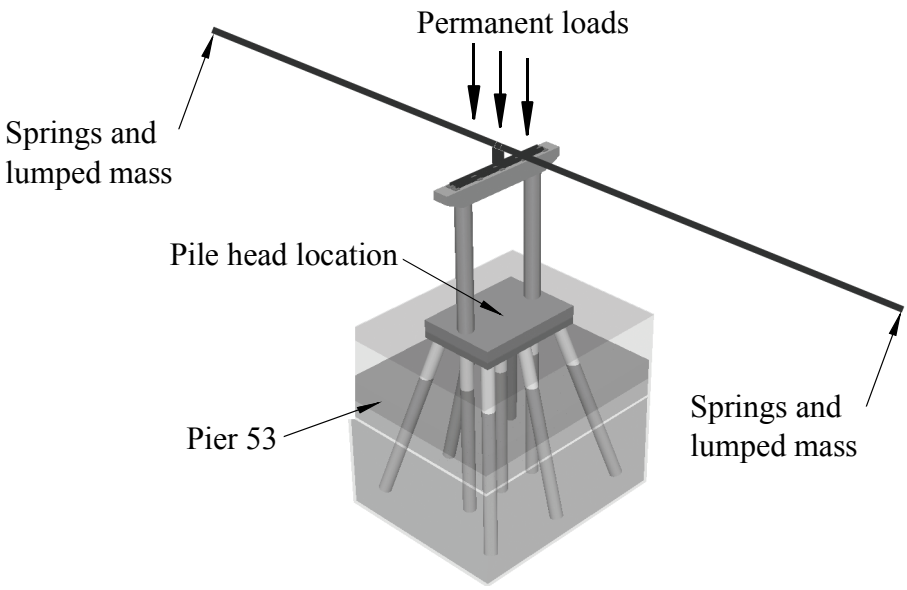

a)

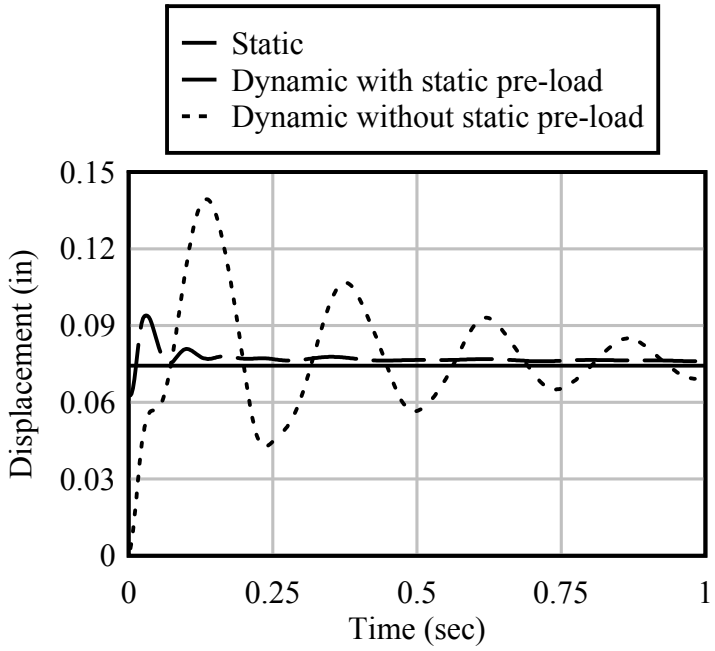

b)

Figure 3.18 Demonstration of permanent load incorporation for dynamic analysis.
a) Structural configuration analyzed; b) Vertical displacement comparison at pile head

CHAPTER 4
BRIDGE FINITE ELEMENT MODEL INVENTORY

4.1 Introduction

Previously developed structural modeling and analysis techniques, discussed in Chapter 3, can be used to accurately and efficiently conduct barge-bridge collision analysis. These techniques, when employed as part of a probabilistic framework (as discussed in Chapter 6), constitute a means of rationally assessing the probability of collapse (associated with waterway vessel collision) for a bridge pier of interest. Probability of collapse assessments, for a representative set of bridges, can be used to form empirical structural collapse relationships that may, in turn, be used in barge-bridge collision design applications. An inventory, consisting of seventeen bridge pier FE models for bridges located throughout Florida, was developed as part of a previous study (Consolazio et al. 2008). As part of the current study, ten representative cases have been identified based on bridge piers from the previously developed bridge model inventory. Furthermore, probability of collapse assessments have been made for each selected case (results are presented in Chapter 8). In the current chapter, structural configurations for each of the selected cases are described.

4.2 Bridge Pier Cases Selected to Represent Existing Bridge Infrastructure

Seven of the ten bridge pier cases considered in the current study (Fig. 4.1–Fig. 4.7) were selected specifically to represent the variety of structural configurations extant in the Florida bridge infrastructure. The structural configuration for each case is described below (additional, structural details are provided in Appendix B). For conciseness, the bridges corresponding to the seven selected bridge pier structures have been assigned three-letter identification codes (Table 4.1). Specific piers within each bridge are further delineated by proximity to the barge transit path: the letters “CHA” appended to a bridge identification code indicate that the pier is a channel pier, whereas the letters “OFF” indicate an off-channel pier (a pier not directly adjacent to the channel). The combined bridge-location identifiers (e.g., “BLT-CHA” for the SR-20 at Blountstown bridge channel pier) are referred to as Case IDs.

Table 4.1 Bridge pier case IDs

Bridge name	Bridge code	Pier location code	Case ID
SR-20 at Blountstown	BLT	CHA	BLT-CHA
I-10 over Escambia Bay	ESB	CHA	ESB-CHA
Gandy Bridge	GND	CHA	GND-CHA
New St George Island	NSG	CHA	NSG-CHA
New St George Island	NSG	OFF	NSG-OFF
Ringling	RNG	OFF	RNG-OFF
Santa Rosa Bay	SRB	CHA	SRB-CHA

4.2.1 State Road 20 (SR-20) at Blountstown, Pier 58 (BLT-CHA)

The Blountstown Bridge—formally known as the New Trammell Bridge—was constructed in 1998 to span the Apalachicola River in northwestern Florida. The Pier 58 OPTS

model (BLT-CHA), which was developed based on structural plans, is shown in Fig. 4.1. Adjacent to the channel pier, the 280 ft channel and 225 ft flanking superstructure spans consist of four, continuous steel plate girders and a reinforced concrete slab. Load transfer devices at the substructure-superstructure interface are evenly spaced under the four steel plate girders along the Pier 58 pier cap beam centerline. Each load transfer device consists of a 3 in. thick steel bearing bevel plate that overlies an elastomeric bearing pad. Four end-threaded, cast-in-place anchor bolts pass through each bearing bevel plate and into the pier cap beam; the threaded tops of the anchor bolts are capped with nuts, which provide resistance against bearing uplift. The channel pier structure consists of two round (5.5 ft diameter, 37 ft tall) pier columns spaced 30 ft apart. The pier columns are axially collinear with two 9 ft diameter drilled shafts. The pier columns and drilled shafts are integrated with a 30.5 ft tall shear wall.

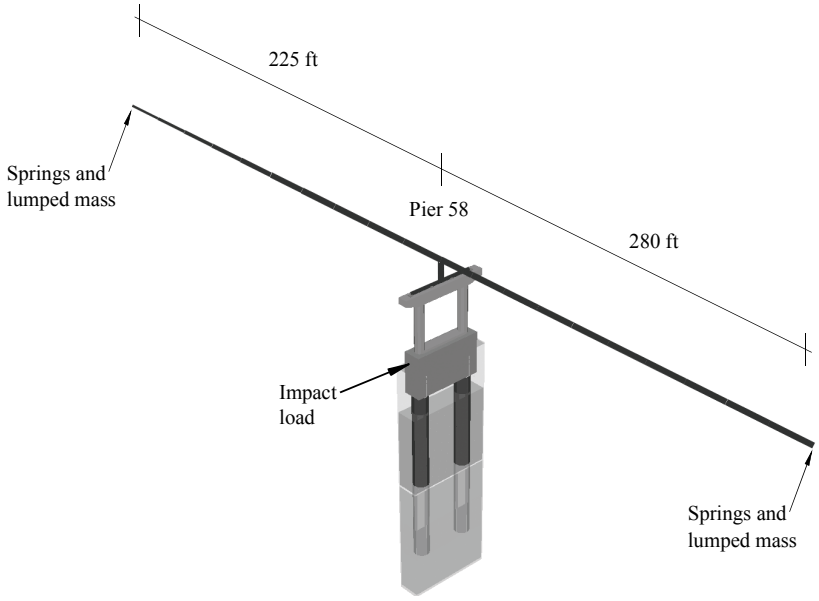

Figure 4.1 SR 20 at Blountstown, Pier 58 OPTS (BLT-CHA) model

4.2.2 Escambia Bay Bridge, Pier 1-W (ESB-CHA)

The Escambia Bay Bridge spans Escambia Bay in northwestern Florida. Structural components of the channel pier OPTS model (Fig. 4.2) were derived from bridge plans developed in the 1960s. The 170 ft superstructure channel span and 120 ft flanking span consist of four continuous, steel plate girders underlying a reinforced concrete slab. Atop the Pier 1-W pier cap are four evenly spaced steel bearing pins, each of which are welded to the respective, overlying girder and bolted to the underlying pier cap beam. The channel pier contains two tapered rectangular pier columns that are spaced 19 ft apart and vertically extend 33.5 ft between the pier cap beam and a 17.5 ft thick, tapered shear wall. The average thickness of the shear wall (in a direction parallel to the superstructure span) is 8.5 ft. The pier columns and shear wall overlie a 5 ft thick mudline footing and 6 ft tremie seal. [A mudline cap elevation indicates that the transition between the piles and overlying pier columns coincide with the soil top (or mudline) elevation.] The channel pier foundation consists of twenty-seven 2 ft square prestressed concrete piles.

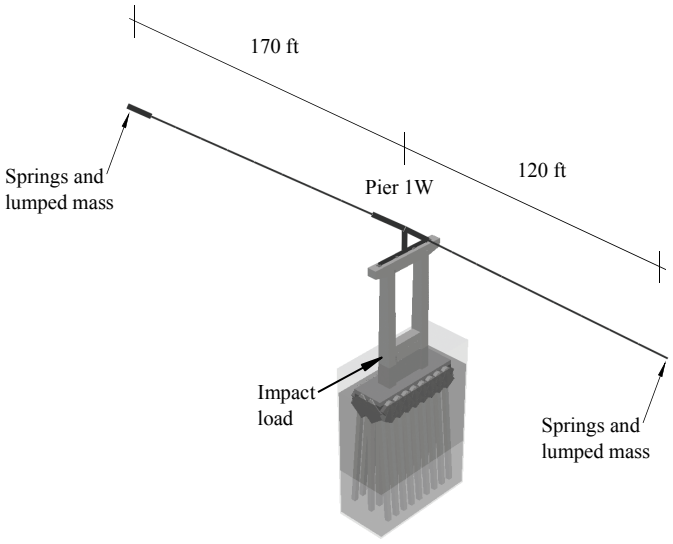

Figure 4.2 Escambia Bay Bridge, Pier 1W (ESB-CHA) OPTS model

4.2.3 Gandy Bridge, Pier 75W (GND-CHA)

The (Westbound) Gandy Bridge, constructed in 1996, spans Tampa Bay in Florida. The OPTS model for Pier 75W (GND-CHA) was developed based on structural plans and is shown in Fig. 4.3. The 235 ft channel span and 144 ft flanking span are continuous over Pier 75W. Furthermore, the spans are comprised of four prestressed concrete AASHTO Type VI girders and a reinforced concrete slab. Load transfer between the superstructure and channel pier is facilitated by four evenly spaced bearing systems, each of which consists of a 0.5 in thick steel bearing plate that overlies an elastomeric bearing pad. Four cast-in-place anchor bolts extend upward from the pier cap beam and through the bearing top plate. The tops of the anchor bolts are threaded and affixed with nuts to resist bearing uplift.

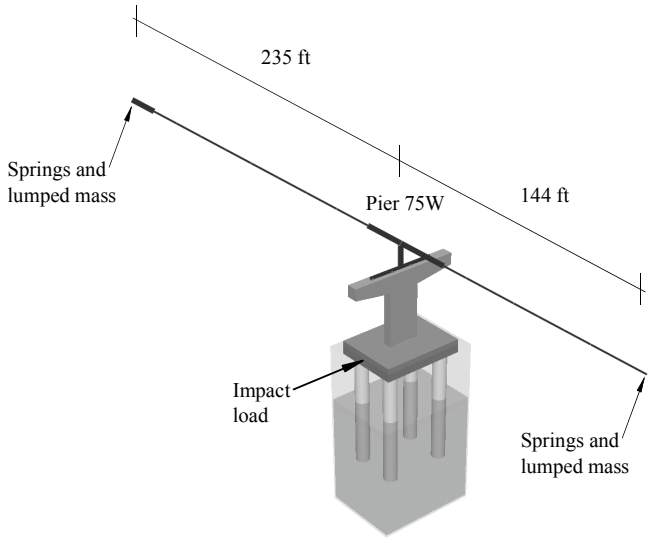

Figure 4.3 Gandy Bridge, Pier 75W (GND-CHA) OPTS model

The channel pier structure consists of a single rectangular (16 ft by 4.5 ft) pier column that extends 28 ft from the bottom of the pier cap beam to the top of a 9 ft thick waterline footing. In this context, "waterline footing" indicates that the foundation begins near the mean high water (MHW) elevation, where—in accordance with current AASHTO design provisions (AASHTO 2009)—the MHW elevation is used to vertically position the static vessel impact loading. Four 7 ft diameter drilled shafts extend from the footing to the underlying soil.

4.2.4 New St. George Island Bridge, Pier 48 (NSG-CHA)

The New St. George Island Bridge, which replaced the Old St. George Island Bridge in 2004, is a coastal bridge that spans Apalachicola Bay in northwestern Florida. The structural OPTS model (Fig. 4.4) of the New St. George Island Bridge channel pier (NSG-CHA) was derived from construction drawings. Per the construction drawings, the channel pier (Pier 48) supports five cantilever-constructed prestressed concrete Florida Bulb-T girder-and-slab segments at span lengths of 250 ft for the channel span and 258 ft for the flanking span. Due to haunching, the depth of the post-tensioned girders vary from 6.5 ft at the drop-in locations to 12 ft at respective pier cap beam bearing locations. Both the girders and deck atop Pier 48 are continuous across the pier cap, and the girders rest on two abutting, elastomeric bearings that surround a cast-in-place shear pin at each of five evenly spaced bearing locations. Pier 48 contains two round (6 ft diameter) pier columns that are spaced 30 ft apart, and braced by a 6 ft deep shear strut at the column mid-height. The 52 ft tall pier columns are supported by a thick (6.5 ft deep) waterline pile cap, and fourteen battered and one plumb 4.5 ft diameter prestressed concrete cylinder piles with 10 ft long reinforced concrete plugs that extend downward from the pile cap.

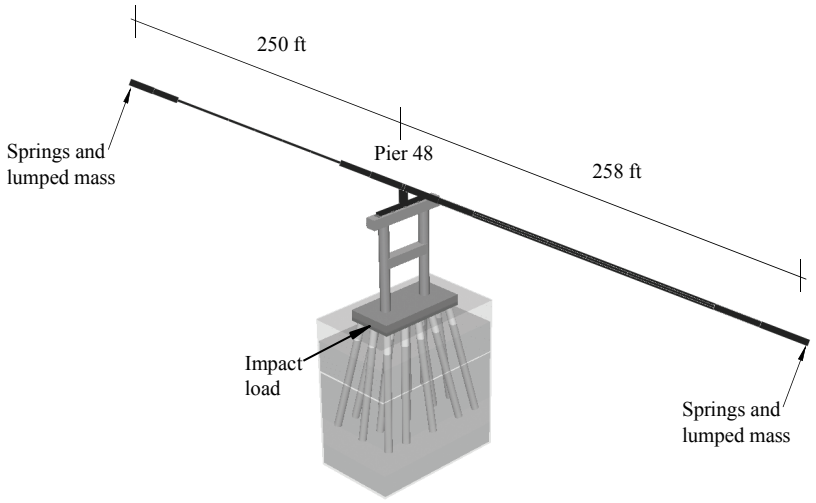

Figure 4.4 New St. George Island Bridge, Pier 48 (NSG-CHA) OPTS model

4.2.5 New St. George Island Bridge, Pier 53 (NSG-OFF)

Per the construction drawings for the New St. George Island Bridge, the off-channel pier (Pier 53) supports five Florida Bulb-T prestressed girders (6.5 ft deep) at span lengths of 140 ft for each of the left and right flanking spans (Fig. 4.5). Although girders atop Pier 53 are separated by an expansion joint across the pier cap, the superstructure deck is continuous. Load transfer devices at the substructure-superstructure interface consist of two elastomeric bearings (one under each girder) and a cast-in-place shear pin at each of five evenly spaced bearing locations. Below the pier cap, Pier 53 contains two round (5.5 ft diameter, 45 ft tall) pier columns spaced at 30 ft apart, and a 6.5 ft thick waterline pile cap foundation. The underlying concrete piles consist of six battered and three plumb 4.5 ft diameter prestressed concrete cylinder piles, where each pile contains a 10 ft reinforced concrete plug extending from the pile cap.

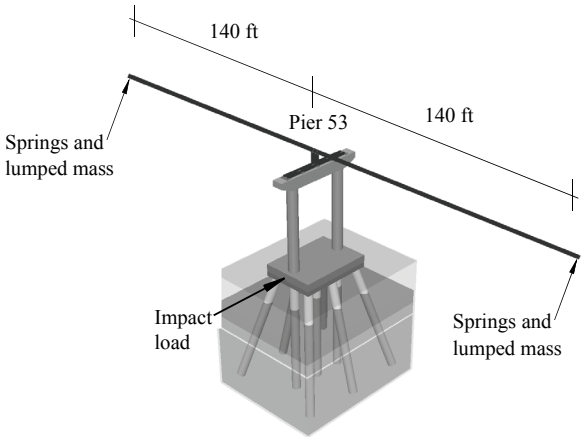

Figure 4.5 New St. George Island Bridge, Pier 53 (NSG-OFF) OPTS model

4.2.6 John Ringling Causeway, Pier 9 (RNG-OFF)

The John Ringling Causeway Bridge, constructed in 2003, spans the southern portion of Sarasota Bay in southwestern Florida. The OPTS structural model (Fig. 4.6) for Pier 9 (RNG-OFF) was generated from structural plans. The superstructure consists of a precast concrete segmental box girder with depths varying from 9 ft at the midspans to 16.5 ft above the pier. The superstructure spans 300 ft to either side of Pier 9. Two evenly spaced pot bearings act to transfer load between the pier and superstructure. The pier contains a 25 ft tall, hollow bullet-shaped reinforced concrete cross-section, which is 13 ft in diameter at the narrow ends. Also, the bullet cross-section has a constant 2.7 ft wall thickness. The pier rests on an 8.8 ft thick bullet-shaped pile cap overlying two round, solid reinforced-concrete drilled shafts of 9 ft diameter.

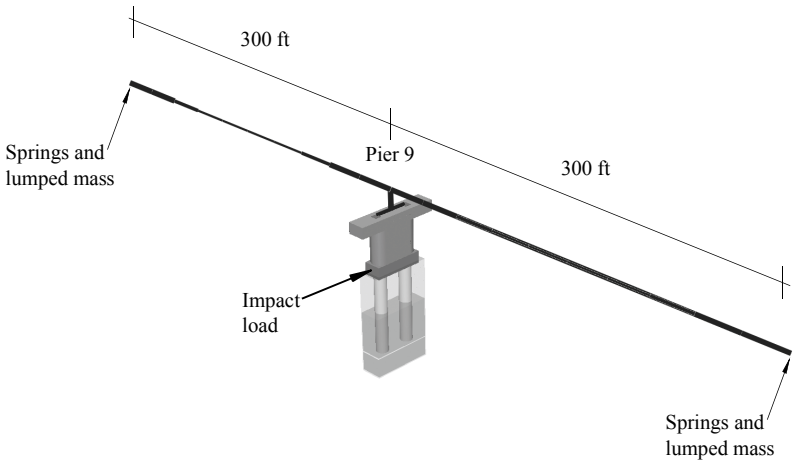

Figure 4.6 John Ringling Causeway, Pier 9 (RNG-OFF) OPTS model

4.2.7 Santa Rosa Bay Bridge, Pier 55 (SRB-CHA)

The Santa Rosa Bay Bridge was constructed in 1999 and spans East Bay in northwestern Florida. Structural plans were used to generate the Pier 55 OPTS structural model (SRB-CHA), which is shown in Fig. 4.7. Extending from Pier 55, the 230 ft channel span and 140 ft flanking span consist of an 8 ft deep, continuous precast concrete segmental box girder. Two, evenly spaced elastomeric bearing pads are used to transfer load between the superstructure and Pier 55. The channel pier structure consists of a single, hollow, rectangular (12 ft by 6 ft) reinforced concrete pier column that extends 58 ft from the top of the column to the top of a 6.75 ft thick waterline footing. The pier column walls are 22 in thick. Supporting the pier column and waterline footing are twenty-two 24 in square prestressed concrete piles.

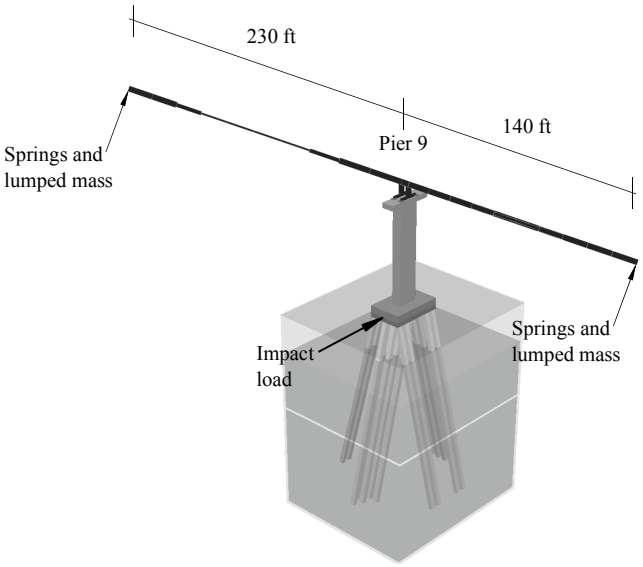

Figure 4.7 Santa Rosa Bay Bridge, Pier 55 (SRB-CHA) OPTS model

4.2.8 Summary of bridge model parameters considered

The seven selected cases, described above, comprise a wide array of pier structural configurations (Fig. 4.8), where the configuration parameters are summarized in Table 4.2. In addition to variations in foundation size and type (pile-and-cap or drilled shaft foundations), the pier columns and foundation cap elevations are also varied. However, the way in which impact load is distributed throughout a bridge structure is not only dependent on the impacted pier configuration, but also upon the mass and stiffness of the overlying superstructure. Accordingly, three different, common superstructure types are included among the seven bridge cases selected: slab on concrete girders; slab on steel girders; and segmental concrete box girder. The superstructure types and span lengths pertaining to the cases, collectively, are intended to be representative of common, medium-span bridge superstructures.

Furthermore, to ensure that a diverse cross-section of bridge designs—with respect to vessel collision design methodology—has been included in the current study, bridges with construction dates ranging from the late 1960s (ESB-CHA) up to 2004 (NSG-CHA and NSG-OFF) have been selected. Consequently, the bridges selected for the current study include structures designed for vessel impact using the AASHTO static provisions (which were first published in 1991), as well as those that were not designed to directly resist vessel collision loads. Finally, impact load magnitudes associated with the bridges studied vary from 100 kips to 3255 kips (Table 4.3).

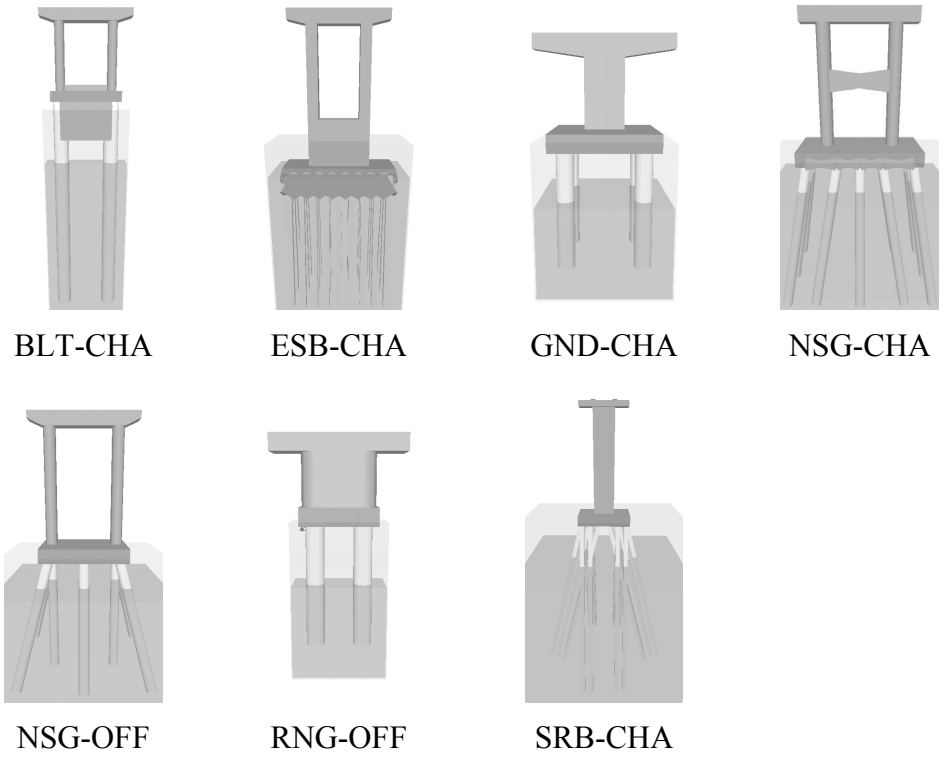

Figure 4.8 Bridge pier structural configurations representative of existing bridge infrastructure (superstructures not shown; Case IDs are shown in Table 4.1)

Table 4.2 Bridge pier configurations representative of existing bridge infrastructure

Case ID	Cap[a,b] elevation	Pier column data			Shaft/pile data			Superstructure type			Span lengths adjacent to pier (ft)	
		No.	Width (ft)	Height[c] (ft)	Type	No. shafts / piles	Width (ft)	Box girder	Steel girders	Concrete girders	North or west	South or east
BLT-CHA	Waterline	2	5.5	37	Drilled shaft	2	9		X		225	280
ESB-CHA	Mudline	2	6	51	Concrete pile	27	2		X		170	120
GND-CHA	Waterline	1	4.5	28	Drilled shaft	4	7			X	235	144
NSG-CHA	Waterline	2	6	52	Concrete pile	15	4.5			X	250	258
NSG-OFF	Waterline	2	5.5	45	Concrete pile	9	4.5			X	140	140
RNG-OFF	Waterline	1	13	25	Drilled shaft	2	9	X			300	300
SRB-CHA	Waterline	1	6	58	Concrete pile	22	2	X			230	140

[a] Waterline footing indicates a foundation top-surface elevation near the MHW elevation.
[b] Mudline footing indicates a foundation top-surface elevation near the soil surface.
[c] Distance from top of foundation to bottom of pier cap.

Table 4.3 Static vessel-collision impact forces

Case ID	Static impact force associated with vessel-bridge collision (kips)
BLT-CHA	2550
ESB-CHA	2067[a]
GND-CHA	2400
NSG-CHA	3255
NSG-OFF	2300
RNG-OFF	100
SRB-CHA	2000

[a] The impact force was not used in the design process, but rather, was determined as part of an investigation subsequent to bridge construction.

4.3 Bridge Pier Cases Selected to Represent Future Bridge Infrastructure

The seven in-service bridge piers that were selected to represent the existing Florida infrastructure were either designed using a static collision-load approach, or not directly designed to resist vessel-bridge collision loading. However, previously conducted analytical (Davidson et al. 2010) and full-scale experimental (Consolazio et al. 2006) studies have identified the need to incorporate dynamic barge-bridge collision phenomena into the bridge design process. Therefore, three additional cases have been formed for the current study, where the pier structural members have been modified (strengthened) to resist dynamically amplified internal forces that can arise during collision events. These three cases—BLT-CHA, GND-CHA, and NSG-OFF—have been developed specifically to represent future bridge infrastructure, where dynamic collision phenomena are incorporated into bridge design for waterway vessel collision.

Bridges selected to undergo structural modification were so chosen with the objective of achieving near-optimal bridge designs under dynamic collision loading. In this context, optimal bridge design (for waterway vessel collision) corresponds to bridge structural configurations that, when subjected to design collision loads, approach all applicable structural limit states simultaneously. Additionally, to facilitate direct comparisons between unmodified bridges and corresponding modified (strengthened) bridges, permissible structural modifications were primarily limited to changes in concrete material strength and longitudinal reinforcement levels. In this way, mass, overall dimensions, number of pier columns, and number of piles (or drilled shafts) comprising the strengthened cases are consistent between the unmodified and modified structural configurations.

4.3.1 Bridge strengthening process

The bridge strengthening process begins with the identification of demand-capacity ratios (D/C) associated with the unmodified (original) bridge model, where the model is subjected to the static loads that were used in the original design process. For each case, static collision analysis is conducted (Fig. 4.9a) using the respective head-on AASHTO static load from Table 4.3. Using the static analysis results, the most severe pile and pier column load-moment force pairs (i.e., those that bring the members closest to structural failure) are identified (Fig. 4.9b). The magnitudes of pile and column flexural demand associated with the load-moment force pairs (D_{st}^{pile} and D_{st}^{col}, respectively) are then compared to the pile and column flexural capacities (C_{st}^{pile} and C_{st}^{col}, respectively) at the same axial load levels. Ratios of the static demand and capacity terms (D/C_{st}^{pile} and D/C_{st}^{col} for the piles and pier columns, respectively) are used as baseline (datum) values that guide subsequent modifications to the structural configurations. The strengthening process is iteratively carried out until the D/C values associated with the modified structure under dynamic loading become (approximately) equal to the static D/C values. In this way, consistent levels of safety are incorporated into the strengthened structure (relative to the unmodified structure).

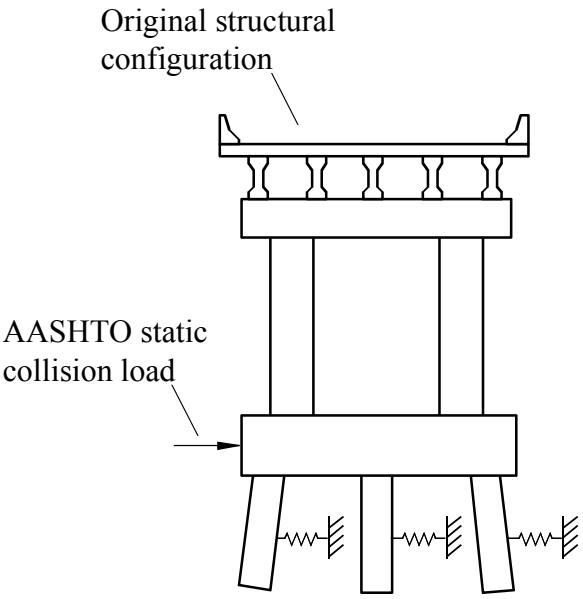

a)

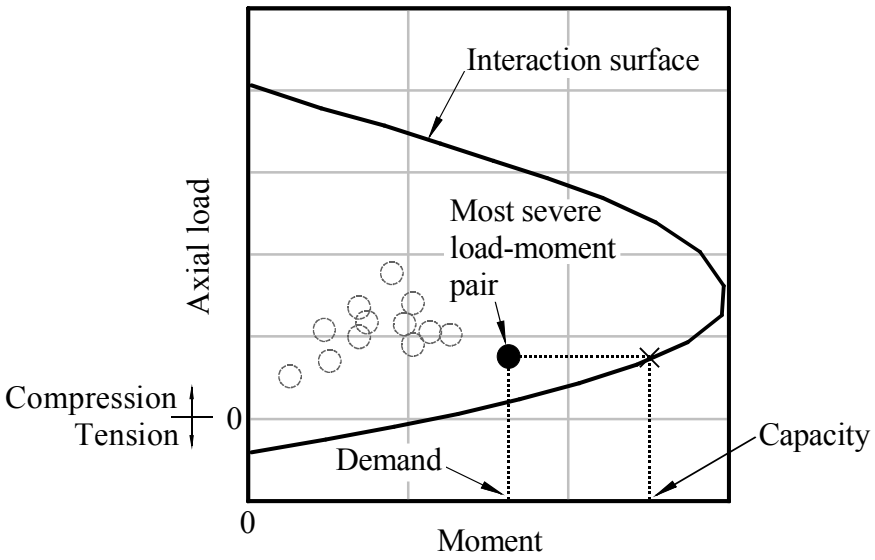

b)

Figure 4.9 Determination of static demand and capacity values. a) Original bridge structure subjected to AASHTO static analysis; b) Load-moment interaction plot of AASHTO static analysis results

4.3.1.1 Stage 1 of the strengthening process

The bridge-pier strengthening procedure is summarized in Fig. 4.10. In stage 1, pile (or drilled shaft) and pier column flexural capacities are iteratively increased by supplying additional longitudinal reinforcement to, or increasing the concrete compressive strength of, pile and pier column members based on the results of successive dynamic collision analyses. For each

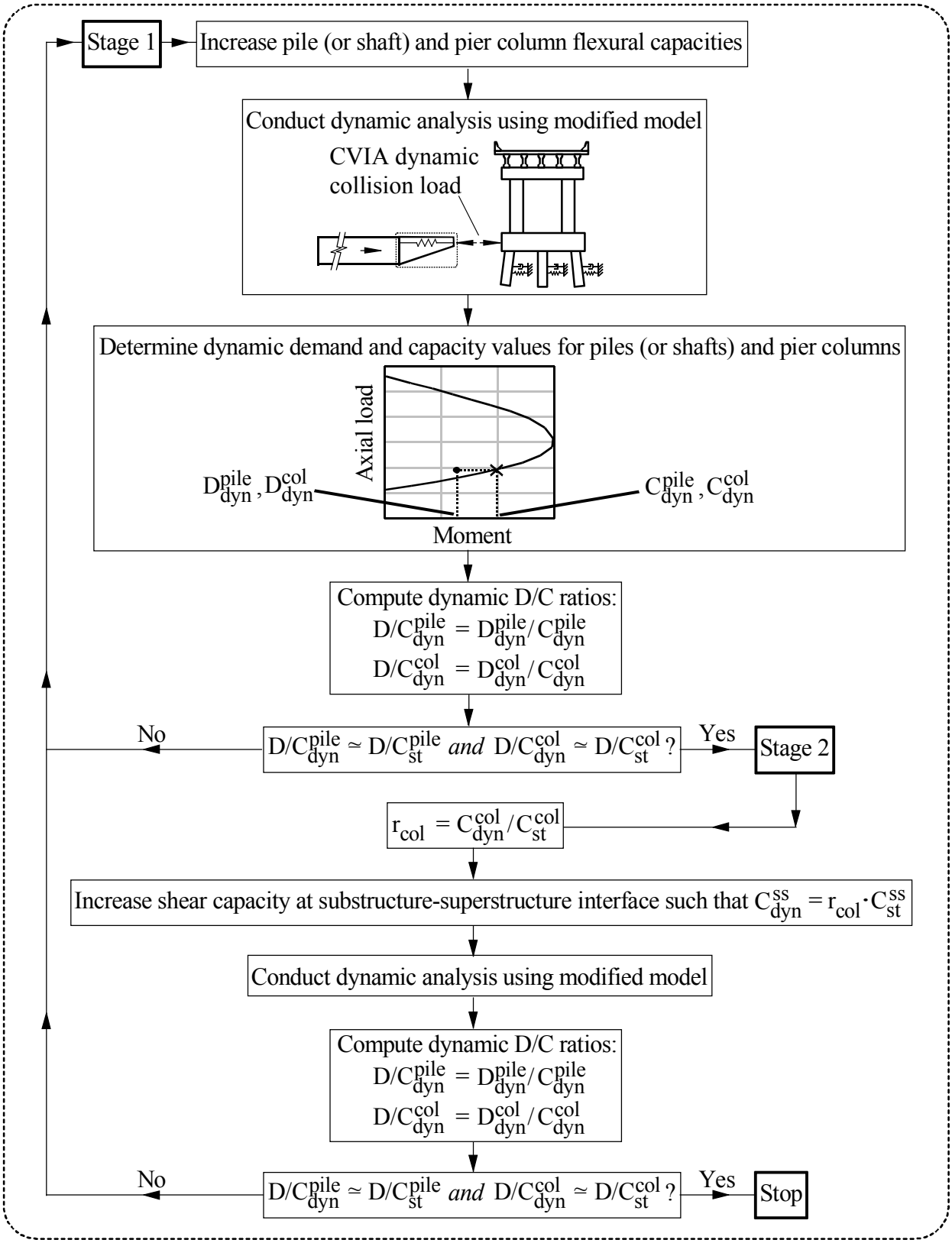

Figure 4.10 Summary of strengthening procedure

dynamic analysis conducted, maximum load-moment force pairs are identified (separately) for the incrementally modified piles and pier columns in the same manner as that described above for the static collision analysis. Moment magnitudes associated with the pile and pier column load-moment force pairs (D_{dyn}^{pile} and D_{dyn}^{col}, respectively) and member capacities (C_{dyn}^{pile} and C_{dyn}^{col}) at the same axial load levels are used to compute dynamic D/C values (D/C_{dyn}^{pile} and D/C_{dyn}^{col} for the piles and pier columns, respectively). The dynamic D/C values are then compared to respective static D/C values. If, for either of the pile or pier column members, the dynamic D/C values and corresponding static D/C values are not approximately equal, then the pile and pier column cross-sections are further modified. Otherwise, stage 2 of the strengthening process is initiated.

4.3.1.2 Stage 2 of strengthening process

Stage 2 of the strengthening process (Fig. 4.10, bottom) consists of modification of shear capacity at the bridge pier substructure-superstructure interface. Given that, during a collision event, impact-induced pier column shear is transferred to the superstructure through bearing shear, modified structure capacity at the substructure-superstructure interface is increased in proportion to the increase in pier column capacity. Specifically, a capacity increase factor (r_{col}) is formed as the ratio of the modified to original pier column flexural capacities (C_{dyn}^{col} and C_{st}^{col}, respectively). Then, the modified (or dynamic-based) substructure-superstructure shear capacity C_{dyn}^{ss} is increased such that:

$$C_{dyn}^{ss} = r_{col} \cdot C_{st}^{ss} \tag{4.1}$$

where C_{st}^{ss} is original (or static-based) substructure-superstructure shear capacity.

Subsequently, a dynamic (CVIA) analysis is conducted and dynamic D/C values are computed in a manner analogous to that described above. If approximate agreement is observed between the newly formed (dynamic) D/C values and the corresponding static D/C values, then the strengthening process is considered to be complete. Otherwise, if modification of the substructure-superstructure interface capacity leads to a markedly different structural response, then the stage 1 process is reentered using the most recently formed (modified) structural model.

4.3.2 Structural configuration changes associated with use of the strengthening procedure

To illustrate the strengthening process, structural configuration changes stemming from use of the strengthening procedure are presented below for the NSG-OFF case. Structural configuration changes applied to the other two selected cases (BLT-CHA and GND-CHA) are described in Appendix A. For all pile and pier column cross-section changes implemented, the resulting cross-sections were verified to satisfy reinforcement limits (where minimum and

maximum reinforcement ratios are given in ACI 2005 as 1% and 8% of the total cross section area, respectively). Additionally, shear capacities associated with all strengthened cross-section layouts (determined using Sec. 5.8.3.3 of the AASHTO 2007 LRFD code) were verified to be greater than maximum dynamically-computed shear forces.

4.3.3 New St. George Island Pier 53 (NSG-OFF)

Original (static-based) and strengthened (dynamic-based) pier member cross-section layouts associated with the NSG-OFF case (recall Fig. 4.5) are shown in Figs. 4.11–4.12. Specific to the 54 in. prestressed concrete cylinder pipe pile members from the original model (Fig. 4.11a), results from an AASHTO static analysis (with a 2300 kip static load) indicate that the maximum load-moment force pair occurs in the plugged region of the piles (near the cap), where the magnitude of D_{st}^{pile} is 2600 kip-ft (Fig. 4.11b). The corresponding value of C_{st}^{pile} is 5840 kip-ft, and therefore, the value of D/C_{st}^{pile} is 0.45.

The barge impact conditions prescribed in the dynamic analysis correspond to a single column of three fully-loaded jumbo hopper barges and tow (weighing 5920 tons) traveling at 5 knots. These conditions were determined as part of a previous study (Consolazio et al. 2008) to be representative for the waterway spanned by the New St. George Island Bridge. The addition of longitudinal reinforcement to the piles (Fig. 4.11c), combined with an increase of plugged concrete compressive strength to 6 ksi (from 5.5 ksi), lead to comparable dynamic D/C values (relative to the static D/C values) when the modified structural configuration is subjected to dynamic collision loads associated with the above-defined barge impact scenario. The load-moment force pair obtained from the dynamic analysis is such that the pile demand, D_{dyn}^{pile}, is 5950 kip-ft (Fig. 4.11d) and the corresponding capacity, C_{dyn}^{pile}, is 12670 kip-ft. Therefore, the value of D/C_{dyn}^{pile} is 0.47, which differs from D/C_{st}^{pile} by only 5%.

Specific to the 66 in. diameter reinforced concrete pier columns from the original NSG-OFF model (Fig. 4.11a), the static analysis results are such that values of D_{st}^{col} and C_{st}^{col} are 3710 kip-ft and 5609 kip-ft, respectively (Fig. 4.11b). The pier column flexural demand and capacity values correspond to a D/C_{st}^{col} value of 0.66. Increasing the column concrete compressive strength to 6 ksi (from 5.5 ksi) and supplying additional longitudinal reinforcement throughout the column (Fig. 4.11c) result in significant increases in both the C_{dyn}^{col} and—as predicted by dynamic collision analysis—D_{dyn}^{col} values (which are 19560 kip-ft and 14720 kip-ft, respectively). However, for the modified configuration, reasonable agreement is attained between D/C_{dyn}^{col} (with a value of 0.73) and D/C_{st}^{col}, where only a 10% difference is observed.

For the column cross-sections shown in Fig. 4.11, the ratio of the strengthened to original column capacities, r_{col}, is 3.5. In accordance with stage 2 of the strengthening process,

modifications were made (Fig. 4.12) such that the substructure-superstructure shear capacity for the NSG-OFF case was increased by a factor of approximately 3.5. Given that the substructure-superstructure interface for the NSG-OFF pier contains cast-in-place shear pins (to aid in span seating-loss prevention during extreme event loading), shear capacities were determined using the ACI (2005) Appendix D provisions, which pertain to anchorage in structural concrete. Specifically, the substructure-superstructure shear capacities for the unmodified NSG-OFF configuration are 270 kips and 220 kips for the transverse and longitudinal (relative to bridge span) directions, respectively. By increasing the shear pin diameters to 5.75 in. (from 3 in.), and increasing the pier cap beam plan dimensions to 9 ft wide by 48 ft long (from 6.5 ft wide by 43 ft long), the substructure-superstructure interface shear capacities increased to 1040 kips and 740 kips (in the transverse and longitudinal directions, respectively).

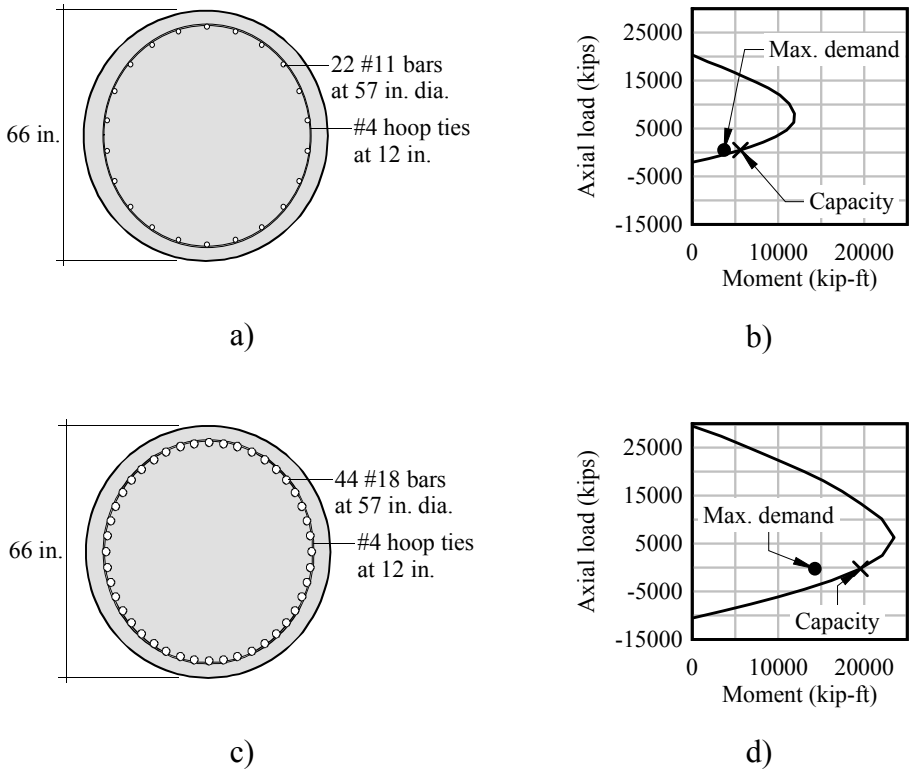

Figure 4.11 Original versus strengthened column cross-section summary for NSG-OFF case. a) Original column cross-section; b) Load-moment interaction for original cross-section in response to AASHTO static load; c) Strengthened column cross-section; d) Load-moment interaction for strengthened cross-section in response to dynamic load

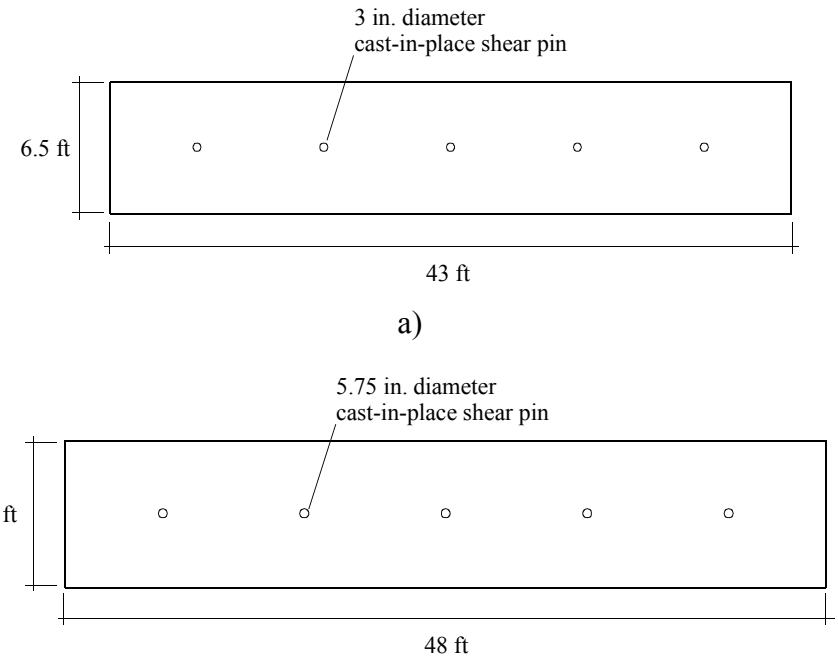

Figure 4.12 Original versus strengthened substructure-superstructure interface for NSG-OFF case. a) Plan view of original pier cap beam; b) Plan view of strengthened pier cap beam

CHAPTER 5
PROBABILISTIC SIMULATION TECHNIQUES EMPLOYED

5.1 Introduction

The primary objective of this study is to develop probability of collapse relationships that serve as an aid in the design of bridges subject to vessel collision. As will be discussed in Chapter 8, these relationships are formed using results from the evaluation of structural limit state exceedance rates for a representative set of bridges. The structural reliability problems investigated in this study can be considered to be special cases of the following structural reliability problem: given random variables of resistance, R, and load, S, find the probability that R is less than or equal to S (Eq. 5.1):

$$P(R \leq S) \tag{5.1}$$

where P() indicates probability evaluation. For instances where resistance (R) is less than or equal to load (S), a limit state is considered to have been reached (i.e., structural failure has occurred).

Furthermore, for the bridge structural reliability problems considered as part of this study, the random variables analogous to R and S are implicit functions of several random variables (as discussed in Chapter 6). Specifically, complex dynamic interactions between waterway vessels and bridge structures during collision events necessitate that expected values of the random variables analogous to those given in Eq. 5.1 be obtained using results from numerous nonlinear dynamic finite element (FE) collision simulations (the FE methods employed were discussed in Chapter 3). Furthermore, when the probability of collision-induced bridge collapse (structural failure) is small (i.e., significantly less than 0.01), highly efficient probabilistic simulation techniques must be employed to maintain the feasibility of obtaining a meaningful probability estimate. In this chapter, expected values of the probability quantity defined in Eq. 5.1 are determined for a simple, two-parameter system using each of the probabilistic simulation techniques that are employed as part of this study. Details of how these methods are employed in the investigation of bridge structural reliability for barge-bridge collisions will be given in Chapter 7.

5.2 Demonstration Case

Consider a system consisting of two random variables (Fig. 5.1): resistance (R) and load (S), with statistical descriptions as given in Table 5.1. Note that, for simplicity and to facilitate probabilistic simulation technique comparisons, both parameters are defined as independent and normally distributed. Consequently, the solution to the problem defined in Eq. 5.1 (when using the parameters from Table 5.1) can be calculated directly.

The process of directly calculating this solution is initiated by rearranging the resistance (R) and load (S) terms from Eq. 5.1:

$$0 \leq R - S \tag{5.2}$$

An additional random variable, Z, is then be defined as a linear function of R and S:

$$Z = R - S \tag{5.3}$$

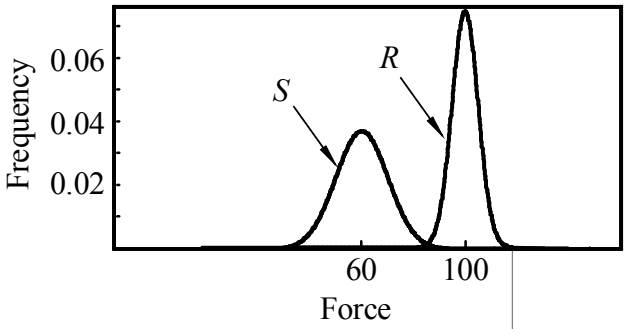

Figure 5.1 Demonstration case random variables

Since R and S are independent and normally distributed, Z is also normally distributed (Ang and Tang 2007) and has the property:

$$\mu_Z = \mu_R - \mu_S \tag{5.4}$$

where μ_Z is the expected value (or mean) of Z; μ_R is the expected value (or mean) of R; and, μ_S is the expected value (or mean) of S. The standard deviation of Z, σ_Z, is given as (Ang and Tang 2007):

$$\sigma_Z = \sqrt{\sigma_R^2 + \sigma_S^2} \tag{5.5}$$

where σ_R is the standard deviation of R; and, σ_S is the standard deviation of S. Numerically, the values of μ_Z and σ_Z are, 40 and 11.2, respectively.

Given the statistical description of Z, the problem defined in Eq. 5.1 (as it applies to the random variables defined in Table 5.1) may be expressed as:

$$P(Z \leq 0) \tag{5.6}$$

The probability quantity in Eq. 5.6 is readily determined by, first, forming a standard normal variate, s_Z:

$$s_Z = \frac{0 - \mu_Z}{\sigma_Z} \tag{5.7}$$

Then, the value of the cumulative distribution function (CDF) associated with Eq. 5.6, p_Z, can be determined using Eq. 5.8:

$$p_Z = 1 - \Phi(-s_Z) \tag{5.8}$$

where Φ is the CDF of the standard normal distribution. The value of p_Z, or the probability that the resistance (R) is less than or equal to the load (S), is 1.73E-04 for the statistical descriptions given in Table 5.1. Furthermore, the value of p_Z (obtained using Eq. 5.8) constitutes the datum for which the results obtained from all other probabilistic simulation techniques (discussed below) are compared.

5.3 Standard Monte Carlo (sMC) Simulation

The standard Monte Carlo simulation technique consists of repeatedly, independently sampling values of random variables within a system and evaluating performance functions (e.g., a limit state function) of interest for each set of sampled values. Each set of sampled random variable values is considered to be one possible (simulated) state for a physical system of interest. As the number of limit state function evaluations increase, a statistical description of the performance function is realized. The effectiveness and pervasiveness of the standard Monte Carlo (sMC) approach as a probabilistic simulation technique is well documented in the literature (e.g., Melchers 1999). In the current study, the sMC approach is used to estimate the probability that a structural failure limit state (i.e., that defined in Eq. 5.1) will be reached. Additionally, in the current study, the sMC approach is adopted as a means of verifying results obtained from more advanced probabilistic simulation techniques.

5.3.1 Random variable value generation for sMC simulation

The sMC simulation technique, as employed in the current study, is used in conjunction with the inverse CDF method of random variable value generation. This process is illustrated in Fig. 5.2 for the random variable U of arbitrary distribution, q_U. The inverse CDF method begins with the generation of a random number, Y_i, which is obtained from a uniform probability distribution function (PDF), q_Y, (Fig. 5.2, lower left). Given Y_i, a CDF value (or cumulative

probability), Q_{Yi} is determined according to the governing CDF, Q_Y (Fig. 5.2, upper left). A CDF value, Q_{Ui}, is then defined subject to the constraint:

$$Q_{Ui} = Q_{Yi} \tag{5.9}$$

Using Q_{Ui} and the CDF, Q_U (which corresponds to the random variable U), a sample U_i is then obtained (Fig. 5.2, right).

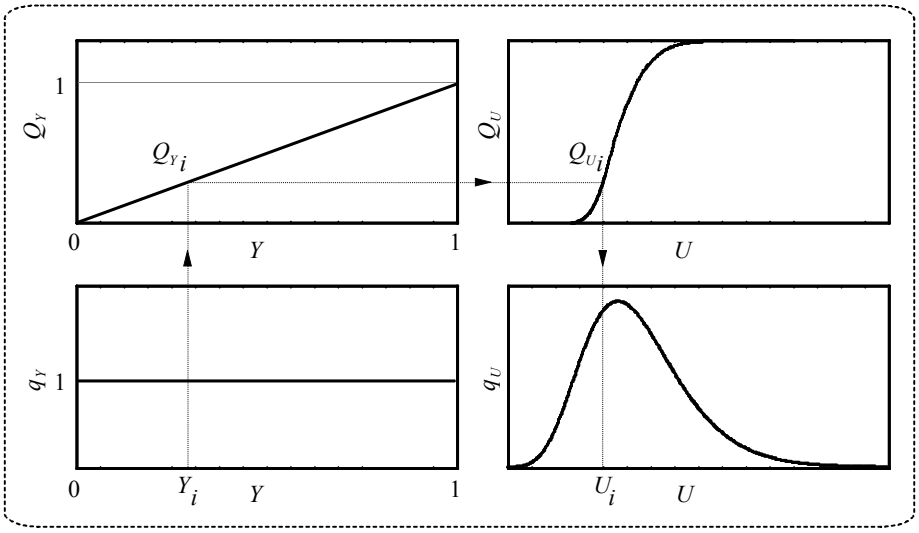

Figure 5.2 Random number generation using the inverse CDF method (after Haldar and Mahadevan 2000)

5.3.2 Overview of the sMC algorithm

An overview of the sMC algorithm, as it pertains to the two-parameter demonstration case, is shown in Fig. 5.3. Given statistical descriptions of the system random variables R and S (Table 5.1); the applicable limit state function (Eq. 5.3); and, the corresponding limit state exceedance probability (1.73E-04, as determined using Eq. 5.8), the approximate number of simulations, n, required to obtain a meaningful sMC estimate of the limit state exceedance rate, p_{sMC}, may be determined. A meaningful estimate is defined as—in the context of the two-parameter demonstration case—a p_{sMC} value with a coefficient of variation (COV) less than or equal to 0.1, such that:

$$n = \frac{1 - p_{sMC}}{\delta_{sMC}^2 \cdot p_{sMC}} \tag{5.10}$$

where δ_{sMC} is the COV associated with p_{sMC}. For the demonstration case the parameter n is estimated (using Eq. 5.10) to be 575,000 sMC simulations.

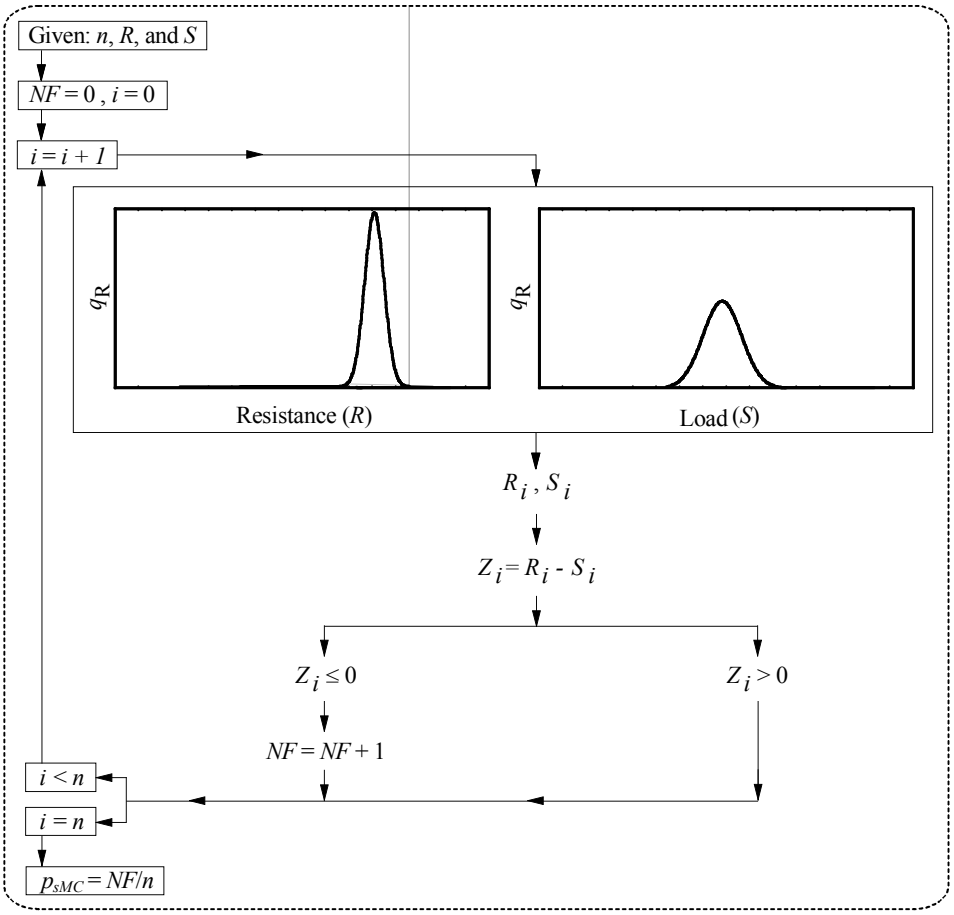

Figure 5.3 Standard Monte Carlo (sMC) simulation algorithm

Given the desired sMC sample size, n, and statistical descriptions of R and S, the sMC approach is carried out by, first, initializing a failure parameter (NF) and simulation number, i. The failure parameter, NF, is incremented for each simulation where the limit state (Eq. 5.3) has been reached (i.e., if R is less than or equal to S). For each simulation, i, values of the random variables R and S are sampled (R_i and S_i, respectively) according to the PDFs q_R and q_S, respectively. Then, the limit sate function, Z, is evaluated. If the limit state function value, Z_i, is less than or equal to 0, then NF is incremented. After n simulations have been carried out, p_{sMC} is estimated as the ratio of NF to n.

Table 5.1 Demonstration case random variable descriptions

Variable	Distribution	Mean	Standard deviation	COV
Resistance	Normal	100	5	0.05
Load	Normal	60	10	0.17

5.3.3 Demonstration case results from sMC simulation

Using the sMC approach, twenty samples (each having a sample size of 575,000 simulations) were generated. The limit state exceedance rate estimate for each sample is shown in Fig. 5.4. The mean-valued estimate of the failure probability, p_{sMC}, is 1.75E-04, which is in excellent agreement with the directly calculated p_Z value of 1.73E-04 (the percent difference between the sMC estimate and the exact, or manually calculated, solution is 1%). Furthermore, the reliability associated with the p_{sMC} value is such that δ_{sMC} is 0.083, which is less than the pre-defined target COV value of 0.1.

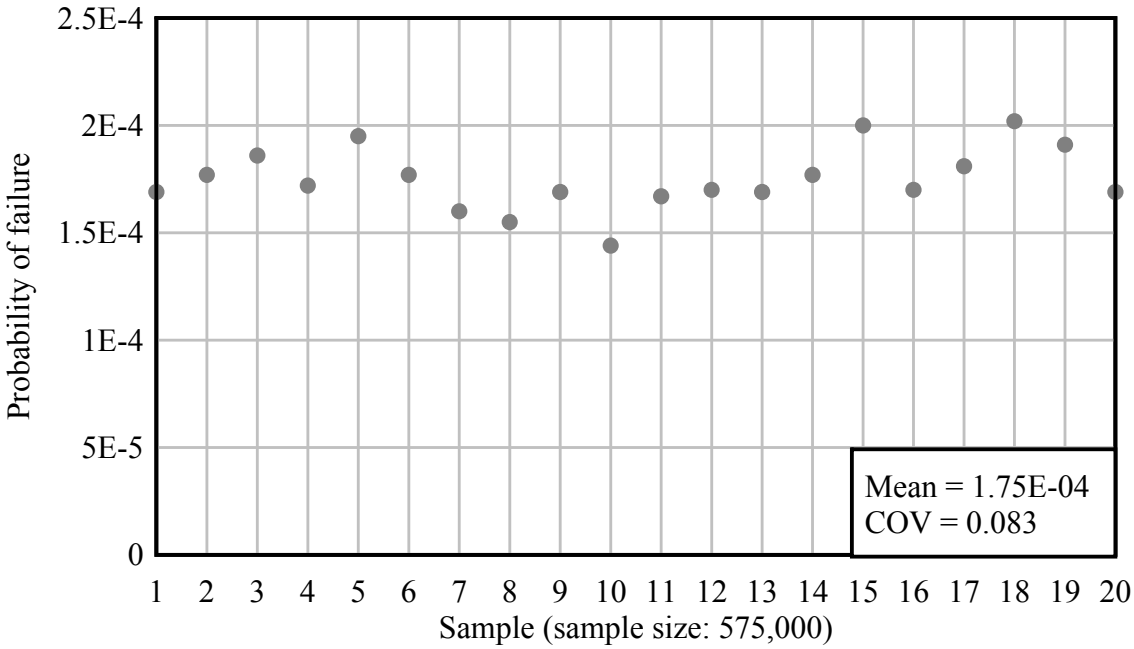

Figure 5.4 Standard Monte Carlo (sMC) simulation results

5.3.4 Limitations of sMC simulation

It is well established that the sMC approach is not an efficient means of estimating small failure probabilities (i.e., probability values significantly smaller than 0.01). Specifically, for a given target reliability level (i.e., COV), the corresponding approximate number of sMC simulations required increases in a manner that is inversely proportional to the system failure probability:

$$n = \frac{1 - p_{sMC}}{\delta_{sMC}^2 \cdot p_{sMC}} \approx \frac{1}{\delta_{sMC}^2 \cdot p_{sMC}} \tag{5.11}$$

where the numerator in Eq. 5.11 reduces to a value that is approximately equal to 1 for small values of p_{sMC}.

For the sMC approach, each simulation (i.e., each limit state function evaluation) is independent. Such independence affords great flexibility with respect to desired sample sizes and the desired number of simulations that comprise a given sample. However, this independence can lead to the presence of duplicate, or redundant, sets of random variable values. In practical applications of sMC simulation, duplicate sets of random variable values do not produce any meaningful refinements to outcome probability estimates.

5.4 Advanced Probabilistic Simulation Techniques

Given the limitations of the sMC approach, the use of more efficient probabilistic simulation techniques is warranted for cases in which simulation efficiency is required. The bridge structural reliability problems considered as part of this study necessitate the use of advanced probabilistic simulation techniques that are capable of efficiently producing small failure probability estimates and are robust (i.e., insensitive) to the number of random variables in the system. Two advanced probabilistic simulation techniques that satisfy these requirements are discussed below:

- Latin Hypercube (LH) simulation
- Markov Chain Monte Carlo with subset simulation (MCMC/ss)

5.4.1 Latin Hypercube (LH) simulation

In light of the limitations of sMC, McKay et al. (1979) proposed a more efficient scheme for conducting probabilistic simulation: Latin Hypercube (LH) simulation. The LH approach is largely similar to the sMC approach. However, for LH simulation, an advanced sampling technique is employed. Specifically, in LH simulation, the PDFs of individual system random variables are divided into a predetermined number of intervals, and sampling is carried out once for each interval. Limit state evaluation is then carried out in a manner similar to that specified for the sMC approach. As a consequence of the one-time, interval-based sampling scheme, LH simulation overcomes the sMC approach limitation associated with duplicate (i.e., redundant) samples. Consequently, using LH simulation, the joint probability space of the physical system of interest can be more fully explored with significantly fewer simulations (relative to the sMC approach).

5.4.1.1 Overview of the LH algorithm

An overview of the LH algorithm, as it pertains to the two-parameter demonstration case, is shown in Fig. 5.5. Given a predetermined stratification level, k_{st}, the domains of the PDFs (q_R

and q_S) of the system random variables are subdivided into k_{st} intervals of equal probability. Then, for each random variable and interval, r_m, sampling is carried out using the inverse CDF method (discussed above) until a random variable within interval r_m is obtained, where samples R_m and S_m correspond to R and S, respectively. For intervals numbered 1 through k_{st}, the interval-based random variable samples (R_m and S_m) are used to populate random variable arrays ({R} and {S} correspond to R and S, respectively).

After the random variable arrays ({R} and {S}) have been populated with k_{st} entries each, limit state evaluation is carried out (Fig. 5.5). Specifically, for the limit state defined in Eq. 5.3, resistance and load parameters R_i and S_i are selected randomly—without replacement—from arrays {R} and {S}, respectively. In this context, "without replacement" signifies that each of the k_{st} entries (i.e., intervals) are sampled from exactly once. The difference between R_i and S_i is then calculated to form Z_i. If Z_i is less than 0, then the limit state has been reached and the failure parameter, NF, is incremented. After k_{st} limit state evaluations have been carried out, the probability of failure, p_{LH}, is estimated as the ratio of the number of limit state exceedances, NF, to the total number of simulations conducted, k_{st}.

5.4.1.2 Demonstration case results from LH simulation

Using the random variables defined in Table 5.1 and the limit state function defined in Eq. 5.3, twenty samples—each having a sample size, or number of k_{st} intervals, equal to 325,000 simulations—were generated using the LH simulation technique. The limit state exceedance rate estimates for the twenty samples are shown in Fig. 5.6. Based on the twenty samples, the mean estimate of the failure probability, p_{LH}, is 1.78E-04, which differs from the (exact) p_Z value (1.73E-04) by only 2.5%. Furthermore, the reliability associated with the p_{LH} estimate (the corresponding COV is 0.085) acceptably falls acceptably below the pre-defined target COV value of 0.1.

5.4.2 Limitations of LH simulation

The LH approach, relative to the sMC approach, requires significantly fewer simulations to obtain meaningful failure probability estimates in many cases. However, the gains in efficiency are not substantial enough to eliminate the potential need to conduct hundreds of thousands of simulations to obtain a meaningful probability of failure estimate for probabilities significantly smaller than 0.01. Furthermore, for the applications of interest in this study, such a computational expense is not feasible. Therefore, the use of a probabilistic simulation technique with an even greater efficiency is employed, specifically, to quantify estimates of small failure probabilities.

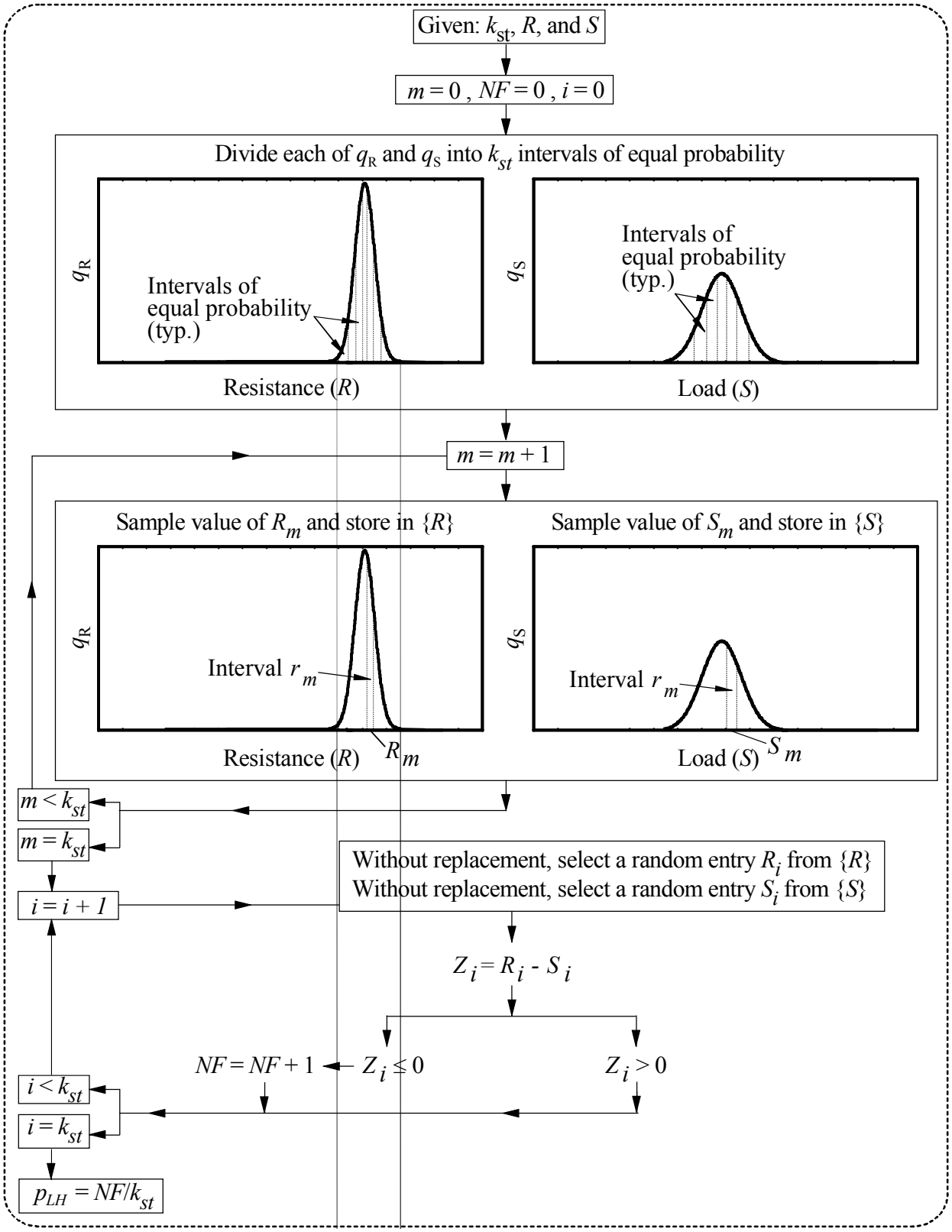

Figure 5.5 Latin Hypercube (LH) simulation algorithm

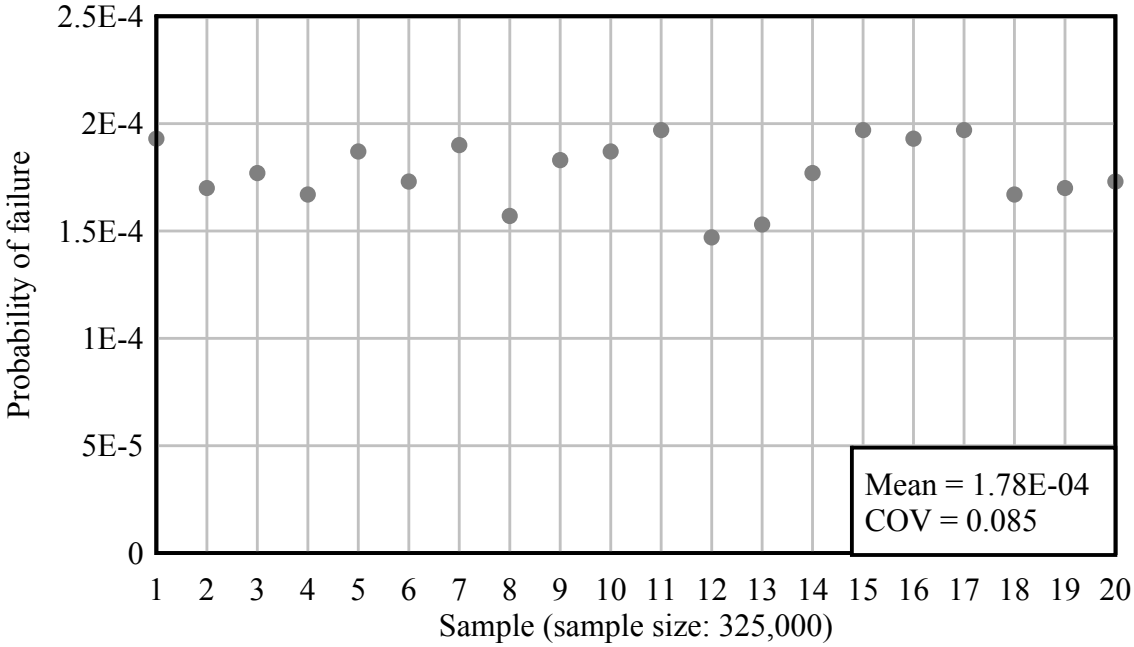

Figure 5.6 Latin Hypercube (LH) simulation results

5.4.3 Markov Chain Monte Carlo with subset simulation (MCMC/ss)

The Markov Chain Monte Carlo with subset simulation (MCMC/ss) approach—originally proposed by Au and Beck (2001)—is a highly efficient probabilistic simulation technique that was specifically developed for the estimation of small failure probabilities of physical systems. For a given target reliability level (e.g., failure probability estimate COV), the computational requirement associated with the sMC approach increases in a manner that is inversely proportional to the system failure probability (recall Eq. 5.3). In contrast, the corresponding computational requirement associated with the MCMC/ss approach increases in an approximately logarithmic manner (Au et al. 2007). Hence, the relative efficiency of the MCMC/ss approach increases slowly (relative to the sMC approach) as the failure probability of interest approaches zero. Additionally, the MCMC/ss approach is robust (i.e., insensitive) to the number of random variables used to model the physical system of interest (Au and Beck 2001). Consequently, the MCMC/ss method is well suited for the estimation of failure probabilities associated with barge-bridge collision, where individual collision simulations involve many (greater than 20) random variables (this topic is discussed in detail in Chapter 7).

Unlike that of the sMC approach, the MCMC/ss procedure is divided into sequential stages of simulation (referred to as subsets). For each subset, simulation parameters are constrained such that only simulation results at or below a prescribed probability of exceedance threshold are generated. Therefore, for systems with small failure probabilities (significantly smaller than 0.01), the process of estimating the failure probability is divided into a series of subsets in which simulated states are generated that satisfy prescribed probability of exceedance thresholds. The probability of exceedance thresholds are then systematically decreased in each

new subset considered. As a result, high levels of efficiency can be achieved through the use of MCMC/ss (relative to the sMC approach).

5.4.4 General overview of the MCMC/ss algorithm

The overall MCMC/ss procedure is illustrated in Fig. 5.7 for an arbitrary limit state function, where the points shown in Fig. 5.7 represent limit state function evaluations for simulated states of a given physical system of interest. Note that the "axes" shown in Fig. 5.7 indicate the boundaries of the limit state zone of interest. For the limit state shown, the distance between a given point (simulated state) and the limit state boundary constitutes the proximity of the simulated state to a failure state. The MCMC/ss process begins with sMC simulation (Fig. 5.7a), which is referred to as subset 0. For subset 0, the minimum probability of exceedance threshold is initialized to 1 (i.e., no constraint is placed on the generation of simulated states since all possible computed probabilities will be less than or equal to 1). Using the results from subset 0, a probability of exceedance threshold is determined for the next stage of simulation, subset 1. Specifically, a pre-determined number of the subset 0 simulation results (points) are selected as subset 1 seed values that, both, define the probability of exceedance threshold for subset 1, and additionally, initialize (or seed) the subset 1 simulations.

It is recommended in the literature that, for all subsets, values at the 90^{th} percentile and greater (in terms of proximity to failure) be carried over from one subset to the next (Au and Beck 2001). This selection dictates the permissible region that can be explored during the next subset. For example, a selection of simulation results (from the pool of subset 0 simulations) at the 90^{th} percentile is tantamount to empirically identifying those simulations with a probability of exceedance less than or equal to 0.1 (since 10% of the subset 0 results, by definition, will lie outside the imposed 90^{th} percentile threshold). The point among the subset 1 seed values that is farthest from the limit state boundary has a probability of exceedance of 0.1 (in an empirical sense), and is used to define a minimum demand boundary (Fig. 5.7a), which is referred to as the subset 1 threshold.

Given the subset 1 seed values and the subset 1 threshold, the next stage of simulation (subset 1) can be carried out. In this stage, random variables are sampled using a modified Metropolis-Hastings (MH) sampling scheme, rather than the inverse CDF method (associated with the sMC approach). For a given simulated state (e.g., a seed value), the modified MH sampling scheme acts to perturb the state so as to produce the next state (rather than sampling the next simulated state in a completely independent manner). Samples formed in this way "step" from one simulation point to the next (Fig. 5.7b), producing a chain of simulations (referred to as a Markov Chain). Specific to the MCMC/ss approach is the constraint that all simulations conducted in subset 1 are constrained such that simulation results cannot fall below the subset 1 threshold.

The subset 1 Markov Chain steps are continued until the total number of simulations conducted in subset 1 becomes equal to the number of simulations, n_{sub}, conducted in the previous subset, subset 0 (Fig. 5.7c). Then, the process of selecting subset 2 seed values and the

subset 2 threshold is carried out in a manner analogous to that used for the previous subset. Given that a 90th percentile selection process is carried out using the pool of subset 1 simulation results, the probability of exceedance threshold associated with the subset 2 seed values then corresponds to a probability of exceedance that is one-tenth of the corresponding subset 1 probability of exceedance level (0.1). Consequently, the probability of exceedance threshold associated with the subset 2 seed values is 0.01. The process of carrying out subsets of Markov Chain simulations, selecting seed values, and determining a minimum threshold for the next subset is repeated until all of the seed values for subset t correspond to values that reach or exceed the limit state boundary (Fig. 5.7d). Subsequently, the failure probability can be estimated as (Au and Beck 2001):

$$p_{MCMC/ss} = \left(f_{exc}\right)^{t} \cdot NF / n_{sub} \tag{5.12}$$

where $p_{MCMC/ss}$ is the MCMC/ss probability of failure estimate; t is the final subset number; f_{exc} is the probability of exceedance threshold factor (e.g., a 90th percentile selection process corresponds to a f_{exc} value equal to 0.1); NF is the number of simulation values in subset t that exceed the limit state boundary; and, n_{sub} is the number of simulations carried out in subset t.

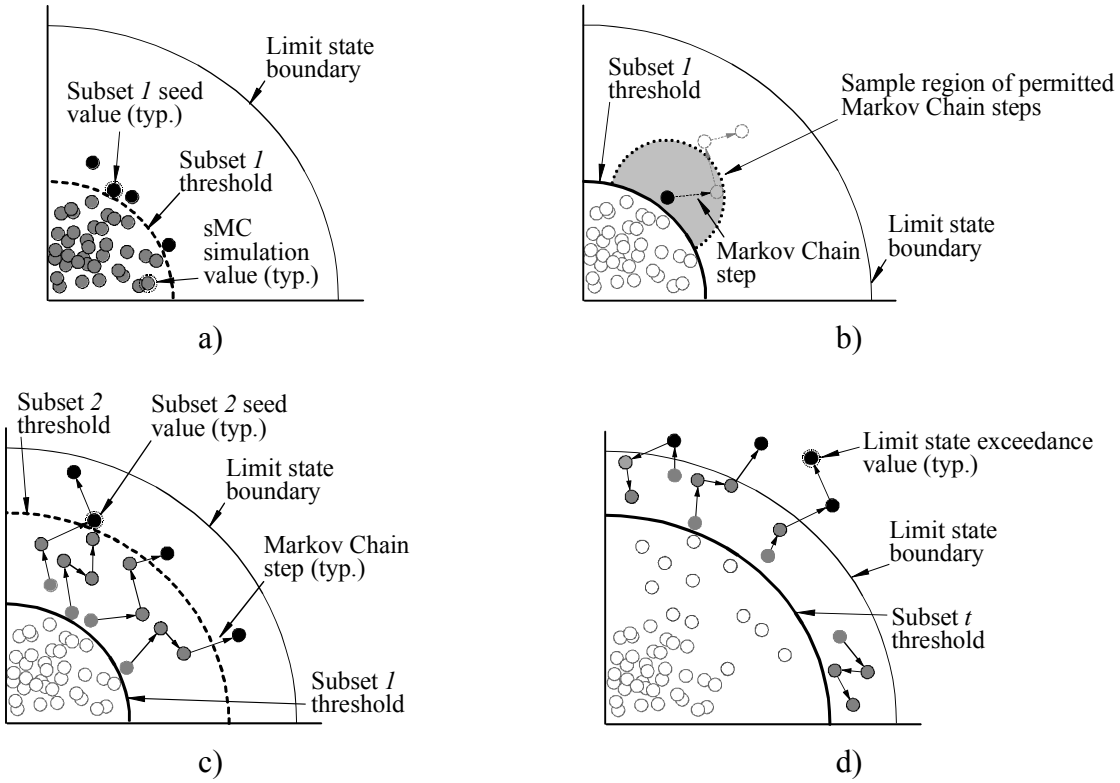

Figure 5.7 Markov Chain Monte Carlo with subset simulation (MCMC/ss) overview. a) Subset 0; b) Markov Chain process; c) Subset 1; d) Subset t

5.4.5 Random variable value generation for MCMC/ss

For all subsets beyond subset 0, the MCMC/ss simulation technique requires the use of the modified Metropolis-Hastings (MH) sampling scheme (and starting seed values of random variables) for random variable value generation as part of the Markov Chain steps. The purpose of modified MH sampling is to facilitate the generation of "candidate" random variable values (Fig. 5.8). Candidate values of random variables are, in turn, used to evaluate a limit state function of interest, and if the candidate values constitute an acceptable simulated state (i.e., if the simulation results satisfy the applicable probability of exceedance threshold, as discussed above), then the candidate random variable values are retained as seed values for the next step in the Markov Chain. Otherwise, the Markov Chain remains in place (the step length is zero), and the sampling process is repeated.

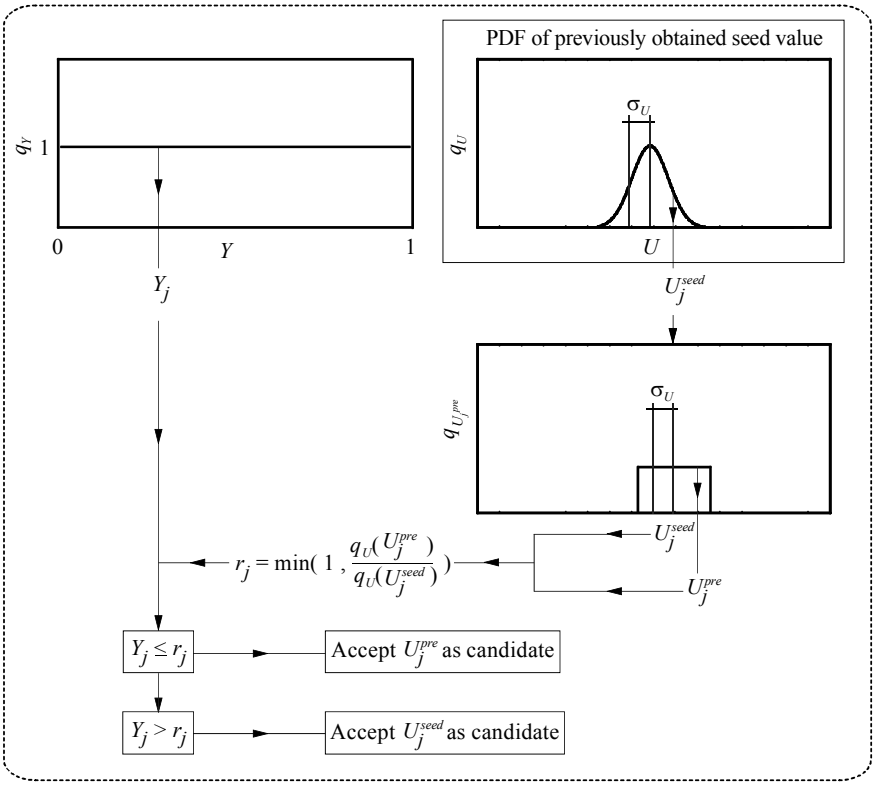

Figure 5.8 Random variable value generation using modified Metropolis-Hastings sampling

The process of generating candidate random variable values is illustrated in Fig. 5.8 for the random variable U of arbitrary distribution, q_U. Given a previously obtained seed value, U_j^{seed}, for simulation j, a uniform PDF, $q_{U_j^{pre}}$, is formed such that the mean value is U_j^{seed} and the standard deviation is equal to that associated with the random variable U (i.e., σ_U). The PDF $q_{U_j^{pre}}$ is then used to generate a "pre-candidate" sample value, U_j^{pre}. An acceptance ratio, r_j, is then calculated as:

$$r_j = \min(1, \frac{q_U(U_j^{pre})}{q_U(U_j^{seed})}) \tag{5.13}$$

where $q_U()$ indicates the evaluation of the PDF frequency. The acceptance ratio, r_j, is then compared to Y_j, which is between 0 and 1 and is randomly sampled from the uniform distribution, q_Y. If Y_j is greater than or equal to r_j, U_j^{seed} is retained as the candidate sample. Otherwise, the pre-candidate sample, U_j^{pre}, is accepted as the candidate sample.

5.4.6 Demonstration case solution using the MCMC/ss algorithm: subset 0

The MCMC/ss algorithm pertaining to subset 0—and as applied to the two-parameter demonstration case—is shown in Fig. 5.9. Given values of n_{sub}, f_{exc}, and statistical descriptions for R and S, the sMC method is employed. For each simulation i, values of R_i, S_i, and Z_i are stored in arrays $\{R_i\}_0$, $\{S_i\}_0$, and $\{Z_i\}_0$, respectively; additionally, for any instances where Z_i is less than or equal to zero (recall Eq. 5.3), the failure tabulation parameter, NF, is incremented. After n_{sub} sMC simulations have been carried out, the entries of $\{Z\}_0$ are ranked (sorted) in increasing algebraic order, and the ranked values are stored in $\{Z^{sort}\}_0$. Arrays for the R and S parameters are then formed ($\{R^{sort}\}_0$ and $\{S^{sort}\}_0$, respectively) to maintain consistency with the ranked entries in $\{Z^{sort}\}_0$. Then, a threshold entry parameter, j_{TH}, is calculated:

$$j_{TH} = \lfloor n_{sub} \cdot f_{exc} \rfloor \tag{5.14}$$

where for any real number, x, $\lfloor x \rfloor$ denotes the largest integer value less than or equal to x. Entries 1–j_{TH} in $\{Z^{sort}\}_0$ make up the subset 1 seed values, and the entry $\{Z_{j_{TH}}^{sort}\}_0$ is used to form the subset 1 threshold. If $\{Z_{j_{TH}}^{sort}\}_0$ is less than or equal to zero (i.e., all of the subset 1 seed values exceed the limit state threshold), then $p_{MCMC/ss}$ is estimated using the sMC approach and no further simulations are necessary (Fig. 5.9, bottom right). Otherwise, the subset 1 seed value arrays ($\{R^{seed}\}_1$, $\{S^{seed}\}_1$, and $\{Z^{seed}\}_1$) are formed. Additionally, the subset 1 threshold is formed (Fig. 5.9, bottom left):

$$Z_1^{max} = \{Z_{j_{TH}}^{sort}\}_0 \tag{5.15}$$

where the threshold quantity Z_1^{max} reduces to a maximum permitted limit state function value. After the subset 1 seed values have been formed, and the subset 1 threshold has been determined, the subset 1 simulations are carried out.

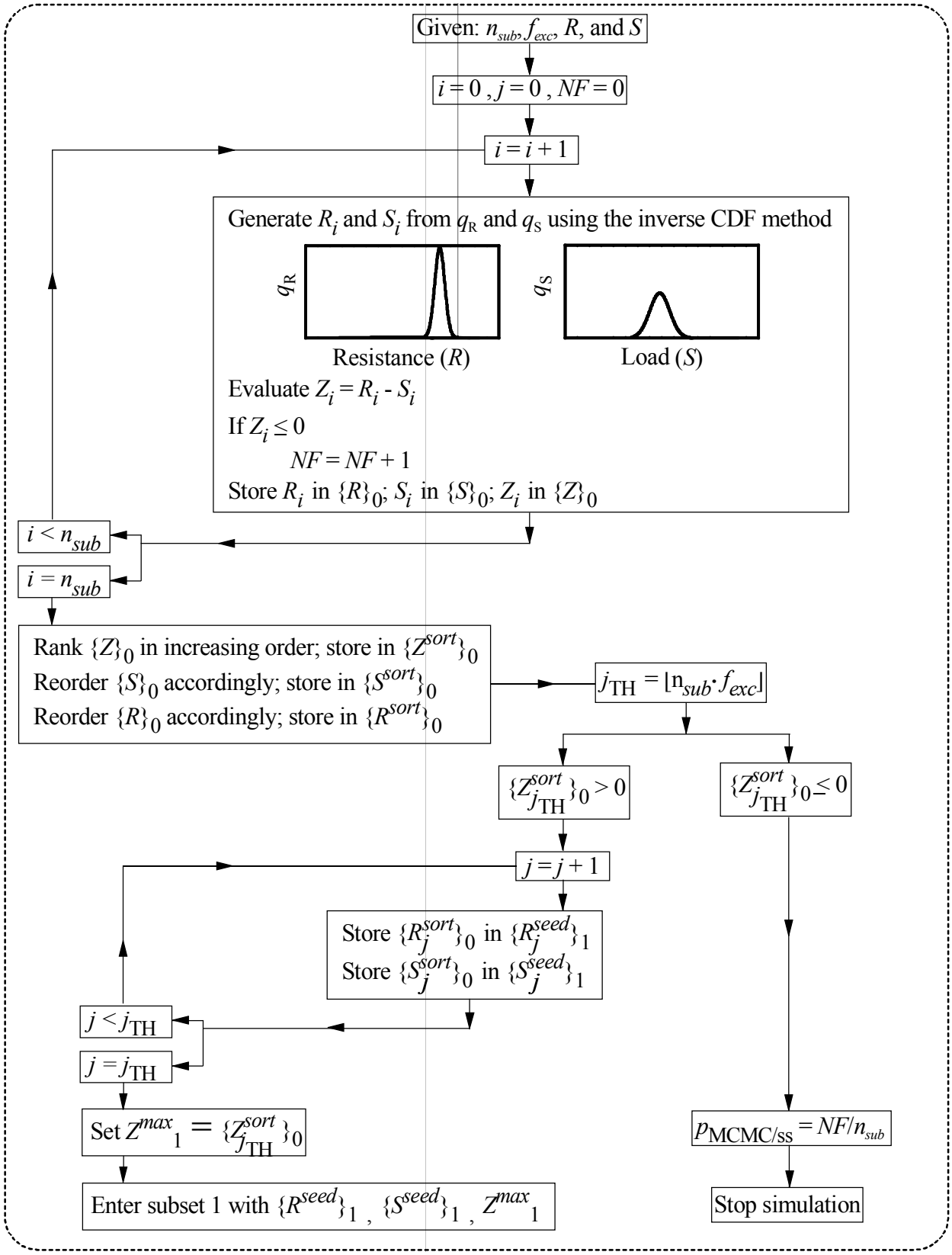

Figure 5.9 Markov Chain Monte Carlo with subset simulation (MCMC/ss) subset 0 summary

5.4.7 Demonstration case solution using the MCMC/ss algorithm: subset 1

The MCMC/ss algorithm pertaining to subset 1, and the two-parameter system, is shown in Fig. 5.11. Given values of n_{sub}; f_{exc}; the subset 1 seed values; and, the subset 1 threshold value, Markov Chains are formed, where one Markov Chain is initialized at each subset 1 seed value. The length (number of steps) of each Markov Chain, n_{step}, is dictated by:

$$n_{step} = \lfloor n_{sub} / j_{TH} \rfloor \tag{5.16}$$

where j_{TH} is equal to the number of entries in $\{Z^{seed}\}_1$. Then, for each subset 1 seed, a Markov Chain consisting of n_{step} simulation points is formed using modified MH sampling (Fig. 5.11, middle). During formation of the Markov Chains, if any values stored in $\{Z\}_1$ are found to be less than or equal to zero (recall Eq. 5.3), then the failure tabulation parameter, NF, is incremented. When the total number of simulations conducted becomes equal to n_{sub}, the ranked $\{Z^{sort}\}_1$ array, and the corresponding arrays $\{R^{sort}\}_1$ and $\{S^{sort}\}_1$, are formed in the same manner as that described for subset 0. Then, the threshold entry parameter, j_{TH}, is calculated for subset 1 using Eq. 5.14. Analogous to that of subset 0, if the entry $\{Z^{sort}_{j_{TH}}\}_1$ is less than or equal to zero, then no additional simulations are required and the failure probability estimate, $p_{MCMC/ss}$, can be calculated (recall Eq. 5.12). If, however, the entry $\{Z^{sort}_{j_{TH}}\}_1$ is greater than zero, then the subset 2 seed values and the subset 2 threshold value are formed (Fig. 5.11, bottom left), where the formation process is identical to that described for the corresponding subset 1 quantities. Subsequently, the subset 2 simulations can be carried out.

5.4.8 Demonstration case solution using the MCMC/ss algorithm: summary

The MCMC/ss algorithm, as it applies to the demonstration case, is summarized in Fig. 5.12. For subset t—using results from the simulations conducted for subset t—the quantities NF, j_{TH}, and $\{Z^{sort}_{j_{TH}}\}_t$ are calculated. Then, if the value of $\{Z^{sort}_{j_{TH}}\}_t$ is calculated to be greater than zero, the quantities necessary to begin subset t+1 (the subset t+1 seed values and the subset t+1 threshold) can be formed. Otherwise, the $p_{MCMC/ss}$ failure probability can be estimated using Eq. 5.12.

5.4.9 Demonstration case results from MCMC/ss simulation

Using the random variables defined in Table 5.1 and the limit state function defined in Eq. 5.3, twenty samples were generated using the MCMC/ss approach. For each sample, four subsets were carried out, where each subset consisted of 15,000 simulations. Consequently, each of the twenty MCMC/ss samples required 60,000 simulations. Also, a probability of exceedance threshold factor, f_{exc}, of 0.1 was employed. The limit state exceedance rate estimate for each sample is shown in Fig. 5.13. The mean-valued estimate of the failure probability, $p_{MCM/ss}$, from the twenty samples is 1.78E-04. This empirical estimate differs from the direct solution (1.73E-

04) by only 2.5%. Additionally, the COV associated with the $p_{MCM/ss}$ estimate, 0.087, falls below the pre-defined target COV of 0.1.

5.5 Efficiency Comparison of Probabilistic Simulation Techniques

The relative computational expense associated with generating demonstration-case probability of failure estimates for each of the sMC, LH, and MCMC/ss approaches (normalized by the number of sMC simulations) are displayed in Fig. 5.10. Additionally, the sample sizes and pertinent simulation outcomes used for each simulation approach are given in Table 5.2. The probability of failure estimates and relative dispersion (COV) measures show excellent agreement among all of the probabilistic simulation techniques employed, where such agreement demonstrates that the simulation outcomes are comparable. The relative computational expense associated with the LH approach is less than 60% of that associated with the sMC approach. Furthermore, the relative computational expense associated with the MCMC/ss approach is approximately an order of magnitude less than that of the sMC approach. Clearly, the use of advanced probabilistic simulation techniques is warranted for small failure probabilities when—as is the case for the simulation of barge-bridge collision—individual simulations require substantial computational resources.

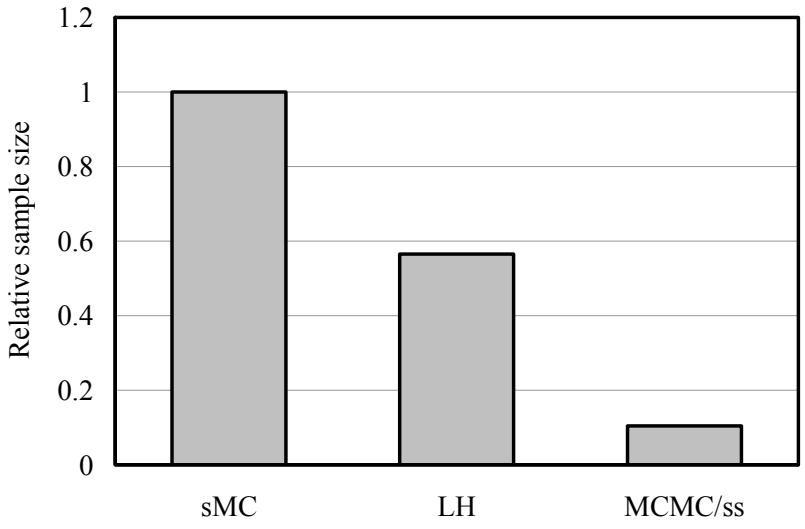

Figure 5.10 Relative sample size required to obtain comparable probability of failure estimates for the demonstration case

Table 5.2 Probability of failure estimates for the demonstration case

Random variable	Sample size	Mean	Standard deviation	COV
p_{sMC}	575,000	1.75E-04	1.45E-05	0.083
p_{LH}	325,000	1.78E-04	1.51E-05	0.085
$p_{MCMC/ss}$	60,000	1.78E-04	1.55E-05	0.087

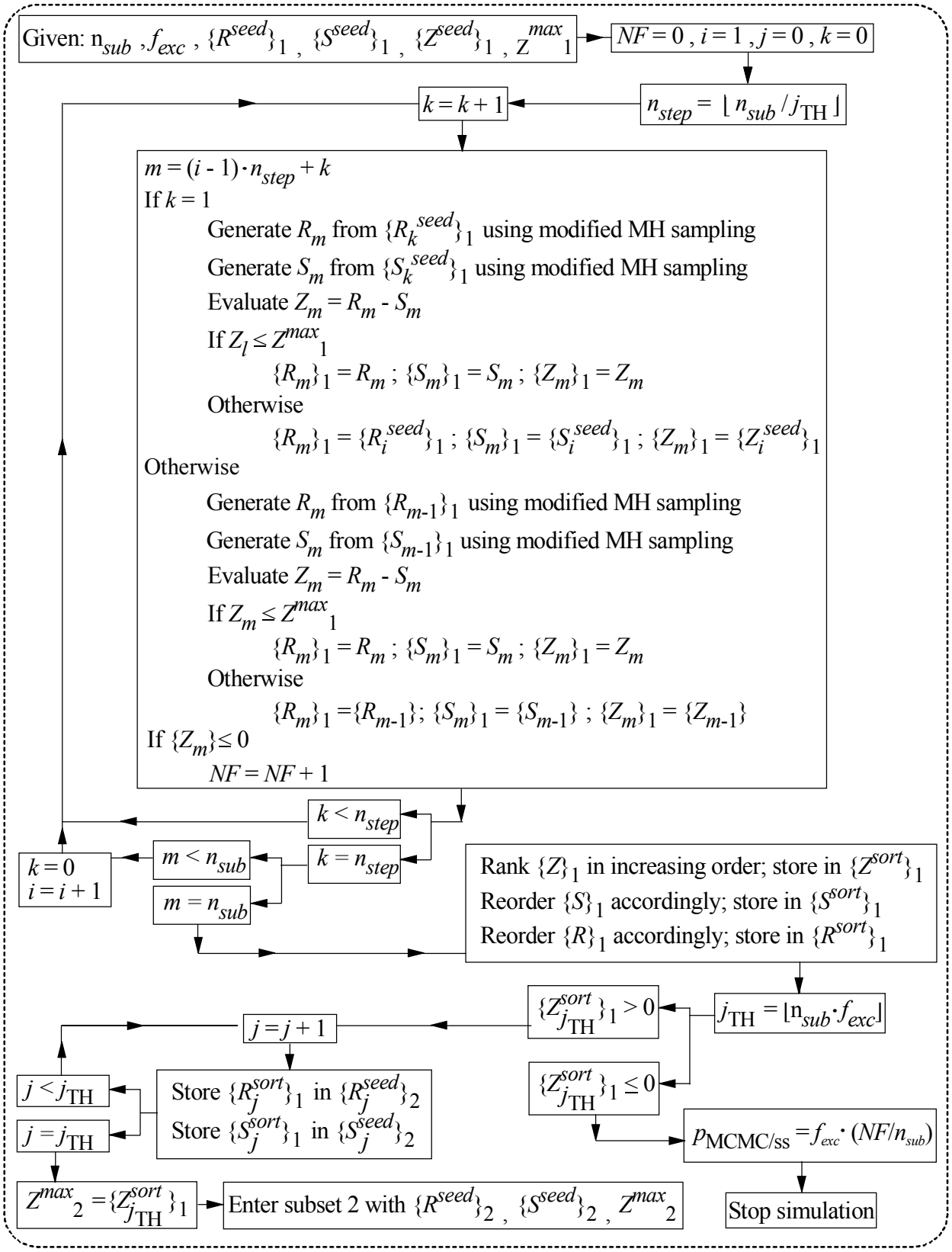

Figure 5.11 Markov Chain Monte Carlo with subset simulation (MCMC/ss) subset 1 summary

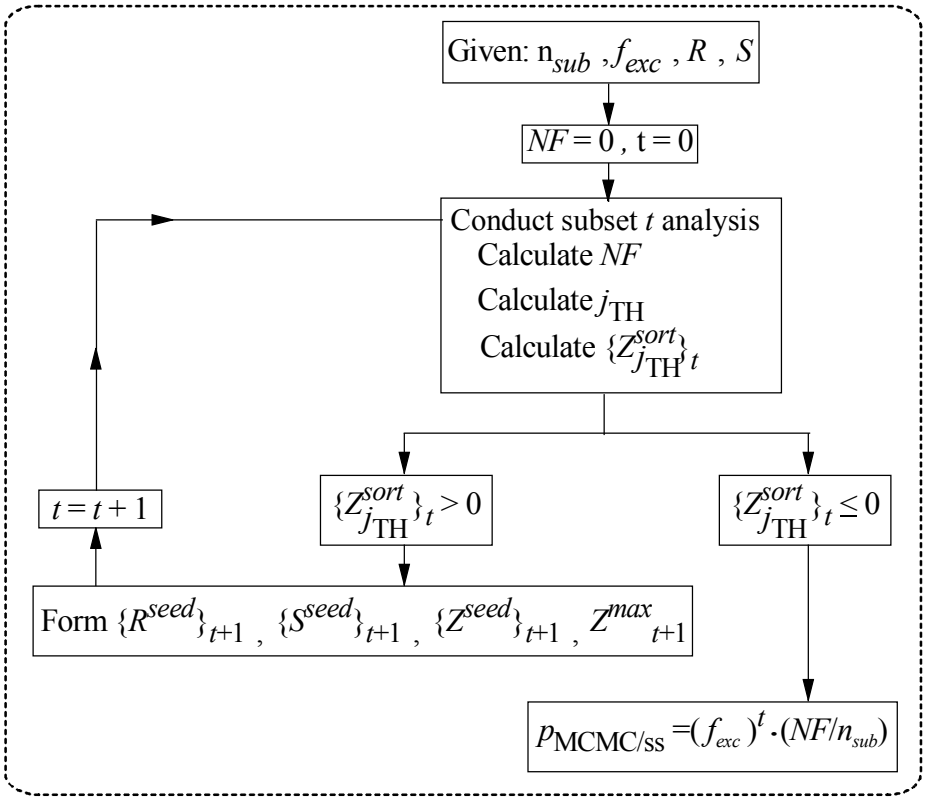

Figure 5.12 Markov Chain Monte Carlo with subset simulation (MCMC/ss) algorithm summary

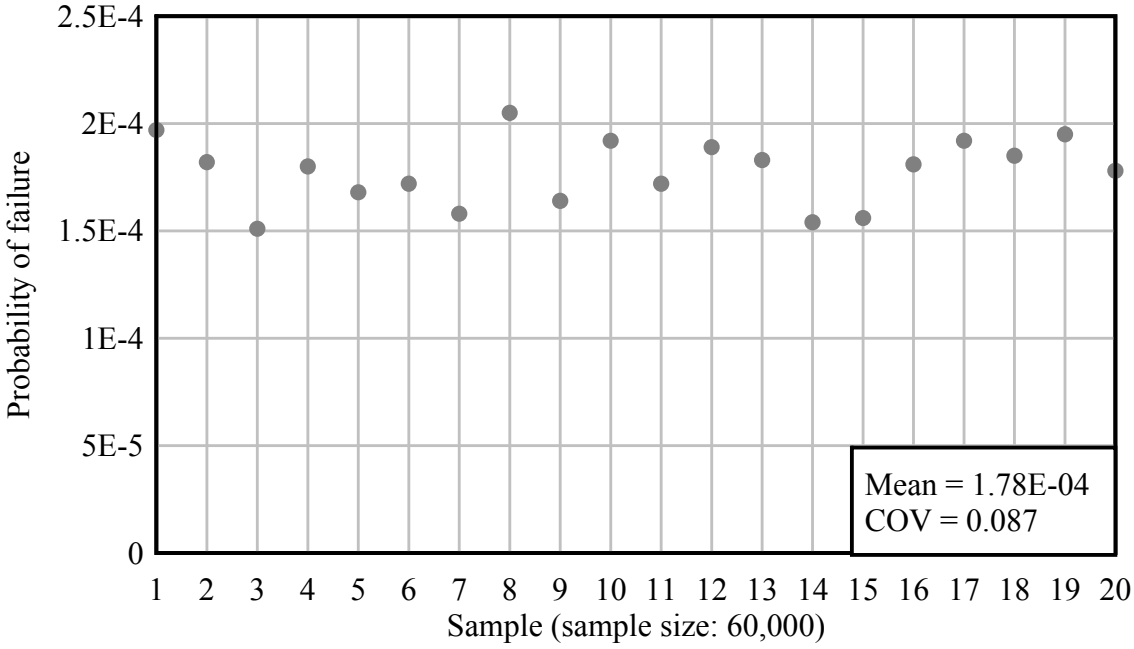

Figure 5.13 Markov Chain Monte Carlo with subset simulation (MCMC/ss) results

CHAPTER 6
PROBABILISTIC FRAMEWORK FOR ESTIMATING BRIDGE COLLAPSE

6.1 Overview

Recent advances in vessel-bridge collision analysis facilitate rapid assessment of barge impact force and bridge response where constitutive nonlinearity, kinematic nonlinearity, and dynamic effects are incorporated into the analytical framework. The efficacy of combining efficient analytical and modeling techniques with probabilistic simulation makes feasible the task of assessing the probability of collapse (i.e., limit state exceedance rates) for bridge piers that are subject to barge impact.

The proposed process of assessing the probability of collapse for bridge piers is summarized in Fig. 6.1. The proposed framework requires, for a bridge of interest, the identification of owner-defined limit states; the selection of a pier of interest; the development of a corresponding finite element (FE) model; and collection of vessel traffic data. Using bridge and vessel traffic data, statistical descriptions of barge and bridge parameters—including limit state capacities—are formed. Subsequently, probabilistic vessel collision simulations are conducted. Finally, PC is estimated based on the ratio between the total number of failures (the number of individual simulations where one or more applicable limit states are reached) and the total number of simulations conducted.

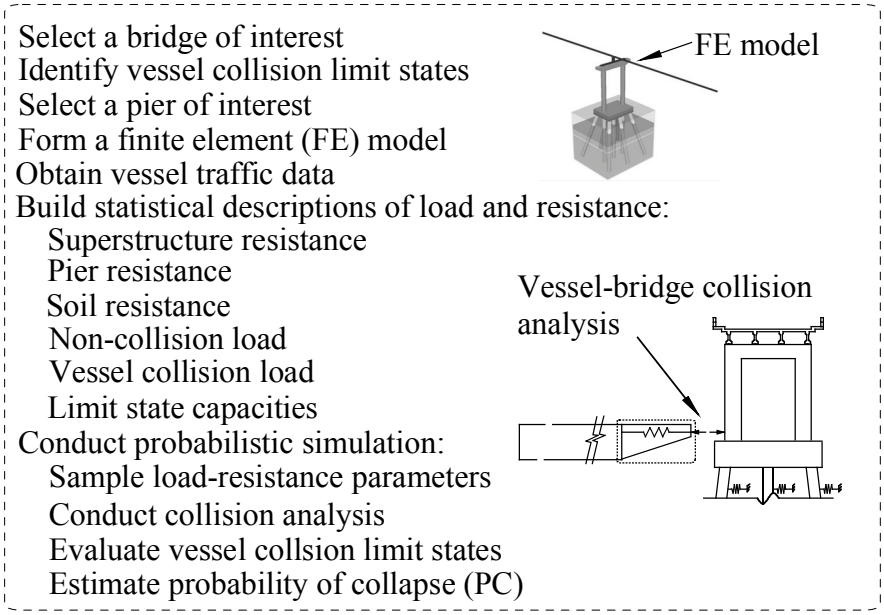

Figure 6.1 Overview of probability of collapse assessment for bridge piers subject to barge impact

6.2 Illustration Case

An OPTS model of the New St. George Island Bridge (Fig. 6.2) was selected to gauge the feasibility of incorporating probabilistic descriptors into the FE bridge models; and, determining probability of collapse through simulation. The New St. George Island Bridge, which replaced the Old St. George Island Bridge in 2004, is a coastal bridge located in northwestern Florida. The impacted off-channel pier of interest (Pier 53) supports five Florida Bulb-T girders (78 in. deep) at span lengths of 140 ft for each of the left and right flanking spans. Although girders atop Pier 53 are separated by an expansion joint across the pier cap, the superstructure deck is continuous. Load transfer devices at the substructure-superstructure interface consist of two elastomeric bearings and a cast-in-place shear pin at each of five evenly spaced bearing locations. Below the pier cap, Pier 53 contains two round (5.5 ft diameter) pier columns and a 6.5 ft thick waterline pile cap foundation. The underlying concrete piles consist of six battered and three plumb 4.5 ft diameter prestressed concrete cylinder piles, where each pile contains a 10 ft reinforced concrete plug extending downward from the pile cap.

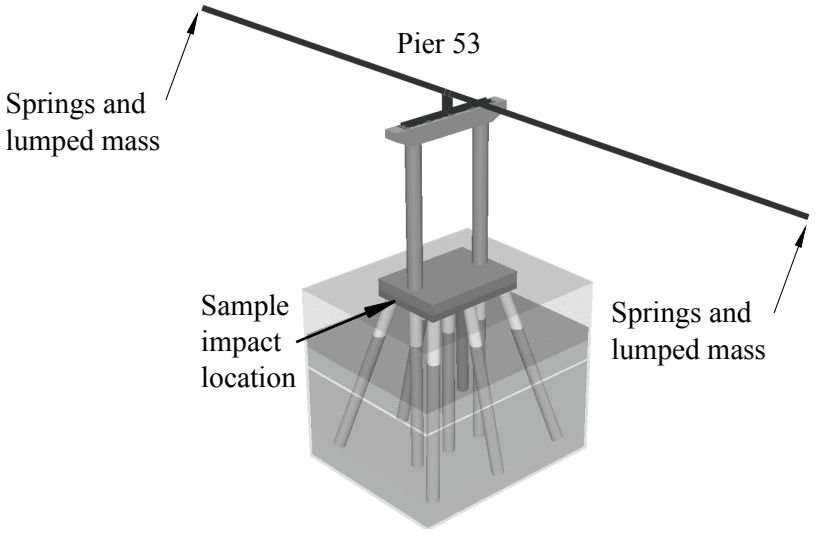

Figure 6.2 New St. George Island Bridge Pier 53 OPTS model

Pier 53 was designed to resist a static impact load (2300 kips) in accordance with current AASHTO barge collision design provisions. The FE model used for this proposal (Fig. 6.2) was confirmed to reach a collapse limit state (as defined below) at a comparable static load level before any probabilistic simulations were carried out. Data specific to this model are used to illustrate certain probability and simulation concepts discussed below.

6.3 Definition of Collapse

For bridges subject to vessel collision, quantitative definitions of the extreme limit state (bridge failure) are provided neither by the AASHTO vessel collision guide specifications nor by the AASHTO LRFD bridge design specifications (2007). Rather, the requirements are general in nature: the AASHTO code states that inelastic behavior and load redistribution are permitted but superstructure collapse must be prevented. Furthermore, it is stated that the bridge owner is responsible for approving the degree of damage that bridge components are allowed to sustain during impact events. Given that all bridges considered in the current study are publicly owned and located in Florida, it is appropriate to define bridge collapse in terms that are consistent with those specified in the Florida Department of Transportation (FDOT) Structures Design Guidelines (2009).

The FDOT guidelines clearly delineate the following vessel-collision limit states:

- Forces transferred to the superstructure must not exceed the capacity of load transfer devices (e.g., shear pins) at the superstructure-substructure interface;

- Load redistribution must not be permitted when the ultimate bearing capacity (UBC) of axially loaded piles is reached; and,

- The superstructure must not collapse.

The first two limit states can be evaluated on a member-by-member basis by comparing member capacity to internal force; limit states such as these are readily transformed into D/C ratios. Regarding bearing capacity, it is generally assumed that during collision a lateral bearing failure mode will occur before other possible failure modes (i.e., those due to tension or compression forces). As a result, the bearing location limit state may be expressed as:

$$V_N \geq V_B \tag{6.1}$$

where V_N is the nominal bearing shear capacity and V_B represents imparted bearing shear force. Additionally, the pile UBC limit state may be expressed as:

$$Q_N \geq Q_P \tag{6.2}$$

where Q_N is the UBC of the pile and Q_P represents axial force at the soil-pile interface.

Evaluating the superstructure collapse limit state requires a global assessment of bridge response. To facilitate formulation of a quantitative limit state expression for superstructure collapse, two assumptions are made:

- If an impacted pier collapses then the overlying superstructure will collapse;

- Until pier collapse occurs or until the bearing location limit state (Eq. 6.1) is reached, forces transferred to the superstructure are not sufficient to cause failure of superstructure members.

Consequently, the superstructure collapse limit state may be expressed in relation to the number of plastic hinges formed in pier structural members. A plastic hinge is defined herein as the simultaneous occurrence of axial load and biaxial bending moments that surpass the load-interaction failure surface for a given structural member (this definition implicitly assumes that sufficient shear resistance is present in structural members).

Several of the pier structural configurations considered in this study contain thick waterline pile caps. When impact occurs on a pile cap, it is assumed that load transfers to adjoining pier columns and piles (or drilled shafts) without producing plastic hinges within the pile cap itself. Collapse mechanisms for piers impacted at the pile cap level, therefore, can be defined in reference to load as it travels from the base of the pier columns to the superstructure (Fig. 6.3a); or, from the pile (or drilled shaft) heads to the underlying soil (Fig. 6.3b). Specifically, for pile cap impacts, two failure mechanisms are considered: the formation of two or more plastic hinges in every pier column; or, the formation of two or more plastic hinges in every pile (or drilled shaft).

Other pier structural configurations considered in this study contain deep shear walls that overlie buried (or mudline) pile caps. For impact scenarios associated with these types of structures, two additional failure mechanisms are considered: if impact occurs above the shear wall, directly on a pier column, a mechanism is then defined as the formation of three or more plastic hinges on the impacted column (Fig. 6.3c). If impact occurs on the shear wall, then the formation of two or more plastic hinges in each pier column is considered as a mechanism (Fig. 6.3d).

As a limit state, superstructure collapse may be defined as:

$$D / C_{mech} \leq 1 \tag{6.3}$$

where D/C_{mech} is a measure of the structural proximity to collapse for a given, applicable collapse mechanism, and is defined as:

$$D/C_{mech} = \frac{\sum_{i=1}^{m} \sum_{j=1}^{n} D/C_{ij}}{m} \tag{6.4}$$

where m is the number of members (e.g., piers, piles) associated with the applicable collapse mechanism; n is the number of hinges per member that are necessary to form the applicable collapse mechanism; and, D/C_{ij} is the j^{th} largest demand-capacity value along member i. If multiple collapse mechanisms are applicable for a given impact scenario, then the maximum D/C_{mech} for all applicable collapse mechanisms is retained.

To illustrate evaluation of the collapse limit state defined in Eq. 6.3–6.4, consider Pier 53 of the New St. George Island Bridge, which contains a thick waterline pile cap. The corresponding range of practical impact scenarios is associated with the collapse mechanisms shown in Fig. 6.3a–6.3b. For evaluation of the load path extending upward through the pier columns (Fig. 6.3a), the value of m is equal to 2 (because there are two pier columns); and, the value of n is equal to 2 (because the applicable collapse mechanism requires the formation of two plastic hinges per pier column). Regarding the load path extending downward through the piles (Fig. 6.3b), the value of m is equal to 9 (because there are nine piles); and, the value of n is equal to 2 (because the formation of two plastic hinges per pile is applicable for this collapse mechanism). The maximum value of D/C_{mech} (as calculated for the two applicable collapse mechanisms) is retained for a given impact simulation.

Measureable D/C ratios are obtained for Eq. 6.1–6.2 by dividing both side of each equation by the respective nominal resistance term. As a result, the three limit states considered in this study are expressed as:

$$\frac{V_B}{V_N} \leq 1 \tag{6.5}$$

$$\frac{Q_P}{Q_N} \leq 1 \tag{6.6}$$

$$D/C_{mech} \leq 1 \tag{6.7}$$

Furthermore, a series limit state may be defined as the maximum value of the three individual limit states:

$$D/C_{series} = \max\left(\frac{V_B}{V_N}, \frac{Q_P}{Q_N}, D/C_{mech}\right) \leq 1 \tag{6.8}$$

Through probabilistic simulation, expected values and exceedance rates for each of the D/C ratios expressed in Eq. 6.5–6.8 can be quantified. However, statistical descriptions for pertinent random variables must first be identified.

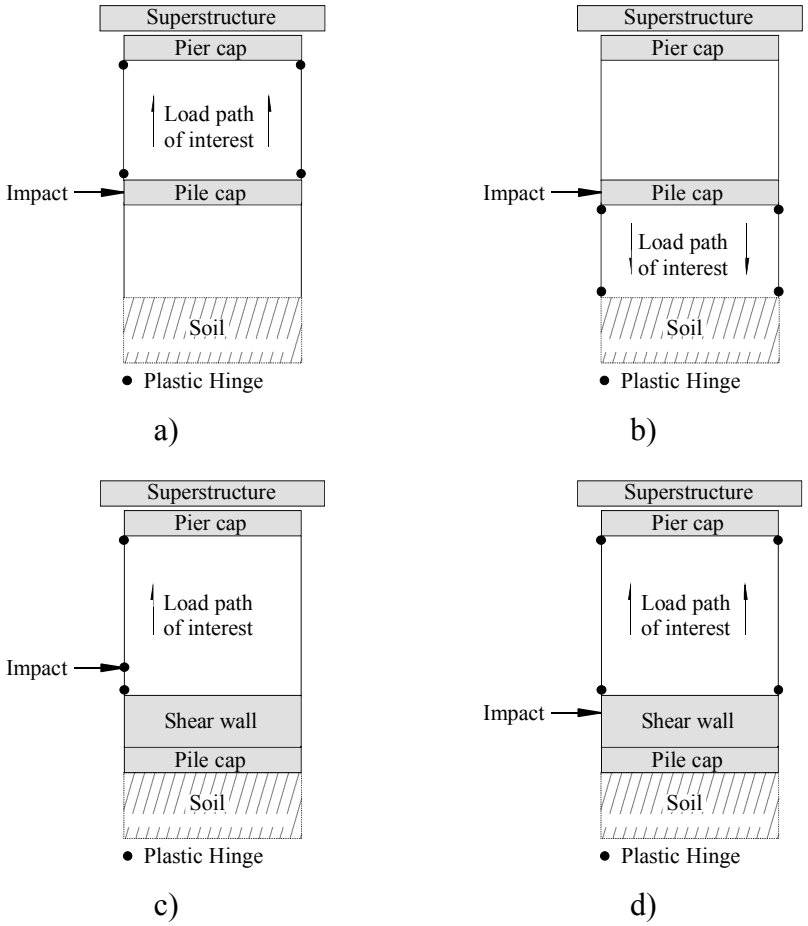

Figure 6.3 Collapse mechanisms considered. a) Pier column collapse mechanism for pile cap impact; b) Pile collapse mechanism for pile cap impact; c) Pier column collapse mechanism for pier column impact; d) Pier column collapse mechanism for shear wall impact

6.4 Statistical Descriptions of Resistance

A detailed probabilistic treatment of barge-bridge collision requires incorporation of a large number of random variables. Parameters or data necessary to statistically describe random variables are available in the literature (including various government agency databases). Given that the bridge finite element analysis (FEA) software FB-MultiPier (2009)—which contains the CVIA and OPTS bridge modeling features—has been validated against full-scale experimental

measurements (Consolazio and Davidson 2008), FB-MultiPier is selected as the analytical vehicle for carrying out the structural analysis components of the probabilistic simulations. Consequently, the set of random variables obtained from the literature are primarily discussed in relation to FB-MultiPier input. Furthermore, the set of random variables is divided into three main groups—those of resistance (superstructure, pier, soil); those of non-collision load (permanent, water, scour); and, those of vessel collision.

6.4.1 Superstructure resistance

6.4.1.1 Concrete and prestressed concrete girder superstructures

Statistical parameters of moment and shear capacity were identified by Nowak and Collins (2000) for superstructures that contain reinforced concrete or prestressed concrete bridge girders (Table 6.1). Both bias (the ratio of actual value to predicted value) and coefficient of variation (COV) were derived for each girder type based on differences between analytical predictions and actual measurements of ultimate moment and shear capacities. These parameters are not directly compatible with FB-MultiPier (2009), which uses resultant frame elements to model bridge spans (Fig. 6.4), where stiffness is largely dependent on modulus of elasticity (E_{span}) and shear modulus (G_{span}). However, by assuming that moment and shear capacity parameters in Table 6.1 approximately correspond to bending stiffness (E_{span}) and shear stiffness (G_{span}), respectively, the statistical parameters are adapted to the current study.

Table 6.1 Statistical descriptions of structural resistance

Variable	Applicability	Distribution	Bias	COV	Source
Concrete compressive strength	Ordinary ready mix (3–6 ksi)	Normal	1.38–1.14	0.111–0.080	MacGregor and Wight (2004)
Concrete compressive strength	Ordinary plant-precast (5–6.5 ksi)	Normal	1.38–1.14	0.10	MacGregor and Wight (2004)
Concrete compressive strength	High-strength (7–12 ksi)	Normal	1.19–1.04	0.115–0.105	MacGregor and Wight (2004)
Elastic modulus	Structural steel (mild)	Lognormal	1.00	0.033	Melchers (1999)
Moment capacity factor	Prestressed concrete superstructure	Lognormal	1.05	0.075	Nowak and Collins (2000)
Moment capacity factor	Reinforced concrete superstructure	Lognormal	1.14	0.13	Nowak and Collins (2000)
Shear capacity factor	Prestressed concrete superstructure	Lognormal	1.15	0.14	Nowak and Collins (2000)
Shear capacity factor	Reinforced concrete superstructure	Lognormal	1.2	0.155	Nowak and Collins (2000)
Ultimate stress	Prestressed strands	Lognormal	1.00	0.025	Nowak and Collins (2000)
Unit weight factor	All structural members	Normal	1.05	0.10	Nowak and Collins (2000)
Yield stress	Steel reinforcement	Lognormal	1.00	0.098	Nowak and Collins (2000)

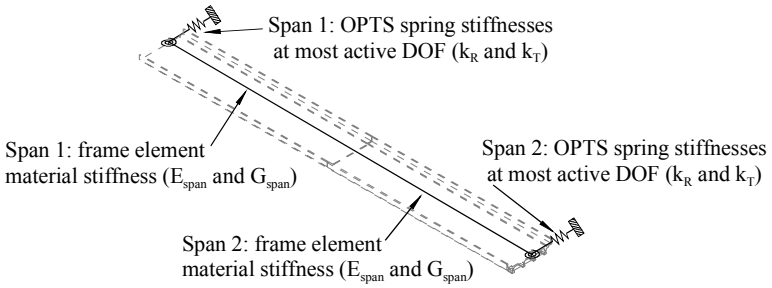

Figure 6.4 Random variables used to model superstructure resistance

To maintain consistency, moment and shear capacity statistical parameters for concrete and prestressed concrete bridge girders (Table 6.1) are again assumed to approximately correspond to bending (rotational) and shear (translational) stiffness, respectively, for OPTS model springs. Furthermore, efficiency is gained by limiting the probabilistic treatment to spring stiffnesses for only the most active degrees-of-freedom (DOF) at each span end, where such activity is attributable to vessel collision load effects (Fig. 6.4). Spring stiffnesses corresponding to these DOF are: vertical (plan-view) rotational stiffness (k_R) and horizontal translational stiffness (k_T) transverse to the span (Consolazio et al. 2008), which correspond to bending and shear stiffness, respectively. For a given concrete girder type, all random variable values related to superstructure bending stiffness (E_{span} and k_R) are generated by multiplying each mean value by a single sample of the moment capacity factor (Table 6.1). Random variable values of shear stiffness (G_{span} and k_T) are generated similarly, only with the use of a single shear factor (Table 6.1) sample.

6.4.1.2 Steel girder superstructures

Unlike that of structural concrete, the stiffness (e.g., elastic modulus) of structural steel is generally independent of ultimate strength. Therefore, a separate treatment of superstructure resistance variability is given for superstructures containing steel girders. Given that FB-MultiPier employs resultant frame elements for superstructure span members, superstructure cross-sections are modeled using transformed section properties. The process of modeling the superstructure in a probabilistic manner is initiated by sampling a value of the structural steel elastic modulus (for the girder members of a given span), E_S, according to the statistical description given in Table 6.1 (Melchers 1999). A sample of the elastic modulus for the concrete deck portion of a given span, E_c, of the superstructure is obtained by, first, sampling a value of concrete compressive strength (Table 6.1), f'_c, in accordance with MacGregor and Wight (2004). Then, given the compressive strength of the concrete (and assuming normal weight concrete), the modulus of elasticity of the concrete deck portion of the superstructure is estimated as (from ACI 2005):

$$E_c = 57000\sqrt{f'_c \cdot 1000} \tag{6.9}$$

where E_c is the elastic modulus (ksi), and f'_c is in units of ksi. A lack of statistical descriptors for direct sampling of steel girder shear stiffness necessitates that the span shear moduli are calculated by assuming Poisson's ratio values of 0.2 and 0.3 for concrete and steel components, respectively, and using the relationship:

$$G = \frac{E}{2 \cdot (1 + \nu)} \tag{6.10}$$

where G is the shear modulus, E is the sampled elastic modulus, and υ is the Poisson's ratio of the material. Using the sampled moduli values and the span cross-section geometry, the transformed section properties of the superstructure can then be determined.

To maintain consistency between sampled values of superstructure moduli and the corresponding OPTS spring stiffness values, a weighted average approach is taken. Given sampled values of E_s and E_c, weighted average factors are calculated for the steel and concrete members using the transformed geometry of the span cross-section (Fig. 6.5). The factor associated with the transformed cross-sectional area of the steel girders is determined as:

$$F_S = \frac{A_S^{tr}}{A_C + A_S^{tr}} \tag{6.11}$$

where F_S is the weighted area factor associated with the transformed cross-sectional area of the steel girders; A_S^{tr} is the transformed cross-sectional area of the steel girders; and, A_C is the cross-sectional area of the concrete deck. The factor, F_C, associated with the cross-sectional area of the concrete deck is:

$$F_C = \frac{A_C}{A_C + A_S^{tr}} \tag{6.12}$$

The factors in Eqs. 6.11–6.12 can then used to determine the statistical parameters (e.g., bias, COV) that are necessary to generate samples of OPTS spring stiffness values. For example, the weighted average COV value associated with k_R can be expressed as:

$$COV_{k_R} = F_C \cdot COV_{E_C} + F_S \cdot COV_{E_S} \tag{6.13}$$

where COV_{k_R} is the COV associated with k_R; COV_{E_C} is the COV associated with the concrete deck elastic modulus; and, COV_{E_S} is the COV associated with the steel girder elastic modulus. Note that, to maintain consistency with the probabilistic modeling of concrete and prestressed concrete girder superstructures, sampled values of elastic and shear moduli for the span members are assumed to approximately correspond to bending (rotational) stiffness, k_R and shear (translational) stiffness, k_T, respectively, at the span-ends of OPTS models.

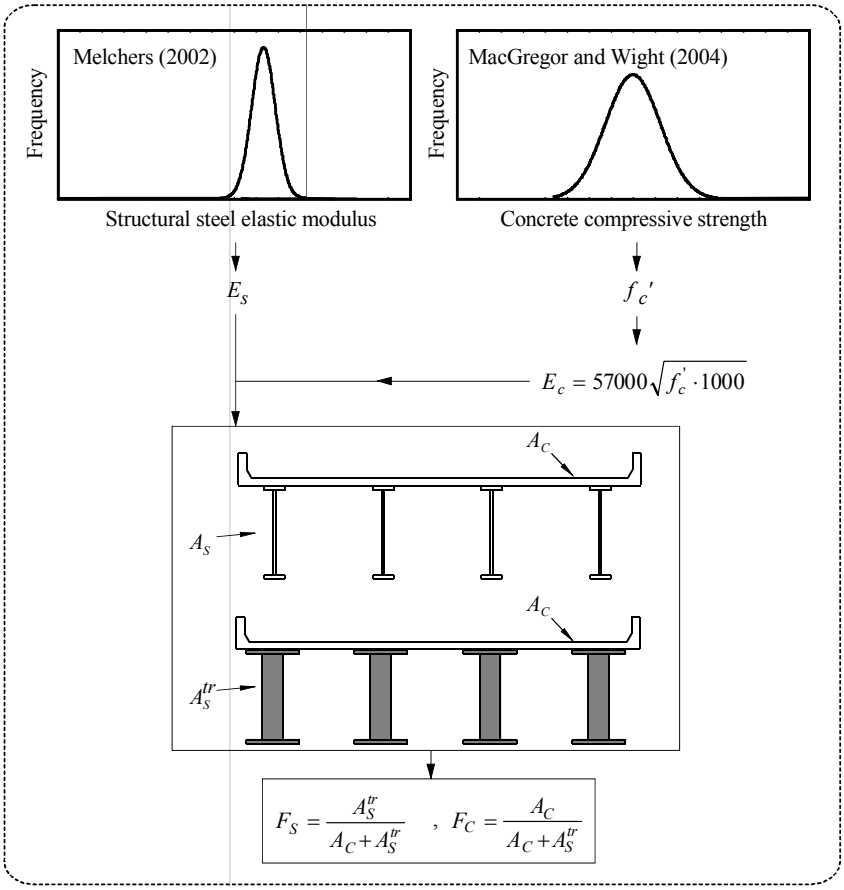

Figure 6.5 Weighted average factor calculation for steel girder superstructures

6.4.2 Pier resistance

Structural (non-soil) pier components—aside from bearing pads and pile caps—are modeled in FB-MultiPier using fiber-based frame elements. Fiber elements allow for discrete cross-section descriptions for each member, which facilitate a probabilistic treatment of member and reinforcement dimensions. However, available statistical descriptions (pertaining primarily to reinforced concrete beams) indicate that cross-section dimension error is roughly independent of member size (Nowak and Collins 2000). For typical dimensions of concrete members within pier structures (where dimensions commonly exceed several feet), only a nominal benefit is gained by incorporating variability into member cross-section dimensions. Additionally, size variations are considered to be small for reinforcing bars of concrete members and hot rolled

steel shapes (e.g., steel h-piles in pier foundations) (Melchers 1999). Cross-section dimensions (including size and placement of reinforcement) are therefore treated in a deterministic manner.

In contrast to cross-section dimension variability, the relatively larger variability of constituent material properties in pier structural members can significantly affect internal force distributions throughout an impacted pier. The effect is especially pronounced for steel reinforcement in concrete members subject to transverse loads, where under-reinforcement schemes are employed to promote ductility (Melchers 1999). Independent random variables (Table 6.1) are used to form constitutive relationships for structural materials in piles (or drilled shafts), shear walls, shear struts, pier columns, and pier cap beams.

Sampled values of material properties attributed to the pier cap beam are, in turn, employed to determine the capacity of substructure-superstructure load transfer devices composed of steel and concrete (e.g., cast-in-place shear pin capacity per ACI 2005). Although the capacity of stiff concrete-and-steel load transfer devices is modeled in a probabilistic manner, the stiffness of non-rigid load transfer devices such as elastomeric bearings is modeled deterministically due to insufficient statistical data. In FB-MultiPier, non-rigid load transfer devices can be modeled discretely using load-deformation relationships (e.g., those available in Podolny and Muller 1982) at bearing pad locations.

Non-prestressed steel reinforcement is modeled constitutively in FB-MultiPier using an elastic-perfectly-plastic relationship. Consequently, a complete and probabilistic material description can be generated for steel using random values of elastic modulus and yield stress (Table 6.1). Prestressed strands are modeled in FB-MultiPier using the stress-strain relationships given in PCI (1999) for 250 ksi strands and 270 ksi strands (where these stresses indicate the strand ultimate stress). In the proposed study, statistical parameters are employed to determine strand ultimate stress values (Table 6.1). For these values, the corresponding strand stress-strain relationship is formed using linear interpolation and the curves given in PCI (1999).

Generation of the constitutive relationship for concrete in FB-MultiPier (2009)—which employs the modified Hognestad curve for compression and piecewise-linear functions for tension (including tension stiffening)—requires specification of concrete compressive strength and modulus of elasticity. Given that the modulus of elasticity of concrete may be determined using compressive strength (recall Eq. 6.9), specification of concrete compressive strength alone is sufficient to define the entire constitutive relationship for concrete in FB-MultiPier. Statistical parameters for a variety of concrete types are available in Table 6.1. For a given concrete type, and a specified value of compressive strength, the bias and COV are determined by linear interpolation. The concrete statistical data are described by a normal distribution, which has an unbounded domain. To prevent generation of physically meaningless values, normally distributed resistance variables are limited to non-negative values.

Pile caps are modeled using flat shell elements in FB-MultiPier (2009). Since pile caps are typically thick (several feet) and cast monolithically, it is assumed that load will transfer to

adjoining structural members without inducing nonlinear constitutive behavior in the pile cap itself. Hence, a linear material model—through specification of an elastic modulus—is employed for the pile cap. Values of elastic modulus are determined based on sampled values of compressive strength (using the descriptors given in Table 6.1) and Eq. 6.9.

6.4.3 Soil resistance

Soil resistance is represented in FB-MultiPier (2009) by distributed nonlinear springs along each below-soil pile (or drilled shaft) node. For a given soil type (e.g., sand, clay, limestone) empirical equations are used that relate applicable soil strength properties to load-deformation curves. Each of the applicable soil properties are, in turn, obtained from correlations to soil boring data, such as those available for standard penetration test (SPT) blow counts (FB-Deep 2008). In this study, soil-springs are generally quantified by means of a multi-tiered sampling process based on SPT to soil-strength correlations. Two significant sources of variability are reflected in this process: the uncertainty associated with the measured SPT blow counts throughout the profile; and, the uncertainty associated with relating SPT blow counts to soil-strength parameters.

As a means of incorporating the uncertainty associated with the measured SPT blow counts, a database of SPT boring profiles is assembled from all profiles available for a bridge site of interest. It should be noted that only those profiles that permit impact (i.e., soil profiles that contain reasonable water depths) are included in the pool of available SPT borings. Furthermore, only those profiles that contain soil layering characteristic to the bridge site are retained for sampling. To illustrate this latter constraint as it affects the assembly of SPT boring profile databases, consider that among the available borings for the New St. George Island Bridge, a single, distant boring, B-72 (located approximately 0.5 mi from the pier of interest), was found to contain a layer largely consisting of wood timbers. Given the distance between boring B-72 and Pier 53, and that the layer (containing wood timbers) is only present at boring B-72, it is inappropriate to include B-72 in the SPT profile database for the Pier 53 simulations.

For each vessel collision simulation conducted, the process of characterizing the soil resistance is initiated by uniformly sampling (i.e., randomly selecting) an SPT boring profile from the profile database. Using the selected profile, the uncertainty associated with SPT to soil-strength correlations is then incorporated by employing the selected SPT blow count profile as a set of mean-valued parameters. Specifically, each blow count (within the randomly selected profile) is used as a mean blow count value to sample through-depth SPT blow count values using a lognormal distribution with bias of 1.0 and COV of 0.5 (as proposed by Barker et al. 1991). Pertinent soil properties, and ultimately, load-deformation curves are then quantified using the empirical equations that relate SPT values to soil strength, and in turn, soil stiffness relationships.

All applicable soil resistance properties for driven pile foundations (e.g., internal friction angle, subgrade modulus) are classified as dependent random variables of the originally sampled profile of SPT values. However, the characterization of soil resistance for drilled shaft

foundations embedded in intermediate geomaterials (e.g., limestone) requires specification of additional soil-strength parameters (e.g., split tensile strength of limestone). Statistical descriptions of parameters specific to the limestone-embedded drilled shaft foundations considered in this study are given in Appendix B.

6.5 Statistical Descriptions of Non-Collision Load

The load combination for vessel collision analysis is given in FDOT (2009) as:

$$EV = DL + WA + FR + CV \tag{6.14}$$

where EV indicates that the load case definition is of type Extreme Event II; DL represents permanent loads; WA represents loads due to water surrounding the pier; FR represents friction load (friction load is inherently accounted for through inclusion of substructure-superstructure load transfer); and, CV represents vessel collision load. It is important to note that, per FDOT, live loads are excluded from Eq. 6.14. Also, FDOT provisions exist that include bridge scour in the load combination. Load types present in Eq. 6.14 (vessel collision load is discussed below) and scour are employed in all barge impact analyses conducted in this research.

Bridge member permanent (dead) loads (DL) are included in FB-MultiPier models through specification of unit weight. Additionally, a global unit weight factor can be specified that proportionally modifies the self-weight of each member. A normally distributed unit weight factor (Table 6.2) is employed in the current study, including a bias factor of 1.05. The bias factor accounts for the tendency of designers to underestimate the dead load of bridge structures (Nowak and Collins 2000). As with normally distributed resistance models, sampled values of the unit weight factor are restricted to non-negative values.

Table 6.2 Statistical descriptions of non-collision load

Variable	Applicability	Distribution	Bias	COV	Source
Scour depth factor	Top soil elevation	Normal	0.55	0.52	Johnson (1995)
Unit weight factor	All members	Normal	1.05	0.1	Nowak and Collins (2000)
Water level	Waterline elevation	Varies	Varies	Varies	Various government agencies

In contrast to permanent loads, water loads (WA) reduce compression forces within submerged members through buoyancy. In FB-MultiPier, buoyancy forces are calculated, in part, as a function of the specified water elevation. However, for coastal and even inland waterways, water elevations can fluctuate significantly. Such fluctuations warrant a probabilistic treatment of the specified water level. Water elevation data are available for many coastal and some inland waterways from various government agencies (e.g., the National Oceanic and Atmospheric

Administration, NOAA 2010). Case-specific data related to the statistical descriptions of waterline elevations are given in Appendix B.

Water can severely disturb soil during storm events—causing scour—near the foundation-soil interface of submerged bridge members. In the FDOT guidelines (FDOT 2009), the type of scour to be used in conjunction with vessel collision loading is dependent on the respective, specified impact velocity. Specifically, drifting vessel velocities are paired with the scour caused by a 100-year storm event. Also, the velocities of flotillas operating under normal conditions are paired with one-half of ambient (long-term) scour conditions. Since all impact simulations conducted for this proposal involve barge flotillas traveling at normal operating speeds, scour depth (the mean value) is defined as one-half of long-term scour.

Extreme variability in scour depth is apparent from the high COV (0.52) specified in Table 6.2. Furthermore, it is apparent from the large specified bias (0.55) that design values of scour are highly conservative. In the proposed study, normally distributed scour depths are bounded between the undisturbed top soil layer elevation and the pile (or drilled shaft) tip elevation for the impacted pier. Sampled scour depths are modeled in FB-MultiPier by simply eliminating soil layering such that the top of soil elevation matches the given scour elevation.

6.6 Statistical Descriptions of Vessel Collision Load

Barge impact forces calculated using the AASHTO provisions are dependent on flotilla weight, flotilla velocity, and barge width. Recent studies (Consolazio and Cowan 2005, Yuan et al. 2008, Consolazio et al. 2009a) have shown that impact force is not dependent on barge width but rather the width (and shape) of the impacted bridge surface. Accordingly, probabilistic characterization of barge impact load is carried out in this study with consideration of flotilla weight, flotilla velocity, and impacted surface type.

6.6.1 Vessel traffic characterization

Vessel traffic characterization is accomplished by, first, obtaining deterministic vessel traffic data for pertinent waterway locations. For example, traffic that passes under the New St. George Island Bridge is categorized (by draft) into eight vessel groups (Table 6.3), where data are expressed in one-year intervals (Liu and Wang 2001). In Table 6.3, N is the vessel group trip frequency (the average number of annual passages under the bridge); B_{barge} and L_{barge} are the width and length of individual barges (ft), respectively within the vessel group; LOA is the overall flotilla length (ft); W is the flotilla weight (tonne); and, V is the flotilla velocity (knots).

Barge flotilla velocities are not explicitly provided. Therefore, guidelines for determining normal operating velocities for inland waterway traffic in Florida are employed (Liu and Wang, 2001, Wang and Liu 1999). Given that the total number of barge trips per year (i.e., the sum of all vessel group passages, N) from Table 6.3—which does not include the number of ship and recreational vessel trips per year—is greater than once per day (523 trips in 365 days), vessels

are assumed to operate in crowded conditions. Such conditions correspond to a base flotilla velocity of 6 knots. For vessels with a draft greater than 2.5 ft, the base velocity is reduced by 1 knot (Wang and Liu 1999). The base velocity is also decreased or increased by a current velocity of 0.4 knots for vessels traveling upstream or downstream, respectively.

Table 6.3 Annually averaged vessel traffic data for New St. George Island Bridge

Vessel group	Direction	N	Draft (ft)	No. barges	B_{barge} (ft)	L_{barge} (ft)	LOA (ft)	W (tonne)	V (knots)
1	up	85	2.1	1	51	216	291	971	5.6
2	up	25	5.6	1	58.6	316	391	3288	4.6
3	up	117	8.3	1	50.6	246	321	3259	4.6
4	up	92	11	1	54	319	439	5907	4.6
5	down	135	2	1.9	50.9	267	582.3	1777	6.4
6	down	22	4.9	1.9	62.4	328	698.2	6026	5.4
7	down	19	8.2	1.9	45.2	251	551.9	5945	5.4
8	down	28	11.8	1.9	72.4	256	606.4	12346	5.4

A discrete probability density function (DPF) that governs vessel group selection is formed by normalizing trip frequencies for each vessel group by the total number of vessel trips. This yields weighted vessel trip frequencies (or trip weights) for each vessel group. Vessel group characteristics (e.g., W, V, LOA) are then selected in proportion to respective vessel trip weights per the DPF. For example, characteristics for vessel group 1 (Table 6.3) are selected at a rate of 16% (85 trips out of 522.5 total trips).

6.6.2 Impact weight

For each vessel group that is selected, the respective flotilla weight (W) is subsequently sampled using a normal distribution with COV of 0.10 (Ghosn et al. 2003), where this sampling is limited to non-negative values. Draft associated with the sampled flotilla weight (W_{samp}) is then determined using weight-draft relationships in AASHTO (2009). The appropriate weight-draft relationship is selected for the barge type (e.g., hopper, tanker, deck) most closely matching individual barge characteristics (B_{barge}, L_{barge}) of the randomly selected vessel group. Draft is then related to hydrodynamic mass coefficient (C_H)—which accounts for the mass of water surrounding and moving with the flotilla (AASHTO 2009). Specifically, C_H is taken as 1.05 for underkeel clearances greater than $0.5 \cdot$ draft; and, C_H is taken as 1.25 for underkeel clearances less than $0.1 \cdot$ draft. Linear interpolation is used to obtain intermediate values of C_H. Given W_{samp} and C_H, flotilla impact weight (W_{impact}) is expressed as:

$$W_{impact} = C_H \cdot W_{samp} \tag{6.15}$$

6.6.3 Impact velocity

In contrast to impact weight, flotilla impact velocity (V_{impact}) is dependent not only on vessel group characteristics, but flotilla orientation and flotilla distance (relative to the flotilla centerline) from the intended vessel transit path. The process of deriving V_{impact} from V is summarized in Fig. 6.6. The first step of this process is selection of the vessel group—for example, using data from Table 6.3—where values of V, LOA, and B_{barge} are obtained (Fig. 6.6, top left). Also, flotilla orientation (or impact angle, ϕ_{impact}) is determined using the truncated normal distribution proposed by Kunz (1998), where the deterministic angle of vessel transit, ϕ, (e.g., 61.4° for the New St. George Island Bridge) is taken as the mean (Fig. 6.6, top right).

The impact angle (ϕ_{impact}) orients an axis used to measure the distance from channel centerline to flotilla centerline for aberrant flotillas (Fig. 6.6, center). A normally distributed PDF (with standard deviation equal to LOA) governing this distance—the flotilla centerline offset (x_{LOA})—is taken from the AASHTO provisions pertaining to the geometric probability of impact (PG). Specifically, as part of the vessel collision risk assessment, PG is defined as the integral of this PDF over the range of distances that would result in collision with a pier of interest (e.g., Pier 53 for the New St. George Island Bridge).

The same distribution and range of permitted offset distances are employed in the proposed study to obtain x_{LOA}. Using V and x_{LOA}, an adjusted velocity (V_{adj}) is determined (Fig. 6.6, bottom left) based on the distance, x_{LOA}, relative to channel edge distance and $3 \cdot LOA$ (per AASHTO 2009). For x_{LOA} distances greater than $3 \cdot LOA$, the adjusted velocity, V_{adj}, is reduced to the velocity of a drifting (non-propelled) vessel (1 knot is commonly used in design).

After V_{adj} is obtained, the impact velocity, V_{impact}, is sampled (Fig. 6.6, bottom right). The Joint Committee on Structural Safety (JCSS) proposed a lognormal distribution (with a mean of 5.8 knots and standard deviation of 1.9 knots) to describe vessel transit velocities in canals (JCSS 2006). A lognormal distribution with a mean of V_{adj} and COV of 0.33 (which matches that of JCSS 2006) is used to determine V_{impact} in the current study.

6.6.4 Impact surface

The CVIA technique, as implemented in FB-MultiPier, requires specification of: an impact node on the bridge structure, W_{impact}, V_{impact}, and a barge bow stiffness model (the means by which W_{impact} and V_{impact} are generated were discussed previously). Selection of an appropriate impact node and barge bow stiffness model is facilitated by employing sampled flotilla impact characteristics (including centerline location and impact angle). Pier 53 of the New St. George Island Bridge is used to illustrate the impact node and barge bow stiffness model selection procedure established as part of the proposed study. Details of impact cases that required additional considerations are given in Appendix C.

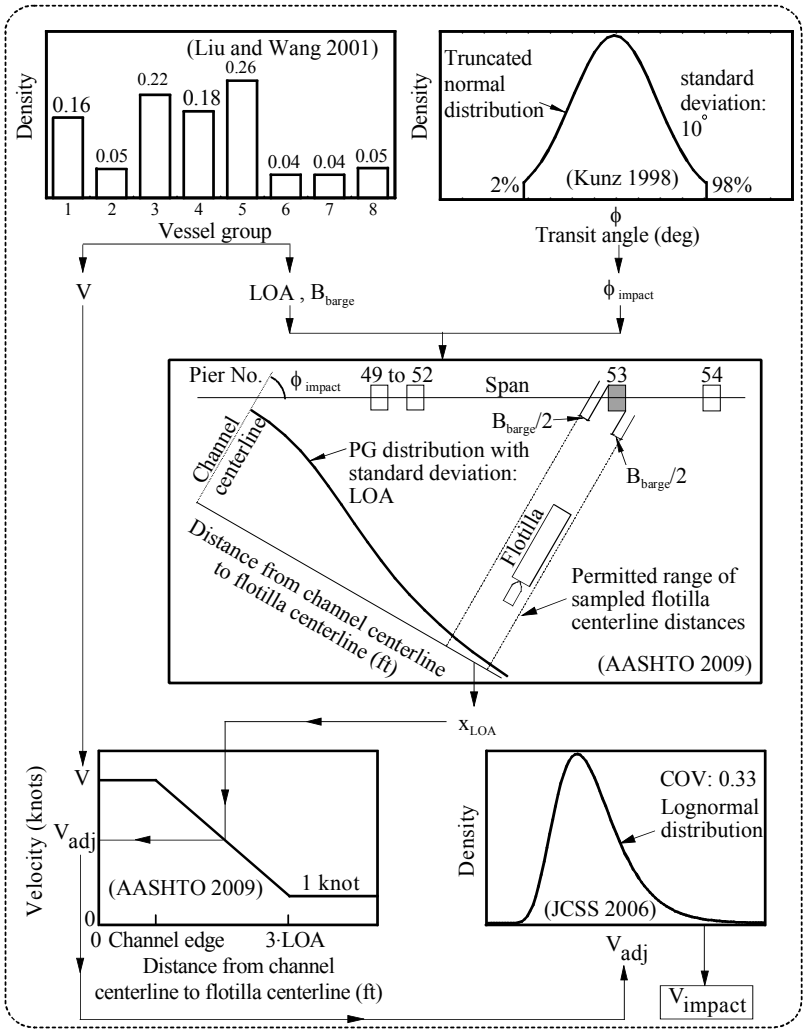

Figure 6.6 Impact velocity (V_{impact}) flowchart

Due to a thick waterline pile cap, two likely impact scenarios are afforded for Pier 53: a sharp-corner impact; and, an oblique impact (Fig. 6.7). In both impact scenarios, flotilla characteristics pertaining to location (x_{LOA} and the respective impact angle), B_{barge}, and nodal coordinates along the pile cap boundary are used in conjunction with trigonometric relationships to determine the initial contact node on the pile cap. For the sharp-corner impact scenario (Fig. 6.7a), the initial contact node coincides with the pile cap corner. Hence, a sharp-corner barge bow force-deformation relationship is employed and the pile cap corner node is designated as the impact node.

For the oblique impact scenario (Fig. 6.7b), the initial contact node is not coincident with the pile cap corner, which warrants additional consideration. First, the projected impact width (w_P) must be determined using sampled barge and waterway parameter values and trigonometric relationships. In this case, the parameters are: x_{LOA}, θ_O, B_{barge}, pile cap nodal coordinates, and the overall pile cap width. Then, the maximum force (P_{BY}) for a head-on impact with a flat impactor of width w_P is calculated. Subsequently, P_{BY} is adjusted using θ_O and the oblique impact force

reduction expression (discussed in Chapter 3), yielding the maximum oblique impact force, P_{BYO}. Finally, P_{BYO} is paired with the design yield crush depth (2 in) to form an elastic-perfectly-plastic barge bow stiffness model. Since the maximum (plastic) force is reached at a small crush depth (2 in), the initial contact node is selected for the impact node.

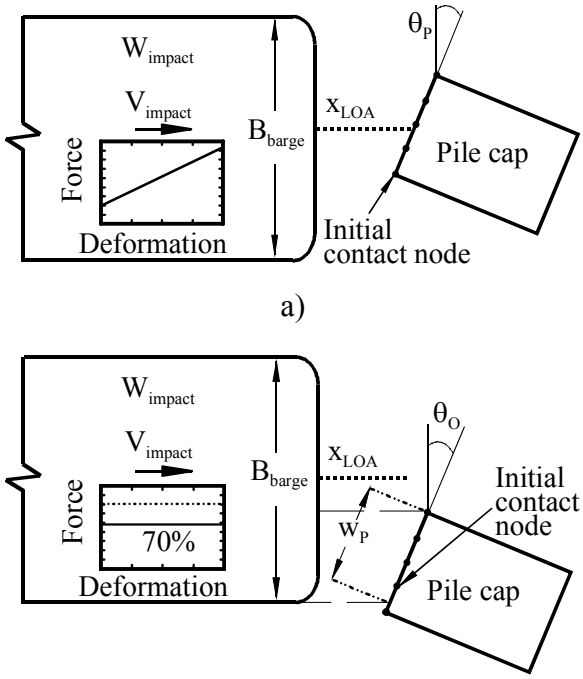

Figure 6.7 Impact scenarios for Pier 53 of the New St. George Island Bridge
a) Sharp-corner; b) Oblique

6.7 Probability of Collapse Assessment for Illustration Case

In this section, the probability of collapse of Pier 53 from the New St. George Island Bridge is assessed using two approaches:

- AASHTO risk assessment for vessel collision; and,
- The proposed probabilistic framework.

Predictions of collapse (limit state exceedance rates) obtained from each approach are presented, and then comparisons are made between the AASHTO and proposed framework results.

6.7.1 Probability of collapse assessment using AASHTO provisions

Using the AASHTO risk assessment procedure, probabilities of bridge collapse for Pier 53 of the New St. George Island Bridge were obtained for each vessel group. Per the AASHTO procedure, values of C_H were determined for each vessel group (Table 6.4) based on the deterministic water depth at Pier 53 (17.72 ft, including one-half of ambient scour) and the respective draft value (recall Table 6.3). Then, V_{adj} were determined for each vessel group (Table 6.4) using a deterministic value of x_{LOA} (1150 ft) and the respective flotilla velocities (V) and LOA values.

Table 6.4 AASHTO PC data for Pier 53 of the New St. George Island Bridge

Vessel group	N	CH	W (tonne)	V_{adj} (ft/sec)	KE (kip-ft)	a_B (ft)	P_B (kips)	PC
1	85	1.05	971	1.69	100	0.06	367	0
2	24.6	1.05	3288	1.82	390	0.21	1419	0
3	117	1.05	3259	1.69	335	0.21	1219	0
4	92.2	1.05	5907	2.51	1335	0.74	2206	0
5	135	1.05	1777	4.95	1563	0.91	2107	0
6	21.6	1.05	6026	5.16	5784	2.41	2878	0.022
7	19.4	1.05	5945	4.07	3537	2.17	2050	0
8	27.7	1.05	12346	4.54	9156	3.04	3483	0.038

The impact kinetic energies (KE) (kip-ft) associated with each group were then determined as (AASHTO 2009):

$$KE = \frac{C_H \cdot W \cdot V_{adj}^{\ 2}}{29.2} \tag{6.16}$$

where W must be expressed in tonne and V_{adj} must be expressed in ft/sec. Values of KE were then translated into values of barge bow crush depth (AASHTO 2009):

$$a_B = \frac{10.2}{R_B}\left[\left(1+\frac{KE}{5672}\right)^{1/2} - 1\right] \tag{6.17}$$

where a_B is the barge crush depth (ft) and R_B is the ratio of B_{barge} to 35 ft. The crush depth, a_B, was then related to static impact force (P_B):

$$P_B = 4112 \cdot a_B \cdot R_B,\ a_B < 0.34;\ P_B = \left[1349 + 110(a_B)\right] \cdot R_B,\ a_B \geq 0.34 \quad (6.18)$$

Finally, PC values for each vessel group were obtained using the static pushover capacity of Pier 53 (2300 kips) and P_B from the AASHTO PC equations (defined in Chapter 2).

6.7.2 Probability of collapse assessment using probabilistic simulation

The process of employing the probabilistic simulation framework is summarized in Fig. 6.8. The bridge of interest for the illustration case was selected as the New St. George Island Bridge. The bridge is located in Florida and publicly owned, and therefore, is subject to the limit states defined in Eqs. 6.5–6.8. Pier 53 of this bridge was selected as the illustration case, and an OPTS model has been created (recall Fig. 6.2). Also, the applicable traffic data have been characterized (recall Table 6.3). Load and resistance statistical descriptions have been adapted to the Pier 53 structural configuration (case-specific framework components, in addition to those given above, are detailed in Appendix B). These parameters, necessary to describe the multiple-degree-of-freedom (MDF) bridge and single-degree-of-freedom (SDF) vessel models, were used to carry out nonlinear dynamic vessel collision analyses (OPTS-CVIA). Standard Monte Carlo (sMC) simulation was employed for this illustration case to maintain focus on the physical concepts of the framework (the use of advanced probabilistic simulation techniques is discussed in Chapter 7). Using the sMC approach, 14,000 OPTS-CVIA simulations were carried out (divided into 10 samples with a sample size of 1400) to provide probability of collapse estimates for Pier 53. A sample size of 1400 was iteratively arrived at by increasing the number of sMC simulations until probability of collapse (failure) estimates with COV values of approximately 0.1 or less were obtained.

For each analysis, the four D/C ratios defined in Eqs. 6.5–6.8 were evaluated. If, during evaluation, any ratio was found to reach 1.0, then the corresponding limit state (i.e., structural failure) was considered to have occurred. In these instances, the total number of failures associated with the limit state (NF_i) observed over all analyses was incremented and a maximum D/C_i value of 1.0 was tabulated for the respective, individual simulation. After the number of failures for each limit state, NF_i, were tabulated for all simulations conducted, the corresponding limit state exceedance rates, PC_i, were estimated as the ratio of NF_i to the number of simulations conducted (n, or 1400 for each of 10 samples, for the illustration case).

Results obtained for the illustration case (when using the proposed framework and an sMC approach) are shown in Fig. 6.9. The limit state associated with substructure-superstructure interface capacity is estimated to be exceeded most often (at 0.22, this rate is approximately three times larger than either of the pile UBC limit state or the hinge-based superstructure collapse limit state exceedance rates). This finding is consistent with the findings of collision-induced dynamic amplification from recent studies (Consolazio et al. 2006, Davidson et al. 2010), where this phenomenon has been shown to lead to amplified load transfer at pier top locations during collision events.

A comparison of the series limit state exceedance rate from Fig. 6.9d (0.26) to that obtained using the AASHTO provisions reveals a stark contrast. First, collapse rates per vessel group, as predicted by AASHTO, are not directly comparable to the integrated collapse rate predicted probabilistically. To facilitate comparison, the AASHTO PC prediction is expressed as a weighted average (PC_{avg}^{AASHTO}):

$$PC_{avg}^{AASHTO} = \frac{\sum_{i=1}^{N_{VG}} N_i \cdot PC_i^{AASHTO}}{\sum_{i=1}^{N_{VG}} N_i} \tag{6.19}$$

where N_{VG} is the number of vessel groups; N_i is the vessel trip frequency associated with vessel group i; and, PC_i^{AASHTO} is the AASHTO PC estimate associated with vessel group i. For the vessel trip frequencies and AASHTO PC estimates given in Table 6.4, the corresponding PC_{avg}^{AASHTO} value is 0.0029. The trip-averaged AASHTO PC value is two orders of magnitude smaller than the value obtained using probabilistic simulation. Clearly, further investigation into the existing AASHTO PC framework is warranted.

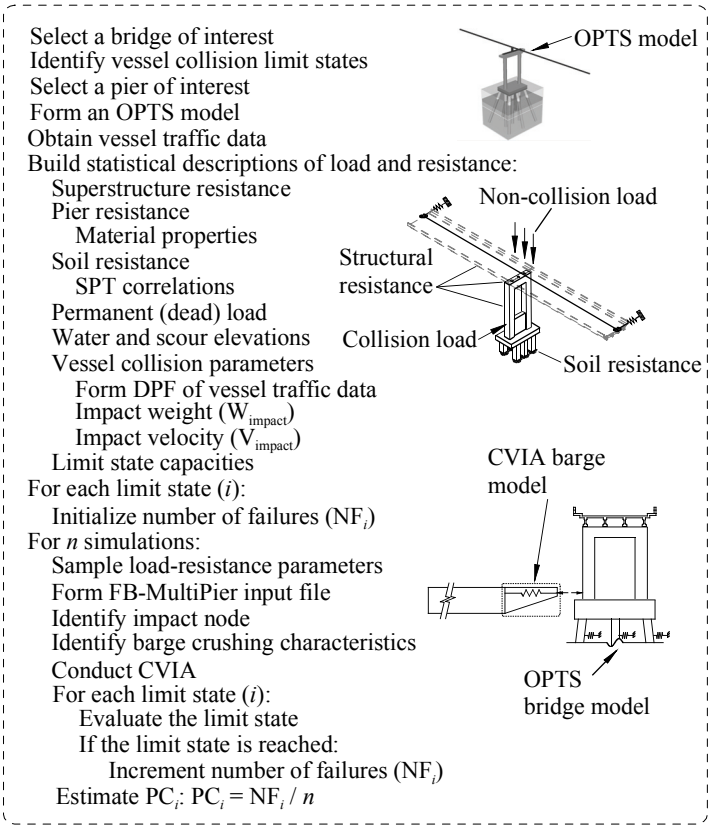

Figure 6.8 Summary of probability of collapse assessment for bridge piers subject to barge impact

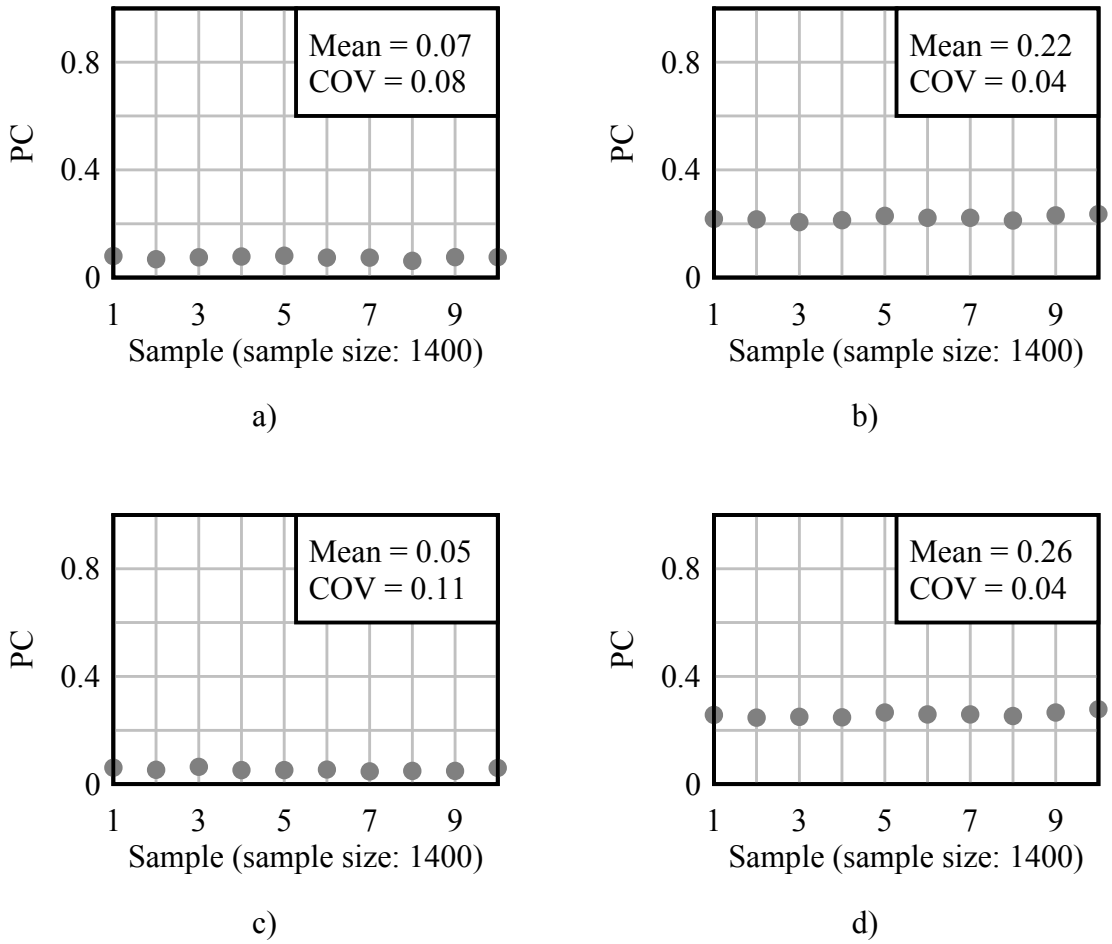

Figure 6.9 Proposed framework PC estimates. a) Pile UBC limit state;
b) Substructure-superstructure interface limit state;
c) Hinge-based superstructure collapse limit state; d) Series limit state

6.8 Concluding Remarks

A rational framework for determining the probability of bridge collapse (failure) in the event of barge-bridge collision has been presented in this chapter. The proposed framework employs efficient, yet accurate nonlinear dynamic collision analysis and bridge modeling techniques. Statistical descriptions of load and resistance (barge and bridge) parameters are used in conjunction with these techniques to assess bridge collapse rates through probabilistic simulation. The proposed framework has been used to estimate the probability of collapse for an illustration case. Significant differences between this estimate and that obtained using current bridge design provisions suggest the need for revisions in the existing vessel collision risk assessment.

CHAPTER 7
ADVANCED PROBABILISTIC SIMULATION TECHNIQUES FOR BARGE-BRIDGE COLLISION

7.1 Introduction

Throughout this study, bridge structural response to waterway vessel (barge) collision is quantified through use of nonlinear dynamic finite element (FE) simulation (bridge modeling and barge-bridge collision analysis techniques are discussed in Chapter 3). Given that a single FE collision simulation can require several minutes of computation time, simulation-based probabilistic assessment of bridge structural demand parameters (introduced in Chapter 6) can become impractical in many cases. More specifically, use of the standard Monte Carlo (sMC) approach (discussed in Chapter 5) in probabilistic simulation is highly inefficient for the assessment of small (significantly less than 0.01) failure probabilities, where potentially millions of sMC simulations are needed to form a reliable failure estimate. Therefore, when the probability of collision-induced bridge structural failure is small, highly efficient probabilistic simulation techniques must be employed to facilitate practical determination of a meaningful failure probability estimate. In this chapter, advanced probabilistic simulation techniques, first introduced in general terms in Chapter 5, are specifically tailored to barge-bridge collision simulation. The advanced probabilistic simulation techniques are verified (for a selected bridge case) to produce failure rate estimates comparable to the sMC approach, and are simultaneously shown to result in substantial gains in the efficiency of bridge failure rate estimation.

7.2 Overview of Advanced Probabilistic Simulation Techniques

The sMC approach, which can require millions of simulations to obtain meaningful failure probability estimates (for failure rates significantly less than 0.01), is undesirable for cases in which simulation efficiency is paramount. Bridge structural reliability problems considered in this study, where structural demands are quantified through FE simulations of barge-bridge collisions, necessitate the use of advanced probabilistic simulation techniques that are capable of efficiently producing small failure probability estimates and are robust to the number of system random variables. Two highly efficient, advanced probabilistic simulation techniques have been selected for use in this study: Latin Hypercube (LH) simulation and Markov Chain Monte Carlo with subset simulation (MCMC/ss).

7.2.1 Latin Hypercube (LH) simulation

The Latin Hypercube (LH) approach, originally proposed by McKay et al. (1979), is largely similar to the sMC approach (discussed in Chapter 5). However, instead of independent identically distributed (i.i.d.) parameter sampling, the LH approach employs interval-based (or stratified) sampling of random variables. The concept of interval-based sampling is illustrated for the random variable, θ, with probability distribution function (PDF), q, in Fig. 7.1. In the Latin Hypercube (LH) approach, random variable PDFs (e.g., q) are divided into intervals of equal probability, and all intervals (or strata) are sampled exactly once, where intervals are chosen randomly without replacement. Interval-based samples for all system random variables are then

combined and used to evaluate performance functions (i.e., limit state functions, evaluated using the results of FE barge-bridge collision simulations).

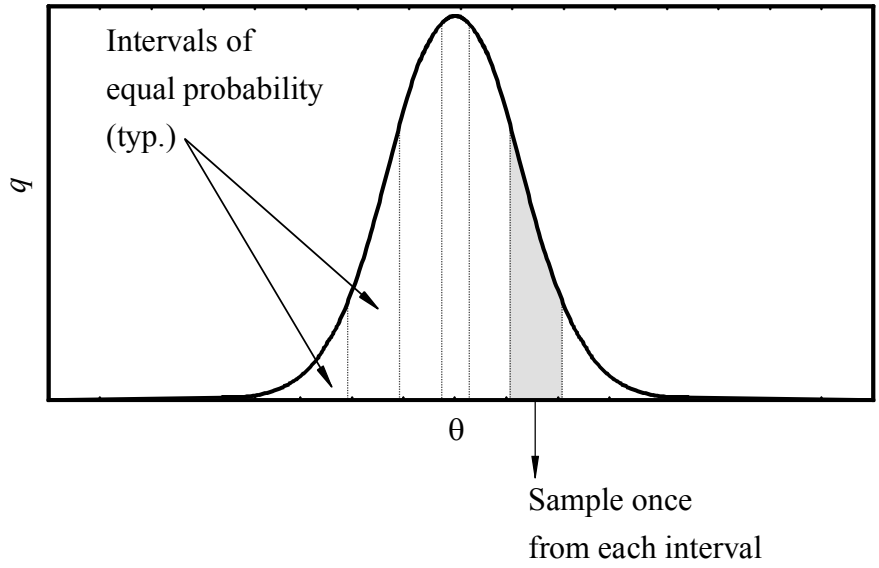

Figure 7.1 Latin Hypercube (LH) simulation overview

As a consequence of the interval-based sampling scheme, the LH approach ensures that the full domain of each random variable is represented in the performance function evaluations. In contrast, no such surety is present in the sMC approach. Therefore, stronger agreement is generally observed among estimates made from LH-based samples, relative to sMC-based samples. The LH approach (like the sMC approach), however, is limited by the need to conduct, on average, a number of simulations inversely proportional to the failure probability. For example, if a bridge failure probability is equal to 1E-03, then (on average) 1000 simulations are necessary to observe one failure. Consequently, the LH approach, (while capable of predicting more uniform failure probability estimates than the sMC approach) can still require millions of simulations before acceptable failure probability estimates are generated in certain cases.

7.2.2 Markov Chain Monte Carlo with subset simulation (MCMC/ss)

The Markov Chain Monte Carlo with subset simulation (MCMC/ss) approach was specifically developed for the estimation of small failure probabilities in high-dimensional spaces (Au and Beck 2001). Consequently, the MCMC/ss method has been selected for use in the estimation of small failure probabilities associated with barge-bridge collisions, where individual collision simulations are a function of many (greater than 20) random variables. The MCMC/ss procedure (Fig. 7.2) is divided into sequential stages (subsets) of simulation, where selected data are supplied from one subset to the next subset until a failure probability estimate is obtained. For each subset beyond the first, only those system states that lie beyond a performance threshold (determined from the previous subset simulations) are considered. Consequently, the process of estimating small failure probabilities can be divided (very efficiently) into the estimation of several larger, conditional probabilities.

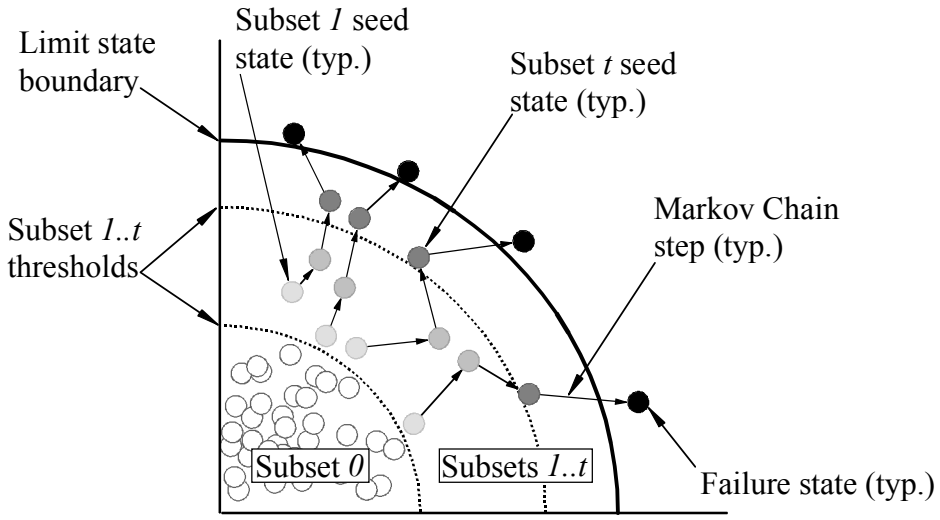

Figure 7.2 Markov Chain Monte Carlo with subset simulation (MCMC/ss) overview

The overall MCMC/ss procedure (Fig. 7.2) begins with subset 0, wherein sMC simulation is conducted to map simulated states in the limit state space. Simulated states from subset 0 that are in closest proximity to the limit state boundary are then used to both define the probability of exceedance threshold for subset 1, and additionally, initialize (or seed) the subset 1 simulations. For each subset 1 seed state, Metropolis-Hastings (MH) sampling—which acts to perturb the current state so as to conditionally produce the next state, as opposed to independently sampling the next state—is used to "step" from one state to the next, forming a Markov Chain (see Chapter 5 for additional details related to MH sampling). However, all simulated states in the Markov Chain are constrained to the region beyond the subset 1 threshold. Markov Chain stepping is continued until the total number of simulations conducted in all chains of subset 1 reaches the total number of sMC simulations conducted in subset 0.

For all subsequent subsets, the process of selecting seed states and a threshold value (from the previous subset results), and generating Markov Chains (with states that lie beyond the threshold) is repeated for t subsets, such that the number of states (in subset t) that fall above the limit state boundary is equal to or greater than the number of seed states. The failure probability can then be estimated as (Au and Beck 2001):

$$PC = \left(f_{exc}\right)^{t} \cdot NF / n_{sub} \tag{7.1}$$

where PC is the probability of failure (or in the context of the current study, probability of collapse) estimate; t is the final subset number; f_{exc} is the probability of exceedance threshold factor; NF is the number of failure states in subset t; and, n_{sub} is the number of simulations

carried out in subset t. Commonly, f_{exc} and n_{sub} are taken as 0.1 and 500, respectively (Au and Beck 2007), and accordingly, the same values are used for these two parameters in the current study.

Use of MCMC/ss in structural reliability benchmark problems (Au and Beck 2007) has revealed that the computational requirement associated with the MCMC/ss approach increases in an approximately logarithmic manner (as the failure probability approaches zero). In contrast, the sMC approach corresponds to a computational increase that is inversely proportional to the estimated failure probability. Consequently, substantial gains in computational efficiency are attained through use of the MCMC/ss approach (relative to the sMC approach).

7.3 Subset Simulation with Latin Hypercube Seeding (LH/ss)

In the current study, the LH and MCMC/ss approaches are combined in a new way, such that the Markov Chain subset simulations are initially seeded using LH simulation results; the as-combined, advanced probabilistic simulation technique is referred to as subset simulation with Latin Hypercube seeding (LH/ss). Through use of LH/ss (relative to MCMC/ss), fewer simulations are required to sample from the full range of system random variables. Use of the LH/ss algorithm, in the context of barge-bridge collision simulation, is discussed below.

7.3.1 Subset simulation with Latin Hypercube seeding (LH/ss) algorithm

7.3.1.1 Subset 0

The LH/ss algorithm is summarized in Fig. 7.3. For subset 0 (Fig. 7.3, top), which is the first stage of LH/ss, the LH approach is employed. Specifically, for barge and bridge random variables of load and resistance ($\theta_1,\ldots,\theta_m$), the corresponding, respective PDFs ($q_1,\ldots,q_m$) are divided into k_{st} intervals (or strata) of equal probability, where 500 intervals are employed in the current study. Then, parameter values for $\theta_1,\ldots,\theta_m$ are sampled once uniformly from within each interval and stored, respectively, in parameter arrays $\{\theta_1\}^0,\ldots,\{\theta_m\}^0$. Randomly selected parameter values, without replacement, are then taken from $\{\theta_1\}^0,\ldots,\{\theta_m\}^0$ and used to form each of the k_{st} (i.e., 500) FE barge-bridge models. The bridge finite element analysis (FEA) software FB-MultiPier (2009), with bridge modeling and collision analysis features discussed in Chapter 3, is used for analysis of the FE barge-bridge models in this study.

Predictions of bridge structural demand from the nonlinear dynamic FE barge-bridge collision analyses are paired with corresponding capacity terms to evaluate bridge structural limit states (expressed as demand-capacity ratios, D/C). Specifically, for each of i bridge structural limit states (e.g., those identified in Chapter 6 for Florida bridges), instances of the corresponding D/C_i that are equal to or greater than 1 are monitored by incrementing a corresponding failure tabulation parameter, NF_i. After k_{st} (equal to 500) simulations have been conducted, the probability of failure (i.e., probability of collapse) estimate, PC_i, is estimated for each limit state:

$$PC_i = NF_i / k_{st} \tag{7.2}$$

For PC_i estimate values that are approximately 0.01 or greater, the LH approach can feasibly be employed to carry out any further probabilistic simulations (given that each FE simulation requires several minutes of computation time). However, for small PC_i estimates (those values significantly less than 0.01), the use of subset simulation is required.

7.3.1.2 Subsets 1,…,t

Subset 1 (and all subsequent subsets), in contrast to subset 0, involves the generation of conditional system states through Markov Chain simulation (Fig. 7.3, bottom). For each subset, a total number of n_{sub} simulations are conducted, where n_{sub} is equal to k_{st} (i.e., n_{sub} is set equal to 500 simulations). Specific to subset 1, for limit state i, the subset number (t) is incremented from zero and the failure tabulation parameter, NF_i is reset to zero. Then, the set of LH-based D/C_i evaluations (from subset 0) are sorted in decreasing order and the sampled parameter arrays $\{\theta_1\}^{t-1},\ldots,\{\theta_m\}^{t-1}$ (also from subset 0) are rearranged accordingly. Once rearranged, sampled parameter value entries 1 through j_{TH} are retained as subset 1 seed states, where j_{TH}—the threshold entry parameter—is calculated as:

$$j_{TH} = \lfloor n_{sub} \cdot f_{exc} \rfloor \tag{7.3}$$

and, where the threshold exceedance factor, f_{exc}, is taken as 0.1. Additionally, the subset 1 threshold D/C value, D/C_i^{min}, is set equal to the minimum D/C_i value associated with the subset 1 seed states.

Given the subset 1 seeds and threshold D/C value (D/C_i^{min}), a Markov Chain is formed for each seed. Specifically, for a given seed state, MH sampling is used to perturb the seed parameter values ($\theta_1,\ldots,\theta_m$), which are then supplied as candidate parameter values to populate a FB-MultiPier barge-bridge model. Subsequently, nonlinear dynamic FE barge-bridge collision analysis is conducted to quantify bridge structural demand for the candidate state. If the calculated demand—paired with the corresponding bridge capacity term—results in a D/C_i value greater than or equal to 1, then the failure tabulation parameter (NF_i) is incremented. Separately, if the D/C_i value is less than D/C_i^{min}, then the candidate parameter values are rejected and the seed values for $\theta_1,\ldots,\theta_m$ are stored in $\{\theta_1\}^t,\ldots,\{\theta_m\}^t$. Otherwise, the candidate parameter values for $\theta_1,\ldots,\theta_m$ are accepted (i.e., stored $\{\theta_1\}^t,\ldots,\{\theta_m\}^t$).

Using the current Markov Chain state, the process of generating additional candidate states; populating barge-bridge FE models; conducting collision analyses; and, accepting or rejecting the candidate states is repeated n_{step} times for each seed state, such that:

$$n_{step} = \lfloor n_{sub} / j_{TH} \rfloor \tag{7.4}$$

where n_{step} is the length of each Markov Chain in the subset. When, after a total of n_{sub} (i.e., 500) simulations have been conducted, the failure tabulation parameter (NF_i) is compared to the total number of seeds (which, in turn, is equal to j_{TH}). If, NF_i is less than the total number of seeds, then the next subset is entered using the parameter arrays $\{\theta_1\}^t,\ldots,\{\theta_m\}^t$ and corresponding D/C_i values. The process of generating Markov Chains is then repeated until, for subset t, NF_i becomes equal to or greater than the number of seed states. Subsequently, the probability of structural failure (collapse) estimate, PC_i, can be calculated using Eq. 7.1.

7.3.2 Incorporation of LH/ss into the proposed PC framework

Generally, barge and bridge parameters of load and resistance (identified as part of the proposed PC framework in Chapter 6) are readily sampled using the modified MH sampling procedure (discussed in Chapter 5). However, for discrete random variables extant in the PC framework, the development of variable-specific sampling schemes was necessary to ensure proper generation of respective Markov Chain components in the subset simulations. Discrete random variable sampling schemes, as part of the incorporation of the LH/ss approach into the PC framework, are described below.

7.3.2.1 Soil-strength parameters

Probabilistic formulation of soil resistance in the present study (summarized in Fig. 7.4) consists of, first, cataloging all SPT boring profiles for a bridge site of interest. Then, for each collision analysis conducted, an SPT boring profile is randomly selected, using a uniform distribution, from the entire catalog of SPT borings for the bridge site (where profile selection is discussed below). Using the through-depth SPT blow counts from the selected profile as expected (or mean) blow count values, sampled SPT blow count values are then generated in accordance with the statistical description given in Barker et al. (1991), where a lognormal distribution with bias of 1.0 and coefficient of variation (COV) of 0.5 is suggested. Subsequently, soil-strength parameters are calculated based on correlations (e.g., those referenced in FB-MultiPier 2009, FB-Deep 2010) to the sampled SPT blow count values.

As part of the subset 0 (or LH) simulations in the LH/ss approach, SPT boring profiles are sampled according to the ratio of k_{st} (taken as 500 simulations) to the total number of catalogued SPT boring profiles. Since fewer than 100 SPT borings were taken for any one of the bridge cases considered in the current study, there is a probability of 1 that each SPT boring profile is sampled several times in subset 0. In contrast, for sMC simulation—which is used in subset 0 as part of the MCMC/ss approach—no such surety exists.

Subset *0*

Conduct Latin Hypercube (LH) simulations:
- For random variables $\theta_1,...,\theta_m$:
  - Form k_{st} intervals of equal probability in the PDFs $q_1,...,q_m$
  - Sample from each interval once, store samples in $\{\theta_1\}^0,...,\{\theta_m\}^0$
- For k_{st} simulations:
  - Without replacement, sample randomly from $\{\theta_1\}^0,...,\{\theta_m\}^0$
  - Using sampled parameters, form FB-MultiPier model
  - Conduct nonlinear dynamic FE barge-bridge collision analysis
  - For each limit state (i):
    - Evaluate the limit state, $D/C_i = D_i / C_i$
    - If $D/C_i \geq 1$, increment NF_i
- Estimate PC_i: $PC_i = NF_i / k_{st}$

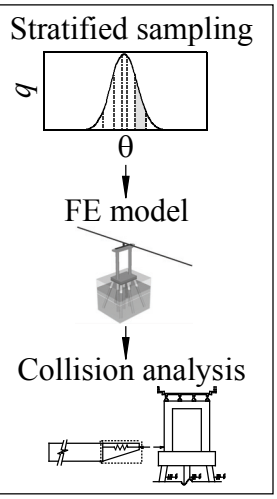

For each PC_i estimate significantly less than 0.01

Subsets *1,...,t*

Conduct Markov Chain subset simulations (ss):
- Set t = 0
- Set $n_{sub} = k_{st}$
- Increment t
- Set $NF_i = 0$
- Sort D/C_i evaluations from previous subset in decreasing order
- Rearrange $\{\theta_1\}^{t-1},...,\{\theta_m\}^{t-1}$ from previous subset accordingly
- Retain first j_{TH} parameter samples as seeds; $j_{TH} = \lfloor f_{exc} \cdot n_{sub} \rfloor$
- Set D/C_i^{min} equal to $\min(D/C_i)$ from retained seed parameters
- Starting at each seed:
  - Sample candidate values of $\theta_1,...,\theta_m$ using MH sampling
  - Using candidate parameter values, form FB-MultiPier model
  - Conduct nonlinear dynamic FE barge-bridge collision analysis
  - Evaluate the limit state, $D/C_i = D_i / C_i$
  - If $D/C_i \geq 1$
    - Increment NF_i
  - If $D/C_i < D/C_i^{min}$
    - Reject candidate; Markov Chain stays in place
  - Otherwise
    - Accept candidate; Markov Chain moves to candidate state
  - For current Markov Chain state, store $\theta_1,...,\theta_m$ in $\{\theta_1\}^t,...,\{\theta_m\}^t$
  - Repeat n_{step} times for each seed; $n_{step} = [n_{sub}/j_{TH}]$
- If $NF_i < j_{TH}$
  - Go to next subset
- Otherwise
  - Estimate PC_i: $PC_i = f_{exc}^t \cdot NF_i / n_{sub}$

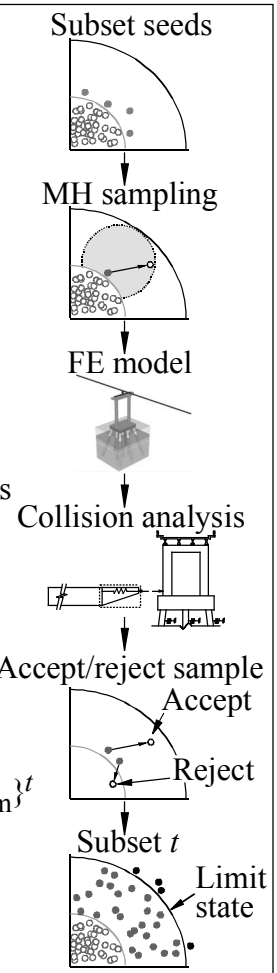

Figure 7.3 Subset simulation with Latin Hypercube seeding (LH/ss) summary

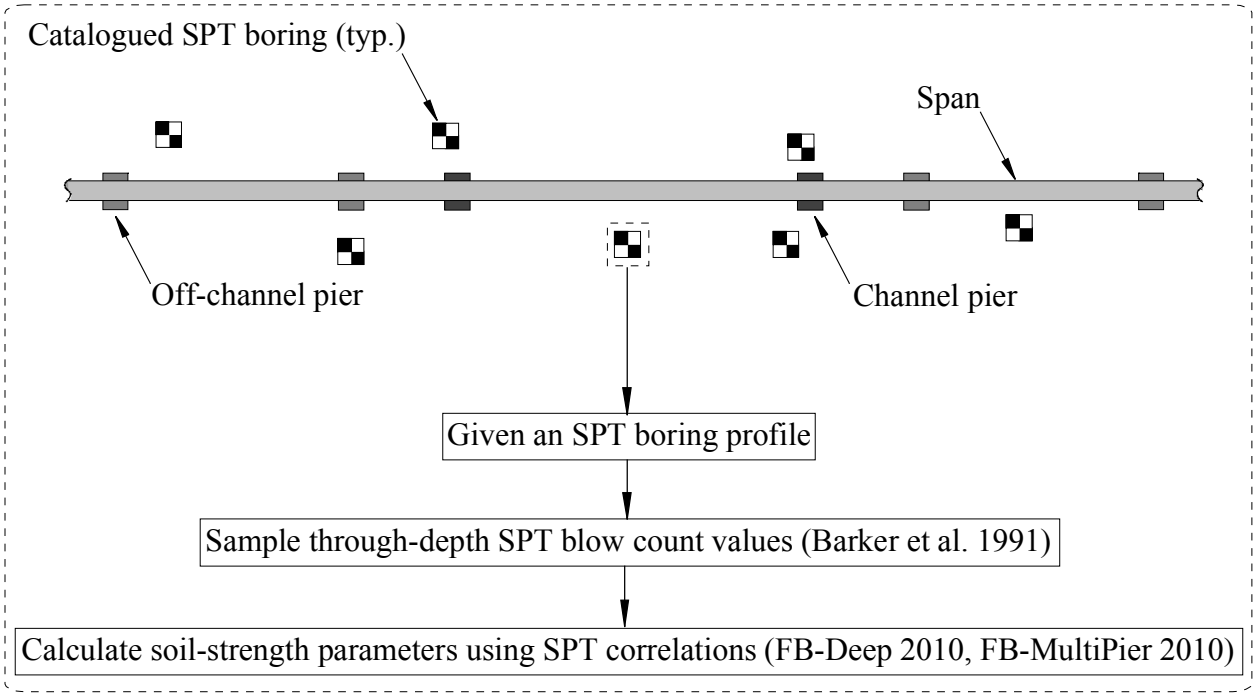

Figure 7.4 Determination of soil-strength parameters from SPT boring profiles

For subsets 1,…,t (in which Markov Chain simulations are conducted), SPT boring profiles associated with the subset 1 seed states are used to propagate the Markov Chains for all subsequent Markov Chain steps. Consequently, those SPT boring profiles that correspond to the largest D/C values (where all catalogued SPT borings have been sampled multiple times in subset 0) are retained for MH sampling in all subsequent simulations. It is critical to note that the alternative—namely, arbitrary reselection of SPT boring profiles in determining candidate Markov Chain states—can result in sudden, substantial changes in structural response, which are antithetical to the conditional (i.e., linked) nature of the Markov Chain simulations.

7.3.2.2 Barge impact velocity

A database of barge flotilla characteristics—where such characteristics strongly influence barge impact velocity—has been compiled for navigable waterways in the state of Florida (Liu and Wang 2001). In this database, waterway vessel traffic is divided into vessel groups (denoted by a vessel group number) with similar physical and transit-related characteristics. For a given vessel group number, barge physical parameters as well as the flotilla trip frequency for the waterway can be identified. In the proposed PC framework, vessel group characteristics are selected in proportion to vessel trip frequency. Specifically, for subset 0 of the LH/ss approach, the use of stratified (or LH-based) sampling ensures that each vessel group is selected exactly in proportion to the corresponding vessel trip frequency. Additionally, consistent with that described above for SPT boring profiles, reselection of vessel group numbers is not carried out for simulations beyond those used to obtain the subset 1 seed states. Consequently, sudden, substantial changes in impacted bridge structural response (as a result of arbitrary reselection of impacting barge flotilla characteristics) from one Markov Chain step to the next are prevented.

Barge flotilla impact velocity, V_{impact}, as defined in the proposed PC framework, is strongly dependent on vessel group (i.e., barge flotilla) characteristics as well as the relative barge-pier orientation for a given impact scenario. The process of sampling values of V_{impact} from vessel group characteristics (for simulations conducted as part of subsets 1,…,t) is summarized in Figs. 7.5a-b. Specifically, given a vessel group number, the following barge characteristics are identified (Fig. 7.5a, top): barge width (B_{barge}), overall flotilla length (LOA), and flotilla base transit velocity (V). Subsequently, a flotilla impact angle ϕ_{impact} is sampled (using MH sampling) and used in conjunction with B_{barge} and LOA to orient a set of axes that pass through the channel centerline (Fig. 7.5a, middle). Specifically, the normally-distributed geometric probability (PG) distribution defined in AASHTO (2009), with standard deviation equal to LOA, is projected onto the oriented axes and used to sample (using MH sampling) a flotilla position, x_{LOA}, that results in collision between the barge flotilla and pier of interest. Given the flotilla position (x_{LOA}) and vessel group velocity (V), an adjusted velocity (V_{adj}) is calculated to account for the distance between the flotilla centerline and the channel centerline (Fig. 7.5a, bottom).

Using the process summarized in Fig. 7.5a, and given a vessel group number, the adjusted velocity for a candidate Markov Chain state (V_{adj}^{m}) can be determined. Subsequently, using V_{adj}^{m} as well as adjusted and impact velocities from the previous Markov Chain state (respectively denoted as V_{adj}^{m-1} and V_{impact}^{m-1}), the impact velocity for the candidate Markov Chain state (V_{impact}^{m}) can be sampled (Fig. 7.5b). Conceptually, given a PDF that governs impact velocity for the candidate Markov Chain state (q_{adj}^{m}) and a seed value of impact velocity (V_{seed}^{m}), a corresponding value of V_{impact}^{m} can readily be determined using MH sampling. However, in the proposed PC framework, the PDF governing impact velocity is dependent on the adjusted velocity determined for a given simulated state. Therefore, the PDF of impact velocity associated with the previous Markov Chain state (q_{adj}^{m-1}) is generally not equal to q_{adj}^{m}, and furthermore, the seed value of the impact velocity for the candidate Markov Chain state (V_{seed}^{m}, which otherwise would be equal to V_{impact}^{m-1}) must be adjusted to produce a proper seed value. In this context, "proper" indicates equivalent cumulative probability values between V_{seed}^{m} and V_{impact}^{m-1}.

As illustrated in the top of Fig. 7.5b, a cumulative probability value (CP^{m-1}) is determined from the CDF, Q_{adj}^{m-1}, based on the sampled value of impact velocity from the previous Markov Chain state (V_{impact}^{m-1}). A cumulative probability value (CP^{m}) equal to CP^{m-1} is then defined (Fig. 7.5b, middle) and used in conjunction with the CDF of impact velocity for the candidate Markov Chain state (Q_{adj}^{m}) to determine the adjusted seed value for the candidate Markov Chain state (V_{seed}^{m}). Given the proper seed value of impact velocity for the candidate Markov Chain state and the lognormal PDF, q_{adj}^{m}, (with a mean value of V_{adj}^{m}), the impact velocity for the candidate Markov Chain state (V_{impact}^{m}) is readily determined using MH sampling. Finally, it

should be noted that for all cases in which V_{adj}^{m} is equal to V_{adj}^{m-1}, the above-described sampling scheme will produce equal values of V_{seed}^{m} and V_{impact}^{m-1}.

7.4 Verification of LH/ss

To assess the efficacy of the LH/ss approach, the SR-20 at Blountstown Bridge Pier 58 case has been selected for use as a verification case (the structural configuration is shown in Fig. 7.6). The Pier 58 pier structure, which is comprised entirely of reinforced concrete members, consists of two 5.5 ft diameter pier columns and two 9 ft diameter drilled shafts that are integrated by a 30.5 ft tall shear wall (additional structural configuration details are given in Chapter 4 and case-specific PC framework components are described in Appendices B–C).

For the soil conditions applicable to Pier 58 of the SR-20 at Blountstown Bridge, the pier foundation members (two drilled shafts) are embedded approximately 100 ft into the underlying soil, and furthermore, the ultimate soil-shaft axial resistance for similarly configured drilled shafts tested at the bridge site have been measured to be on the order of several thousand kips (McVay et al. 2003). From the expectation that significant levels of drilled shaft bearing capacity would be observed (relative to impact-induced demands) in collision simulations involving Pier 58, it follows that estimates of exceedance rates for limit states pertaining to the bearing capacity of foundation members would be small (significantly less than 0.01). Given this expectation, probabilistic simulations were carried out for the Pier 58 case (Fig. 7.6) using both the sMC and LH/ss approaches, where (in each approach) the Florida Department of Transportation (FDOT) vessel collision limit state pertaining to ultimate bearing capacity (UBC) of foundation elements (defined in Chapter 6) was considered. Estimates of structural failure (collapse) probabilities for the foundation UBC limit state are presented below, where the sMC-based results are used as a benchmark for judging the corresponding LH/ss results.

7.5 Verification Case Results

Using the sMC approach, ten samples (each having a sample size of 5500 barge-bridge collision simulations) were generated for the SR-20 at Blountstown Bridge Pier 58 case. A sample size of 5500 was iteratively arrived at by increasing the number of sMC simulations until probability of collapse (failure) estimates with COV values of (approximately) 0.2 or less were obtained (uncertainty of limit state exceedance rate estimates is discussed in Chapter 8). The foundation UBC limit state exceedance rate estimate for each sample is shown in Fig. 7.7. The sMC-based mean-valued estimate of the foundation UBC limit state exceedance rate is 2.7E-03. This value will serve as the benchmark for the corresponding LH/ss results.

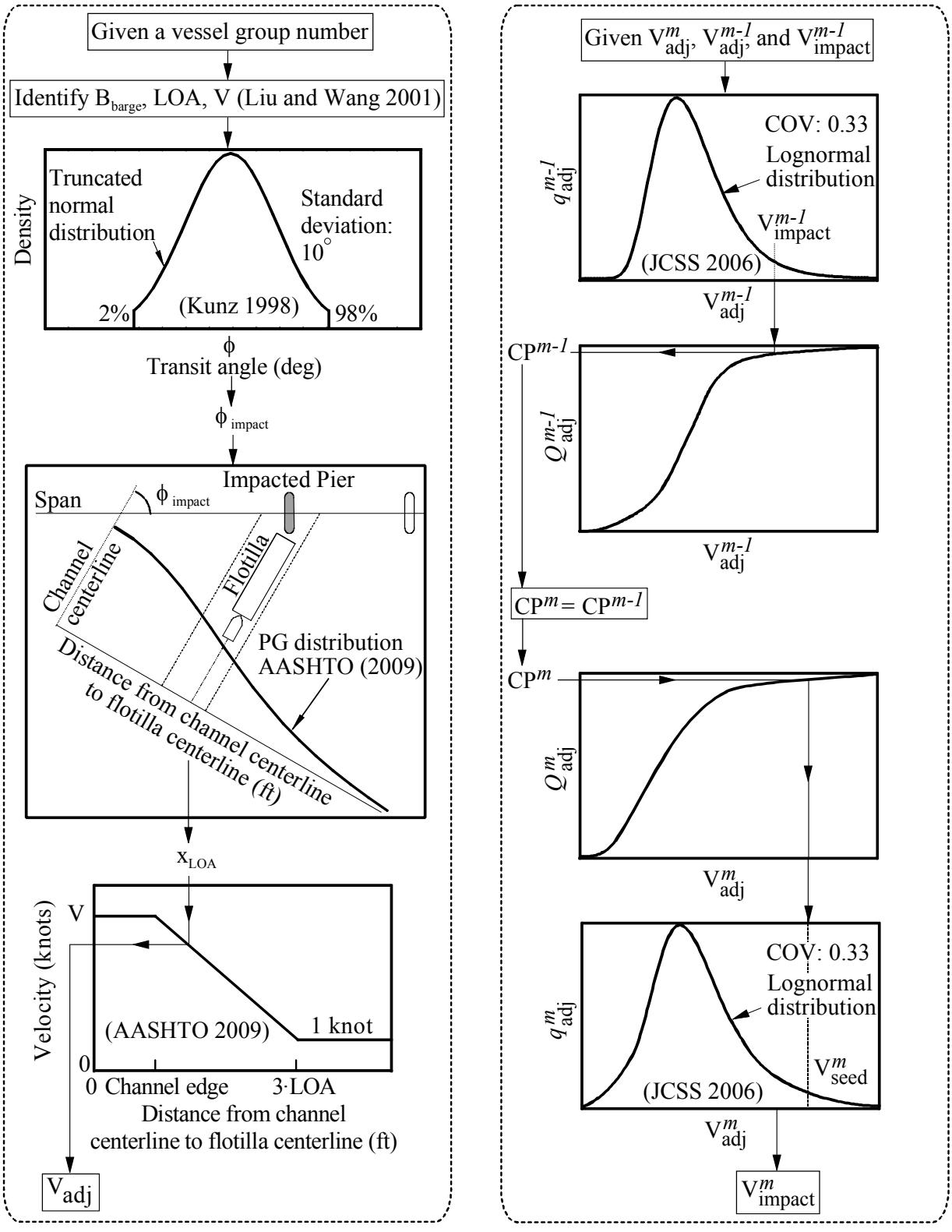

Figure 7.5 Barge velocity flowcharts: a) Adjusted velocity (V_{adj}); b) Impact velocity (V_{impact})

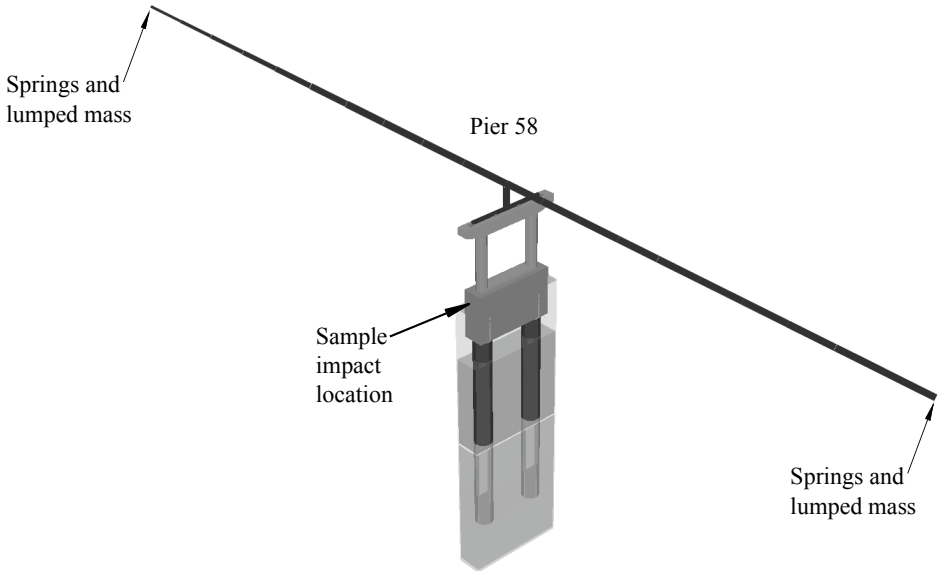

Figure 7.6 SR-20 at Blountstown Bridge Pier 58 OPTS model

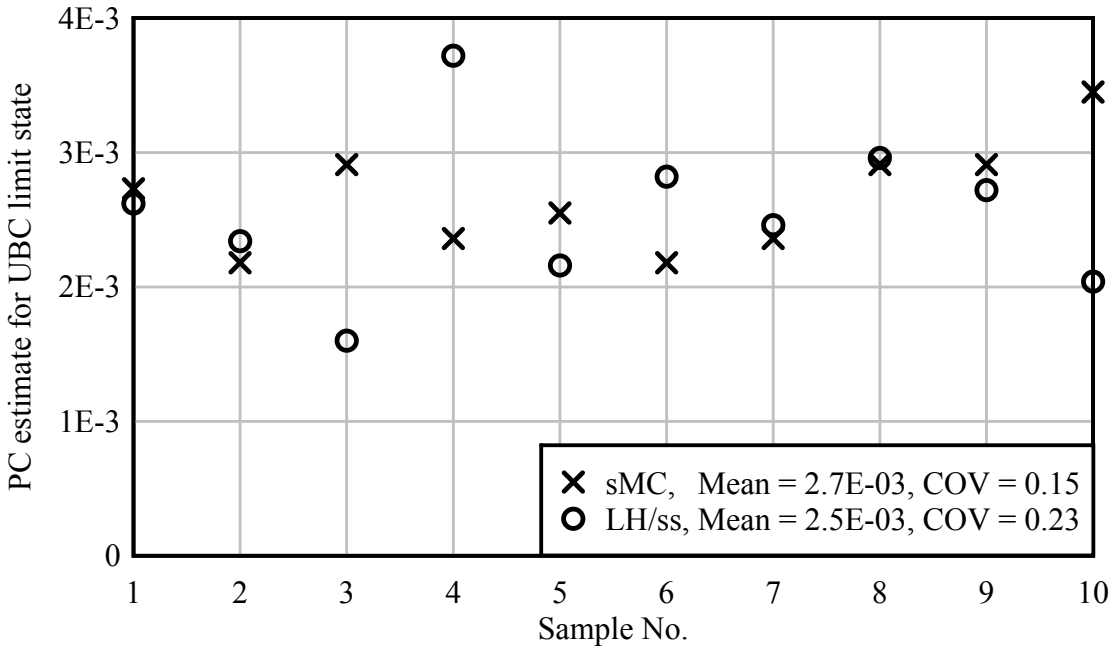

Figure 7.7 Comparison of standard Monte Carlo (sMC) and Latin Hypercube seeded subset simulation (LH/ss) results

Ten additional samples were generated, using the LH/ss approach, for comparison to the sMC-based results. Each sample consisted of four subsets (subsets 0–3), where each subset (in turn) consisted of 500 barge-bridge collision simulations. Consequently, each of the ten LH/ss samples required 1500 simulations, where the total computational expense associated with the LH/ss approach is approximately one-fourth of that required for the sMC simulations. The limit

state exceedance rate estimate for each sample is shown in Fig. 7.7, and the mean-valued failure estimate from the ten LH/ss samples is 2.5E-03.

The LH/ss failure estimate differs from the benchmark (sMC-based) estimate by less than 10%. However, to ensure that differences in the estimates are not statistically meaningful, a single-factor analysis of variance (ANOVA) was carried out using the sample estimates shown in Fig. 7.7. The F-statistic obtained from single-factor ANOVA, which is the ratio of the between-groups mean squared error to the within-groups mean squared error for the twenty total failure estimates (Ross 2009), was found to be 0.25. This statistic is relatively small compared to the critical F-value at the 5% significance level (which is 4.4). The LH/ss verification is, therefore, considered to be successful since differences between the sMC-based and LH/ss-based failure estimates are not statistically meaningful at the 5% significance level.

CHAPTER 8
FORMATION OF IMPROVED BRIDGE COLLAPSE RELATIONSHIPS

8.1 Introduction

In this study, several shortcomings have been identified for the probability of collapse (PC) expression extant in the AASHTO (2009) bridge design provisions for waterway vessel collision. Specifically, as discussed in Chapter 2, the current AASHTO PC expression neglects important dynamic phenomena; utilizes capacity-demand ratios (as opposed to demand-capacity ratios, D/C); and, is derived from ship-ship collision structural damage cost estimates (Fujii and Shiobara 1978). Given these limitations, the development of improved probability of collapse relationships is warranted. In this chapter, improved probability of collapse expressions are developed for bridge piers subject to barge impact loading. In contrast to the AASHTO PC expression, the bridge collapse expressions developed here are based on results from rational nonlinear dynamic barge-bridge collision analyses. The development is further facilitated by employing probabilistic descriptions for a multitude of random variables related to barge and bridge structures. Through joint use of the advanced probabilistic simulation and vessel collision analysis techniques discussed in previous chapters, expected values of probability of collapse—and furthermore, demand-capacity ratios for applicable limit states—can be efficiently quantified for a wide array of bridge types. The structural reliability parameters can then, in turn, be used to form improved probability of collapse expressions for bridge piers subject to barge collision.

8.2 Bridge Cases Considered

Ten bridge cases, selected from a larger catalog of more than 200 Florida bridges, are used to assess structural reliability parameters (probability of collapse values and demand-capacity ratios), and form improved PC expressions. Of the ten bridge cases considered, seven bridges (with widely varying structural configurations, as discussed in Chapter 4) are selected to represent existing Florida bridge infrastructure. Additionally, three bridge cases have been formed to represent potential (future) Florida bridge infrastructure, where bridge pier elements are strengthened to more aptly resist dynamic—as opposed to static—barge impact loads. As first introduced in Chapter 4, bridge cases discussed here are each assigned a three-letter identification code (Table 8.1). Individual piers within each bridge are delineated by proximity to the barge transit path (the letters "CHA" appended to a bridge identification code indicate that the pier is a channel-adjacent pier, whereas the letters "OFF" indicate that the pier is not directly adjacent to the channel). Additionally, identification codes for bridge cases with strengthened piers (the strengthening process is described in Chapter 4) are further appended with a lowercase "s". Combined bridge-location identifiers (e.g., "BLT-CHA" for the SR-20 at Blountstown bridge channel pier) are referred to as Case IDs.

8.3 Procedure for Forming Improved Probability of Collapse Expressions

The efficacy of combining modeling and analysis techniques with statistical descriptions of bridge, soil, and barge impact parameters makes feasible the task of determining collapse rates for each of the ten selected bridge cases. Subsequently, structural reliability parameters quantified for these cases are used to form improved PC expressions (this process is summarized

in Fig. 8.1). For each bridge case, the process begins with the following steps: determine the limit states associated with vessel collision; develop a bridge finite element (FE) model; and, collect corresponding waterway vessel traffic data. Then, using bridge structural data and waterway vessel traffic data, statistical descriptions of relevant parameters (random variables) are formed. Among these parameters are load and resistance quantities that pertain to the previously identified vessel collision limit states (details of probabilistic descriptions selected for individual load and resistance parameters, and how these descriptions are adapted to a bridge pier of interest, are discussed in Chapter 6).

Table 8.1 Bridge pier case IDs

Bridge name	Bridge code	Pier location code	Structural Configuration		Case ID
			Original	Strengthened	
SR-20 at Blountstown	BLT	CHA	X		BLT-CHA
SR-20 at Blountstown	BLT	CHA		X	BLT-CHA-s
I-10 over Escambia Bay	ESB	CHA	X		ESB-CHA
Gandy Bridge	GND	CHA	X		GND-CHA
Gandy Bridge	GND	CHA		X	GND-CHA-s
New St George Island	NSG	CHA	X		NSG-CHA
New St George Island	NSG	OFF	X		NSG-OFF
New St George Island	NSG	OFF		X	NSG-OFF-s
Ringling	RNG	OFF	X		RNG-OFF
Santa Rosa Bay	SRB	CHA	X		SRB-CHA

Subsequently, probabilistic simulations are carried out by sampling values of each random variable and conducting nonlinear dynamic vessel collision analyses (in accordance with the subset simulation with Latin Hypercube seeding, LH/ss, scheme). For each simulation conducted, the proximity to limit state exceedance is quantified and expressed as a demand-capacity value, D/C_i, for each of i limit states. If a given D/C_i value is found to be equal to or greater than 1, then the corresponding limit state is considered to be exceeded (i.e., the bridge has failed to adequately resist loading associated with limit state i). Additionally, for each instance of structural failure (collapse) associated with limit state i, the corresponding failure tabulation parameter (NF_i) is incremented. Upon completion of the (LH/ss) probabilistic simulations, expected values of D/C_i and—based on the number of limit state exceedances (NF_i)—each corresponding probability of collapse (PC_i) value are estimated.

Since, as part of the probabilistic simulations, expected values of demand-capacity ratios (D/C_i) are quantified in addition to limit state exceedance rates (or structural failure probabilities, PC_i), it is possible to form relationships between expected values of D/C_i and PC_i (Fig. 8.1, bottom). Specifically, probabilistic simulation results for a given bridge pier can be represented as a point on a coordinate system that pairs expected values of structural demand-capacity ratio (D/C_i) and probability of failure, or collapse, (PC_i). By carrying out probabilistic assessments for each of the ten selected bridge cases, ten corresponding (paired) values of D/C_i-PC_i are formed.

Subsequently, trend lines are fitted through these points, ultimately leading to improved probability of collapse expressions for pertinent limit states.

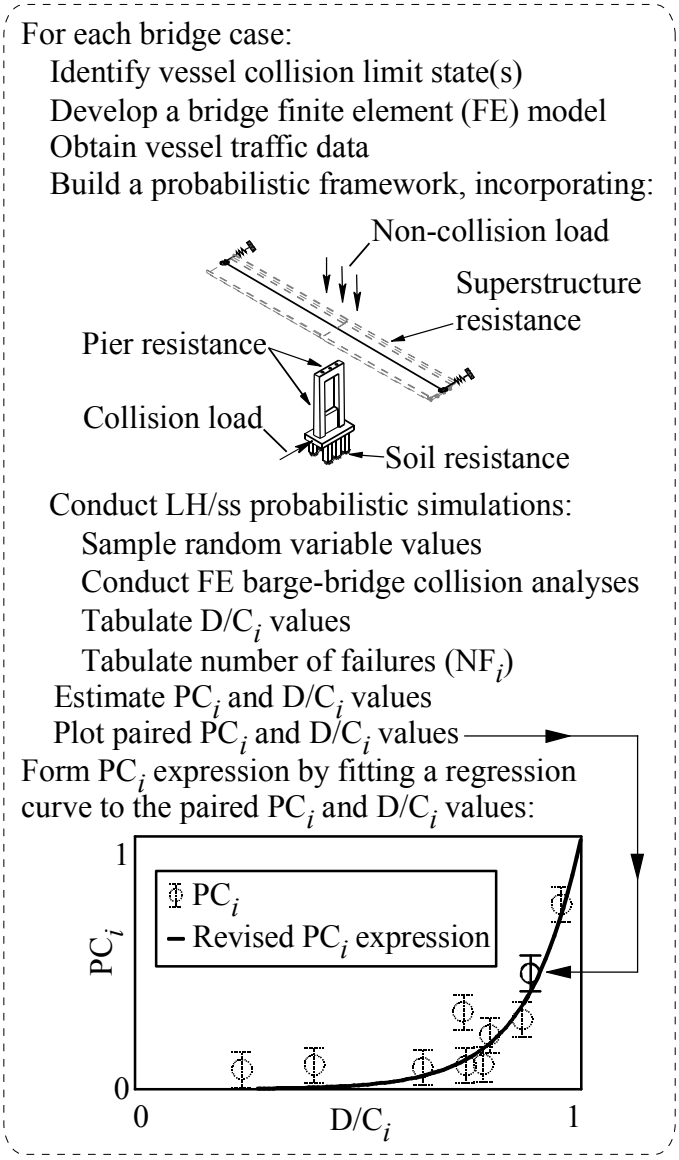

Figure 8.1 Improved probability of collapse expression formation summary

8.4 Probability of Collapse (PC_i) and Demand-Capacity (D/C_i) Estimates

Although it is stated in the AASHTO (2009) provisions that bridges must be designed to prevent superstructure collapse in the event of vessel-bridge collision, a set of clearly defined (i.e., readily quantifiable) limit states are not provided. However, it is stated in the AASHTO provisions that the bridge owner is permitted to define the degree of damage that bridge components are allowed to sustain during impact events. Given that the bridge cases considered in this study are all located in Florida and publicly owned, bridge collapse (structural failure) is

defined in terms that are consistent with those specified in the Florida Department of Transportation (FDOT) Structures Design Guidelines (2009):

- Load redistribution must not be permitted when the ultimate bearing capacity (UBC) of axially loaded piles is reached;

- Forces transferred to the superstructure must not exceed the capacity of load transfer devices at the substructure-superstructure interface; and,

- The superstructure must not collapse

In design applications, the FDOT limit states are taken in series (i.e., if any one of the three limit states is reached as a result of vessel collision loading, then structural failure is considered to have occurred).

Mean-valued estimates of proximity to limit state exceedance (D/C_i) and corresponding limit state exceedance rates (PC_i) are presented in Tables 8.2–8.3 for the ten selected bridge cases. Specifically, computed demand-capacity ratios and exceedance rates are reported in Tables 8.2–8.3 for the foundation member UBC limit state (denoted D/C_{UBC} and PC_{UBC}, respectively); substructure-superstructure interface shear capacity limit state (denoted D/C_{int} and PC_{int}, respectively); and, superstructure collapse limit state (denoted D/C_{sup} and PC_{sup}, respectively). Additionally, estimates are given in Tables 8.2–8.3 for the three FDOT limit states taken in series (denoted D/C_{series} and PC_{series}, respectively). The probabilistic simulation technique (e.g., standard Monte Carlo, sMC; Latin Hypercube, LH; subset simulation with Latin Hypercube seeding, LH/ss), number of samples, sample size, and estimate dispersions (expressed as coefficients of variation, COVs) are also given in Tables 8.2–8.3 for each D/C_i and PC_i estimate.

As shown in Fig. 8.2, significant nonlinearity is present in the sets of paired D/C_i and PC_i values for each limit state. Specifically, PC_i estimates with corresponding D/C_i values less than approximately 0.7 tend to be small (less than 0.1). In contrast, PC_i estimates with corresponding D/C_i values greater than approximately 0.7 rapidly tend toward exceedance rates of 1. This observation is well-founded considering that the estimates of D/C_i are reasonably well distributed from 0 to 1 for each limit state (Fig. 8.2). Importantly, this finding additionally supports the assertion that a representative set of bridges has been considered in the current study. Also, the D/C_i estimates (Table 8.2) exhibit very small levels of relative dispersion (the set of corresponding COV values ranges from 0.01 to 0.04). Moreover, small COV values are expected among the D/C_i estimates given that one D/C_i observation is generated for every collision analysis conducted (using the sMC and LH approaches), and therefore, only a relatively small number of simulations are necessary (per sample) to obtain D/C_i estimates with small levels of uncertainty.

Table 8.2 Mean-valued D/C_i estimates

Case	Sim. Type	No. samples	Sample size	D/C type	Mean-estimate	COV
BLT-CHA	sMC	10	5500	D/C_{UBC}	7.27E-01	0.01
	sMC	10	5500	D/C_{int}	5.40E-01	0.01
	sMC	10	5500	D/C_{sup}	4.53E-01	0.01
	sMC	10	5500	D/C_{series}	7.45E-01	0.01
BLT-CHA-s	LH	10	4700	D/C_{UBC}	7.30E-01	0.01
	LH	10	4700	D/C_{int}	4.06E-01	0.01
	LH	10	4700	D/C_{sup}	4.25E-01	0.01
	LH	10	4700	D/C_{series}	7.32E-01	0.01
ESB-CHA	LH	10	100	D/C_{UBC}	7.64E-01	0.01
	LH	10	100	D/C_{int}	9.96E-01	0.01
	LH	10	100	D/C_{sup}	9.92E-01	0.01
	LH	10	100	D/C_{series}	9.97E-01	0.01
GND-CHA	sMC	20	750	D/C_{UBC}	1.12E-01	0.01
	sMC	20	750	D/C_{int}	6.16E-01	0.01
	sMC	20	750	D/C_{sup}	5.81E-01	0.01
	sMC	20	750	D/C_{series}	6.42E-01	0.01
GND-CHA-s	LH	10	500	D/C_{UBC}	1.21E-01	0.01
	LH	10	500	D/C_{int}	5.16E-01	0.01
	LH	10	500	D/C_{sup}	2.44E-01	0.01
	LH	10	500	D/C_{series}	5.16E-01	0.01
NSG-CHA	LH	10	500	D/C_{UBC}	6.76E-01	0.01
	LH	10	500	D/C_{int}	4.00E-01	0.02
	LH	10	500	D/C_{sup}	6.62E-01	0.01
	LH	10	500	D/C_{series}	7.24E-01	0.01
NSG-OFF	sMC	10	1400	D/C_{UBC}	7.15E-01	0.01
	sMC	10	1400	D/C_{int}	4.69E-01	0.02
	sMC	10	1400	D/C_{sup}	5.38E-01	0.02
	sMC	10	1400	D/C_{series}	7.55E-01	0.01
NSG-OFF-s	LH	10	500	D/C_{UBC}	7.28E-01	0.01
	LH	10	500	D/C_{int}	2.85E-01	0.04
	LH	10	500	D/C_{sup}	3.89E-01	0.02
	LH	10	500	D/C_{series}	7.38E-01	0.01
RNG-OFF	LH	20	750	D/C_{UBC}	6.91E-01	0.01
	LH	20	750	D/C_{int}	3.07E-01	0.01
	LH	20	750	D/C_{sup}	2.74E-01	0.01
	LH	20	750	D/C_{series}	7.07E-01	0.01
SRB-CHA	LH	10	750	D/C_{UBC}	5.65E-01	0.02
	LH	10	750	D/C_{int}	3.86E-01	0.01
	LH	10	750	D/C_{sup}	6.77E-01	0.01
	LH	10	750	D/C_{series}	6.98E-01	0.01

Table 8.3 Mean-valued PC_i estimates

Case	Sim. Type	No. samples	Sample size	PC type	Mean-estimate	COV	p_{SW}
BLT-CHA	sMC	10	5500	PC_{UBC}	2.65E-03	0.15	0.34
	sMC	10	5500	PC_{int}	2.47E-02	0.10	0.37
	sMC	10	5500	PC_{sup}	2.00E-04	0.90	0.15
	sMC	10	5500	PC_{series}	2.70E-02	0.10	0.37
BLT-CHA-s	LH/ss	8	500	PC_{UBC}	5.31E-04	0.51	0.64
	LH	10	4700	PC_{int}	4.64E-03	0.17	0.21
	LH	10	4700	PC_{sup}	5.42E-04	0.70	0.35
	LH	10	4700	PC_{series}	7.25E-03	0.10	0.51
ESB-CHA	LH	10	100	PC_{UBC}	3.01E-01	0.12	0.33
	LH	10	100	PC_{int}	9.73E-01	0.02	0.29
	LH	10	100	PC_{sup}	9.13E-01	0.06	0.59
	LH	10	100	PC_{series}	9.75E-01	0.02	0.29
GND-CHA	sMC	20	750	PC_{UBC}	N/A	N/A	N/A
	sMC	20	750	PC_{int}	4.98E-02	0.18	0.10
	LH/ss	10	500	PC_{sup}	5.37E-04	0.80	0.06
	sMC	20	750	PC_{series}	4.98E-02	0.18	0.10
GND-CHA-s	LH	10	500	PC_{UBC}	N/A	N/A	N/A
	LH/ss	10	500	PC_{int}	4.54E-05	0.75	0.06
	LH/ss	10	500	PC_{sup}	N/A	N/A	N/A
	LH/ss	10	500	PC_{series}	4.54E-05	0.75	0.06
NSG-CHA	LH	10	500	PC_{UBC}	2.26E-02	0.23	0.82
	LH	10	500	PC_{int}	4.72E-02	0.16	0.22
	LH	10	500	PC_{sup}	1.83E-02	0.29	0.09
	LH	10	500	PC_{series}	7.49E-02	0.12	0.24
NSG-OFF	sMC	10	1400	PC_{UBC}	7.43E-02	0.08	0.20
	sMC	10	1400	PC_{int}	2.21E-01	0.04	0.94
	sMC	10	1400	PC_{sup}	5.40E-02	0.11	0.30
	sMC	10	1400	PC_{series}	2.58E-01	0.04	0.46
NSG-OFF-s	LH	10	500	PC_{UBC}	4.94E-02	0.22	0.07
	LH	10	500	PC_{int}	5.06E-02	0.18	0.91
	LH/ss	10	500	PC_{sup}	3.21E-04	0.50	0.35
	LH	10	500	PC_{series}	8.68E-02	0.10	0.77
RNG-OFF	LH	20	750	PC_{UBC}	3.40E-02	0.18	0.07
	LH	20	750	PC_{int}	1.71E-02	0.32	0.46
	LH/ss	10	500	PC_{sup}	2.49E-22	2.84	<0.001
	LH	20	750	PC_{series}	5.05E-02	0.16	0.89
SRB-CHA	LH	10	750	PC_{UBC}	3.43E-02	0.15	0.29
	LH	10	750	PC_{int}	2.40E-03	0.57	0.19
	LH	10	750	PC_{sup}	8.00E-03	0.49	0.76
	LH	10	750	PC_{series}	3.69E-02	0.17	0.56

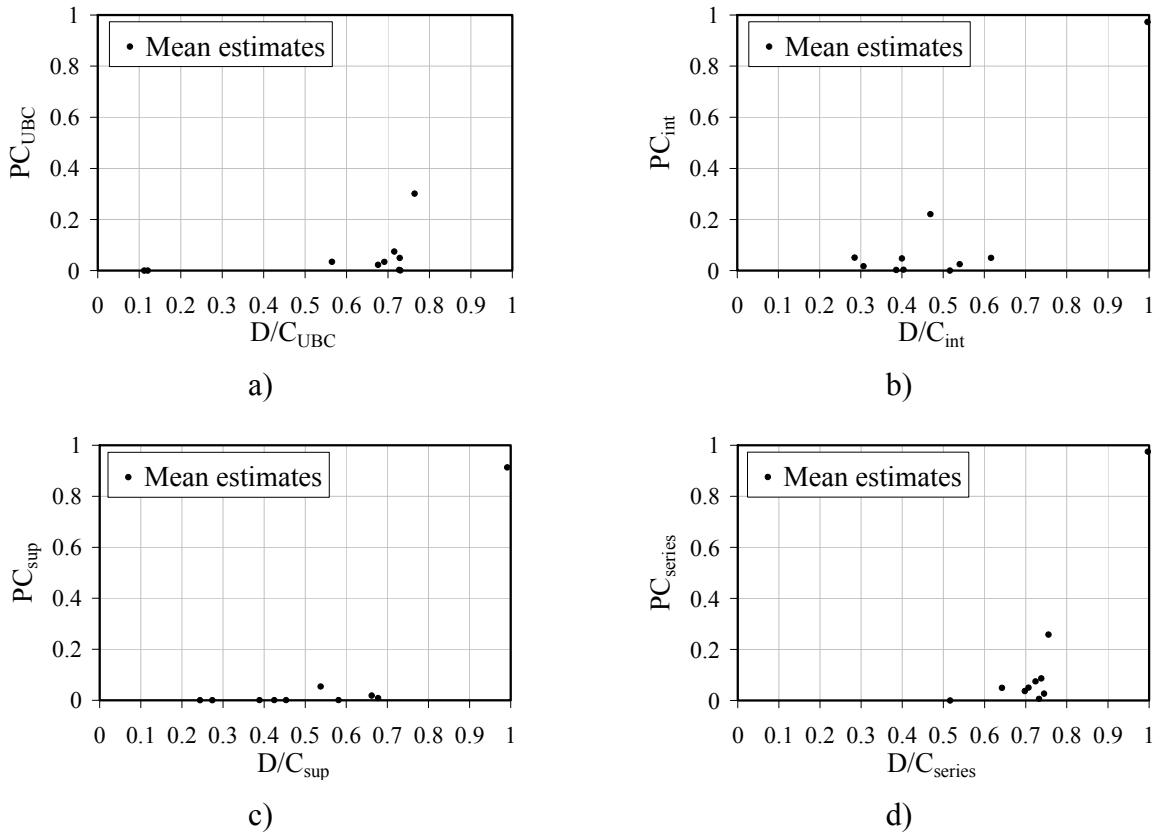

Figure 8.2 Paired estimates of PC_i and D/C_i. a) Foundation member UBC limit state; b) Substructure-superstructure interface shear capacity limit state; c) Superstructure collapse limit state; d) Series limit state

In contrast, relative dispersion levels (COV values) associated with the PC_i estimates vary substantially (Table 8.3), where the COV values tend to be larger for small-valued PC_i estimates (i.e., those less than 0.01). This outcome is necessarily associated with using probabilistic simulation to estimate small failure probabilities, where—in relation to the PC_i estimates—one observation of limit state exceedance requires a number of simulations that is (approximately) inversely proportional to the failure probability (i.e., one collision analysis does not, generally, produce one observation of limit state exceedance).

Structural reliability parameters (PC_i and D/C_i estimates) and the associated estimate uncertainties reported in Tables 8.2–8.3 were estimated using the results from approximately 500,000 FE analyses, where each analysis typically required between 2–15 minutes of computation time. A cluster of four computational servers (each containing eight 2.1 GHz CPUs) and three personal computing machines (each with between two and four CPUs of varying speeds) were utilized continuously for approximately four-months to carry out the analyses. Furthermore, analyses carried out for each of the ten bridge cases were predicated upon random variable value generation from customized probabilistic frameworks (developed in the mathematical computing language Matlab, Mathworks 2005). Pertinent analytical output (relating to structural reliability parameters) was quantified by parsing computed results with

scripts (developed in the Perl scripting language), where the parsing process for each analysis required between 1–3 minutes of computation time.

8.5 Accounting for Relative Dispersions of PC_i Estimates

Given the substantial effort required to obtain PC_i estimates (with the associated relative dispersions, or COV values, given in Table 8.3), the task of further reducing estimate uncertainties by conducting a large number of additional simulations (potentially exceeding 1,000,000) was not feasible. Instead, a scheme to directly account for PC_i estimate uncertainty has been incorporated into the development of the improved probability of collapse expressions (a conceptual overview of this process is given in Fig. 8.3). For limit state i, and the corresponding set of mean-valued PC_i estimates (Fig. 8.3a), statistical descriptions of the distributions that govern the estimate uncertainties (discussed below) are used to obtain sampled ordinate values (Fig. 8.3b), where—as afforded by small levels of uncertainty in the D/C_i estimates—the respective abscissa values are held constant. The set of sampled ordinates is then fit with a "trial" regression curve (Fig. 8.3c). These (trial regression) curves constitute rationally derived, alternative outcomes that are possible given the uncertainty levels present in the observed data. After the generation of a large number of trial regression curves (Fig. 8.3d), the D/C_i domain is discretized and, for each discrete D/C_i value, the corresponding 95^{th} percentile upper bound ordinate is identified from the trial regression curve data. A final, overall regression curve is fit to the 95% upper bound ordinates (Fig. 8.3e), and thus, uncertainty in the PC_i estimates is accounted for in a conservative manner.

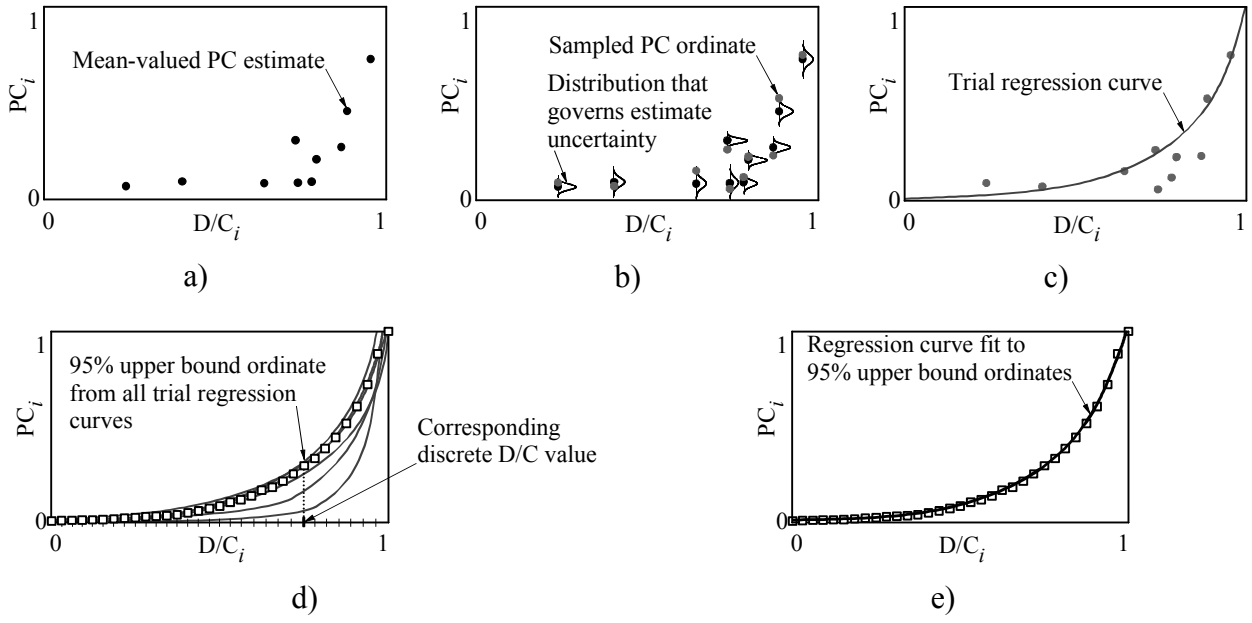

Figure 8.3 Conceptual overview of standard Monte Carlo procedure to account for PC estimate uncertainty. a) Mean-valued PC estimates; b) PC ordinate sampling; c) Trial regression curve fitting; d) Identification of 95% upper bound ordinates; e) Regression curve for 95% upper bound ordinates

8.5.1 Identification of the type of uncertainty that governs the PC_i estimates

Paramount to accounting for the relative dispersions (COV values) observed among the PC_i estimates is the identification of statistical descriptions that govern observed estimate variability (i.e., estimate uncertainty). Given the large number of independent random variables (greater than 30) used to form the set of input parameters for each barge-bridge collision analysis, it follows that multiple estimates of the limit state exceedance rates are approximately normally distributed. Accordingly, tests for normality were carried out for all PC_i estimates, where p-values (denoted as p_{SW}) obtained from Shapiro-Wilk tests for normality are listed in Table 8.3 (Shapiro and Wilk 1965).

In the tests for normality, p-values corresponding to the PC_i estimates are compared to a chosen significance level (5% in this case) and those p-values found to be greater than the chosen significance level are taken as an indication of normality. Overall, the calculated p-values (p_{SW}) support the hypothesis that, at the 5% significance level, variability of the PC_i estimates are approximately normally distributed (a single exception is found in the PC_{sup} estimate for the RNG-OFF case, where treatment of this estimate is discussed later). Given that PC_i estimate variability can be described as approximately normally distributed, and furthermore, because the number of samples used to obtain each of the PC_i estimates is small (20 or fewer), each PC_i estimate is considered to be distributed according to a t-distribution.

8.5.2 Algorithm to incorporate PC_i estimate uncertainty into regression curve fits

The sMC-based procedure—developed to account for varied COV values among the case-specific limit state exceedance estimates (PC_{ij}) for each limit state i and, in turn, bridge case j—is summarized in Fig. 8.4. [The subscript "j" is introduced in this context to emphasize that sampling is performed for each of j bridge cases, for which the limit state i is applicable.] The sMC-based algorithm primarily consists of sampling limit state exceedance values, PC_{ij}^{rnd}, from a respective t-distribution and fitting a large number of "trial" regression curves (n_{reg}) to each set of newly sampled values. More specifically, given the sample size (n_j^{samp}) associated with the mean-valued estimate (PC_{ij}), a t-distribution value, t_j^{rnd} is sampled from a corresponding t-distribution. Then, a sampled value of PC_{ij}^{rnd} is calculated as:

$$PC_{ij}^{rnd} = PC_{ij} + t_j^{rnd} \cdot PC_{ij} \cdot COV_{ij} / \left(n_j^{samp}\right)^{0.5} \tag{8.1}$$

where COV_{ij} denotes the COV value associated with limit state i and bridge case j. After a sampled value of PC_{ij}^{rnd} has been calculated for each of j bridge cases, the newly sampled values are paired with respective, mean-valued D/C_{ij} estimates and a trial regression curve is fit to the set of paired data points. Since COV values among the D/C_{ij} estimates are small (i.e., significantly less than 0.1), only nominal changes in the trial regression curves would be produced as a result of (additionally) varying the D/C_{ij} values.

After n_{reg} trial regression curves have been formed, uncertainties in the PC_{ij} estimates are then accounted for by identifying discrete 95% upper bound ordinates from all trial regression curve fits (Fig. 8.4, bottom) over the entire domain of D/C values (a discretization level of 1000 is used in this study). Convergence of the 95% upper bound ordinates is assured by repeating the process summarized in Fig. 8.4 with an increasing number of trial regression curve fits (nreg), and then, quantifying differences in the enveloped ordinate values at each discrete D/C value from one repetition to the next (a maximum permissible difference of 1% between upper bound ordinates is used in this study). Finally, a regression curve is fit to the converged, upper bound ordinate values, where this curve constitutes a probability of collapse expression.

For limit state *i*:
  For n_{reg} trial regression curve fits:
    For each mean-valued PC_{ij} estimate:
      Generate a random t-distribution value (t_j^{rnd})
      Calculate a sampled PC_{ij} value:
        $PC_{ij}^{rnd} = PC_{ij} + t_j^{rnd} \cdot PC_{ij} \cdot COV_{ij} / (n_j^{samp})^{0.5}$
    Fit a trial regression curve to each set of PC_{ij}^{rnd}
  Identify 95% upper bound ordinates
  Fit a regression curve to the 95% upper bound ordinates

Figure 8.4 Summary of standard Monte Carlo procedure to account for PC estimate uncertainty

8.6 Improved Probability of Collapse Expression for the FDOT Series Limit State

For bridge designers constrained to simultaneously satisfy all three limit states defined in the FDOT (2009) guidelines, use of a probability of collapse expression based on probabilistic assessment of barge-bridge collisions with (simultaneous, or series-based) consideration of those same three limit states constitutes a rational approach to design. Accordingly, a regression curve was fit to the mean-valued PC_{series} estimates (Fig. 8.5), where an exponential curve (with a correlation coefficient equal to 0.81) was found to fit the mean-valued PC_{series} estimates in a statistically meaningful manner. The hypothesis that the correlation coefficient is statistically meaningful at the 5% significance level is accepted since the correlation threshold for a data set with 10 points, 0.63, is less than the observed correlation coefficient (Pearson and Hartley 1958).

While statistically meaningful, the exponential regression curve fit to the mean-valued PC_{series} estimates does not account for variability in the individual estimates (i.e., the COV values reported in Table 8.4), which vary between 0.02 and 0.75. Therefore, the sMC-based process of accounting for uncertainty in the individual estimates (recall Fig. 8.4) was employed to develop a 95% upper bound envelope (Fig. 8.6). Convergence (i.e., a change in ordinate values of less than 1%) of the envelope-based regression curve was found to occur for values of n_{reg} greater than 1E+04 (a value of 1E+05 was used for n_{reg} to produce the envelope-based regression curve shown in Fig. 8.6). Furthermore, correlation between the enveloped ordinate values and the corresponding regression curve (identified in Fig. 8.6) was found to be (approximately) equal to 1.

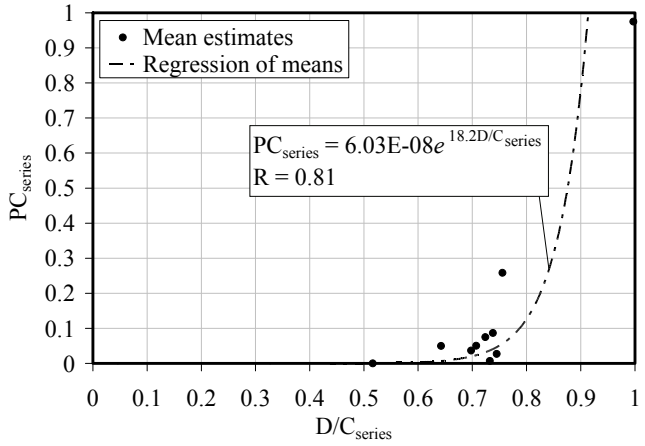

a)

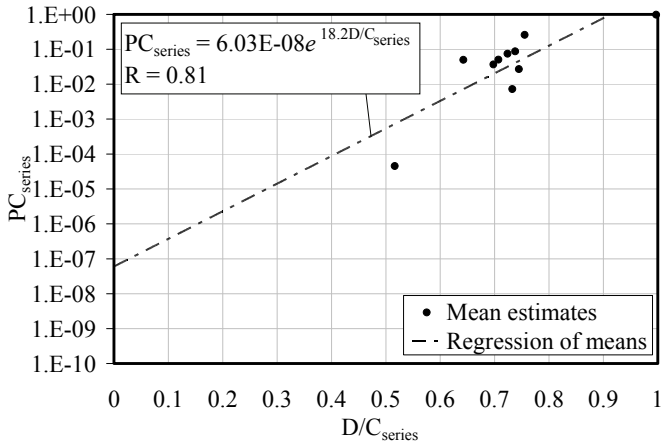

b)

Figure 8.5 Exponential regression curve fit to mean-valued PC_{series} estimates. a) Linear plot; b) Semi-log plot

Excellent agreement is observed between the mean-based and envelope-based regression curves in both linear (Fig. 8.6a) and semi-log (Fig. 8.6b) spaces. Thus, levels of relative dispersion present among the mean-valued PC_{series} estimates are considered to be acceptably small. However, the enveloped ordinate regression curve is universally conservative (i.e., predicts larger magnitude PC_{series} values for all D/C_{series} values) relative to the mean-valued regression curve. Therefore, the envelope-based regression curve (defined in Eq. 8.2):

$$PC_{series} = 9.08 \times 10^{-8} \cdot e^{17.8 D/C_{series}}, \; 0 \le PC_{series} \le 1 \tag{8.2}$$

is proposed for use in bridge design where simultaneous consideration of all three FDOT vessel collision limit states is required.

Table 8.4 Probability of collapse estimates for the FDOT series limit state

Case	Sim. type	No. samples	Sample size	PC_{series}	COV	p_{SW}
BLT-CHA	sMC	10	5500	2.70E-02	0.10	0.37
BLT-CHA-s	LH	10	4700	7.25E-03	0.10	0.51
ESB-CHA	LH	10	100	9.75E-01	0.02	0.29
GND-CHA	sMC	20	750	4.98E-02	0.18	0.10
GND-CHA-s	LH/ss	10	500	4.54E-05	0.75	0.06
NSG-CHA	LH	10	500	7.49E-02	0.12	0.24
NSG-OFF	sMC	10	1400	2.58E-01	0.04	0.46
NSG-OFF-s	LH	10	500	8.68E-02	0.10	0.77
RNG-OFF	LH	20	750	5.05E-02	0.16	0.89
SRB-CHA	LH	10	750	3.69E-02	0.17	0.56

8.7 Improved Probability of Collapse Expression for the AASHTO Superstructure Collapse Limit State

The proposed FDOT (series) probability of collapse expression (Eq. 8.2)—which incorporates superstructure collapse in addition to more stringent limit states—is specific to those levels of resistance to extreme event loading currently required for bridge design in the state of Florida. In contrast, the only limit state identified in the current AASHTO (2009) provisions is that associated with preventing superstructure collapse. Therefore, an improved probability of collapse expression has been developed based on the probabilistic simulation results specific to the assessment of the superstructure collapse limit state.

The superstructure collapse limit state estimates (PC_{sup}) generally correspond to rare-event scenarios (with a majority of the PC_{sup} values estimated to be less than 0.01). Furthermore, extremely small (approximately zero-valued) limit state exceedance estimates found among the PC_{sup} data warrant additional consideration, particularly, in the context of how such values affect the overall bridge failure risk (as determined using the current AASHTO provisions).

8.7.1 Practical minimum values of meaningful PC estimates

Recall that (as discussed in Chapter 2) overall bridge risk (in association with waterway vessel collision) in the AASHTO provisions is expressed as an annual frequency of collapse:

$$AF = N \cdot PA \cdot PG \cdot PC \cdot PF \tag{8.3}$$

where the annual frequency of collapse (AF) probability must be less than 1E-03 and 1E-04 for typical and critical bridges, respectively; N is the number of transits associated with a given vessel group that traverses the waterway; PA is the probability of in-transit vessel aberrancy; PG is the geometric probability that an aberrant vessel will strike a bridge pier of interest; and, PF is

a factor that accounts for external protection structures (e.g., dolphin systems). As part of the AASHTO risk assessment, the products of all right-hand terms in Eq. 8.3 are summed for all piers and, in turn, all vessel groups traversing the waterway.

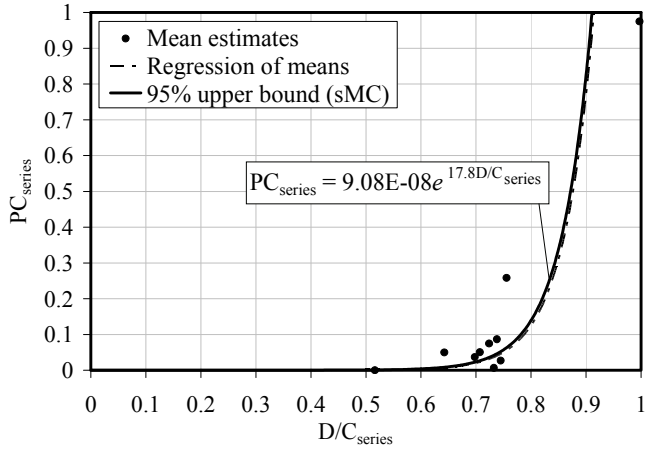

a)

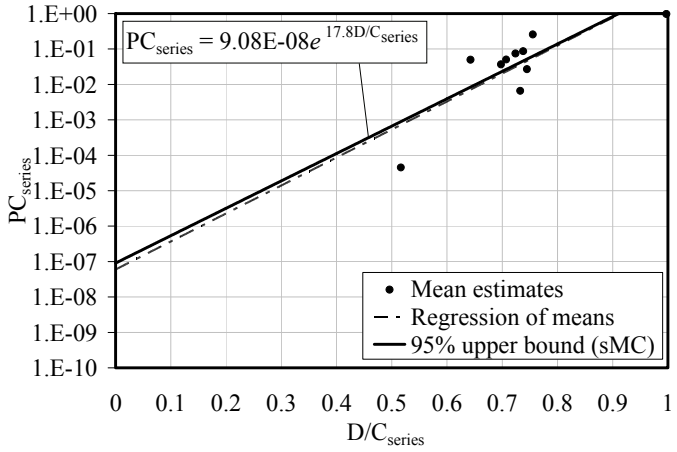

b)

Figure 8.6 Proposed probability of collapse expression for the FDOT series limit state. a) Linear plot; b) Semi-log plot

Consider a worst-case (i.e., extremely high-risk) scenario in which all right-hand terms in Eq. 8.3 (other than N and PC) are equal to 1. Furthermore, consider a bridge layout in which 30 identical bridge piers are subject to vessel collision (the maximum number of piers subject to vessel collision for cases considered in the current study is 26 piers) and that the total number of vessel transits associated with the waterway is equal to 5000 trips for a single vessel group (a study of waterway vessel traffic data for navigable waterways in Florida, Liu and Wang 2001, revealed that no Florida waterway is traversed, on average, more than 5000 times per year). The corresponding AF value for this hypothetical scenario (as a function of PC) can be estimated as:

$$AF \approx 30 \cdot 5000 \cdot 1 \cdot 1 \cdot PC \cdot 1 \approx 1.5 \times 10^5 \cdot PC \quad (8.4)$$

Even for this extremely conservative scenario, PC values less than approximately 1E-12 will result in an AF estimate that is (permissibly) two orders of magnitude less than even the more stringent AF value permitted by AASHTO (i.e., 1E-04 for critical bridges). Consequently, probability of collapse values smaller than 1E-12 are respectively equivalent in that such small values do not meaningfully contribute to the overall bridge failure risk. Therefore, PC values less than or equal to 1E-12 are, in the context of the overall bridge failure risk, considered to be of limited value.

8.7.2 Exclusion of outlier data in regression curve fitting

The PC_{sup} estimate for the RNG-OFF case (2.49E-22, from Table 8.5) is approximately 18 orders of magnitude less than all other PC_{sup} estimates and 10 orders of magnitude less than the (above-defined) minimum meaningful PC value. Inclusion of the RNG-OFF PC_{sup} estimate in the formation of the mean-valued regression curve (Fig. 8.7) results in a distinct—and potentially unconservative—skew relative to a corresponding regression in which the RNG-OFF PC_{sup} estimate is excluded (Fig. 8.8). Furthermore, exponential regression of the PC_{sup} estimates with inclusion of the RNG-OFF estimate does not produce a statistically meaningful curve fit at the 5% significance level (the correlation coefficient associated with the regression, 0.63, is less than the critical correlation value, 0.67, for nine data points, Pearson and Hartley 1958). In contrast, the correlation coefficient that is associated with regression in which the RNG-OFF estimate is excluded, 0.86, is significantly greater than the critical correlation value, 0.71, for eight data points at the 5% significance level (Pearson and Hartley 1958). The RNG-OFF PC_{sup} estimate is, therefore, considered to be an outlier and is excluded from the PC_{sup} dataset.

Table 8.5 Probability of collapse estimates for the superstructure collapse limit state

Case	Sim. type	No. samples	Sample size	PC_{sup}	COV	p_{SW}
BLT-CHA	sMC	10	5500	2.00E-04	0.90	0.15
BLT-CHA-retrofit	LH	10	4700	5.42E-04	0.70	0.35
ESB-CHA	LH	10	100	9.13E-01	0.06	0.59
GND-CHA	LH/ss	10	500	5.37E-04	0.80	0.06
NSG-CHA	LH	10	500	1.83E-02	0.29	0.09
NSG-OFF	sMC	10	1400	5.40E-02	0.11	0.30
NSG-OFF-retrofit	LH/ss	10	500	3.21E-04	0.50	0.35
RNG-OFF	LH/ss	10	500	2.49E-22	2.84	<0.001
SRB-CHA	LH	10	750	8.00E-03	0.49	0.76

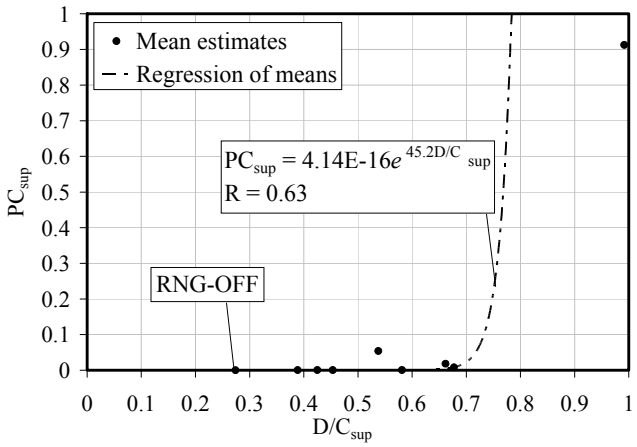

a)

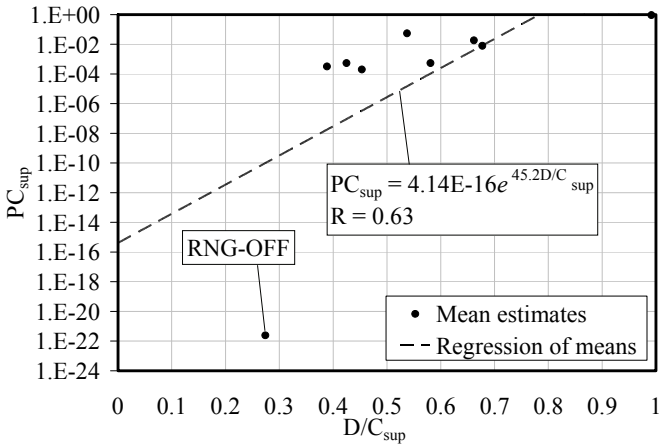

b)

Figure 8.7 Exponential regression curve fit to mean-valued PC_{sup} estimates with inclusion of the RNG-OFF data point. a) Linear plot; b) Semi-log plot

8.7.3 Accounting for relative dispersions in the PC_{sup} estimates

Substantially varying levels of COV values (ranging from 0.06 to 0.90) are associated with the PC_{sup} estimates (Table 8.5). To account for uncertainty in the estimates, a 95% upper bound envelope regression curve was generated (Fig. 8.9) using D/C_{sup} and PC_{sup} estimate data and the sMC-based procedure summarized in Fig. 8.4. Convergence of the 95% upper bound envelope regression curve was achieved for conditions matching those used in the formation of the enveloped regression curve for the FDOT series limit state.

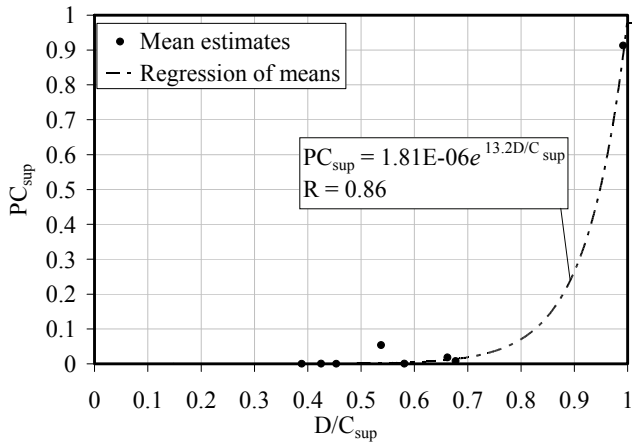

a)

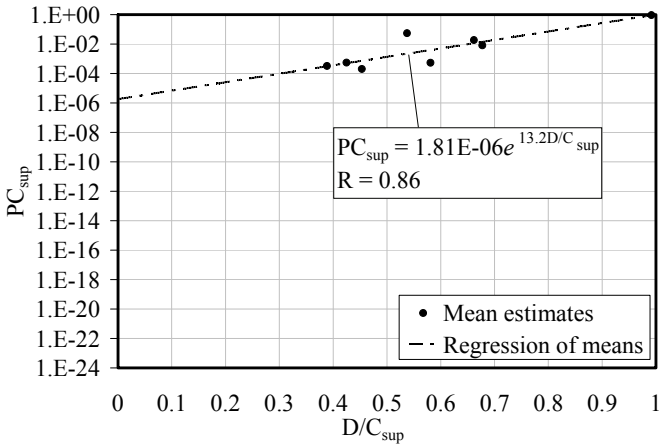

b)

Figure 8.8 Exponential regression curve fit to mean-valued PC_{sup} estimates excluding the RNG-OFF data point. a) Linear plot; b) Semi-log plot

As shown in Fig. 8.9, mean-based and envelope-based regression curves for the superstructure collapse limit state are in good agreement: a maximum difference (in PC value prediction) of less than 0.1 occurs between the two curves, with the envelope-based curve predicting conservative PC_{sup} values. The 95% upper bound envelope regression curve:

$$PC_{sup} = 2.33 \times 10^{-6} \cdot e^{13.0 D/C_{sup}} \ , \ 0 \le PC_{sup} \le 1 \qquad (8.5)$$

which is universally conservative relative to the mean-valued regression, is recommended for use in bridge design where only the superstructure collapse limit state (identified in the AASHTO provisions) is taken into consideration.

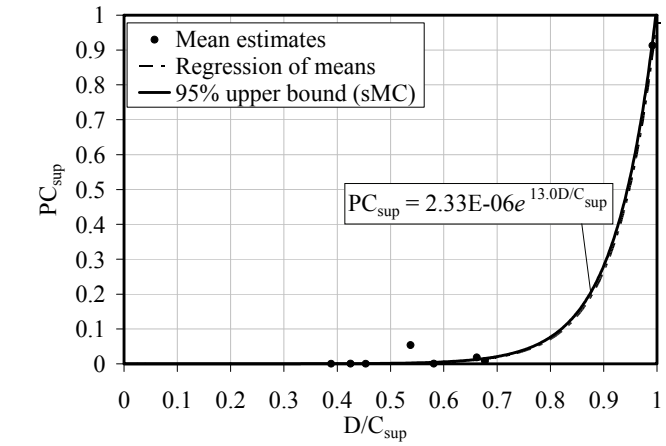

a)

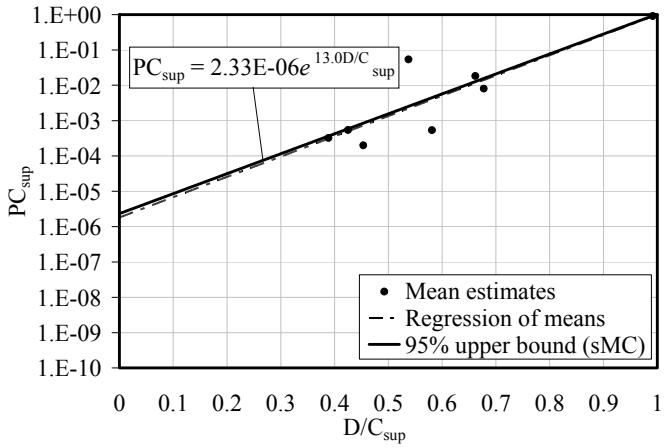

b)

Figure 8.9 Proposed probability of collapse expression for the AASHTO superstructure collapse limit state. a) Linear plot; b) Semi-log plot

8.7.4 Comparison of Proposed PC_i values to AASHTO PC Values

For five of the bridge cases considered in the current study, sufficient data were available from the respective structural plans to—when combined with data from a study of waterway vessel traffic in Florida (Liu and Wang 2001)—quantify PC values in accordance with the current AASHTO provisions (Table 8.6). [Vessel traffic data necessary to determine PC values in accordance with the existing AASHTO PC expression are given, for each case, in Appendix B.] Also given in Table 8.6 are values of limit state exceedance for the FDOT series limit state (PC_{series}) and the superstructure collapse limit state (PC_{sup}), predicted using the proposed PC expressions (Eq. 8.2 and Eq. 8.5, respectively).

Table 8.6 Comparison of proposed PC_i values to AASHTO PC values

Case	PC_{series} values from Eq. 8.2	PC_{sup} values from Eq. 8.5	AASHTO PC
BLT-CHA	5.19E-02	5.03E-04	2.20E-02
GND-CHA	8.40E-03	3.00E-03	6.43E-02
NSG-CHA	3.58E-02	9.30E-03	2.10E-03
NSG-OFF	6.28E-02	2.52E-03	2.90E-03
SRB-CHA	2.25E-02	1.16E-02	5.50E-03

By considering the AASHTO PC values as benchmark values (i.e., values associated with current design practice), relative comparisons to proposed PC_i values can be made. Specifically, predicted PC values obtained from the AASHTO PC expression—expressed as average values, weighted by vessel trip frequency—are used to normalize the proposed PC_i values (shown in semi-log space) in Fig. 8.10 for the superstructure collapse and FDOT series limit states, respectively. Accordingly, a normalized (proposed) PC_i value equal to 1 is in exact agreement with the corresponding (averaged AASHTO PC) benchmark value; a value of 0.1 is smaller than the benchmark value by one order of magnitude; and, a value equal to 10 is one order of magnitude larger.

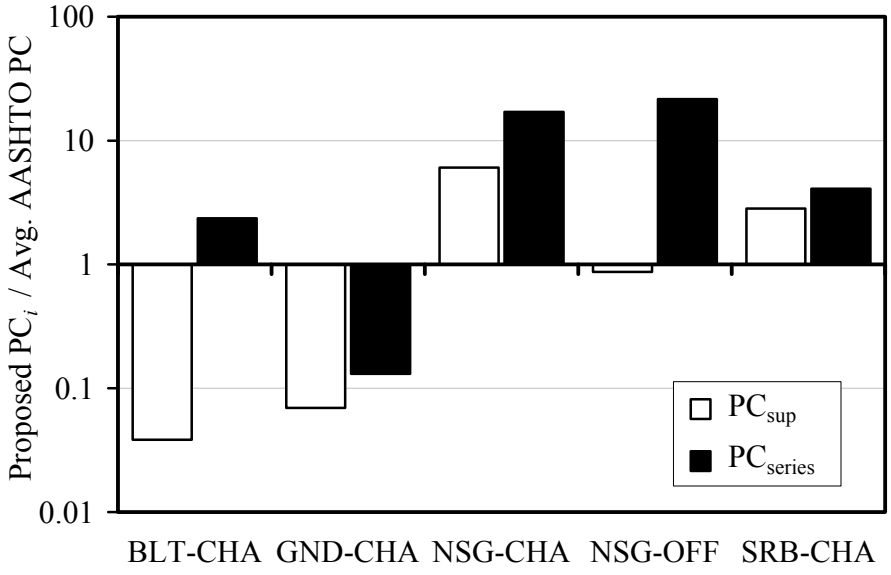

Figure 8.10 Semi-log plot comparison of proposed PC_i values to AASHTO PC values

As shown in Fig. 8.10, the normalized (proposed) PC_i values increase in proportion to the level of stringency associated with the limit state considered. For each of the five cases, the PC_{series} values are greater than the corresponding PC_{sup} values. This follows logically, since the superstructure collapse limit state is included among the FDOT series limit states. Additionally,

(normalized) predicted values obtained from the proposed PC_i expressions (Eq. 8.2 and Eq. 8.5) fall below as well as above the corresponding AASHTO PC values in such a manner that, on average (across the five cases), only small differences are present between the proposed values and current values. However, on an individual case basis, substantial differences are observed between the proposed PC_i values and the respective (individual) AASHTO PC values. These phenomena suggest that the proposed PC_i expressions can be employed in design applications to ascertain more accurate PC_i values for individual cases, while simultaneously, use of the improved PC_i expressions should not lead to substantially altered bridge collapse rate predictions (relative to current design practice) when considered as an ensemble average of PC_i values across several piers. Therefore, the proposed PC_i expressions (Eq. 8.2 and Eq. 8.5) could provide more uniform levels of safety (relative to the current AASHTO PC expression) for individual piers, when employed in bridge design applications, without substantially affecting overall bridge structural costs.

8.8 Concluding Remarks

In this chapter, a rational framework for determining the probability of bridge collapse (failure) in the event of barge-bridge collision has been used to form improved probability of collapse expressions. The proposed framework employs recently developed nonlinear dynamic collision analysis and bridge modeling techniques that are numerically efficient, yet accurate. Statistical descriptions of pertinent load and resistance parameters are used in conjunction with these techniques to assess expected values of structural failure rates and demand-capacity ratios through probabilistic simulation. The proposed framework has been used to estimate structural reliability parameters (demand-capacity, probability of collapse) for a representative set of bridges selected from within the state of Florida. Using these parameters, improved probability of collapse expressions have been developed both for bridges subject to Florida design provisions (series limit state), as well for those bridges designed using national design provisions (superstructure collapse limit state). Significant discrepancies between probability of collapse estimates obtained using the proposed PC expressions and those obtained using the AASHTO bridge design provisions suggest the need to incorporate the improved probability of collapse expressions in the overall bridge risk assessment for waterway vessel collision.

CHAPTER 9
BARGE BOW FORCE-DEFORMATION RELATIONSHIPS FOR DESIGN WITH PROBABILISTIC CONSIDERATION OF OBLIQUE IMPACT SCENARIOS

9.1 Introduction

In prior chapters, probabilistic methods have been employed to quantify the probability of collapse of numerous bridges due to barge collision. For this purpose, parameters related to both bridge structural capacity (e.g., member strength, soil resistance) and structural demands (e.g., impact loads, impact angles, dynamic effects) have been quantified and described probabilistically. Such an approach permits detailed reliability analysis of bridges, involving thousands of dynamic barge impact analyses that encompass a broad range of possible impact scenarios, structural capacities, etc. However, such an exhaustive and computationally expensive approach is not practical in engineering design. Thus, in Chapter 8, generalized expressions have been developed from which bridge designers can estimate the probability that bridges will collapse based on the results of simpler deterministic (non-probabilistic) barge impact analyses.

Widely accepted design procedures exist for estimating structural capacities that conservatively account for inherent uncertainties in such estimates (e.g., resistance factors in LRFD). However, an analogous approach is necessary when estimating structural demands (loads) that are also highly variable. The orientation of impacting barges (impact angle) has been identified as having a significant influence on forces generated during impact with flat-faced bridge pier components such as waterline pile caps or rectangular columns. The sensitivity of loads to impact obliquity, when paired with significant variability in potential impact orientations, leads to uncertainty in impact forces that must be considered as part of bridge analysis. Thus, the focus of the current chapter is to facilitate deterministic bridge analysis by developing design-oriented procedures for estimating barge impact loads while conservatively accounting for impact obliquity.

Loads associated with vessel collisions with bridges are inherently dependent on the force-deformation characteristics of the impacting vessel. Currently in the U.S., barge impact forces used in bridge design are computed based on a force-deformation ("crush-curve") model proposed by AASHTO (2009). However, in a recent study (Consolazio et al. 2009a), important limitations in the AASHTO barge crush model were uncovered, and subsequently a revised procedure for developing barge force-deformation relationships was developed. However, the force-deformation relationships developed in this previous study were based on the assumption that impact occurs in a directly head-on orientation with respect to the impacted pier. However, perfectly head-on alignment is not likely to occur during realistic collision events. It is significantly more likely that impact occurs at some oblique angle, and as is shown in this chapter, barge impact forces with flat-faced pier surfaces—i.e., rectangular columns or waterline pile caps—are typically less severe when collisions occur at even small oblique angles.

By not accounting for oblique impact conditions, the Consolazio et al. (2009a) crush-curve model can predict overly conservative forces for certain barge impact scenarios. Thus, the focus of the current study is to update the prior crush model to probabilistically

account for impact force reductions that result when impact occurs at oblique angles. In this chapter, forces associated with oblique impact scenarios are quantified by means of a series of high-resolution finite element barge bow crushing simulations. Results obtained from these simulations are used in a probabilistic study to develop a force prediction model that implicitly accounts for the relative likelihood of impact occurring at particular angles. Findings from the current study are then integrated into the previously developed barge crushing model to produce a design-oriented calculation framework that permits bridge designers to easily account for force reductions that arise in oblique impact scenarios.

9.2 Barge Bow Force-Deformation Model for Head-On Impacts

Previously, Consolazio et al. (2009a) proposed a new crush-curve model for head-on barge impact with bridge piers. This framework—being based on experimental (Consolazio et al. 2006) and analytical (Consolazio et al. 2008, 2009a) data—is intended to replace the barge crush model in the AASHTO provisions (AASHTO 2009). As part the previous study, Consolazio et al. (2009a) developed high-resolution finite element models (each consisting of 120,000–150,000 elements) of the bow regions for the two most common types of barges that traverse U.S. inland waterways: the jumbo hopper barge, and oversize tanker barge. In these prior studies, both barge bow models were crushed (quasi-statically) into simplified bridge pier models of different shapes (flat, round) and sizes (widths or diameters of 3–35 ft). Crush simulations were conducted both with the pier centered on the barge bow and with the pier positioned at the corner of the barge bow. Force-deformation curves were computed as part of each bow crushing simulation and compared, where applicable, to data obtained from full-scale barge impact experiments (Consolazio et al. 2006).

The Consolazio et al. (2009a) study revealed a variety of significant findings. Most importantly, it was found that crush forces are strongly dependent on the shape and size of the impacted pier surface; i.e., wider pier surfaces generate larger forces, and flat-faced surfaces develop significantly larger forces than comparatively sized rounded surfaces. This dependency was also observed by Yuan et al. (2008), though the study by Consolazio et al. (2009a) revealed further insights into the physical crushing phenomena that lead to this observation. Consolazio et al. suggest that forces generated during barge bow crushing are primarily influenced by the manner in which longitudinal internal stiffening trusses are engaged during crushing. Wide pier surfaces engage a large number of these trusses, thus generating increased crush forces. Additionally, flat-faced pier surfaces tend to engage (and yield) multiple trusses simultaneously, leading to larger forces than would be generated by rounded surfaces, which engage internal trusses more gradually.

The study (Consolazio et al. 2009a) also found that force-deformation behavior in barges can be conservatively idealized as elastic, perfectly-plastic. This is in contrast to the AASHTO (2009) crush-curve, in which crush forces always increase with continued deformation (i.e., hardening behavior). For the crush scenarios considered, softening was generally observed after the barge bow had yielded and the maximum crush force was realized. Based on these findings, Consolazio et al. (2009a) proposed a new barge crush-curve framework (summarized in

Fig. 9.1). For a given pier member shape (round, flat) and width (w_P), the corresponding barge yield force (P_{BY}) is computed using empirical expressions.

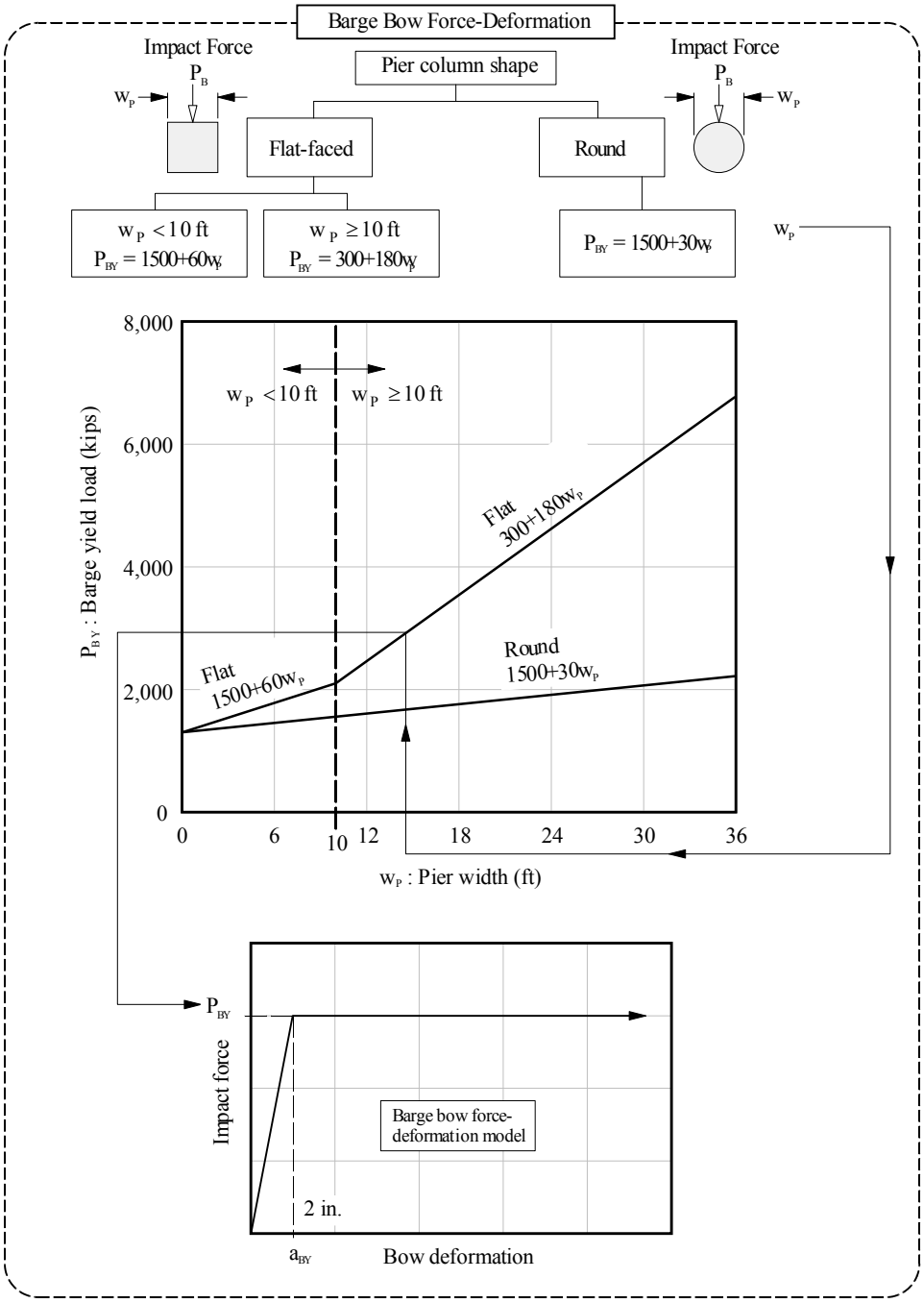

Figure 9.1 Previously proposed barge bow force-deformation relationships (from Consolazio et al. 2009a)

For flat-faced pier surfaces:

$$P_{BY} = 1500 + 60 \cdot w_P \quad \text{if } w_P < 10\,\text{ft} \tag{9.1}$$

$$P_{BY} = 300 + 180 \cdot w_P \quad \text{if } w_P \geq 10\,\text{ft} \tag{9.2}$$

where P_{BY} is in kips and w_P is in feet. For rounded pier surfaces:

$$P_{BY} = 1500 + 30 \cdot w_P \tag{9.3}$$

Given force P_{BY}, an elastic, perfectly-plastic crush-curve is developed. For simplicity, Consolazio et al. (2009a) proposes using a universal barge bow yield deformation (a_{BY}) of 2 in., regardless of impacted pier geometry. Once developed, this force-deformation curve can be used in bridge analysis as a simplified description of the barge bow. Specifically, the simplified crush-curve can be combined with the mass of the barge (or barge flotilla) in dynamic impact analysis (Consolazio and Davidson 2008), or it can be used to develop equivalent static impact loads (Consolazio et al. 2009b). Barge bow force-deformation relationships are an integral part of the dynamic impact simulations conducted as part of the development of the revised probability of collapse expressions documented in prior chapters. See Chapter 3 for a detailed description of how such relationships are used in the context of barge-bridge collision analysis.

9.3 Parametric Study

While the crush-curve model proposed by Consolazio et al. (2009a) constitutes a substantial improvement to current design assumptions regarding barge crushing behavior, all crush simulations involving flat-faced pier surfaces were conducted in a perfectly head-on orientation (i.e. the barge bow was perfectly aligned with the flat pier face). From a design standpoint, this head-on impact assumption is conservative, in that maximum impact forces are developed during perfectly head-on impacts (due to simultaneous engagement of multiple internal trusses in the barge, as discussed in Consolazio et al. 2009a). However, it is unlikely that a realistic impact would occur in this perfectly head-on manner. Thus, the focus of the current study is to quantify forces associated with oblique impact conditions in order to reduce potential conservatism in design-based force predictions associated with flat-faced pier surfaces.

For this task, a parametric study is conducted, consisting of more than fifty (50) high-resolution finite element barge bow crushing simulations, similar to those conducted previously (Consolazio et al. 2009a). However, in the present study, crush simulations involve flat-faced impact surfaces (widths ranging from 6 – 35 ft), oriented at various oblique angles (0° – 45°) from which force-deformation relationships and maximum forces are computed. Data obtained from these simulations are used to develop an empirical expression to estimate maximum crush force [or barge yield force (P_{BY})] as a function of both pier surface width (w_P) and angle of obliquity (θ).

9.3.1 High-resolution finite element barge model

For the current study, bow crushing simulations utilize the same high-resolution finite element model of a jumbo hopper barge bow that was used in (Consolazio et al. 2009a). The data are generated using high-resolution finite element barge models and the nonlinear finite element analysis code, LS-DYNA (LSTC 2009). LS-DYNA is capable of analyzing large-scale nonlinear plastic deformations associated with extreme levels of barge bow crushing; accounting for global and local member buckling of barge bow components; and modeling contact between the barge and the bridge, and between internal components within the barge itself.

Detailed structural barge plans were obtained from manufacturers and used to develop finite the element model. The vessel consists of two primary sections: a bow, and a hopper area (Fig 9.2a). As will be shown later, peak force levels generally occur at low deformation levels (relative to the overall barge length), therefore, only the bow section of the barge is modeled.

The jumbo hopper barge is the primary vessel upon which the AASHTO barge impact provisions are based and is the most common type of barge found operating on the U.S. inland waterway system. Hopper barges are fabricated from steel plates and standard structural steel shapes (channels, angles, etc.). The bow of the hopper barge considered in this study is 27.5 ft long by 35 ft wide, and is composed of fourteen internal rake trusses, transverse stiffening members, and several external hull plates of varying thicknesses (Fig. 9.2b-c). Structural steel members are welded together with gusset plates to form the internal rake truss members (Fig 9.3).

All barge components are modeled using four-node shell elements (totaling more than 120,000 elements), mimicking the actual geometric shape of the barge members. The use of shell elements allows, for example, local and global member buckling to occur in the rake truss members. Legs of structural shapes such as angles are modeled with a sufficient number of elements so that reverse curvature during local buckling can be detected. Additionally, the use of shell elements to model internal structural members of the barge allow these components to undergo local material failure which, in LS-DYNA, results in element deletion.

Individual steel components in barges are joined through combinations of continuous and intermittent welds. In the LS-DYNA models, approximation of the weld conditions is accomplished using `CONSTRAINED_SPOTWELD` constraints (LSTC 2009) which permit the user to define a massless spotweld between two nodes (Fig 9.3). An LS-DYNA spotweld is effectively a rigid beam connecting two nodes together. Weld failures were represented through element deletion when shell element strains reached the defined material failure criteria. By using a sufficient density and distribution of spotwelds, reasonable emulation of the continuous and intermittent welds present in the physical barge is achieved.

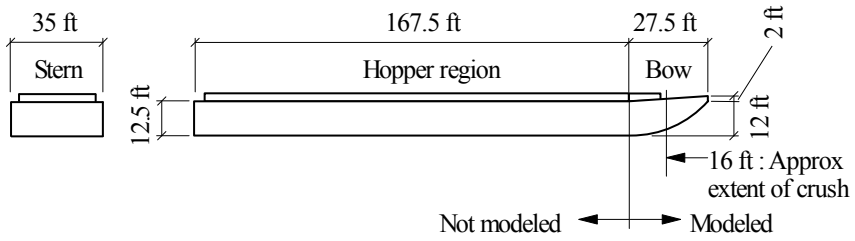

a)

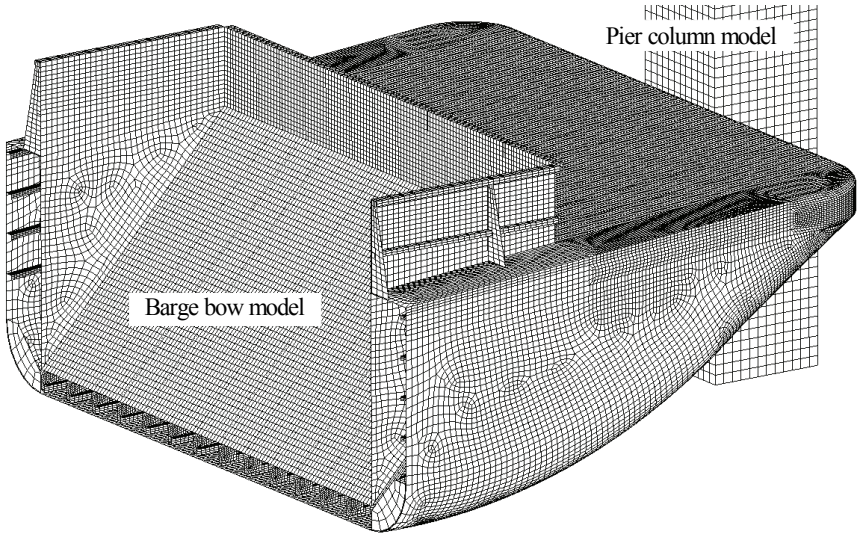

b)

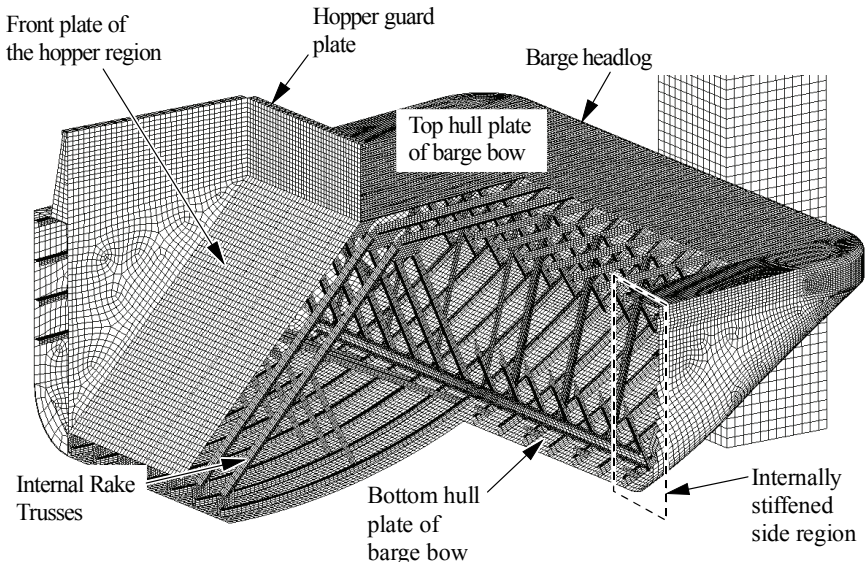

c)

Figure 9.2 Jumbo hopper barge model.
a) Schematic; b) Barge bow model with impactor; c) Cut section showing internal structure

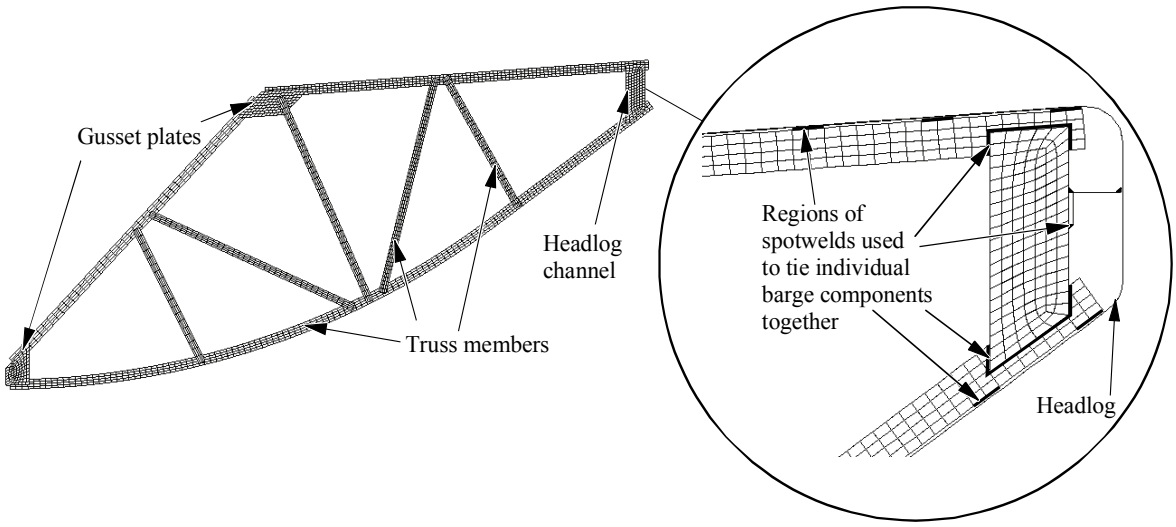

Figure 9.3 Longitudinal rake trusses in jumbo hopper barge model

Since severe levels of crushing deformation (16 ft) are analyzed using this model, a material model capable of representing both nonlinearity and failure, `MAT_PIECEWISE_LINEAR_PLASTICITY`, is employed for all barge components. This elastic-plastic material model is defined by an applicable effective-true-stress vs. effective-plastic-strain relationship. Due to the quasi-static nature of the crush simulations performed in this study, strain-rate effects are not included in the barge bow model. Most barges fabricated in the U.S. are constructed from A36 structural steel, thus material properties and an effective-true-stress vs. effective-plastic-strain relationship for A36 steel (Fig. 9.4) are specified for all barge components.

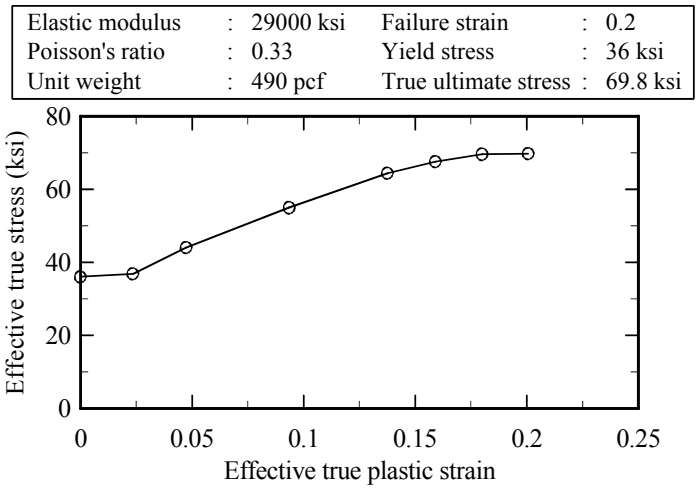

Figure 9.4 Material parameters for A36 structural steel

9.3.2 Barge bow crush analyses with oblique flat-faced surfaces

To quantify the influence of oblique impact conditions on barge bow force-deformation characteristics, a parametric study has been conducted, consisting of more than fifty (50) high-

resolution finite element analyses in LS-DYNA. Each simulation involves quasi-static crushing between the jumbo hopper barge bow model and a flat-faced block—to represent common bridge pier column or pile cap surfaces—of a particular width (6 - 35 ft), at a particular oblique angle (0° - 45°), to a total crush depth of 16 ft [consistent with the prior study (Consolazio et al. 2009a)]. As illustrated in Fig. 9.5, such crush simulations emulate the barge bow force-deformation response expected when impact occurs at an oblique angle (θ) relative to the bridge pier. The line of action of crushing is consistently parallel to the barge axis, regardless of θ. Furthermore, the pier block is arranged such that the center of gravity is aligned with the barge bow centerline.

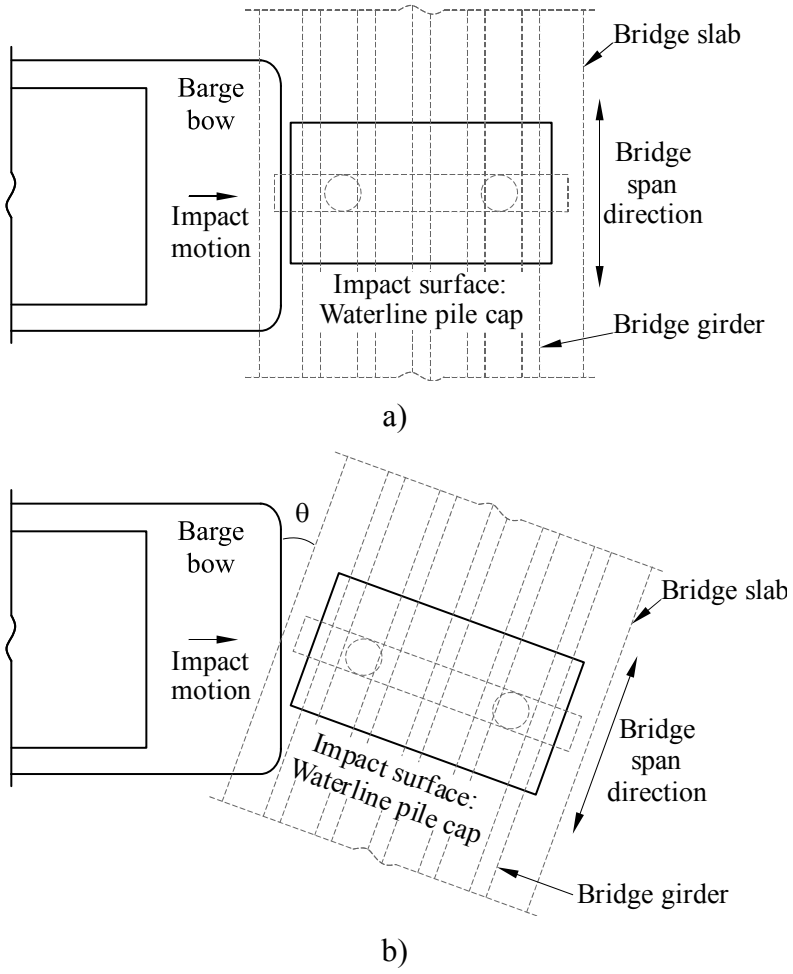

Figure 9.5 Barge impact scenarios. a) Directly head-on, b) Oblique

Specific combinations of pier surface width (w_P), and oblique angle (θ) that have been simulated are reported in Table 9.1. Pier widths are approximately evenly distributed within the range of 6 - 35 ft and have been chosen to represent bridge pier columns or waterline pile caps. Note that typical jumbo hopper barges are 35 ft wide; thus, 35 ft constitutes an effective maximum pier width. Specific pier widths considered are shown schematically (to relative scale) in Fig. 9.6. Oblique angles range from 0° ("head-on" impact) to as high as 45° (crushing about the pier corner). Simulation data—conducted using the 35-ft pier model—indicated that

maximum crush forces reduce rapidly as the angle of obliquity increases. Consequently, oblique angles for the parametric study are distributed with a larger number of simulations conducted at small angles (less than 10°). For each pier width, crush simulations have been conducted at eight (8) or more oblique angles (Fig. 9.7).

Table 9.1 Analysis matrix of oblique crushing simulations

Pier width (ft)	Oblique crushing angles simulated													
	0°	0.25°	0.50°	0.75°	1.0°	1.5°	2°	3°	5°	10°	15°	20°	30°	45°
6	X				X		X		X	X	X		X	X
9	X				X		X		X	X	X		X	X
12	X				X		X		X	X	X		X	X
18	X				X		X		X	X	X		X	X
26	X		X		X		X		X	X	X		X	X
35	X	X	X	X	X	X	X	X	X	X	X	X	X	X

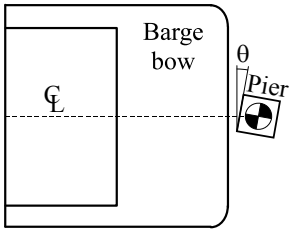

a) 6-ft pier surface

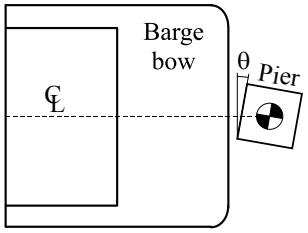

b) 9-ft pier surface

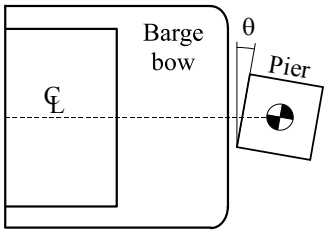

c) 12-ft pier surface

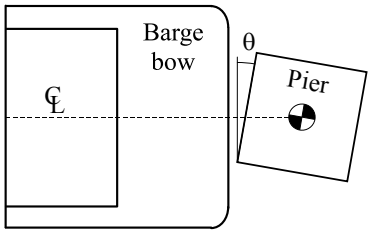

d) 18-ft pier surface

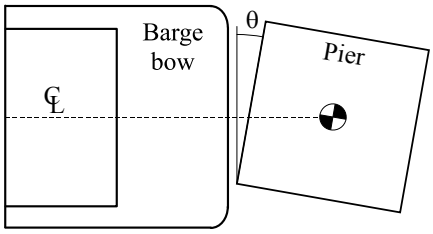

e) 26-ft pier surface

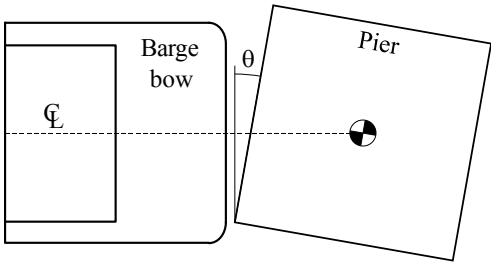

f) 35-ft pier surface

Figure 9.6 Parametric study: pier widths considered

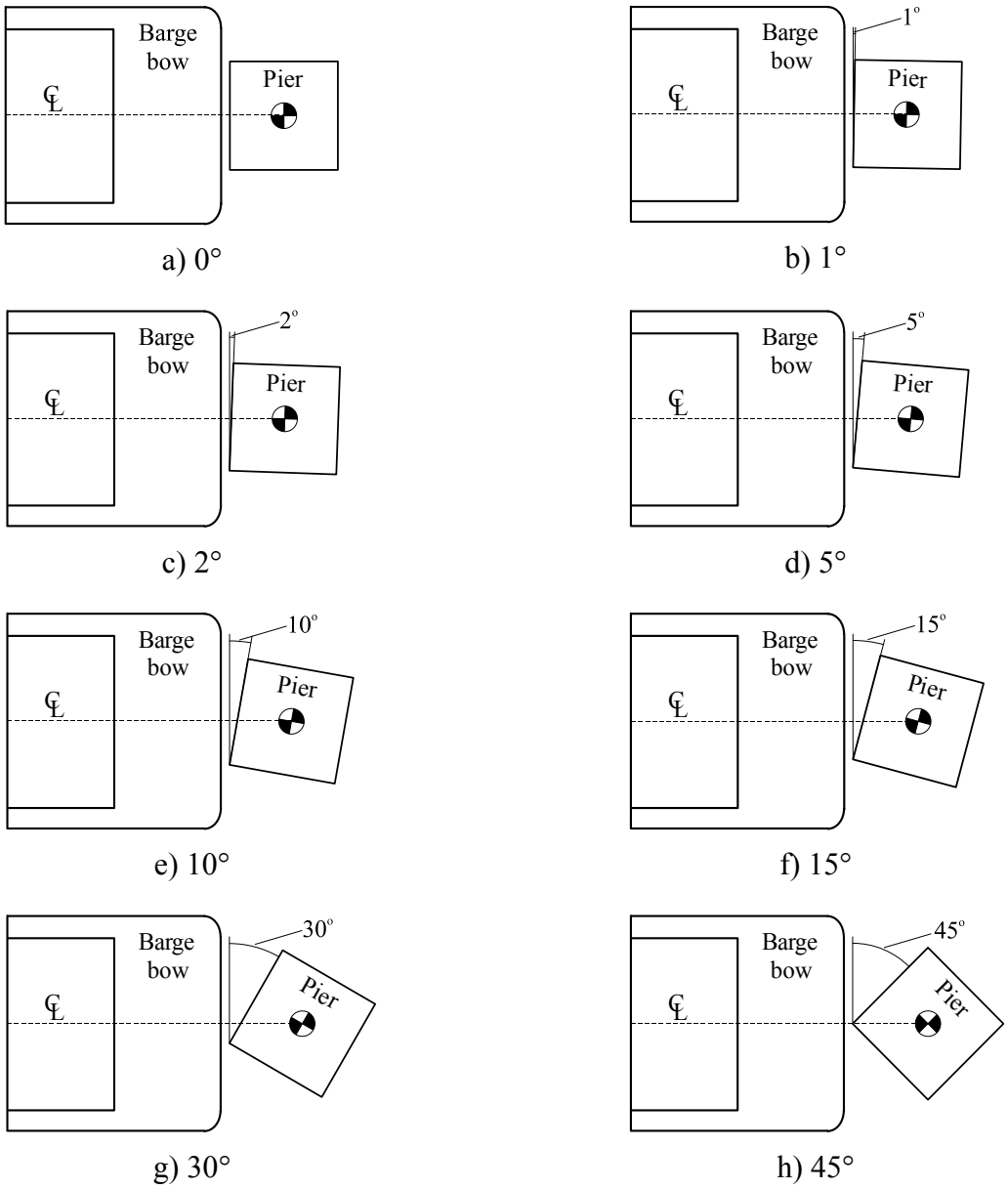

Figure 9.7 Parametric study: typical oblique angles considered
(additional intermediate angles simulated for 26-ft and 35-ft pier surface)

9.3.3 Influence of obliquity on barge bow force-deformation behavior

Throughout each simulation, forces developed between the barge bow and impact block are monitored using the `CONTACT_AUTOMATIC_NODES_TO_SURFACE` contact algorithm in LS-DYNA. Force output is combined with the specified constant crushing rate (4 ft/s) to form relationships between crush force and bow deformation (force-deformation relationships). Selected force-deformation data are presented in Fig. 9.8 - 9.9 for the purpose of demonstrating the influence of impact obliquity on bow crushing behavior.

In Fig. 9.8, representative force-deformation data—obtained from selected 6-ft crushing scenarios—are presented. These results are typical of data obtained from small-width crush simulations (6 - 9 ft). For head-on or nearly head-on scenarios (i.e., those that fall between 0° - 2°), the response is similar: effectively linear for the first 1–2 in. of deformation, at which point the bow yields, ultimately reaching the maximum crush force at a deformation of approximately 20 in. This maximum crush force is heretofore denoted as P_{BY}, because barge bow force-deformation will later be idealized as elastic, perfectly-plastic. At larger oblique angles (5° or more), the crushing region is less stiff, without a well-defined yield point. However, for all crush angles, P_{BY} is approximately equal. In contrast, for wider pier surfaces (12 ft and larger), obliquity influences both bow stiffness and peak forces. Force-deformation data shown in Fig. 9.9—corresponding to the 35-ft pier model—is typical for wide surfaces. Note that even small oblique angles produce significant reductions in overall bow stiffness and maximum crush force. As illustrated in Fig. 9.9, the maximum force (P_{BY}) associated with crushing at an oblique angle of 1° is approximately 15% smaller than that observed from a head-on (0°) condition, and such reductions continue at larger angles. Note that detailed force-deformation data obtained from each simulation in the parametric study are provided in Appendix D.

Bow stiffness and peak crush force are larger for head-on conditions due to the simultaneous engagement and yielding of internal stiffening trusses (Fig. 9.10a). Truss buckling occurs at relatively small bow deformations (less than 5 in.), beyond which, resistance to crushing is greatly reduced. In contrast, if an oblique angle is present between the barge bow and impacted surface, trusses are engaged and yield gradually (Fig. 9.10b). Consequently, trusses in the initial contact region have yielded (and softened) before trusses on the other side of the barge bow have even been engaged. This effect reduces initial bow stiffness—relative to a head-on crushing—and limits maximum crush forces that can be developed.

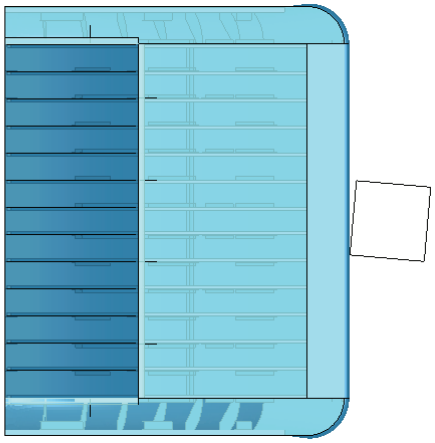

a) 0 ft crush depth

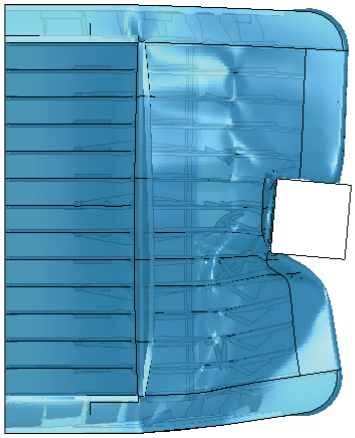

b) 6 ft crush depth

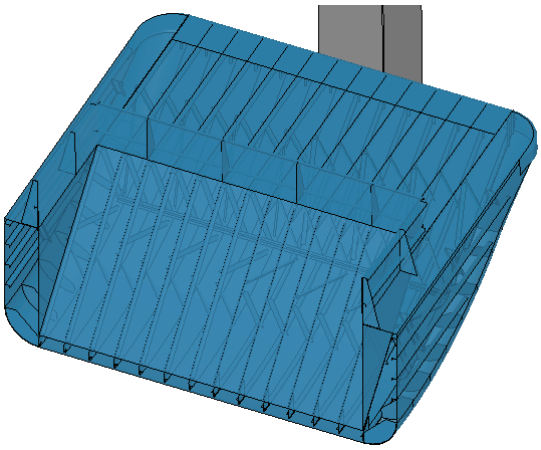

c) 0 ft crush depth

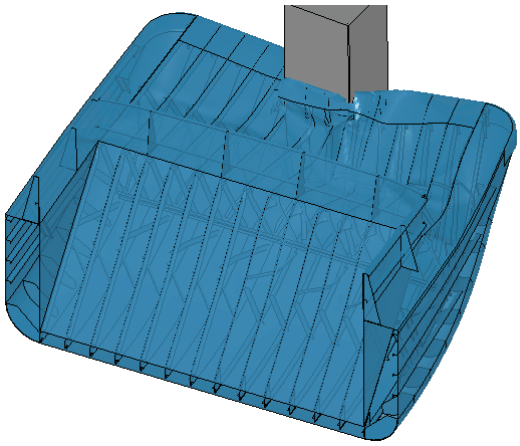

d) 6 ft crush depth

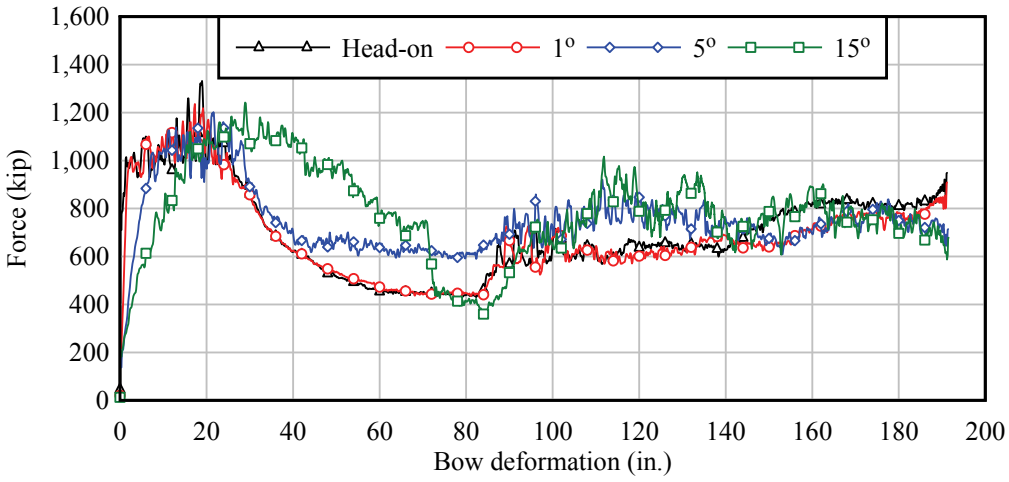

e) Selected force-deformation results

Figure 9.8 Selected oblique crushing simulation results: 6-ft pier surface at 5°

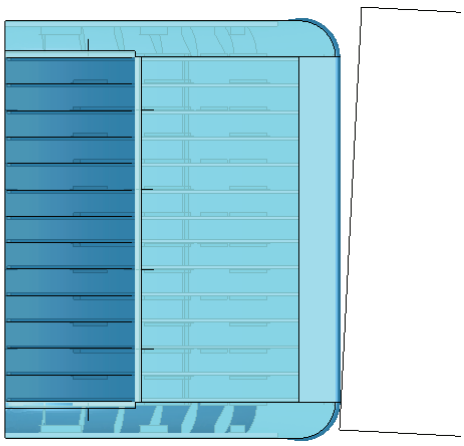

a) 0 ft crush depth

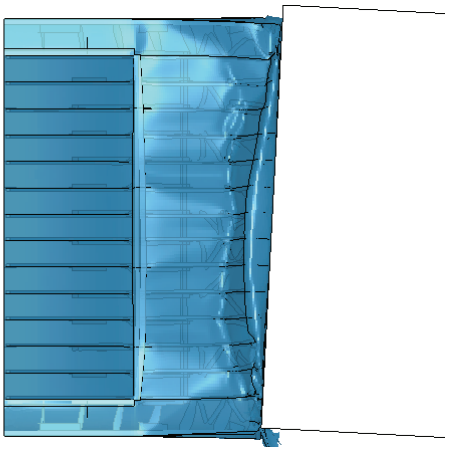

b) 6 ft crush depth

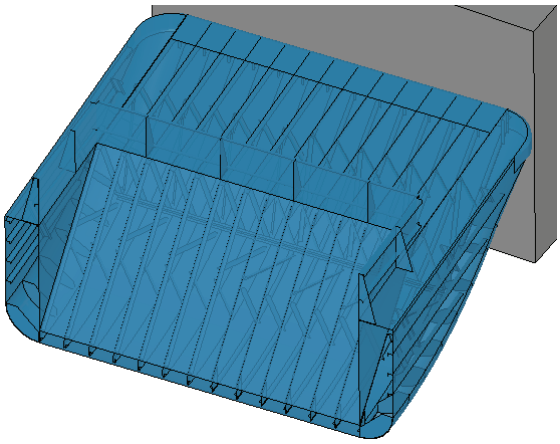

c) 0 ft crush depth

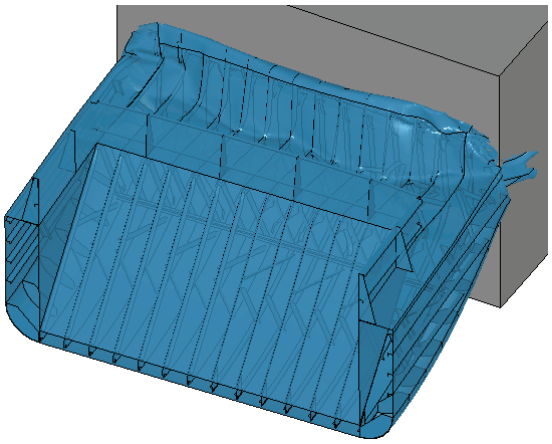

d) 6 ft crush depth

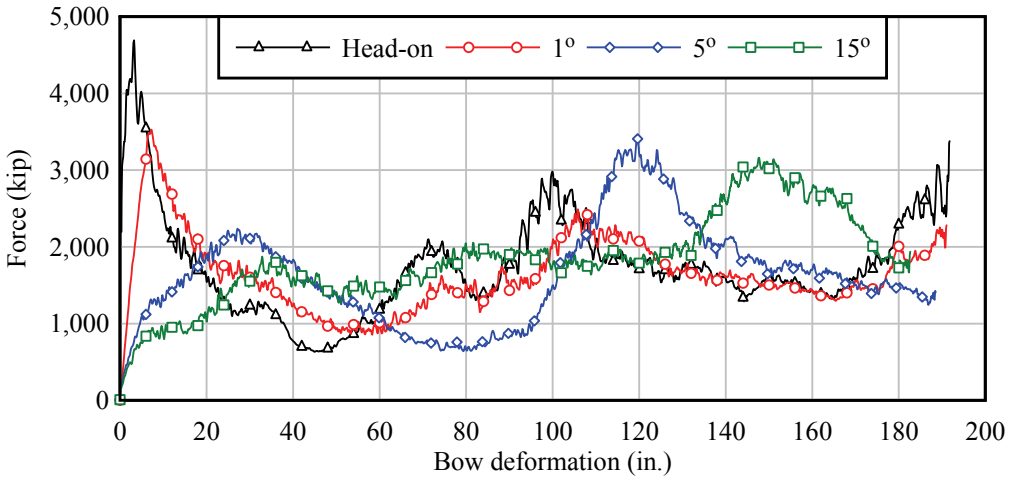

e) Selected force-deformation results

Figure 9.9 Selected oblique crushing simulation results: 35-ft pier surface at 5°

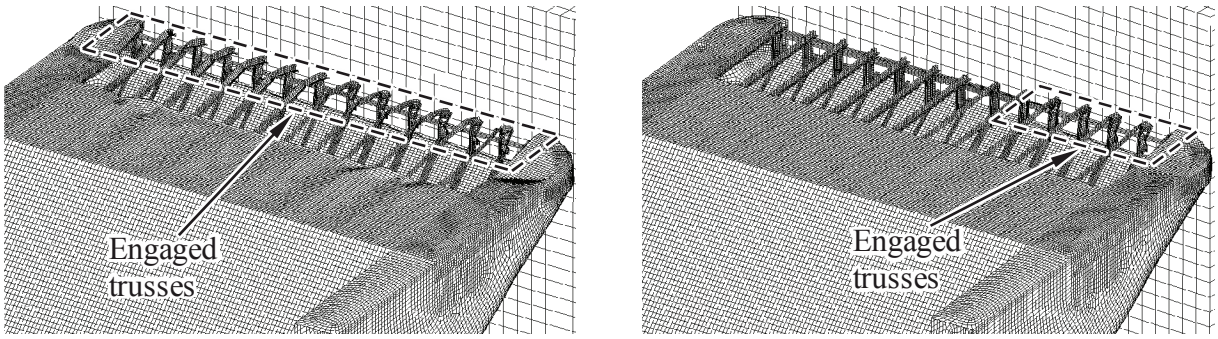

a) b)

Figure 9.10 Truss engagement during crushing with wide flat-faced surfaces. a) Head-on crush with abrupt engagement of all trusses; b) Oblique crush with gradual engagement (hopper guard plate not shown for clarity)

9.3.4 Influence of obliquity on maximum crush forces (P_{BY})

Maximum barge bow crushing forces [barge yield forces (P_{BY})] are quantified for each simulation conducted in the parametric study. These force data are grouped by pier widths—e.g., all simulations involving 6-ft piers are grouped—and barge yield forces (P_{BY}) and are plotted (Fig. 9.11) as a function of the angle of obliquity (θ). From the figure, it is evident that obliquity has virtually no influence on P_{BY} for 6-ft and 9-ft pier surfaces (Figs. 9.11a–b). Yield forces for the 6-ft and 9-ft piers are on average 1260 kips and 1370 kips, respectively, with little variability based on the choice of θ.

However, dependency between P_{BY} and θ is evident for piers 12 ft and wider (Figs. 9.11c–f). For these wider pier surfaces, P_{BY} tends to decrease abruptly as θ increases, ultimately reaching a plateau value at a fairly small oblique angle ($\theta < 5°$). In general, as the pier width becomes larger, the relative difference between head-on and plateau yield forces increases, as does the rate at which the reduction occurs. The overall shape of the $P_{BY}(\theta)$ data for these cases is consistent with a decaying (negative) exponential function that has been shifted vertically to be asymptotic about a nonzero value. Thus, each set of data—grouped by common pier width—has been fit with an exponential function of the form:

$$P_{BY}(\theta) = \alpha_0 + \alpha_1 \cdot e^{-\alpha_2 \cdot \theta} \tag{9.4}$$

where the function parameters α_0, α_1, α_2 are uniquely determined for each pier width using least-square curve fitting. Specific expressions that have been developed for each data set are shown in Figs. 9.11c–f. Close agreement is evident between the raw data and fitted expressions, particularly for small values of θ. These exponential expressions are used as representative empirical models for estimating P_{BY} based on θ in the probabilistic study described below.

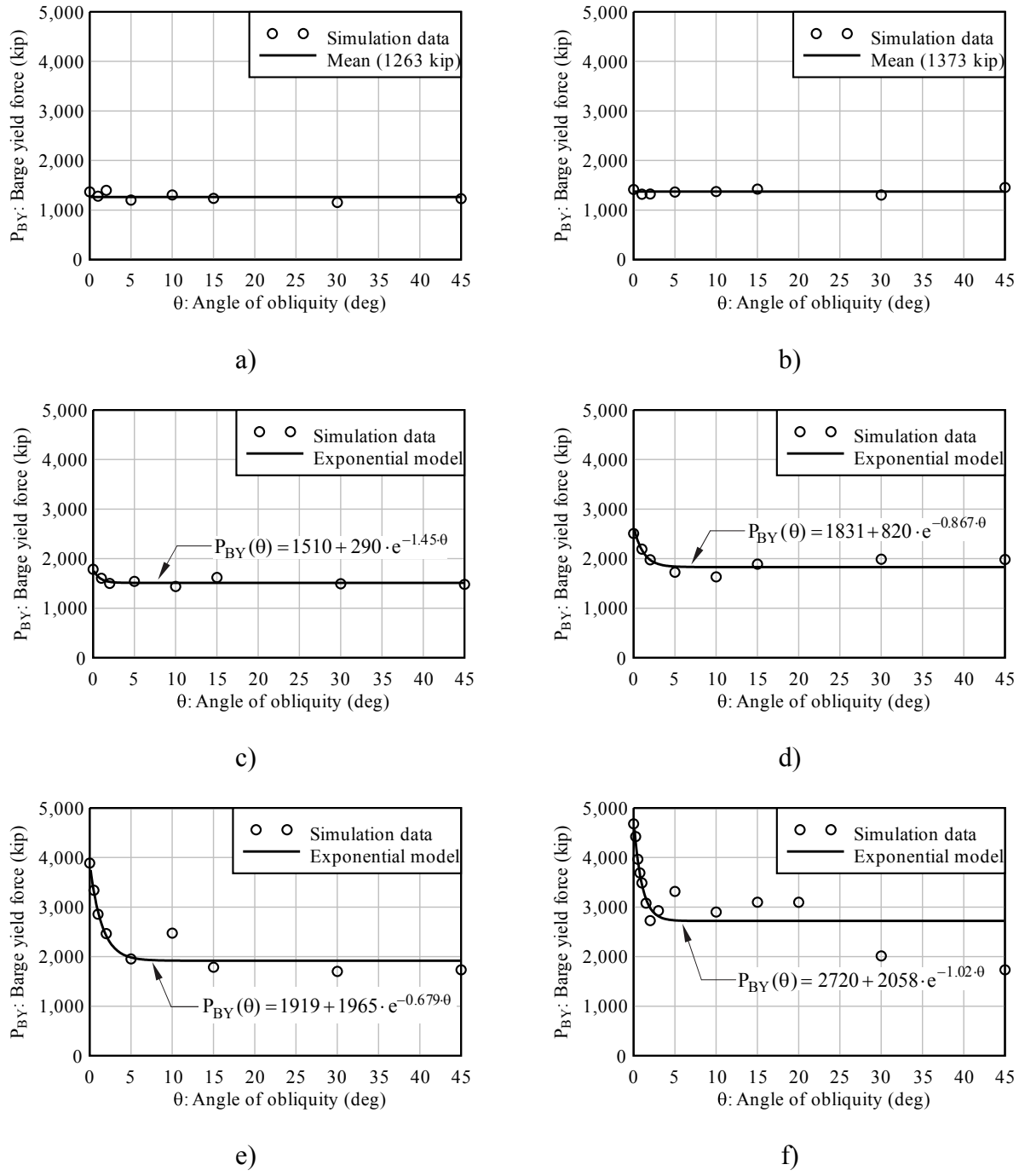

Figure 9.11 Variation in barge bow yield forces (P_{BY}) due to oblique crush angles (θ). a) 6-ft surface; b) 9-ft surface; c) 12-ft surface; d) 18-ft surface; e) 26-ft surface; d) 35-ft surface

9.4 Probabilistic Study

While it has been demonstrated that barge bow crushing forces are strongly dependent on angle, particularly for wide surfaces such as waterline pile caps, this information alone is insufficient to make design-related decisions about forces generated during barge impact with

bridges. This is because the equations presented in Figs.9.11c–f do not take into account the probability of barge impact occurring at particular angles. Thus, empirical models (Figs.9.11c–f) to predict barge bow yield force (P_{BY}) as a function of pier surface width (w_P) and oblique crushing angle (θ) are used in a probabilistic study to account for the relative likelihood of a barge striking a bridge pier at a particular angle. The probabilistic study is used to develop predictions of P_{BY} that are based on a desired probability of exceedance (5% in this case). Such an approach is intended to provide P_{BY} predictions that are more realistic than conservatively assuming that impacts occur in a directly head-on manner.

The probabilistic study, summarized in Fig. 9.12, employs a standard Monte Carlo (MC) simulation approach to account for variability associated with angle of obliquity. A key component of the MC simulation is a probabilistic description of impact angle (θ). Kunz (1998) has proposed a probability density function (PDF) model for use in reliability-based design of bridges for vessel impact. The Kunz model is Gaussian (normally) distributed with mean equal to the expected impact angle (μ_θ) and standard deviation of 10°. The expected impact angle corresponds to the most likely alignment between an impacting barge and bridge piers. For example, if the waterway transit path is exactly perpendicular to the bridge superstructure, the expected impact angle is 0° (head-on impact). However, non-zero values of μ_θ are possible if vessel transit paths and bridge alignments are skewed relative to each other. Kunz (1998) also suggests truncating (bounding) the distribution at the lower 2nd and upper 98th percentiles. The truncation allows for a total range of impact angles of approximately 41°, normally distributed around μ_θ.

Given the Kunz (1998) PDF for θ, a series of MC simulations is conducted, with θ as the only input random variable (Fig. 9.12). Individual MC simulations are conducted for each pier width for which an exponential $P_{BY}(\theta)$ expression has been developed (w_P = 12, 18, 26, 35 ft) and for a range of expected impact angles (μ_θ = 0° - 30°, in 1° increments). Consequently, at total of 124 MC simulations are conducted, constituting each combination of w_P and μ_θ. As illustrated in Fig. 9.12, for a given MC simulation, N samples of θ are generated using the Kunz distribution with mean equal to μ_θ. Note that $N = 10^6$—i.e., one million probabilistic simulation samples—has been found to provide highly reliable estimates of output parameters for this study and is used throughout. For each of the 10^6 samples of θ, the fitted exponential model of $P_{BY}(\theta)$ for the w_P of interest (recall Figs. 9.11c–f) is used to compute a corresponding P_{BY}. The 10^6 resulting values of P_{BY} are then subsequently used to build up an empirical cumulative distribution function (CDF) for P_{BY}. From this CDF, a value of P_{BY} is estimated that corresponds to the desired probability of exceedance (5% exceedance is used for this study). In other words, P_{BY} is expected to be less than this value in 95% of all impact scenarios. This process is repeated for each pier width w_P for which an exponential $P_{BY}(\theta)$ expression has been developed (w_P = 12, 18, 26, 35 ft), resulting in 5% exceedance P_{BY} estimates for those pier widths. Recall that no dependence was observed between P_{BY} and θ for smaller pier widths (w_P = 6, 9 ft), thus MC simulations are unnecessary for these widths, and the mean values of P_{BY} are used.

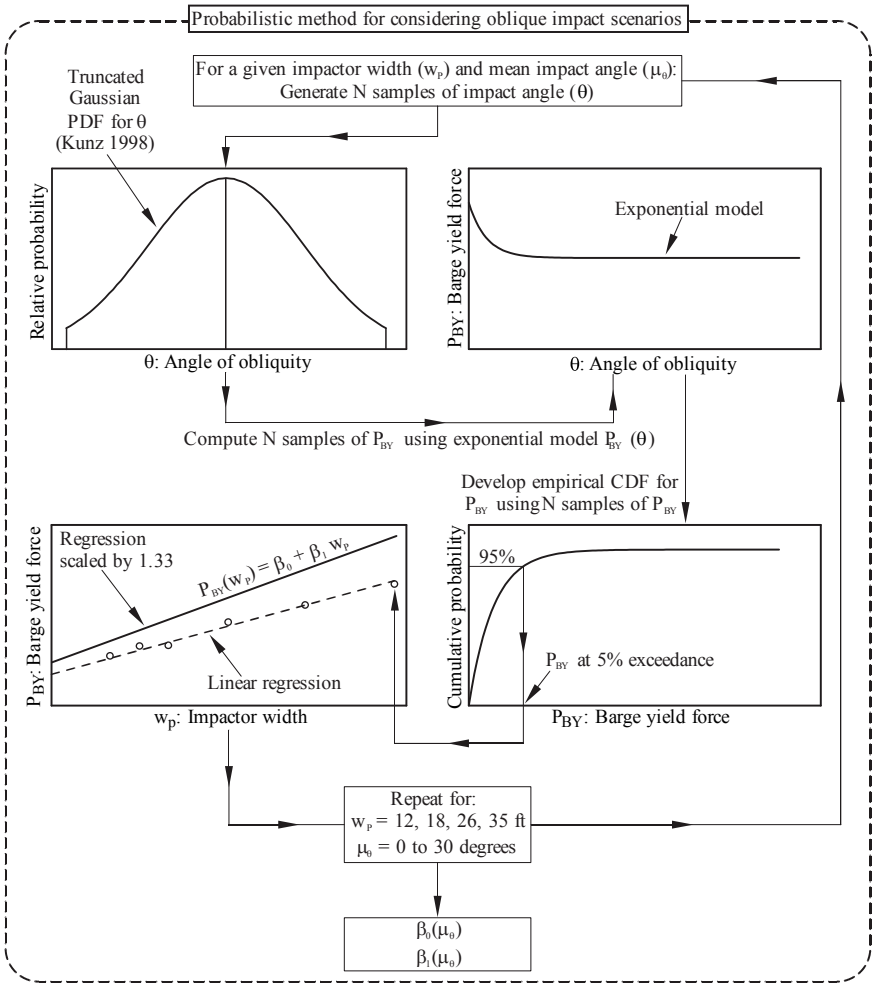

Figure 9.12 Monte Carlo simulation to account for the probability of oblique barge impact

Given the pairs of w_P and 5% exceedance P_{BY} estimates, linear regression is used to develop empirical expressions relating P_{BY} to w_P, similar to that proposed by Consolazio et al. (2009a) for head-on impacts (recall Fig. 9.1). As part of the earlier study, Consolazio et al. scaled $P_{BY}(w_P)$ regression lines by a factor of 1.33 to account for variability in barge bow steel plate thicknesses and material strengths that may be observed among the U.S. barge fleet. Thus, for the present study, $P_{BY}(w_P)$ regressions are scaled by 1.33 to form conservative, design-oriented envelope expressions. Being linear, such envelopes take the general form:

$$P_{BY}(w_P) = \beta_0(\mu_\theta) + \beta_1(\mu_\theta) \cdot w_P \tag{9.5}$$

where β_0 is the envelope intercept, and β_1 is the slope (both parameters vary depending on μ_θ).

Note that a given $P_{BY}(w_P)$ envelope depends upon the expected impact angle (μ_θ) used to form the PDF of θ. Thus, the entire MC simulation process is repeated for $\mu_\theta = 0° - 30°$, resulting

in 31 total $P_{BY}(w_P)$ envelopes, each corresponding to a given value of μ_θ (Fig. 9.13). These envelopes show that P_{BY} values predicted for $\mu_\theta = 0°$ are generally larger than those corresponding to nonzero angles. This outcome is expected, given that a barge traversing a waterway such that $\mu_\theta = 0°$ has the highest possible likelihood of striking a bridge pier head-on or nearly head-on, resulting in the largest possible forces. Conversely, it is highly unlikely for a barge with $\mu_\theta = 30°$ (i.e., waterway and bridge alignments skewed 30° relative to each other) to strike the pier head-on, and the corresponding $P_{BY}(w_P)$ envelope predicts appropriately smaller forces.

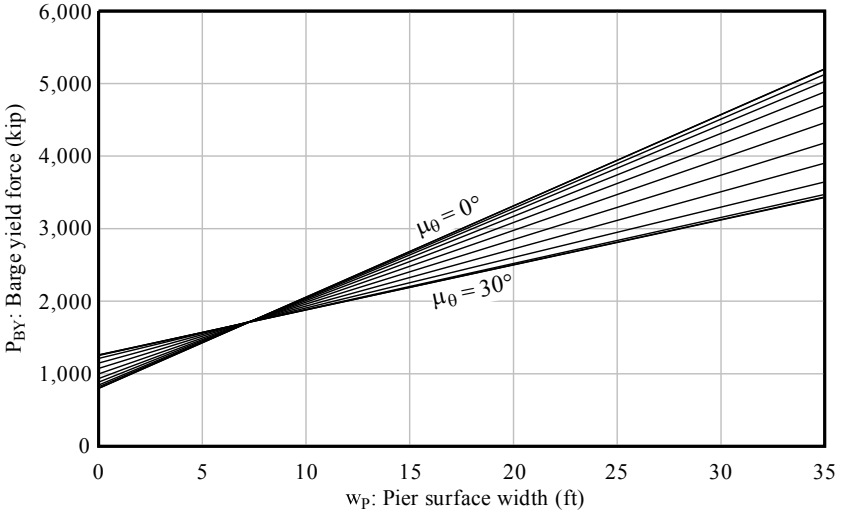

Figure 9.13 Monte Carlo simulation results: linear envelopes for a range of expected impact angles (μ_θ) (envelopes for intervals of $\mu_\theta = 2°$ shown for clarity)

9.5 Proposed Barge Bow Force-Deformation Model for Design

Given the results of the parametric and probabilistic studies described above, generalized design-oriented expressions are developed for predicting barge yield forces as a function of pier width and expected impact angle. Data obtained from the current study for flat-faced pier surfaces (with probabilistic consideration of oblique impacts) are synthesized with data for rounded pier surfaces that were obtained from the Consolazio et al. (2009a) study. By doing so, the results of the current study are integrated into the overall barge bow force-deformation model from Consolazio et al. (2009a), resulting in an updated crush-curve model that is well suited for use in bridge design.

9.5.1 Design expressions for barge bow yield force (P_{BY})

In order to integrate the findings of the current probabilistic study into the Consolazio et al. (2009a) crush-curve framework, it is important to consider $P_{BY}(w_P)$ expressions that were developed for rounded piers as part of the previous study. P_{BY} values generated by rounded piers (from Consolazio et al. 2009a) are shown in Fig. 9.14a, along with the linear regression trend line fit through the data:

$$P_{BY}(w_P) = 1035.1 + 22.5 \cdot w_P \tag{9.6}$$

where P_{BY} is in kips and w_P is in feet. Scaling the regression line by 1.33—again, to account for plate thickness and material strength variability—and rounding the coefficients up, results in a design envelope for rounded pier shapes (also shown on Fig. 9.14a):

$$P_{BY}(w_P) = 1400 + 30 \cdot w_P \tag{9.7}$$

For comparison, $P_{BY}(w_P)$ envelope data for flat-faced piers—derived from the current probabilistic study—are shown in Figs. 9.14b–c. Note that the envelope intercept (β_0) and slope (β_1) vary based on the expected impact angle (μ_θ) (recall Fig. 9.13). Thus, β_0 and β_1 are presented as functions of μ_θ in Fig. 9.14b and Fig. 9.14c, respectively. Envelope intercepts for the flat-faced data vary from approximately 800 - 1250 kips, which is significantly lower than the intercept of the $P_{BY}(w_P)$ expression for round piers (1400 kips from Eq. 9.7). However, it is reasoned that, as w_P approaches zero, the round and flat-faced $P_{BY}(w_P)$ expressions should converge to the same value. Thus, for consistency, β_0 in the flat-faced expression is conservatively rounded up to 1400 kips for all values of μ_θ (Fig. 9.14b).

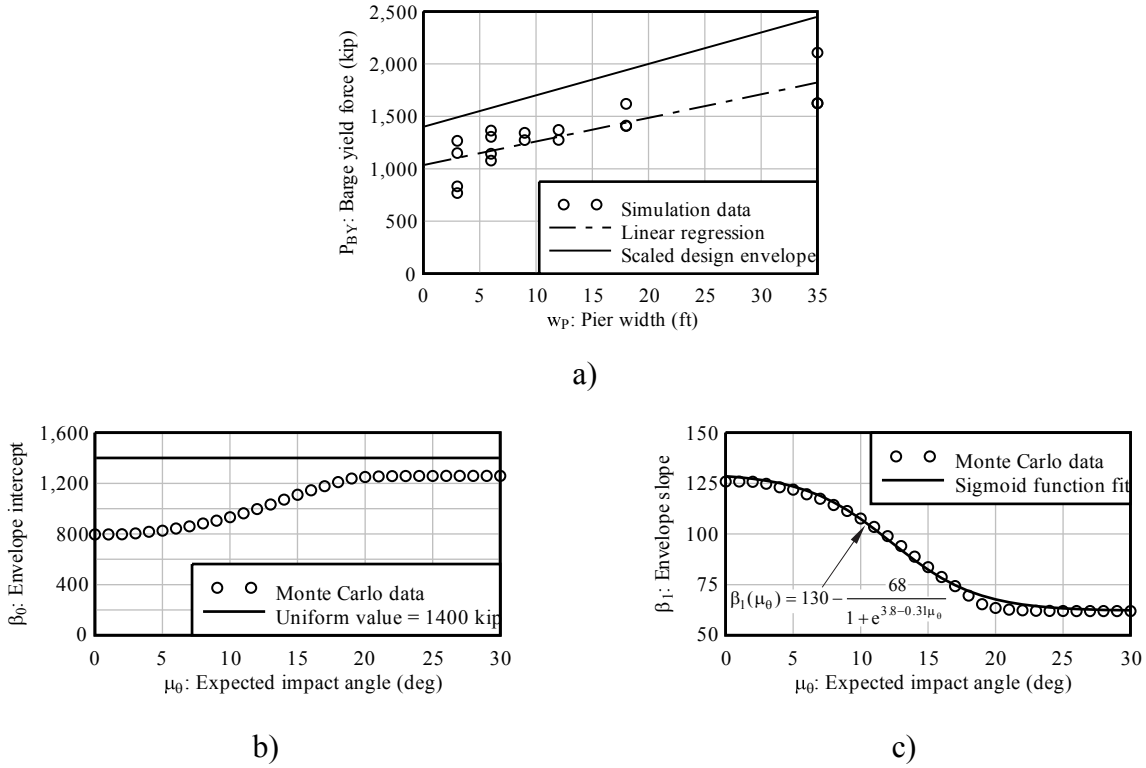

Figure 9.14 $P_{BY}(w_P)$ envelope parameters for round and flat pier surfaces.
a) Data and design envelope for round piers adapted from (Consolazio et al. 2009a); b) Envelope intercept (β_0) for flat piers from probabilistic study; c) Envelope slope (β_1) for flat piers

As shown in Fig. 9.14c, the $P_{BY}(w_P)$ envelope slope (β_1) for flat-faced piers also varies based on μ_θ. Because P_{BY} is quite sensitive to β_1—particularly for very wide surfaces like waterline pile caps—it is important to limit the conservatism associated with estimates of β_1. Thus, a sigmoid (or logistic) function—which has a shape that matches the data closely—is chosen to serve as a design expression for predicting β_1. A basic sigmoid takes the functional form:

$$f(x) = \frac{1}{1 + e^{-x}} \tag{9.8}$$

However, to fit the $\beta_1(\mu_\theta)$ data, the basic functional form must undergo a variety of transformations. Thus, the data is fit with the modified functional form:

$$\beta_1(\mu_\theta) = \gamma_0 - \frac{\gamma_1}{1 + e^{\gamma_2 - \gamma_3 \cdot \mu_\theta}} \tag{9.9}$$

where γ_0, γ_1, γ_2, γ_3 are function parameters. Fitting this expression (using least squares error) to the data and rounding the fitting parameters results in the empirical expression:

$$\beta_1(\mu_\theta) = 130 - \frac{68}{1 + e^{3.8 - 0.31 \cdot \mu_\theta}} \tag{9.10}$$

Lastly, β_0 and β_1 are substituted into the generalized expression for P_{BY} (Eq. 9.5):

$$P_{BY}(w_P, \mu_\theta) = 1400 + \left[130 - \frac{68}{1 + e^{3.8 - 0.31 \cdot \mu_\theta}} \right] \cdot w_P \tag{9.11}$$

For design purposes, the probabilistic notation for expected impact angle (μ_θ) is unnecessary. Thus, μ_θ is replaced with simply θ, resulting in a design-oriented expression for predicting P_{BY}:

$$P_{BY}(w_P, \theta) = 1400 + \left[130 - \frac{68}{1 + e^{3.8 - 0.31 \cdot \theta}} \right] \cdot w_P \tag{9.12}$$

where P_{BY} is in kips, w_P is in feet, and θ is in degrees.

The revised P_{BY} expression for flat-faced surfaces (Eq. 9.12) generally predicts smaller forces than would be predicted by the original expression proposed by Consolazio et al. (2009a) (Eq. 9.2). For example, consider barge impact with a wide, waterline pile cap with width equal to that of a typical jumbo hopper barge (w_P = 35 ft). The previously proposed expression, Eq. 9.2, predicts a barge yield force of 6600 kips. However, the revised expression, Eq. 9.12, predicts a yield force equal to 5900 kips for $\theta = 0°$ (11% reduction) and only 3580 kips for $\theta = 30°$ (46% reduction).

9.5.2 Barge bow deformation at yield (a_{BY})

Recall that P_{BY} is used to form a barge bow force-deformation relationship that is conservatively idealized as being elastic, perfectly-plastic (recall Fig. **9.1**). Consequently, such crush-curves are completely described by two parameters: barge yield force (P_{BY}), and barge bow deformation at yield (a_{BY}). Consolazio et al. (2009a) propose a common a_{BY} equal to 2 in. for all impact scenarios and pier geometries. In the current study, it has been observed that, in oblique crushing scenarios, yield deformations can occur at crush depths greater than 2 in. However, no simple and accurate means have been identified to predict this increase in a_{BY} (decrease in initial bow stiffness); therefore, the typical 2-in. yield deformation is conservatively retained in the revised crush-curve model (described in the following section).

While this simplification is conservative, it is not considered to have a large influence on impact force predictions under typical barge impact conditions. Prior studies (Consolazio et al. 2008, 2009b) have employed the Consolazio et al. (2009a) crush-curve model (with a_{BY} = 2 in.) in fully dynamic barge-bridge collision analyses. Such analyses have illustrated that impact energies associated with even moderate barge collisions—e.g., one fully-loaded barge being propelled at 2.5 knots—are sufficient to yield the barge bow in every case. Thus, due to the elastic, perfectly-plastic crush curve, impact forces are primarily dictated by barge yield force (P_{BY}), not initial bow stiffness. Only in the case of low-energy impact scenarios—e.g., a drifting empty barge—would a_{BY} have a notable influence on predicted impact forces. Therefore, for simplicity, a_{BY} = 2 in. is suggested for all barge-bridge impact scenarios.

9.5.3 Summary of revised design procedure

Given P_{BY} expressions for both round and flat pier surfaces (Eqs. 9.7 and 9.12, respectively), the overall force-deformation model originally proposed by Consolazio et al. (2009a) is updated to reflect findings from the current study. This revised design barge crush-curve framework is illustrated in Fig. 9.15. For flat-faced piers, a barge yield load (P_{BY}) is quantified based on the width of the impacted pier surface (w_P) and most likely impact angle (θ). For round pier surfaces, P_{BY} is computed based only on w_P, because impact angle has no influence on how the barge bow deforms during collision.

Lastly, the barge yield force (P_{BY}) is combined with the yield deformation suggested by Consolazio et al. (2009a) (a_{BY} = 2 in.) to form an elastic, perfectly-plastic force-deformation relationship for the barge bow. Such a relationship can be used as part of a simplified barge model (when combined with a barge mass) in dynamic barge-bridge impact analyses, as demonstrated in (Consolazio et al. 2008, 2009b). Recently, the elastic, perfectly-plastic crush model from Consolazio et al. (2009a) was used to develop simplified equivalent static loading conditions for barge collision analysis of bridges (Consolazio et al. 2009b). The updated crush-curve model proposed here (Fig. 9.15) can be directly incorporated into the equivalent static method to update static impact force predictions.

9.6 Conclusions

In this chapter, a previously developed barge bow force-deformation model—which was based on the assumption of perfectly head-on (non-oblique) impact—has been modified to probabilistically account for reductions in force levels expected when impact occurs at oblique angles with flat-faced pier surfaces. For this task, a parametric study of high-resolution finite element simulations has been conducted, consisting of crushing a jumbo hopper barge bow model with different sized flat-faced pier surfaces at various oblique angles. Using forces predicted by these simulations, empirical expressions have been developed that relate peak crush force to angle of obliquity. These expressions are utilized in a series of Monte Carlo simulations (probabilistic study) for the purpose of developing more realistic predictions of barge impact forces that take into account the probability of barge impact occurring at particular angles. Newly derived expressions predict smaller barge crush forces than those predicted by the previously-developed model, particularly for wide surfaces such as waterline pile caps, for which forces are approximately 10 – 45% lower. Lastly, the new expressions have been integrated into an overall barge bow force-deformation framework, resulting in a design-oriented crush model for use in deterministic barge impact analysis of bridges.

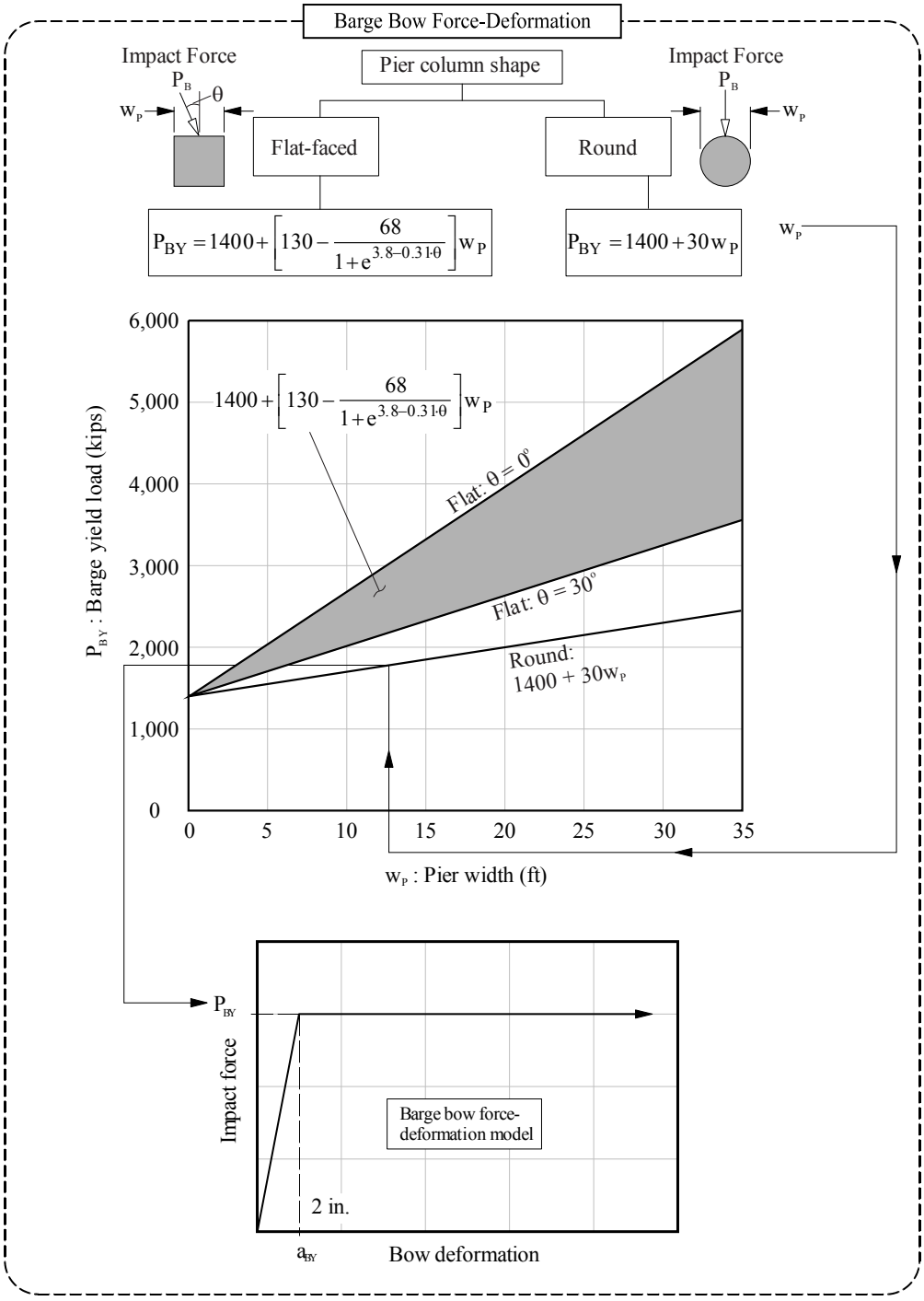

Figure 9.15 Updated barge bow force-deformation model

CHAPTER 10
CONCLUSIONS AND RECOMMENDATIONS

10.1 Summary

Bridges that span navigable waterways are subject to potential extreme event loading through vessel-bridge collision. In the event of a collision, dynamic lateral forces transmitted to the impacted bridge structure can result in the development of significant inertial forces that, in turn, produce amplified structural demands. Collision events can, therefore, lead to severe structural damage and even catastrophic failure of the impacted bridge. Collapses of U.S. bridges spanning navigable waterways prompted the American Association of State Highway and Transportation Officials (AASHTO) to develop provisions for bridge design against waterway vessel collision. The AASHTO provisions consist of prescriptive procedures that are intended to minimize bridge susceptibility to catastrophic collapse. As part of the AASHTO design procedure, the risk of collapse (i.e., structural failure) associated with waterway vessel collision is assessed. Bridge collapse risk is expressed as an annual frequency of collapse, which is the product of several terms, including several conditional probability factors.

Among these factors is the probability of collapse, which is the probability that a bridge structural component will fail in the event that the bridge is struck by an aberrant vessel. The AASHTO probability of collapse term is investigated in the current study for collisions between barges and bridges. Probability of collapse values for bridge piers subject to barge collision are currently determined using an empirical expression that relates bridge capacity and demand to collapse probability. A literature review has revealed three key limitations associated with use of the current AASHTO probability of collapse expression:

- The expression is based on a study of ship-ship collisions. Therefore, the expression may not be applicable to vessel-bridge collisions. Furthermore, the structural configurations of ships and barges differ substantially, and so, the applicability to barge-bridge collisions is additionally conspicuous.

- The expression relies on input capacity and demand parameters from a static analysis framework. However, recent experimental and analytical studies have demonstrated that vessel-bridge collisions are fundamentally dynamic events, and that accurate risk analysis requires incorporation of dynamic amplification effects into the bridge design process.

- Expression input consists of capacity-demand ratios (as opposed to demand-capacity ratios), which can lead to instances where, even though the structural demand is substantially larger than the bridge capacity, the corresponding probability of collapse value is conspicuously small.

Given these limitations, a literature review has been conducted in which studies were identified that focus on the improvement of, or the development of alternative frameworks to, the

probability of collapse determination procedure given in the AASHTO provisions. The literature review revealed that previous studies aimed at quantifying bridge collapse (structural failure) rates have largely focused on the assessment of bridge collapse on a case-by-case basis, or alternatively, the development of probabilistic frameworks that are entirely independent of the existing AASHTO provisions. In contrast, the approach taken in the current study has consisted of working within the existing AASHTO provisions to produce revised (improved) probability of collapse expressions, which can feasibly be implemented in existing bridge design provisions.

10.2 Concluding Remarks

A literature review has been conducted in which probabilistic descriptions for a multitude of random variables related to barge and bridge structures (including pertinent structural limit state parameters) have been identified. In the current study, random variable descriptions (taken from the literature and various government agencies) are combined with recently developed bridge modeling and barge-bridge collision analysis techniques that facilitate rapid assessment of nonlinear dynamic barge impact force and bridge response. The structural (finite element) analysis techniques selected for use have been verified (or validated, as appropriate) to be capable of accurately predicting collision-induced bridge structural responses (internal forces). Using the recently developed collision analysis tools in conjunction with probabilistic descriptions of barge, bridge load, and bridge resistance, a simulation-based probabilistic framework has been developed that is capable of producing probability of collapse (structural failure) estimates for bridge structures and limit states of interest.

Since, in the current study, bridge structural response to barge collision is quantified through use of nonlinear dynamic finite element analysis, a single simulation can require several minutes of computation time. Consequently, simulation-based probabilistic assessment of bridge structural demand parameters can become impractical in many cases (due to excessive computation time requirements), where failure probabilities are typically small. In particular, use of the standard Monte Carlo approach in probabilistic simulation can potentially require millions of simulations to form a reliable failure estimate. Therefore, highly efficient probabilistic simulation techniques documented in the literature have been selected and adapted for use in barge-bridge collision simulations to facilitate the practical obtainment of meaningful small failure probability estimates. The advanced probabilistic simulation techniques have been verified to produce comparable failure rate estimates relative to the standard Monte Carlo approach, and simultaneously, shown to result in substantial gains in computational efficiency for bridge failure rate estimation.

An inventory of previously developed bridge finite element models, corresponding to bridges from around the state of Florida, has been used in the probabilistic assessments of barge-bridge collision, where the individual bridges in the inventory constitute a representative cross-section of Florida bridges that are currently in service. Furthermore, three additional, strengthened bridge cases have been formed for the current study, where the pier structural members have been modified (strengthened) to resist dynamically amplified internal forces that can arise during collision events. These three latter cases have been developed specifically to

represent potential future bridge infrastructure, where dynamic collision phenomena are incorporated into bridge design for waterway vessel collision. The efficacy of combining analytical techniques with probabilistic descriptions of the selected finite element bridge models has made feasible the task of assessing the probability of collapse for a representative set of bridges.

For each bridge case, estimates of limit state exceedance rates have been estimated from probabilistic simulation results, where limit states defined in the existing, applicable Florida and AASHTO design codes have been considered. Namely, four limit states have been considered:

- The bearing capacity of foundation members cannot be exceeded;
- The capacity of load transfer devices at the substructure-superstructure interface cannot be exceeded;
- The superstructure cannot collapse; and,
- As a series limit state, none of the above three limit states can occur (i.e., the above three limit states have been considered simultaneously).

Structural reliability parameters quantified as part of assessing collapse rates (i.e.., limit state exceedance rates) for the ten bridge cases have, in turn, been used to form improved PC expressions. Specifically, for each bridge case, expected values of the proximity to failure—expressed as demand-capacity ratios—have been quantified in addition to estimates of the limit state exceedance rates. Using these parameters, regression curves have been formed that, for a given limit state, relate demand-capacity (D/C) to probability of collapse (PC). Furthermore, variability in the estimated, constituent limit state exceedance rates has been conservatively built into the regression expressions. These regression curves constitute improved probability of collapse expressions, and newly developed expressions have been proposed for bridges subject to Florida design provisions, as well for bridges designed using national design provisions. Significant discrepancies between probability of collapse estimates obtained using the proposed PC expressions and those obtained using current bridge design provisions suggest the need to incorporate the improved probability of collapse expressions in the overall bridge risk assessment for waterway vessel collision.

10.3 Recommendations for Bridge Design

The primary objective of this study has been the development of improved probability of collapse (structural failure) expressions for bridges subject to barge impact. Correspondingly, the following bridge design recommendations are made:

- It is recommended that, for bridge designers constrained to satisfy the three limit states defined in the Florida design provisions, the probability of collapse expression formed with consideration of all limit states taken in series be employed in bridge design for barge collision; and,

- It is recommended that, for bridge designers constrained to satisfy only the superstructure collapse limit state identified in the AASHTO design previsions, the probability of collapse expression formed with consideration of the superstructure collapse limit state be employed in bridge design for barge collision.

A secondary objective of this study has been the development of design-oriented force deformation relationships for use in barge-bridge collision analysis. Such relationships, in large part, dictate impact force magnitudes predicted as part of bridge design. Thus, the following bridge design recommendation is made:

- It is recommended that the revised barge force-deformation model presented in Chapter 9 of this report be used as a means of quantifying forces associated with barge collisions with bridges. Force-deformation relationships formed in accordance with this procedure should be used directly in dynamic bridge analysis or as a basis for estimating static loads in dynamically equivalent static analysis.

10.4 Future Research Recommendations

The following items warrant additional consideration as part of future research efforts:

- Strictly speaking, probability of collapse expressions developed in the current study are specific to structural configurations, soil conditions, and vessel traffic characteristics local to Florida. Although the newly developed expressions constitute substantial improvements over the existing AASHTO probability of collapse expression, the incorporation of structural reliability parameter estimates from additional (nationally distributed) bridge cases into the proposed regression curves could provide additional points for further improvement to the proposed expressions. Upon collection of a sufficiently large number of additional regression points, potentially unwarranted conservatism and forecasting (i.e., the extrapolation of regression curves into regions that not well populated by existing data) that are present in the as-proposed regression curves would be minimized.

- The probability of collapse expressions developed in the current study are only applicable for barge-bridge collision; however, reliability estimates for ship-bridge collision are, in addition to that of barge-bridge collision, integral to bridge design for waterway vessel collision. Using the concepts and tools developed in the current study, improved

probability of collapse expressions pertaining to ship-bridge collision could be formed if given that a catalog of physical ship characteristics were available.

- Probabilistic treatment of impact load, as implemented in the current study, incorporates many factors (e.g., relative barge-bridge orientation, barge impact velocity, barge impact weight). Furthermore, while unique barge force-deformation relationships are formed and employed for each barge-bridge collision scenario that is analyzed, variability in the stiffness of the barge force-deformation curves is not directly considered. Instead, due to a lack of available data, ordinates of all barge force-deformation curves employed are scaled to conservatively account for variations in barge plate material strength and thickness (using a procedure documented in an earlier FDOT research study). The effect of probabilistically varying plate thicknesses and material strengths for common barge configurations should be investigated to determine if such variability should be incorporated into the probabilistic treatment of impact load.

- As part of the probabilistic framework proposed in this study, barge flotillas are modeled as single degree-of-freedom systems in association with use of coupled vessel impact analysis (CVIA). Consequently, interactions between barges within a given flotilla are not incorporated into the analytical framework. Additionally, modeling of barge flotillas as single-degree-of-freedom systems precludes the incorporation of eccentric barge rotational motion, which can occur in certain impact scenarios. Incorporation of these phenomena will produce changes in the resultant impact force direction and magnitude, through time, for a given impact scenario. Therefore, refinements to the CVIA technique may be warranted for applications in which a variety of impact scenarios are considered.

- Modeling of soil resistance in the current study is based on a statistically independent treatment of through-depth soil strength parameters. Studies are currently being conducted, independently by geotechnical researchers, where soil-spatial variability is incorporated into structural reliability estimates of embedded pile and drilled shaft foundation members. Further refinements to probability of bridge collapse estimates could be made upon combined use of the probabilistic framework proposed in the current study and the inclusion of soil-spatial variability in the soil resistance modeling.

REFERENCES

AASHTO. (2009). *Guide specification and commentary for vessel collision design of highway bridges*, 2nd Edition, Washington D.C.

AASHTO. (1991). *Guide specification and commentary for vessel collision design of highway bridges*, 1st Edition, Washington D.C.

AASHTO. (2010). *LRFD bridge design specifications 5th Edition*, Washington D.C.

AASHTO. (2007). *LRFD bridge design specifications 4th Edition*, Washington D.C.

ACI. (2005) *Building code requirements for structural concrete (ACI 318-05)*, Farmington Hills, Mich.

Ang, A. H.-S., and Tang, W. H. (2007). *Probability concepts in engineering, 2nd Ed.*, Wiley, New York, N.Y.

Au, S. K, Ching, S., and Beck, J. L. (2007). "Application of subset simulation methods to reliability benchmark problems." *Structural Safety*, 29(3), 183–193.

Au, S. K., and Beck, J. L. (2007). "Estimation of small failure probabilities in high dimensions by subset simulation." *Probabilistic Engineering Mechanics*, 16(4), 263–277.

Barker, R. M., Duncan, J. M., Rojiani, K. B., Ooi, P., Tan, C. K., and Kim, S. G. (1991). "Manuals for the design of bridge foundations." *Rep. 343*, National Cooperative Highway Research Program, Transportation Research Board, Washington D.C.

Cameron, J., Nadcau, J., and LoSciuto, J. (1997). *Ultimate strength analysis of inland tank barges*. USGC Marine Safety Center, Washington, D.C.

Consolazio, G. R., Davidson, M. T., and Getter, D. J. (2010). "Development and support of dynamic numerical modeling of aberrant rake barges impacting hurricane protection structures subjected to forces from a hurricane environment." *Structures Research Report*, (in press), Engineering and Industrial Experiment Station, University of Florida, Gainesville, Fla.

Consolazio, G. R., Davidson, M. T., and Cowan, D. R. (2009a). "Barge bow force-deformation relationships for barge-bridge collision analysis," *Transportation Research Record. 2131*, Transportation Research Board, Washington, D.C., 3–14.

Consolazio, G. R., Getter, D. J., and Davidson, M. T. (2009b). "A static analysis method for barge-impact design of bridges with consideration of dynamic amplification." *Structures Progress Report No. 68901,* Engineering and Industrial Experiment Station, University of Florida, Gainesville, Fla., November.

Consolazio, G. R., and Davidson, M. T. (2008). "Simplified dynamic barge collision analysis for bridge design." *Transportation Research Record*. *2050*, Transportation Research Board, Washington, D.C., 13–25.

Consolazio, G. R., McVay, M. C., Cowan, D. R., Davidson, M. T., and Getter, D. J. (2008). "Development of improved bridge design provisions for barge impact loading." *Structures Research Report No. 51117*, Engineering and Industrial Experiment Station, University of Florida, Gainesville, Fla., April.

Consolazio, G. R., Cook, R. A., McVay, M. C., Cowan, D. R., Biggs, A. E., and Bui, L. (2006). "Barge impact testing of the St. George Island Causeway Bridge Phase III: Physical testing and data interpretation." *Structures Research Report No. 26868*, Engineering and Industrial Experiment Station, University of Florida, Gainesville, Fla., March.

Consolazio, G. R., and Cowan, D. R. (2005). "Numerically efficient dynamic analysis of barge collisions with bridge piers." *Journal of Structural Engineering*, 131(8), 1256–1266.

Consolazio, G. R., and Cowan, D. R. (2003). "Nonlinear analysis of barge crush behavior and its relationship to impact resistant bridge design." *Computers and Structures*, 81(8–11), 547–557.

COWIconsult, Rådgivende Ingeniører A/S. (1987). *General principles for risk evaluation of ship collisions, strandings, and contact incidents*, Unpublished technical note, Denmark.

Davidson, M. T., and Consolazio, G. R. (2008). "Simplified dynamic head-on barge collision analysis for bridge design." *Proceedings, 25th International Bridge Conference*, Transportation Research Board, Pittsburgh, Penn.

Davidson, M. T., Consolazio, G. R., and Getter, D. (2010). "Dynamic amplification of pier column internal forces due to barge-bridge collision." *Transportation Research Record*. Transportation Research Board, Washington, D.C., (in press).

Davidson, M. T. (2007). "Simplified dynamic barge collision analysis for bridge pier design." Masters' thesis, Dept. of Civil and Coastal Engineering, University of Florida, Gainesville, Fla.

FB-Deep User's Manual. (2010). Florida Bridge Software Institute (BSI), University of Florida, Gainesville, Fla.

FB-MultiPier User's Manual. (2009). BSI, University of Florida, Gainesville, Fla.

Florida Department of Transportation (FDOT). (2009). *Structures Design Guidelines*, Tallahassee, Fla.

Fujii, Y., and Shiobara, R. (1978). "The estimation of losses resulting from marine accidents." *Journal of Navigation*, 31, 117–125.

Freedman, D., and Diaconis, P. (1981). "On the histogram as a density estimator: L2 theory." *Probability Theory and Related Fields*, 57(4), 453–476.

Ghosn, M., Moses, F., and Wang, J. (2003). "Design of highway bridges for extreme events." *Report 489*, National Cooperative Highway Research Program, Transportation Research Board, Washington D.C.

Geng, B., Wang, H., and Wang, J. (2009). "Probabilistic model for vessel-bridge collisions in the Three Gorges Reservoir." *Frontiers of Architecture and Civil Engineering in China*, 3(3), 279–285.

Gluver, H., and Olsen, D. (1998). "Current practice in risk analysis of ship collisions to bridges." *Ship collision analysis*, H. Gluver and D. Olsen, eds., Balkema, Rotterdam, 85–96.

Haldar, A., and Mahadevan, S. (2000). *Reliability assessment using stochastic finite element analysis*, Wiley, New York.

Jacobs, S. A. (2003). "Insitu measurement of Florida limestone modulus and strength properties." Masters' Thesis, Dept. of Civil and Coastal Engineering, University of Florida, Gainesville, Fla.

Joint Committee on Structural Safety (JCSS). (2006). *Probabilistic model code*, ISBN 978-3-909386-79-6, Zürich, Switzerland.

Johnson, P. A. (1995). "Comparison of pier scour equations using field data." *Journal of Hydraulic Engineering*, 121(8), 626–629.

Knott, M., and Prucz, Z. (2000). "Vessel collision design of bridges." *Bridge Engineering Handbook*, W.-F. Chen and L. Duan, eds., CRC Press, Boca Raton, Fla., 60.1–60.9.

Kunz, C. U. (1998). "Ship bridge collision in river traffic, analysis and design practice." *Ship collision analysis*, H. Gluver and D. Olsen, eds., Balkema, Rotterdam, 13–22.

Larsen, O. D. (1993). "Ship collision with bridges: The interaction between vessel traffic and bridge structures." *IABSE Structural Engineering Document 4*, IASBE-AIPCIVBH, Zurich, Switzerland.

Liu, C., and Wang, T. (2001). "Statewide vessel collision design for bridges." *Journal of Bridge Engineering*, 6(3), 213–219.

LSTC. (2009). *LS-DYNA keyword user's manual*, Livermore Software Technology Corporation, Livermore, Calif.

MacGregor, J. G., and Wight, J. K. (2005). *Reinforced concrete: Mechanics and design*, 4th Ed., Pearson Prentice Hall, Upper Saddle River, N.J.

Manuel, L., Kallivokas, L., Williamson, E., Bomba, M., Berlin, K., Cryer, A., and Henderson, W. (2006). "A probabilistic analysis of the frequency of bridge collapses due to vessel impact." *Center for Transportation Research Technical Report No. 0-4650-1*, University of Texas at Austin, Austin, Texas, November.

Mathworks Inc. The (2005). *MATLAB 7 Full product family help manual*, The Mathworks Inc., Natick, Mass.

McKay, M. D., Beckman, R. J., and Conover, W. J. (1979). "A comparison of three methods of selecting values of input variables in the analysis of output from a computer code." *Technometrics,* 21(2), 239–245.

McVay, M. C., Wasman, S. J., and Bullock, P. J. (2005). "St. George geotechnical investigation of vessel pier impact." *Geotechnical Research Report No. 4910-4554-016-12*. Engineering and Industrial Experiment Station, University of Florida, Gainesville, Fla.

McVay, M. C., Ellis, R. D., Kim, M., Villegas, J., Kim, S., Lee, S. (2003). "Static and dynamic field testing of drilled shafts: Suggested guidelines on their use for FDOT structures." *Geotechnical Research Report No. 4910-4504-725-12*. Engineering and Industrial Experiment Station, University of Florida, Gainesville, Fla., October.

Meier-Dörnberg, K. E. (1983). "Ship collisions, safety zones, and loading assumptions for structures in inland waterways." *Verein Deutscher Ingenieure (Association of German Engineers) Report No. 496*, 1–9.

Melchers, R. E. (1999). *Structural reliability analysis and prediction*, 2nd Ed., Wiley, New York.

National Transportation Safety Board (NTSB). (1981). "Ramming of the Sunshine Skyway Bridge by the Liberian Bulk Carrier Summit Venture, Tampa Bay, Florida, May 9, 1980." *NTSB Marine Accident Report No. MAR-81/03*, National Transportation Safety Board, Washington D.C.

National Transportation Safety Board (NTSB). (2002). "U.S. towboat Robert Y. Love allision with Interstate 40 Highway Bridge near Webbers Falls, Oklahoma." *NTSB Highway/Marine Accident Report No. HAR-04/05*, National Transportation Safety Board, Washington D.C.

National Oceanic and Atmospheric Administration (NOAA), "NOAA tides and currents." <tidesandcurrents.noaa.gov> (May 17, 2010).

Nowak, A. S., and Collins, K. (2000). *Reliability of structures*, McGraw-Hill, New York.

Pearson, E. S., and Hartley, H. O. (1958). *Biometrika tables for statisticians*, Cambridge University Press, Cambridge, U.K.

Podolny, W., Jr., and Muller, J. M. (1982). *Construction and design of prestressed concrete segmental bridges*, Wiley, New York.

Precast/Prestressed Concrete Institute (PCI). (1999). *PCI design handbook*, 5th Ed., PCI, Chicago, Ill.

Proske, D., and van Gelder, P. (2009). *Safety of historical arch bridges, Springer-Verlag, Berlin, Germany.*

Proske, D., and Curbach, M. (2005). "Risk to historical bridges to ship impact on German inland waterways." *Reliability Engineering & System Safety,* 90, 261–270.

Ross, S. (2009). *Probability and statistics for engineers and scientists*, 4th Ed., Elsevier Academic Press, London, U.K.

Shapiro, S. S., and Wilk, M. B. (1965). "An analysis of variance test for normality (complete samples)." *Biometrika*, 52(3-4), 591–611.

United Stated Coast Guard (USCG). (2005). "Investigation Report into the Circumstances Surrounding the Allision Between the Barge Tow of the M/V Brown Water V and the Queen Isabella Causeway Bridge, Texas, on 15 September 2001, Resulting in Multiple Loss of Life." *USCG Investigative Report Case Number 1482244*, United states Coast Guard, Washington D.C.

Wang, T. L., and Liu, C. (1999). "Synthesizing commercial shipping (barge/tug trains) from available data for vessel collision design." *HPR Study No. 0510841*, Florida International University, Miami, Fla.

Wilson, J. (2003). *Allison involving the M/V Brownwater V and the Queen Isabella Causeway Bridge*, United States Coast Guard, Washington, D.C.

Yuan, P., Harik, I. E., and Davidson, M. T. (2008). "Multi-barge flotilla impact forces on bridges." *Kentucky Transportation Center Research Report No. KTC-05/SPR261-03-1F*, University of Kentucky, Lexington, Ky.

APPENDIX A
STRUCTURAL CONFIGURATION CHANGES FOR STRENGTHENED BRIDGE CASES

A.1 Introduction

A previously developed bridge inventory, consisting of seventeen bridge pier finite element (FE) models for bridges located throughout Florida (Consolazio et al. 2008), was used to form ten cases that, in turn, were investigated in the current study. Seven of the ten bridges were selected to represent existing (or in-service) Florida bridge infrastructure. However, the seven in-service bridge piers that were selected to represent existing Florida infrastructure were either designed using a *static* collision-load approach, or not directly designed to resist vessel-bridge collision loading. From these seven bridge cases, three additional bridge cases were formed to represent future Florida bridge infrastructure, where design for *dynamic* barge-bridge collision forces are taken into account. To facilitate the development of the three additional bridge cases, a bridge pier strengthening procedure has been developed to incorporate additional structural resistance such that the modified bridge structure can appropriately resist dynamically amplified, collision-induced internal forces. The strengthening procedure and the structural configuration modifications for one of the three strengthened bridge cases (Pier 53 of the New St. George Island Bridge) are detailed in Chapter 4. The structural configuration changes associated with the other two bridge cases (listed in Table A.1) are presented in this appendix.

Table A.1 Bridge pier case descriptions

Bridge name	Pier name	Pier location	AASHTO static impact force (kips)
SR-20 at Blountstown	Pier 58	Adjacent to channel	2550
Gandy Bridge	Pier 75W	Adjacent to channel	2400

Although the strengthening process is intended to primarily increase flexural capacity of the pier pile (or drilled shaft) and column structural members, additional design-based calculations are incorporated into the strengthening process. Specifically, strengthened cross-sections are verified to satisfy reinforcement limits (where minimum and maximum reinforcement ratios are given in ACI 2005 as 1% and 8% of the total cross section area, respectively). Also, for all modified cross-sections, the corresponding shear capacities (determined using Sec. 5.8.3.3 of the AASHTO 2007 LRFD code) are verified to be greater than maximum shear forces predicted by the corresponding dynamic analyses.

A.2 SR-20 at Blountstown Pier 58

The Pier 58 bridge model, which was developed based on structural plans, is shown in Fig. A.1. The channel pier (pier 58) underlies a continuous steel plate girder and reinforced concrete slab superstructure. Load transfer devices at the substructure-superstructure interface are evenly spaced along the Pier 58 pier cap beam centerline, where each load transfer device consists of a 3 in. thick steel bearing bevel plate that overlies an elastomeric bearing pad. Four end-threaded, cast-in-place anchor bolts pass through each bearing bevel plate and into the pier

cap beam. The channel pier structure consists of two round (5.5 ft diameter, 37 ft tall) reinforced concrete pier columns spaced 30 ft apart. The pier columns are axially collinear with two 9 ft diameter drilled shafts. The pier columns and drilled shafts are integrated with a 30.5 ft tall reinforced concrete shear wall.

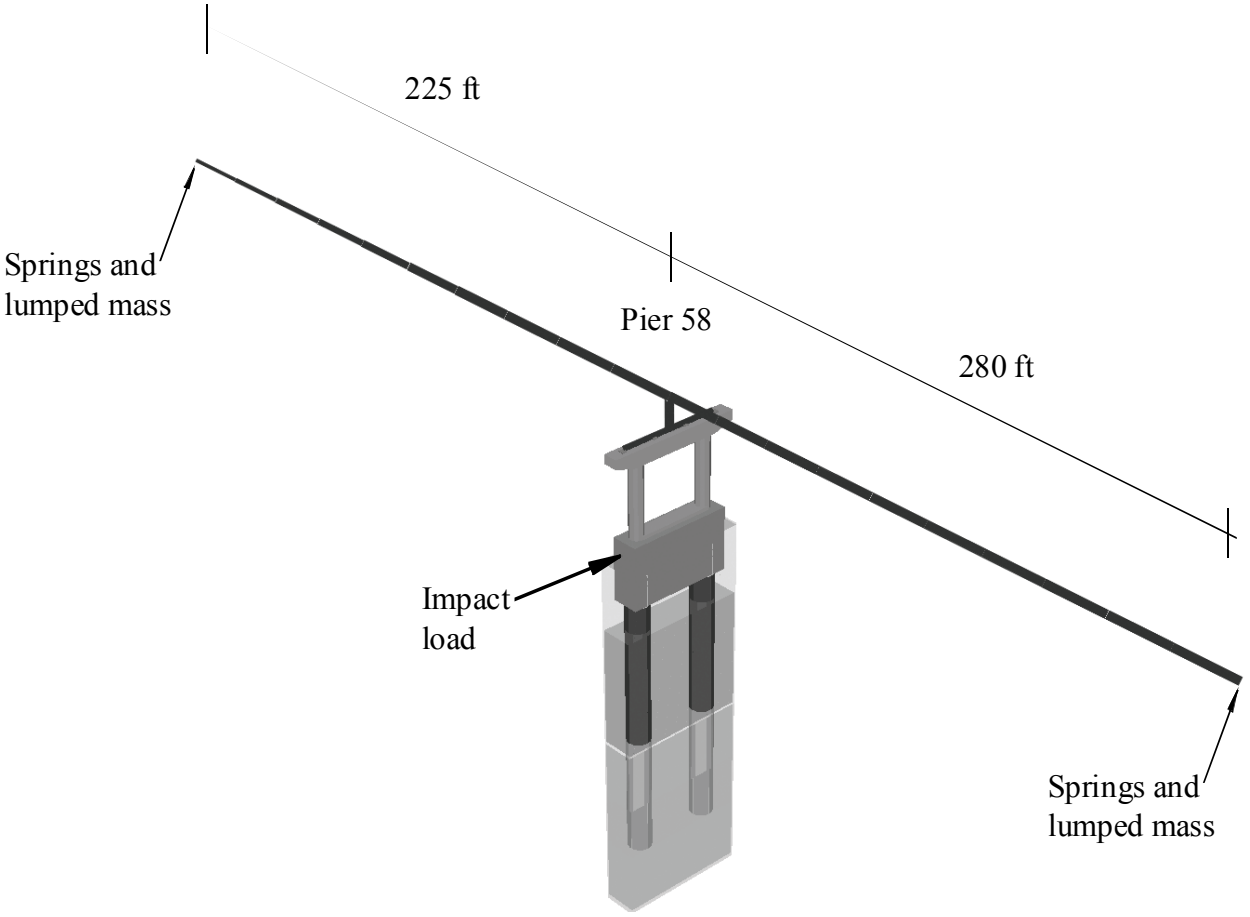

Figure A.1 SR 20 at Blountstown, Pier 58 FE model

Original and modified pier member cross-section layouts pertaining to the Pier 58 case are shown in Figs. A.2–A.3. Specific to the 108 in. reinforced concrete drilled shaft members from the original model (Fig. A.2a), results from an AASHTO static analysis (with a 2550 kip head-on static load) indicate that the maximum load-moment force pair occurs near the shaft-soil interface, where the moment (flexural) demand magnitude is 17310 kip-ft (Fig. A.2b). The corresponding capacity (at the same axial load level) is 32380 kip-ft, and therefore, the static D/C value for the drilled shafts is 0.53.

In addition to the AASHTO static analysis of the original Pier 58 structural configuration, a dynamic (CVIA) collision analysis has been carried out for Pier 58 using the strengthened structural configuration (pier column and substructure-superstructure modifications are discussed below). The initial barge impact conditions prescribed in the dynamic analysis correspond to a single column of three fully-loaded jumbo hopper barges and tow (weighing 5920 tons) traveling

at 5 knots. These conditions were determined as part of a previous study (Consolazio et al. 2008) to be representative for the waterway spanned by the SR-20 at Blountstown Bridge. Results from the dynamic analysis indicate that no strengthening is required for the drilled shafts. More specifically, the load-moment force pair obtained from the dynamic analysis results is such that the moment magnitude is 17340 kip-ft (Fig. A.2d) and the corresponding capacity (at the same axial load level) is 31760 kip-ft. Therefore, the dynamic drilled shaft D/C value is 0.55, which differs from the static drilled shaft D/C value by less than 5%.

Specific to the 66 in. diameter reinforced concrete pier columns from the original Pier 58 model (Fig. A.3a), AASHTO static analysis results are such that the maximum moment (flexural) demand and capacity values are 3290 kip-ft and 8820 kip-ft, respectively (Fig. A.3b). The pier column flexural demand and capacity values lead to a static D/C value of 0.37 for the pier columns. By supplying additional longitudinal reinforcement throughout the column (Fig. A.3c), comparable dynamic D/C levels (relative to the static D/C) are obtained from the dynamic analysis results. Specifically, the load-moment force pair obtained from the modified configuration dynamic analysis results contains a moment demand component with a magnitude of 4420 kip-ft (Fig. A.3d). The corresponding flexural capacity (at the same axial load level) is 12120 kip-ft, and furthermore, the column dynamic D/C value is 0.36, which is approximately equal (a percent difference of less than 5% is observed) to the column member static D/C.

Given the original and modified column cross-sections shown in Fig. A.3, the ratio of the modified to unmodified column capacities is 1.4. Accordingly, modifications were made to the structural configuration such that substructure-superstructure shear capacities for the Pier 58 case was increased by a factor of approximately 1.4. Given that the substructure-superstructure interface for the Pier 58 structural configuration contains four cast-in-place anchor bolts at each bearing location, shear capacities were determined using the ACI 2005 Appendix D provisions, which pertain to anchorage in structural concrete. Specifically, the substructure-superstructure shear capacity for the unmodified Pier 58 configuration has been determined (per bearing location) to be 450 kips and 130 kips for the transverse and longitudinal (relative to bridge span) directions, respectively. By increasing the pier cap beam width (in a span-longitudinal direction) to 7.25 ft wide (from 5.75 ft wide), the substructure-superstructure shear capacities increased to 630 kips and 190 kips (in the transverse and longitudinal directions, respectively).

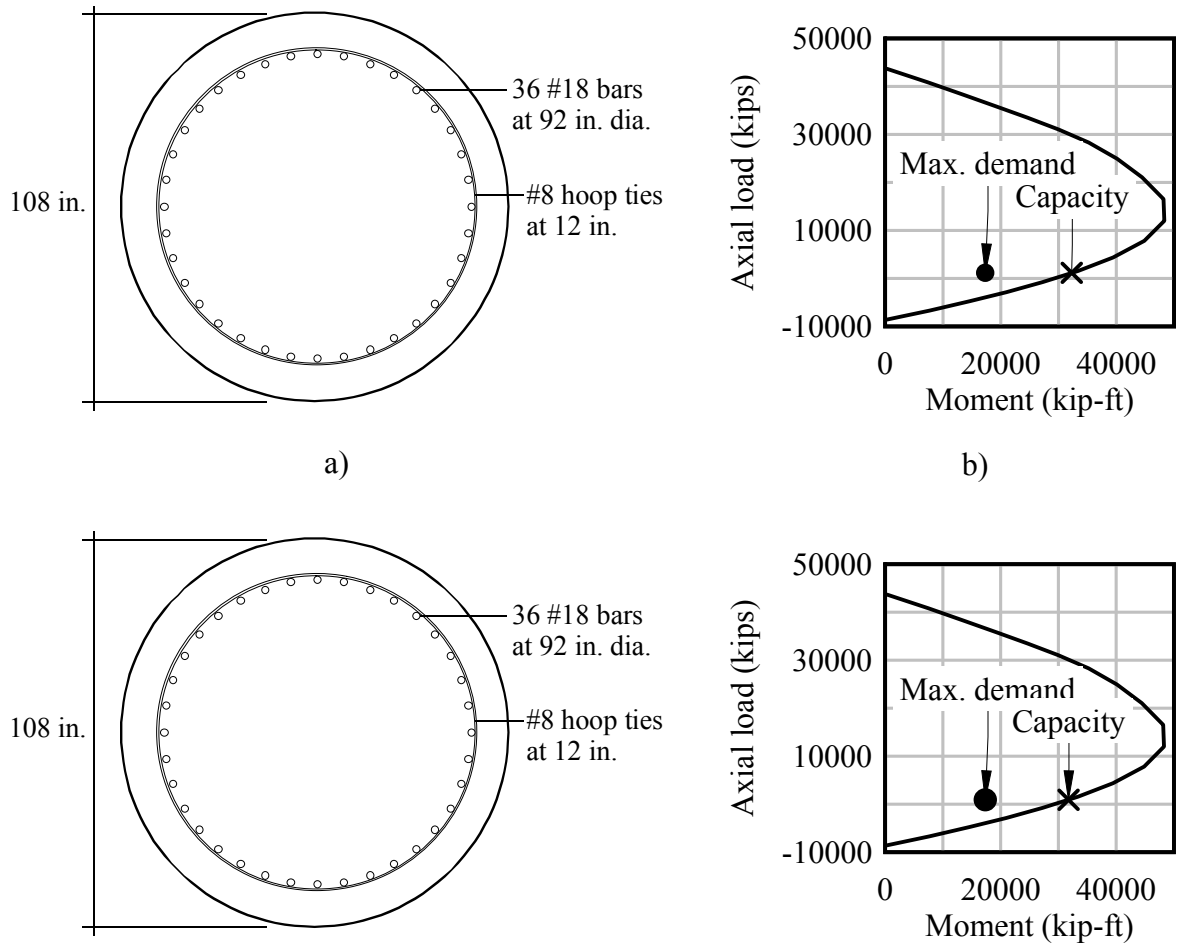

Figure A.2 Original versus strengthened drilled shaft cross-section summary for the SR-20 at Blountstown Pier 58 case. a) Original drilled shaft cross-section; b) Load-moment interaction for original cross-section in response to AASHTO static load; c) Strengthened drilled shaft cross-section; d) Load-moment interaction for strengthened cross-section in response to dynamic load

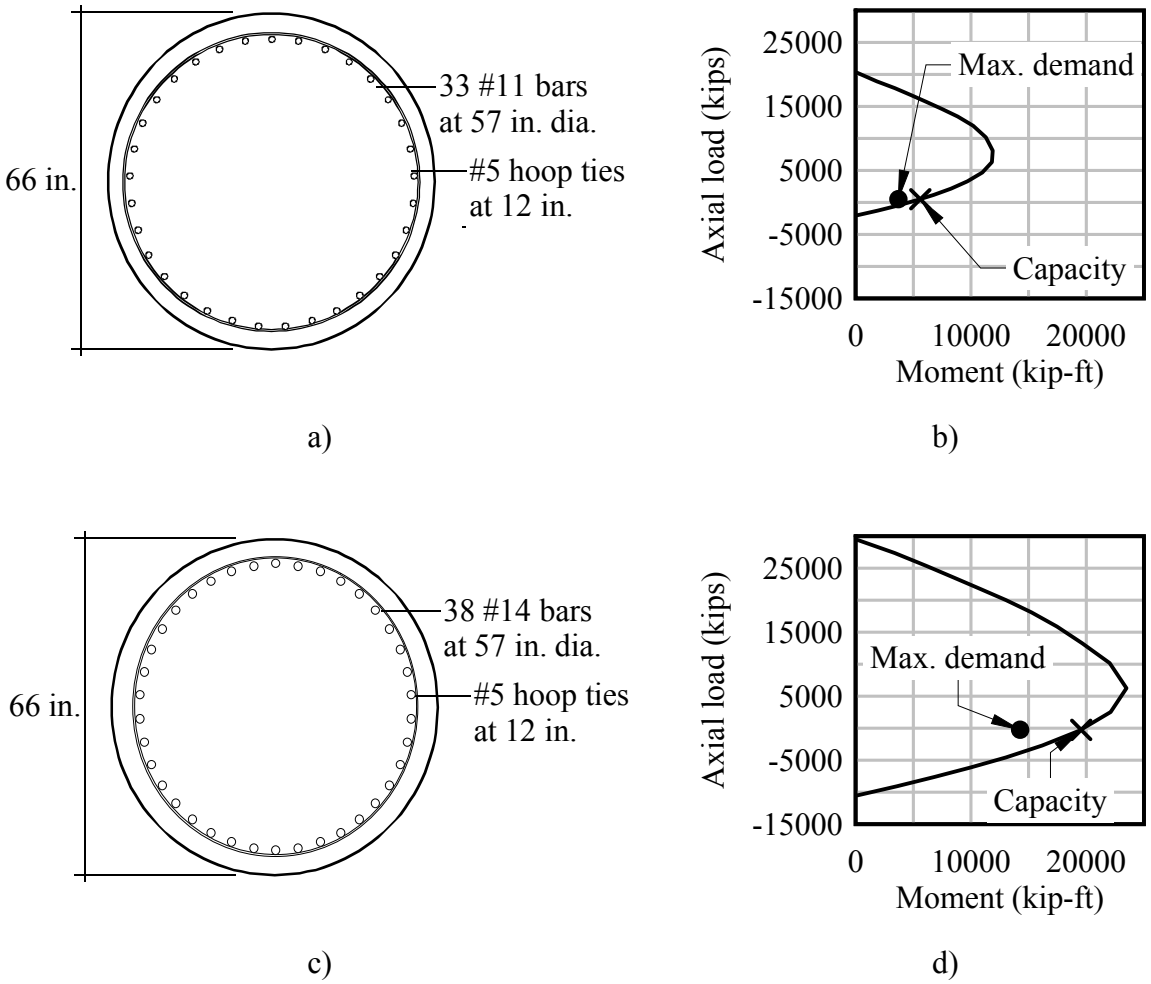

Figure A.3 Original versus strengthened column cross-section summary for the SR-20 at Blountstown Pier 58 case. a) Original column cross-section; b) Load-moment interaction for original cross-section in response to AASHTO static load; c) Strengthened column cross-section; d) Load-moment interaction for strengthened cross-section in response to dynamic load

A.3 Gandy Bridge Pier 75W

The FE model for the Gandy Bridge channel-adjacent pier, Pier 75W, was developed based on structural plans and is shown in Fig. A.4. Extending from Pier 75W are prestressed concrete girders that underlie a reinforced concrete slab. Load transfer between the superstructure and channel pier is facilitated by four evenly spaced bearing systems, which each consist of a 0.5 in thick steel bearing plate that overlies an elastomeric bearing pad. Four cast-in-place anchor bolts extend upward from the pier cap beam and through the bearing top plate. The tops of the anchor bolts are threaded and affixed with nuts to resist bearing uplift. The channel pier structure consists of a single rectangular (16 ft by 4.5 ft) pier column that extends 28 ft from the bottom of the pier cap beam to the top of a 9 ft thick footing vertically positioned at the waterline. Four 7 ft diameter drilled shafts extend from the footing to the underlying soil.

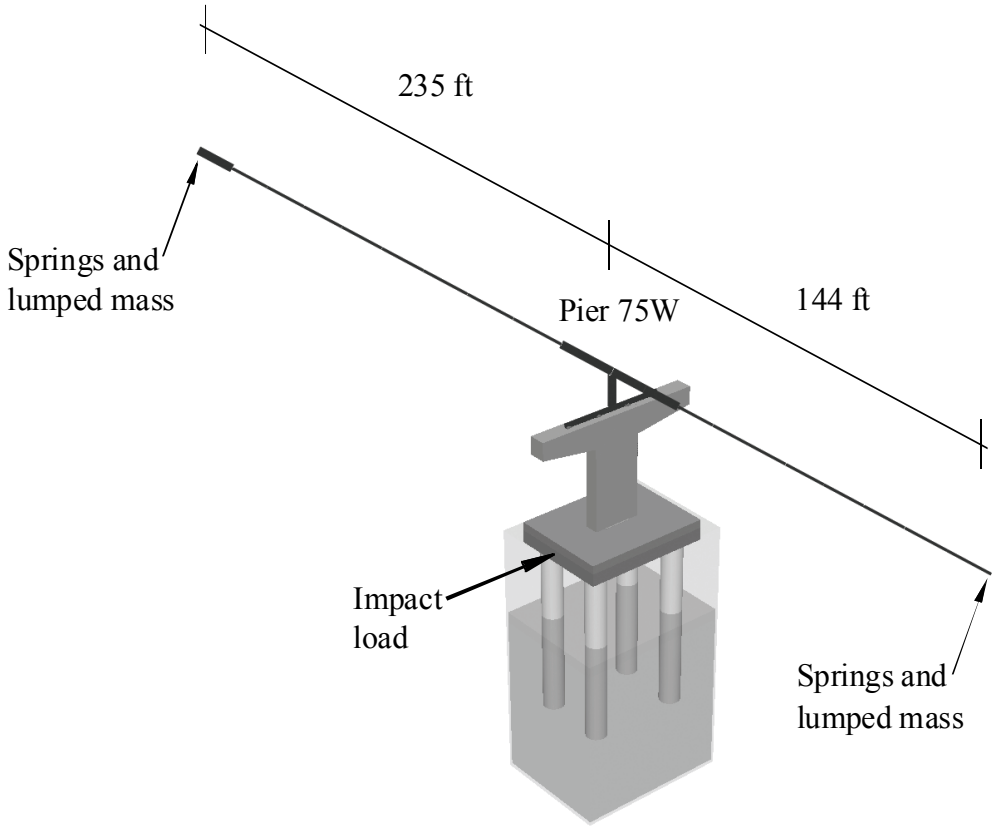

Figure A.4 Gandy Bridge, Pier 75W FE model

Original and strengthened pier member cross-section layouts relating to the Pier 75W case are shown in Figs. A.5–A.7. Results from an AASHTO static analysis (with a 2400 kip head-on static load) indicate that the 84 in. reinforced concrete drilled shaft members from the original model (Fig. A.5a) are subjected to a maximum load-moment force pair with moment (flexural) demand and capacity magnitudes of 9270 kip-ft and 20360 kip-ft, respectively (Fig. A.5b). The corresponding static D/C value for the drilled shafts is 0.46.

The addition of longitudinal reinforcement to the drilled shafts (Fig. A.5c) leads to comparable D/C levels (relative to the static D/C) when the modified structural configuration is subject to dynamic (CVIA) loading. The initial barge impact conditions prescribed in the dynamic analysis are identical to those used for the other strengthening cases, where the impact conditions were determined as part of a previous study (Consolazio et al. 2008) to be representative for bridges spanning navigable waterways in Florida. The load-moment force pair obtained from the dynamic analysis results is such that the moment magnitude is 29440 kip-ft (Fig. A.5d) and the corresponding capacity (at the same axial load level) is 53280 kip-ft. Therefore, the dynamic drilled shaft D/C value is 0.55 (as compared to a static D/C value of 0.46).

Specific to the 192 in. by 54 in. rectangular (reinforced concrete) pier columns from the original Pier 75W model (Fig. A.6a), AASHTO static analysis results are such that the maximum

moment (flexural) demand and capacity values are 11660 kip-ft and 70900 kip-ft, respectively (Fig. A.6b). The pier column flexural demand and capacity values lead to a static D/C value of 0.16 for the pier columns. By both increasing the column concrete compressive strength to 6 ksi (from 5.5 ksi) and supplying additional longitudinal reinforcement throughout the column (Fig. A.6c), comparable dynamic D/C values (relative to the static D/C values) are obtained from the dynamic analysis results. Specifically, the load-moment force pair obtained from the dynamic analysis results contains a moment demand component with a magnitude of 46660 kip-ft (Fig. A.6d). The corresponding flexural capacity (at the same axial load level) is 256420 kip-ft, and furthermore, the dynamic column D/C value is 0.18, which agrees well with the static column D/C value (a 10% difference is observed).

Given the original and modified column cross-sections shown in Fig. A.6, the ratio of the strengthened to original column capacities is 3.6. Using this ratio, modifications were made to the structural configuration (Fig. A.7) such that the substructure-superstructure shear capacity for the Pier 75W case was increased by the approximately same factor. Given that the substructure-superstructure interface for the Pier 75W structural configuration contains cast-in-place anchor bolts to transfer load between the substructure and superstructure, bearing load transfer (shear) capacities were determined using the ACI 2005 Appendix D provisions, which pertain to anchorage in structural concrete. Specifically, the substructure-superstructure shear capacities for the unmodified Pier 75W configuration are 410 kips and 160 kips for the transverse and longitudinal (relative to bridge span) directions, respectively.

At the time of formation of the Pier 75W strengthening case, preliminary probabilistic simulation results pertaining to the unmodified model were available (probabilistic simulation results for each case are presented in Chapter 8). An examination of the bearing shear reactions obtained from the probabilistic simulations revealed that bearing forces in the span-longitudinal direction were much more likely to reach respective bearing capacities relative to those bearing forces (and capacities) in the span-transverse direction. Consequently, modifications made to the Pier 75W substructure-superstructure interface were primarily focused on increasing bearing shear capacity in the span-longitudinal direction. Specifically, by increasing the anchor bolt diameters to 4 in. (from 2 in.); increasing the pier cap beam plan dimensions to 6.5 ft wide by 50 ft long (from 5.5 ft wide by 40 ft long); and, increasing the pier cap beam concrete compressive strength to 6 ksi (from 5.5 ksi), the substructure-superstructure shear capacity in the span-longitudinal direction correspondingly increased to 550 kips.

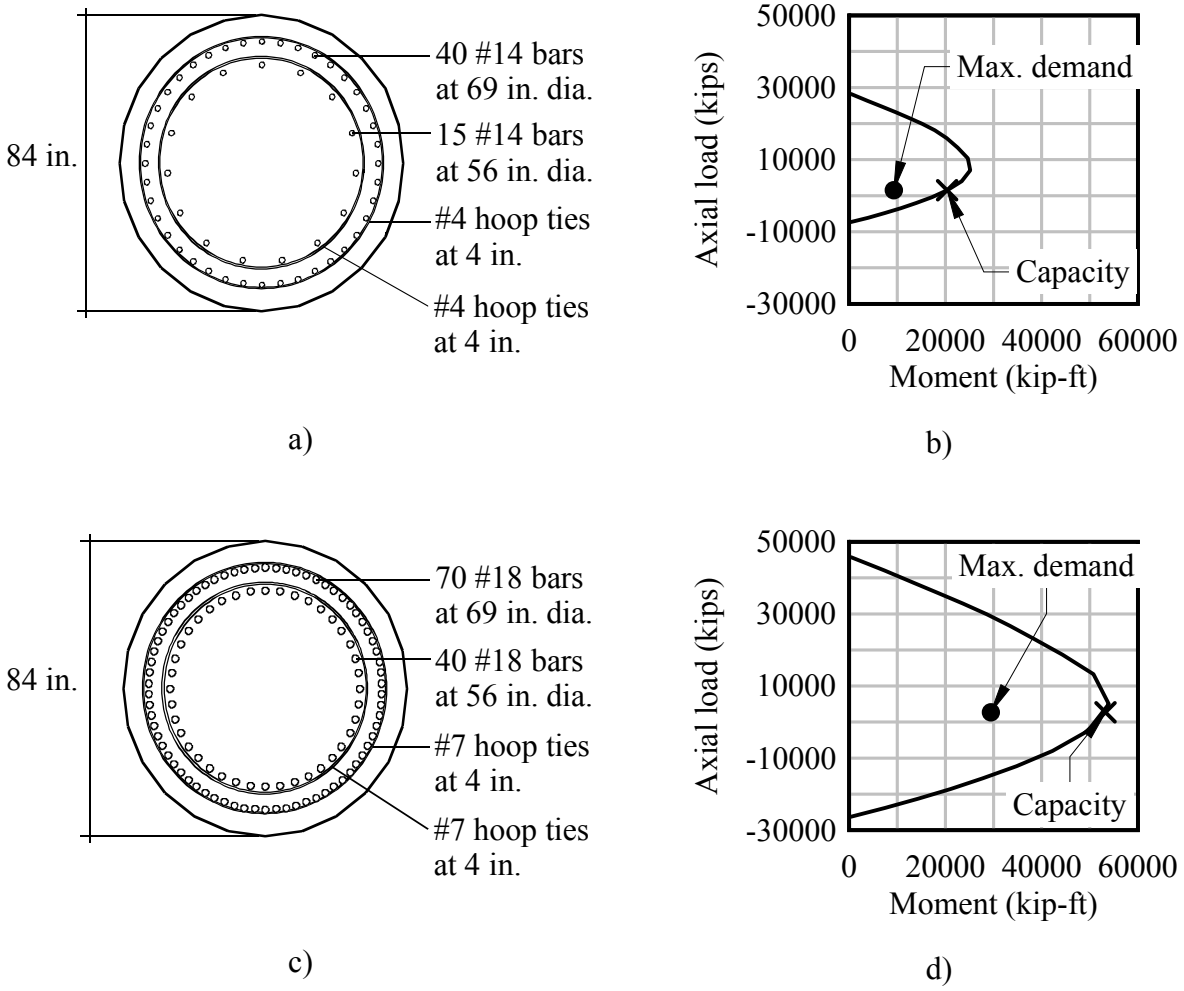

Figure A.5 Original versus strengthened drilled shaft cross-section summary for the Gandy Bridge Pier 75W case. a) Original drilled shaft cross-section; b) Load-moment interaction for original cross-section in response to AASHTO static load; c) Strengthened drilled shaft cross-section; d) Load-moment interaction for strengthened cross-section in response to dynamic load

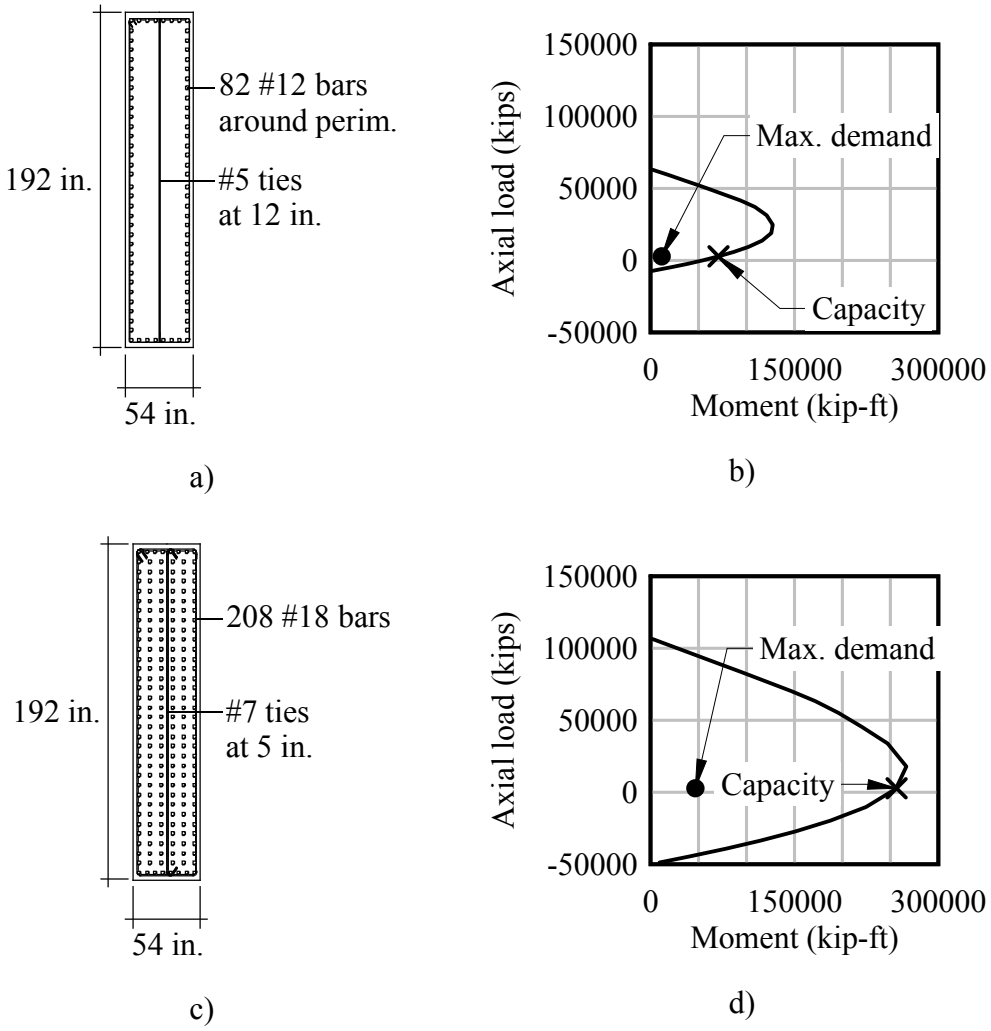

Figure A.6 Original versus strengthened column cross-section summary for the Gandy Bridge Pier 75W case. a) Original column cross-section; b) Load-moment interaction for original cross-section in response to AASHTO static load; c) Strengthened column cross-section; d) Load-moment interaction for strengthened cross-section in response to dynamic load

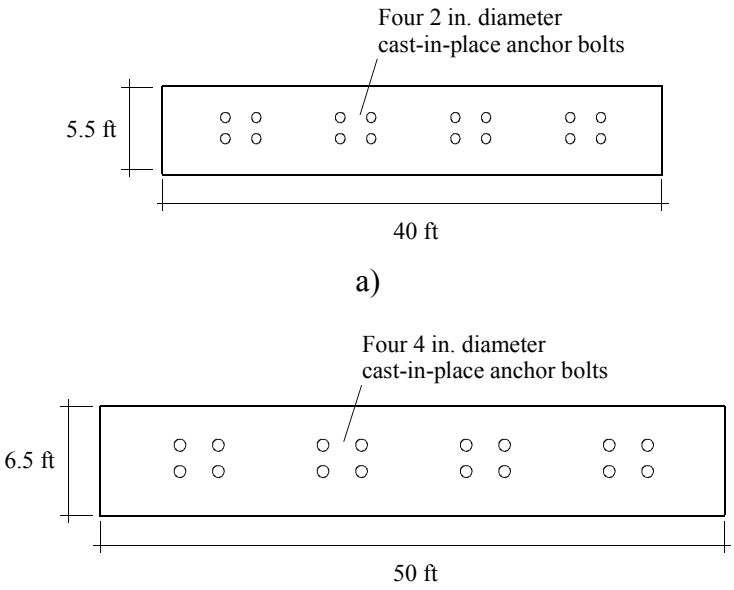

Figure A.7 Original versus strengthened substructure-superstructure interface for Gandy Bridge Pier 75W case. a) Plan view of original pier cap beam; b) Plan view of strengthened pier cap beam

APPENDIX B
CASE-SPECIFIC PROBABILISTIC FRAMEWORK COMPONENTS

B.1 Introduction

In the current study, a probabilistic framework has been developed for use in probabilistic simulations of barge-bridge collisions. Using the newly developed framework, probabilistic assessments of structural failure—as defined in the Florida Department of Transportation *Structures Design Guidelines* (FDOT 2009)—were made for a representative set of Florida bridges. For the bridge cases considered (see Chapter 4 for structural descriptions), the incorporation of many random variables into the frameworks, such as structural member material strengths, was straightforward due to extant probabilistic descriptions in the literature and the direct availability of mean (or expected) parameter values given in the structural plans. However, certain other framework parameters (e.g., waterway vessel traffic properties) required the formation of customized, case-specific statistical descriptions for use in the probabilistic simulations. Details relevant to this latter group of parameters are given in this appendix.

Consistent with that of Chapter 4, bridge cases discussed in this appendix have each been assigned a three-letter identification code (Table B.1). Individual piers within each bridge are delineated by proximity to the barge transit path (the letters "CHA" appended to a bridge identification code indicate that the pier is a channel pier, whereas the letters "OFF" indicate that the pier is not directly adjacent to the channel). Combined bridge-location identifiers (e.g., "BLT-CHA" for the SR-20 at Blountstown bridge channel pier) are referred to as Case IDs.

Table B.1 Bridge pier case IDs

Bridge name	Bridge code	Pier location code	Case ID
SR-20 at Blountstown	BLT	CHA	BLT-CHA
I-10 over Escambia Bay	ESB	CHA	ESB-CHA
Gandy Bridge	GND	CHA	GND-CHA
New St George Island	NSG	CHA	NSG-CHA
New St George Island	NSG	OFF	NSG-OFF
Ringling	RNG	OFF	RNG-OFF
Santa Rosa Bay	SRB	CHA	SRB-CHA

B.2 Mean High Water (MHW)

For barges traversing a waterway, the water surface elevation largely dictates barge vertical position and—in the event of barge-bridge collision—which bridge pier elements are susceptible to being impacted. Bridge design for vessel collision, per AASHTO (2009), is carried out by placing impact load on the bridge pier at the corresponding mean high water (MHW) elevation. The MHW elevation is defined by the NOAA (2010) as the average of all high water heights observed over a 19-year period (commonly, high water observations from 1983–2001 are used). Probabilistic descriptions of MHW for gage stations near bridge sites are generally not available from the literature; however, waterline elevation data are available from various government agencies for many U.S. waterways (e.g., the National Oceanic and Atmospheric

Administration, NOAA, for coastal waterways; the United States Army Corps of Engineers, USACE, for inland waterways).

In the current study, probabilistic descriptions of MHW are formed for each waterway by, first, obtaining high water elevation data from the government agencies. In the event that high water elevation data are not directly available, comparable data are (instead) approximated by identifying maximum values (over a regular time interval) among the available waterline elevation data. A histogram of the directly available, or approximated, high water elevation data is then formed, and finally, a probability distribution function (PDF) is fit to the histogram using the Chi-square goodness-of-fit test (as described in Ang and Tang 2007).

The process of forming probabilistic descriptions of MHW is described, as illustration, for the SR-20 at Blountstown Bridge, which spans the Apalachicola River in western Florida. High water measurements were not directly available for gage stations near the bridge, and so, high water data were approximated by identifying semi-annual maximum waterline elevations from daily measurements of waterline elevation data. The daily measurement data were obtained from the USACE for the years dating from 1981 to 2008.

A histogram of the approximated high water elevation data, with bin widths dictated by the Freedman-Diaconis rule (Freedman and Diaconis 1983), is shown in (Fig. B.1a). Out of several candidate PDFs that were tentatively fit to the histogram, only the t-location scale distribution (Fig. B.1b) was found to be acceptable when subjected to a Chi-square goodness-of-fit test (Mathworks 2005). Specifically, the Chi-square error associated with the fitted t-location scale PDF was found to be 12.25, which was less than the corresponding Chi-square threshold statistic of 14.07 (at a significance level of 0.05 for 8 degrees-of-freedom). The Chi-square goodness-of-fit test results suggest that the t-location scale PDF (Fig. B.1b) fits the approximated high water data in a statistically meaningful manner.

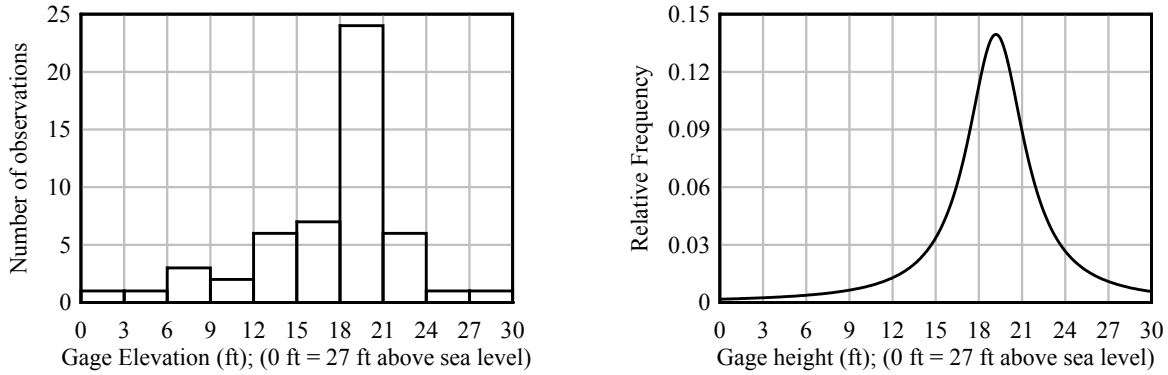

a) b)

Figure B.1 Formation of MHW PDF for SR-20 at Blountstown Bridge. a) Histogram of high water elevation data; b) Fitted t-location scale PDF

For the other bridge cases considered in this study, PDFs of various forms were fitted to high water data in an analogous manner (Table B.2). To prevent generation of irrelevant MHW values (e.g., MHW elevations above the superstructure span or below the soil-surface elevation), lower and upper elevation bounds were determined and applied to the PDFs. Specifically, for each PDF, lower and upper bounds were defined as the historically observed minima and maxima (respectively) at the corresponding stations.

Table B.2 Statistical descriptions of waterline elevation (relative to mean sea-level) distributions

Bridge Case	Waterline distribution	Mean (ft)	COV	Lower (ft)	Upper (ft)	Gov't. Agency
BLT-CHA	T-location scale	45.73	0.10	27	56.3	USACE [a]
ESB-CHA	Normal	1.26	0.18	-2.39	6.36	NOAA [b]
GND-CHA	Lognormal	2.21	0.20	0.00	4.75	NOAA [c]
NSG-CHA	Shifted Lognormal	0.22	1.20	-2.60	6.54	NOAA [d]
NSG-OFF	Shifted Lognormal	0.22	1.20	-2.60	6.54	NOAA [d]
RNG-OFF	Normal	1.33	0.19	0.81	2.91	USC [e]
SRB-CHA	Normal	1.26	0.18	-2.39	6.36	NOAA [b]

[a] http://water.sam.usace.army.mil/acfframe.htm, last accessed on 05/17/2010

[b] http://tidesandcurrents.noaa.gov/geo.shtml?location=8729840, last accessed on 05/17/2010

[c] http://tidesandcurrents.noaa.gov/geo.shtml?location=8726607, last accessed on 05/17/2010

[d] http://tidesandcurrents.noaa.gov/geo.shtml?location=8728690, last accessed on 05/17/2010

[e] University of South Carolina (USC), Department of Biological Sciences, Wethy Lab, http://tbone.biol.sc.edu/tide/tideshow.cgi?site=Cortez%2C+Sarasota+Bay%2C+Florida, last accessed on 05/17/2010

B.3 Waterway Vessel Traffic Data

For an impacting barge (or barge flotilla), the corresponding width, weight, and in-transit velocity play a significant role in the impact forces generated. As described in Chapter 6, discrete probability distribution functions, DPFs, are employed in the current study to sample impacting barge flotilla characteristics. For each bridge case, the associated DPF is derived from previously catalogued vessel traffic data (Liu and Wang 2001), which consists of annually averaged waterway vessel traffic characteristics for all navigable waterways in Florida. The types of vessels traversing each of the Florida waterways were divided, by draft, into vessel groups, where data were expressed in one-year intervals (Liu and Wang 2001).

Barge vessel group data pertinent to each of the bridge cases considered in the current study are listed in Tables B.3–B.8. Specifically, barge group parameters consist of: vessel group trip frequency, N, (the average number of annual passages under the bridge); width and length (B_{barge} and L_{barge}, respectively) of individual barges (ft) within the barge group; overall flotilla length (LOA, ft); flotilla weight (W, tonne); and, flotilla transit velocity (V, knots). For each

barge-bridge collision simulation conducted in the current study, barge flotilla characteristics are selected in proportion to vessel trip frequency (N), which constitutes a DPF approach.

Table B.3 Annually averaged vessel traffic data for the SR-20 at Blountstown Bridge

Vessel group	Direction	N	Draft (ft)	No. barges	B_{barge} (ft)	L_{barge} (ft)	LOA (ft)	W (tonne)	V (knots)
1	up	3	2	2.7	50.9	281	833.7	2472	6.6
2	up	1	5.3	2.7	47.7	263	785.1	5420	5.6
3	up	51.2	8.1	2.7	47	239	720.3	7548	5.6
4	up	1	10	2.7	41.3	229	738.3	8151	5.6

Table B.4 Annually averaged vessel traffic data for the Escambia Bay Bridge

Vessel group	Direction	N	Draft (ft)	No. barges	B_{barge} (ft)	L_{barge} (ft)	LOA (ft)	W (tonne)	V (knots)
1	up	154	2	2.3	41	226	594.8	1540	5.6
2	up	24	5.4	2.3	47	247	643.1	4519	4.6
3	up	126	8.3	2.3	45	233	610.9	6206	4.6
4	up	28	10.4	2.3	50	265	729.5	9664	4.6
5	up	2	17	2.3	66	361	950.3	27125	4.6
6	down	239	2	2.2	45	232	585.4	1383	6.4
7	down	3	5	2.2	46	254	633.8	3876	5.4
8	down	89	8.2	2.2	41	226	572.2	5220	5.4
9	down	3	10	2.2	35	195	549	4796	5.4
10	down	3	23	2.2	66	361	914.2	34956	5.4

Table B.5 Annually averaged vessel traffic data for the Gandy Bridge

Vessel group	Direction	N	Draft (ft)	No. barges	B_{barge} (ft)	L_{barge} (ft)	LOA (ft)	W (tonne)	V (knots)
1	up	1	19	1	76.2	442	562	18794	5.6
2	down	1	19	1	76.2	442	562	18794	6.4

Table B.6 Annually averaged vessel traffic data for the New St. George Island Bridge

Vessel group	Direction	N	Draft (ft)	No. barges	B_{barge} (ft)	L_{barge} (ft)	LOA (ft)	W (tonne)	V (knots)
1	up	85	2.1	1	51	216	291	971	5.6
2	up	25	5.6	1	58.6	316	391	3288	4.6
3	up	117	8.3	1	50.6	246	321	3259	4.6
4	up	92	11	1	54	319	439	5907	4.6
5	down	135	2	1.9	50.9	267	582.3	1777	6.4
6	down	22	4.9	1.9	62.4	328	698.2	6026	5.4
7	down	19	8.2	1.9	45.2	251	551.9	5945	5.4
8	down	28	11.8	1.9	72.4	256	606.4	12346	5.4

Table B.7 Annually averaged vessel traffic data for John Ringling Causeway Bridge

Vessel group	Direction	N	Draft (ft)	No. barges	B_{barge} (ft)	L_{barge} (ft)	LOA (ft)	W (tonne)	V (knots)
1	up	23.9	1.8	1	42.8	193	268	586	5.6
2	up	5.9	4.8	1	42.4	173	248	1343	4.6
3	down	12	1.9	1	43.4	183	258	600	6.4
4	down	8.2	5	1	43.1	186	261	1560	5.4
5	down	9.6	8	1	43	219	294	2420	5.4

Table B.8 Annually averaged vessel traffic data for the Santa Rosa Bay Bridge

Vessel group	Direction	N	Draft (ft)	No. barges	B_{barge} (ft)	L_{barge} (ft)	LOA (ft)	W (tonne)	V (knots)
1	up	154	2	2.3	41	226	594.8	1540	5.6
2	up	24	5.4	2.3	47	247	643.1	4519	4.6
3	up	126	8.3	2.3	45	233	610.9	6206	4.6
4	up	28	10.4	2.3	50	265	729.5	9664	4.6
5	up	2	17	2.3	66	361	950.3	27125	4.6
6	down	239	2	2.2	45	232	585.4	1383	6.4
7	down	3	5	2.2	46	254	633.8	3876	5.4
8	down	89	8.2	2.2	41	226	572.2	5220	5.4
9	down	3	10	2.2	35	195	549	4796	5.4
10	down	3	23	2.2	66	361	914.2	34956	5.4

B.4 AASHTO PC Data

Using vessel traffic characteristics given in Tables B.3–B.8 in conjunction with the respective bridge pier static pushover capacities (H)—where available (as-designed) capacity terms are listed in Table B.9—AASHTO probability of collapse (PC) estimates have been calculated for several bridge cases (Tables B.10–B.14). Static impact force (P_B, kips), a required

parameter in the AASHTO PC expression, is empirically calculated based on energy-related parameters of the impacting vessel (which are also listed for each vessel group in Tables B.10–B.14). These parameters: hydrodynamic mass coefficient (C_H); flotilla weight (W, tonnes); and, adjusted transit velocity (V_{adj}, ft/sec)—which is dependent on flotilla position relative to the channel centerline—are used to quantify the kinetic energy (KE, kip-ft) of the impacting vessel. Upon impact, the vessel undergoes deformation (e.g., barge bow deformation), a_B (ft), which is empirically determined from KE. Once quantified, a_B is empirically related to impact force P_B. Finally, the static impact force associated with each vessel group (P_B) is compared to the respective capacity, H, to determine the AASHTO PC estimate. Additional details of the calculation of AASHTO PC values are given in Chapter 6.

Table B.9 Static pushover capacity (H) of bridge piers (obtained from structural plans)

Case ID	H (kips)
BLT-CHA	2550
GND-CHA	2400
NSG-CHA	3255
NSG-OFF	2300
SRB-CHA	2000

Table B.10 AASHTO PC data for the BLT-CHA case

Vessel group	N	C_H	W (tonne)	V_{adj} (ft/sec)	KE (kip-ft)	a_B (ft)	P_B (kips)	PC
1	3	1.05	2472	10.89	10555	4.85	2738	0.008
2	1	1.05	5420	9.24	16640	7.36	2942	0.015
3	51.2	1.05	7548	9.22	23069	9.5	3215	0.023
4	1	1.05	8151	9.22	24944	11.44	3077	0.019

Table B.11 AASHTO PC data for the GND-CHA case

Vessel group	N	C_H	W (tonne)	V_{adj} (ft/sec)	KE (kip-ft)	a_B (ft)	P_B (kips)	PC
1	1	1.05	18794	8.98	54575	10.58	5472	0.062
2	1	1.05	18794	10.25	71077	12.55	5942	0.066

Table B.12 AASHTO PC data for NSG-CHA case

Vessel group	N	C_H	W (tonne)	V_{adj} (ft/sec)	KE (kip-ft)	a_B (ft)	PB (kips)	PC
1	85	1.05	971	8.8	2708	1.51	2208	0
2	24.6	1.05	3288	7.4	6472	2.82	2778	0
3	117	1.05	3259	7.31	6263	3.18	2456	0
4	92.2	1.05	5907	7.44	11763	4.98	2926	0
5	135	1.05	1777	10.44	6970	3.46	2515	0
6	21.6	1.05	6026	8.87	17070	5.73	3530	0.009
7	19.4	1.05	5945	8.8	16581	7.75	2843	0
8	27.7	1.05	12346	8.83	34663	8.22	4661	0.034

Table B.13 AASHTO PC data for NSG-OFF case

Vessel group	N	C_H	W (tonne)	V_{adj} (ft/sec)	KE (kip-ft)	a_B (ft)	P_B (kips)	PC
1	85	1.05	971	1.69	100	0.06	367	0
2	24.6	1.05	3288	1.82	390	0.21	1419	0
3	117	1.05	3259	1.69	335	0.21	1219	0
4	92.2	1.05	5907	2.51	1335	0.74	2206	0
5	135	1.05	1777	4.95	1563	0.91	2107	0
6	21.6	1.05	6026	5.16	5784	2.41	2878	0.022
7	19.4	1.05	5945	4.07	3537	2.17	2050	0
8	27.7	1.05	12346	4.54	9156	3.04	3483	0.038

Table B.14 AASHTO PC data for the SRB-CHA case

Vessel group	N	C_H	W (tonne)	V_{adj} (ft/sec)	KE (kip-ft)	a_B (ft)	P_B (kips)	PC
1	154	1.05	1540	6.34	2227	1.57	1782	0
2	24	1.05	4519	5.52	4953	2.8	2225	0.011
3	126	1.05	6206	5.4	6502	3.69	2256	0.013
4	28	1.05	9664	5.8	11679	5.35	2768	0.031
5	2	1.06	27125	10.08	100062	17.95	6266	0.076
6	239	1.05	1383	7.09	2500	1.59	1959	0
7	3	1.05	3876	6.33	5585	3.17	2232	0.012
8	89	1.05	5220	6.01	6795	4.2	2122	0.006
9	3	1.05	4796	5.88	5960	4.41	1834	0
10	3	1.25	34956	10.97	180279	25.56	7846	0.083

B.5 Barge-Pier Impact Scenarios

Using vessel traffic characteristics given in Tables B.3–B.8 in conjunction with the respective ranges of vessel transit angles listed in Table B.15 (where transit angle, ϕ, is defined as depicted in Fig. B.2), the range of relative barge-pier orientations can be determined for each case. Note that the impact angles (and bounding values) listed in Table B.15 were determined in accordance with the normal distribution proposed by Kunz (1998), in which (given a mean transit angle) a standard deviation of 10° is employed and impact angles are limited to the 0.02 and 0.98 percentile values of the distribution.

Table B.15 Mean vessel transit angles

Bridge Case	Mean vessel transit angle (ϕ)	Lower bound	Upper bound
BLT-CHA	90°	69.5°	110.5°
ESB-CHA	70.78°	50.2°	91.3°
GND-CHA	90°	69.5°	110.5°
NSG-CHA	61.43°	40.9°	82.0°
NSG-OFF	61.43°	40.9°	82.0°
RNG-OFF	83.93°	63.4°	104.5°
SRB-CHA	81.5°	61.0°	102.0°

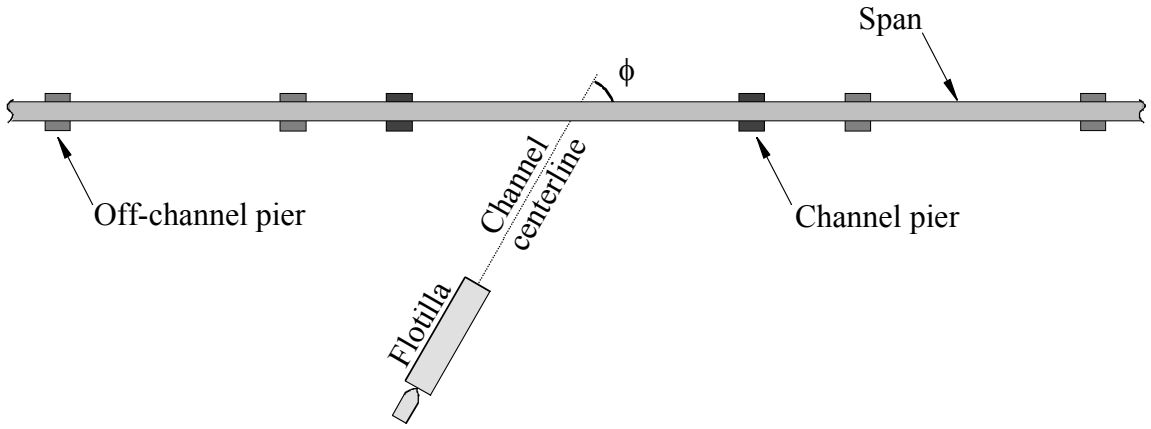

Figure B.2 Vessel transit angle (ϕ) relative to bridge span

For the selected bridges that span coastal waterways (e.g., bays), the variation of MHW elevations, as listed in Table B.2, are small (with minima and maxima that vary by less than 10 ft) relative to the substantial fluctuations found on inland waterways (e.g., the range of MHW elevations for BLT-CHA is approximately 30 ft). Consequently, for the bay-spanning bridge cases with thick waterline pile caps and, furthermore, that are subject to impacting vessels at angles ranging from less than to greater than 90°, four types of vessel collision (with respect to barge-pier orientation) are considered (Fig. B.3). Specifically, for the GND-CHA and SRB-CHA cases (structural configuration descriptions are given in Chapter 4), head-on pile cap impacts

(Fig. B.3a); oblique impacts on the front face of the pile cap (Fig. B.3b); pointed impacts on the pile cap corners (Fig. B.3c); and, oblique impacts on the side faces of the pile cap (Fig. B.3d) are considered in the probabilistic simulations. Barge bow force-deformation relationships applicable to each type of impact are discussed in Chapter 3. Specific to the NSG-CHA and NSG-OFF cases, the maximum impact angle that can be sampled is less than 90°, and consequently, only those orientations shown in Fig. B.3b–d are considered.

Four analogous types of barge-pier orientation are considered in the probabilistic simulations for the ESB-CHA case (Fig. B.4). However, in contrast to the thick, waterline pile caps common to the previously discussed cases, the ESB-CHA case contains a 17.5 ft tall shear wall that extends upward from the mudline pile cap (see Chapter 4 for a detailed structural description). Consequently, for the ESB-CHA case, impact scenarios are considered in which impact occurs on the relatively narrow front face of the shear wall. Descriptions of the barge-pier orientations considered in the probabilistic simulations for the BLT-CHA and RNG-OFF cases are discussed in Appendix C.

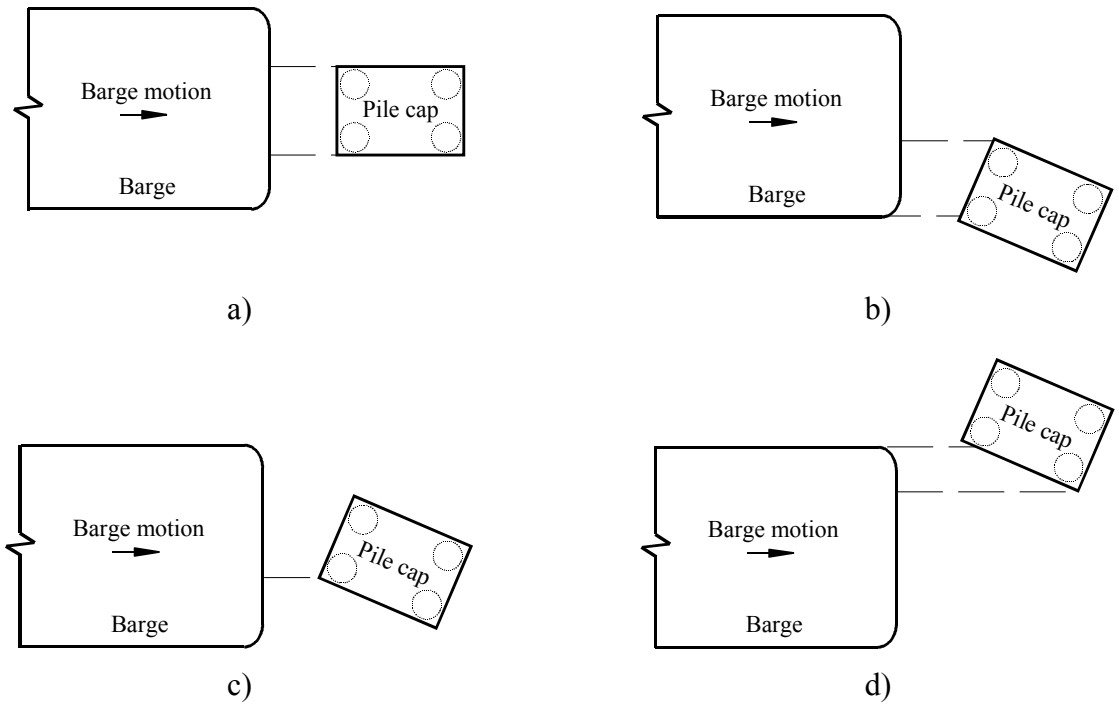

Figure B.3 Relative barge-pier orientations considered in the probabilistic simulations conducted for cases with thick rectangular pile caps vertically positioned at the waterline.
a) Head-on impact; b) Oblique impact on front face of pile cap; c) Pointed impact; d) Oblique impact on side face of pile cap

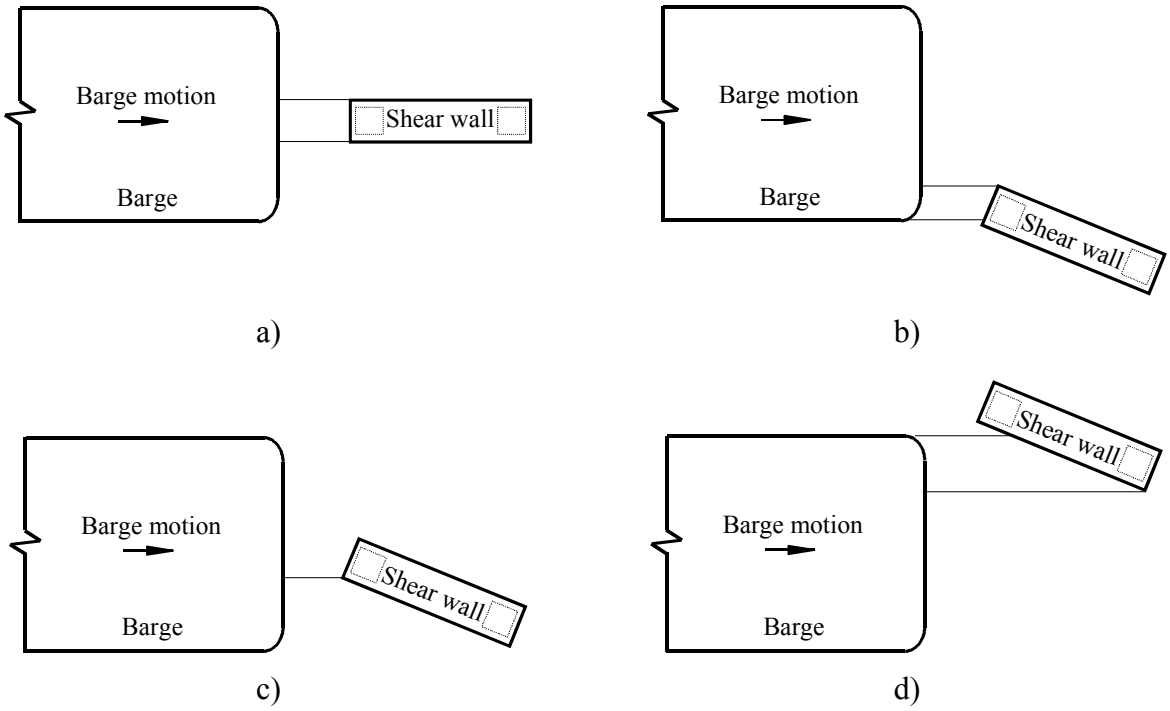

Figure B.4 Relative barge-pier orientations considered in the probabilistic simulations conducted for the ESB-CHA case. a) Head-on impact; b) Oblique impact on narrow face of shear wall; c) Pointed impact; d) Oblique impact on wide face of shear wall

B.6 Florida Department of Transportation (FDOT) Limit States

For bridges subject to vessel collision, the AASHTO provisions state that the bridge owner is responsible for approving the degree of damage that bridge components are allowed to sustain during impact events. Given that all bridges considered in the current study are publicly owned, bridge collapse (i.e., structural failure) is defined in terms that are consistent with those specified in the FDOT *Structures Design Guidelines* (2009).

The FDOT guidelines clearly delineate three vessel-collision limit states:

- The superstructure must not collapse;
- Load redistribution must not be permitted when the ultimate bearing capacity (UBC) of axially loaded piles is reached; and,
- Forces transferred to the superstructure must not exceed the capacity of load transfer devices (e.g., shear pins) at the superstructure-substructure interface.

Case-specific probabilistic framework components associated with the three FDOT limit states (as applied to each bridge case) are discussed below.

B.6.1 Bridge collapse mechanisms corresponding to superstructure collapse

As discussed in Chapter 6, pier collapse was assumed to be tantamount to superstructure collapse. Accordingly, the formation of plastic hinges (where, in this context, a plastic hinge is defined as the simultaneous occurrence of axial load and biaxial bending moments that surpass the load-interaction failure surface for a given structural member) that constitute collapse mechanisms have been identified for the range of vertical impact locations applicable to each bridge case.

For the BLT-CHA case (which contains a 30.5 ft tall shear wall), widely varying MHW elevations necessitate that three plastic hinge configurations be considered (Fig. B.5). Namely, in the event that a pier column is directly impacted, local collapse of the impacted pier column (Fig. B.5b) is monitored in the respective simulation. For impacts on the pier shear wall, collapse of the two pier columns (Fig. B.5c) and collapse of the two drilled shafts along the shaft free lengths (Fig. B.5d) are monitored.

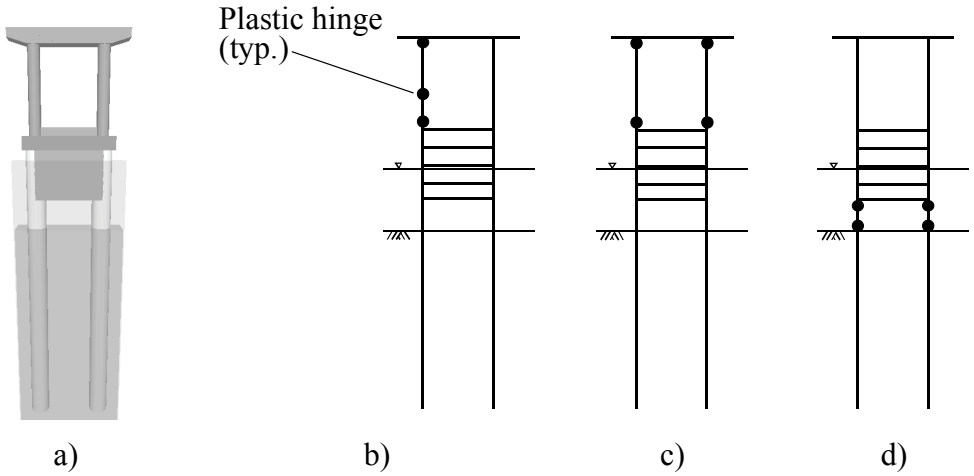

Figure B.5 Collapse mechanisms considered in the probabilistic simulations conducted for the BLT-CHA case. a) Structural configuration; b) Collapse mechanism for direct pier column impact; c) Pier column collapse mechanism; d) Drilled shaft collapse mechanism

Although the structural configuration for the ESB-CHA case (Fig. B.6a) also includes a tall shear wall (17.5 ft in the vertical dimension), the MHW elevation variability (in contrast to that of the BLT-CHA case) is not large enough to result in direct pier column impacts (i.e., impacts are limited, vertically, to the shear wall). Furthermore, because the ESB-CHA case contains a mudline footing (in which the driven piles and pile cap are fully embedded in the soil), only collapse of the two pier columns is monitored in the corresponding probabilistic simulations (Fig. B.6b).

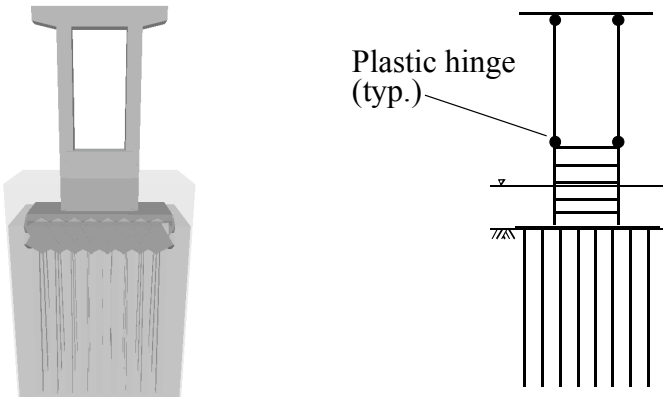

a) b)

Figure B.6 Collapse mechanisms considered in the probabilistic simulations conducted for the ESB-CHA case. a) Structural configuration; b) Pier column collapse mechanism

Each of the bridge cases shown in Figs. B.7–B.11 possess thick (ranging from 6.5 ft to 9 ft in the vertical dimension) waterline pile caps, and furthermore, the bridges span coastal waterways with small fluctuations in waterline elevations (relative to inland waterways). Consequently, two collapse mechanisms are monitored for the corresponding probabilistic simulations: collapse of the pier columns, and collapse of the piles (or drilled shafts). Note that for pier configurations with single pier columns, collapse was considered to occur as a result of the formation of a single plastic hinge located anywhere throughout the pier column.

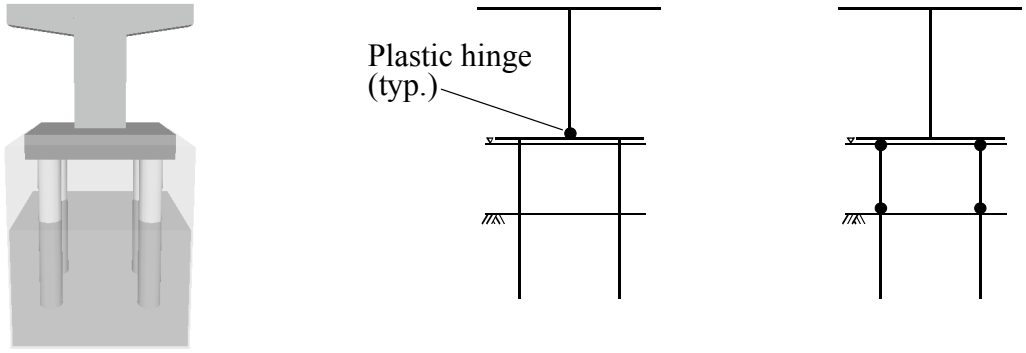

a) b) c)

Figure B.7 Collapse mechanisms considered in the probabilistic simulations conducted for the GND-CHA case. a) Structural configuration; b) Pier column collapse mechanism; c) Drilled shaft collapse mechanism

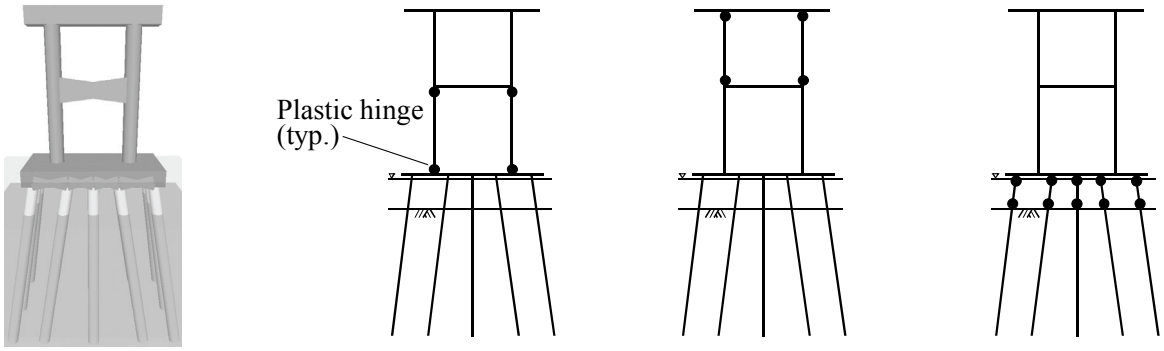

Figure B.8 Collapse mechanisms considered in the probabilistic simulations conducted for the NSG-CHA case. a) Structural configuration; b) Lower pier column collapse mechanism; c) Upper pier column collapse mechanism; d) Driven pile collapse mechanism

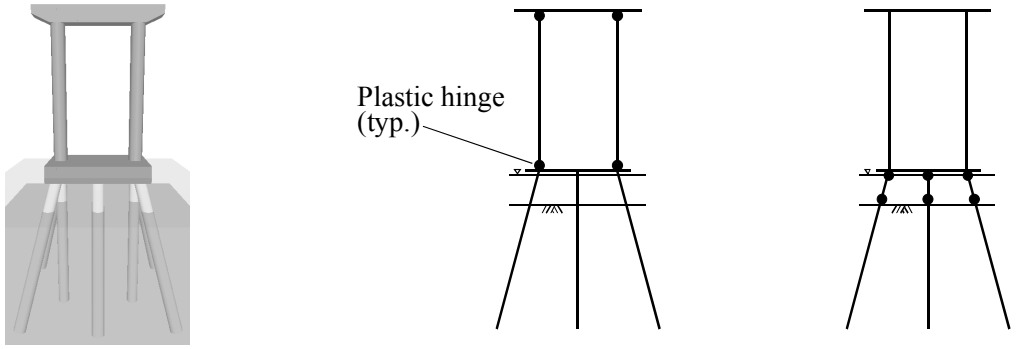

Figure B.9 Collapse mechanisms considered in the probabilistic simulations conducted for the NSG-OFF case. a) Structural configuration; b) Pier column collapse mechanism; c) Driven pile collapse mechanism

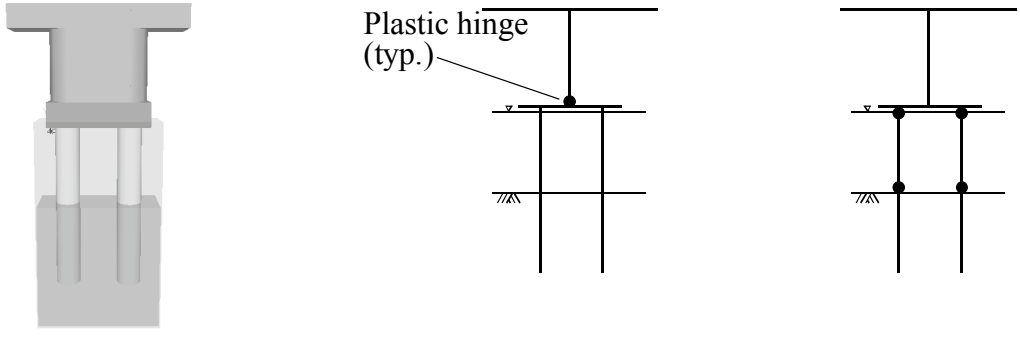

Figure B.10 Collapse mechanisms considered in the probabilistic simulations conducted for the RNG-OFF case. a) Structural configuration; b) Pier column collapse mechanism; c) Drilled shaft collapse mechanism

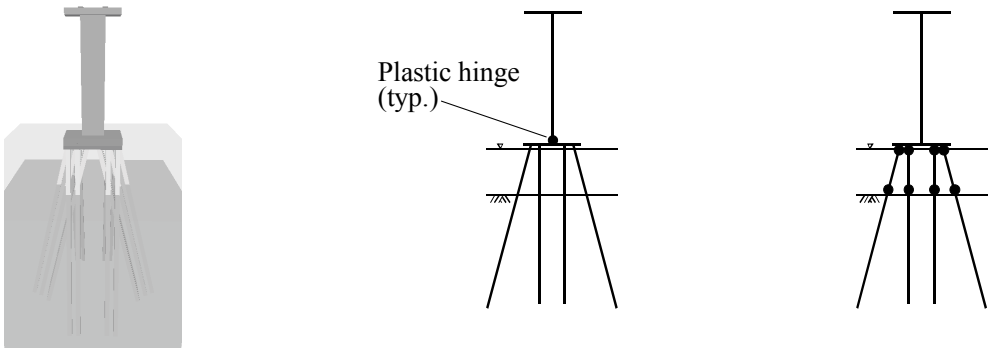

a) b) c)

Figure B.11 Collapse mechanisms considered in the probabilistic simulations conducted for the SRB-CHA case. a) Structural configuration; b) Pier column collapse mechanism; c) Driven pile collapse mechanism

B.6.2 Pile and drilled shaft axial capacity

Two types of embedded (below-soil) foundation members are present among the bridge pier structural configurations considered in the current study: driven piles and drilled shafts. As described in Chapter 6, for foundations that contain driven piles, the use of site-specific SPT boring profiles combined with SPT to soil-strength correlations (e.g., those referenced in FB-MultiPier 2009 and FB-Deep 2010) are sufficient to quantify the ultimate skin and tip resistance of driven piles (Fig. B.12a). For driven piles, failure is considered to have occurred when the total soil-pile skin and tip forces exceed the ultimate skin and tip resistances, respectively.

Drilled shaft capacity, in contrast, is defined in FDOT (2009) as a displacement-dependent phenomenon (Fig. B.12b). Specifically, the FDOT guidelines define drilled shaft failure as the occurrence of a shaft bottom displacement equal to $1/30^{th}$ of the shaft diameter. For drilled shafts embedded in soils other than limestone (e.g., clay, sand, clay-silt-sand mixtures), the use of site-specific SPT boring profiles combined with SPT to soil-strength correlations (e.g., those referenced in FB-MultiPier 2009 and FB-Deep 2010) are, similar to that of driven piles, sufficient to quantify the failure load (i.e., the vertical load that corresponds to a shaft bottom displacement equal to $1/30^{th}$ of the shaft diameter). However, for drilled shafts embedded in limestone, site-specific limestone strength parameters are required, as discussed below, in addition to other soil parameters that are used to characterize soil resistance.

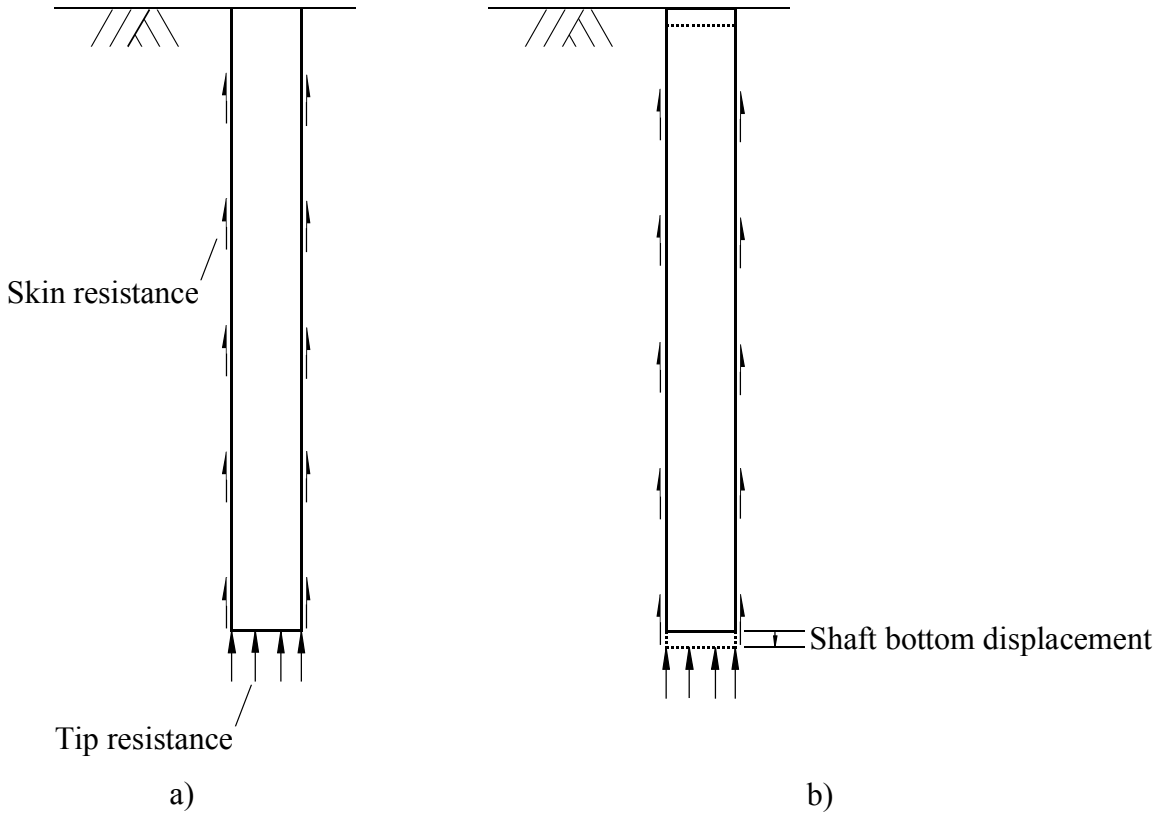

Figure B.12 Types of foundation members embedded in soil. a) Driven pile; b) Drilled shaft

B.6.3 Soil strength parameters for drilled shafts embedded in limestone

Modeling of distributed nonlinear soil springs for drilled shafts embedded in limestone requires the specification of several strength parameters specific to the limestone local to the bridge site: site-wide averages of rock quality designation (RQD) and recovery; unconfined compressive strength (q_u); intact modulus (E_i); and, split tensile strength (q_t). [Additionally, the drilled shaft concrete slump and 28-day elastic modulus are required; however, these latter two parameters are readily determined from information given in the structural drawings.]

McVay et al. (2003) performed extensive field testing and sampling to quantify limestone strength properties for the SR-20 at Blountstown Bridge and the Gandy Bridge (in addition to several other bridges). Specific to the SR-20 at Blountstown Bridge (which corresponds to the BLT-CHA case), site-wide averages of RQD and recovery were found to be 0.30 and 0.56, respectively. Additionally, non-parametric frequency distributions were developed for q_u (tsf) and q_t (tsf), as shown in Figs. B.13–B.14, respectively. Furthermore, correlation was observed between measured q_u and E_i values, which lead to the development of the regression expression (McVay et al. 2003):

$$E_i = 8.1160 \cdot q_u \tag{B.1}$$

where E_i is in units of ksi, and q_u is in units of tsf.

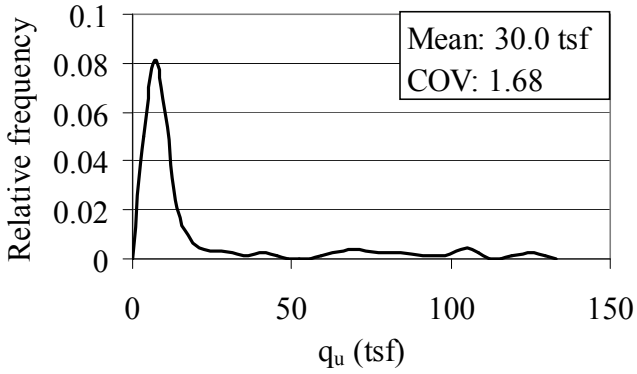

Figure B.13 Limestone unconfined compressive strength (q_u) frequency plot for SR-20 at Blountstown Bridge (from McVay et al. 2003)

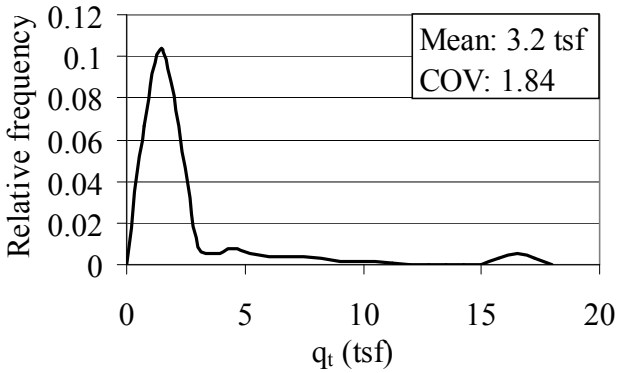

Figure B.14 Limestone split tensile strength (q_t) frequency plot for SR-20 at Blountstown Bridge (from McVay et al. 2003)

For each BLT-CHA barge-bridge collision simulation, site-wide averages of RQD and recovery are employed directly in the soil resistance modeling. Additionally, the non-parametric distributions of q_u and q_t are sampled (Figs. B.13–B.14, respectively), and the correlated value of E_i is determined (given q_u) using Eqn. B.1.

Analogous parameters (pertaining to the Gandy Bridge, or GND-CHA case) are shown in Figs. B.15–B.16 and given in Eqn. B.2:

$$E_i = 1.9197 \cdot q_u + 271.643 \tag{B.2}$$

where E_i is in units of ksi, and q_u is in units of tsf.. Site-wide averages of RQD and recovery at the Gandy Bridge were found to be 0.56 and 0.83, respectively. Limestone strength properties are employed in the GND-CHA probabilistic simulations in a manner analogous to that of the BLT-CHA case.

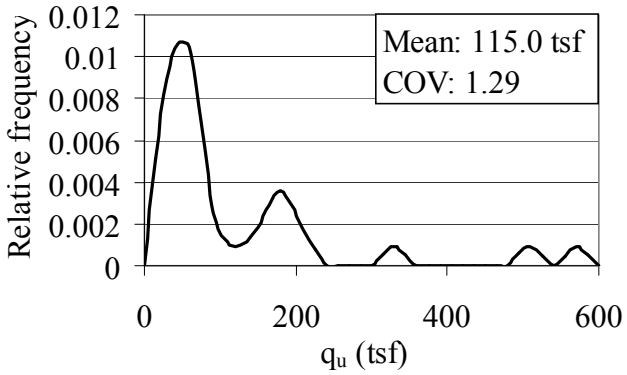

Figure B.15 Limestone unconfined compressive strength (q_u) frequency plot for Gandy Bridge (from McVay et al. 2003)

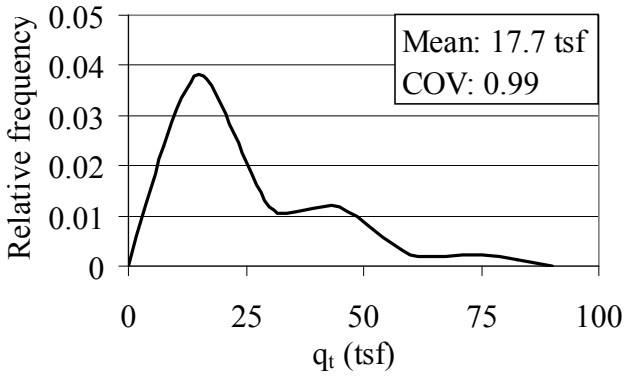

Figure B.16 Limestone split tensile strength (q_t) frequency plot for Gandy Bridge (from McVay et al. 2003)

For the John Ringling Causeway Bridge (RNG-OFF), due to a lack of pre-compiled data, it was necessary to form the required limestone parameters using boring log records of limestone strength properties. Using values of unconfined compressive strength (q_u) and split tensile strength (q_t), where samples were taken from throughout the John Ringling Causeway Bridge site (as indicated in the boring logs), PDFs were fitted to the data in a manner similar to that used in the formation of the MHW PDFs (as described above). Specifically, lognormal distributions (Figs. B.17–B.18) were found to pass Chi-square goodness-of-fit testing for both the q_u and q_t parameters. Additionally, site-wide averages of RQD and recovery were found to be 0.63 and 0.76, respectively.

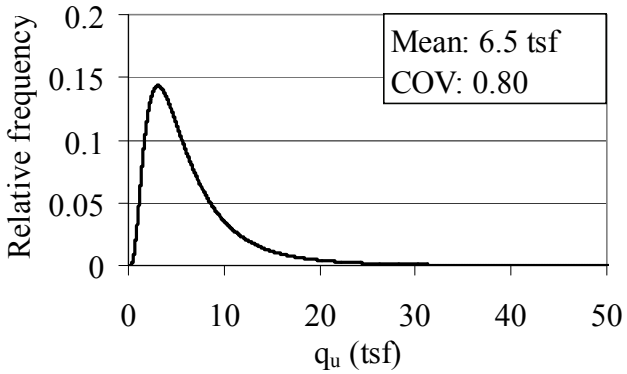

Figure B.17 Limestone unconfined compressive strength (q_u) frequency plot for John Ringling Causeway Bridge

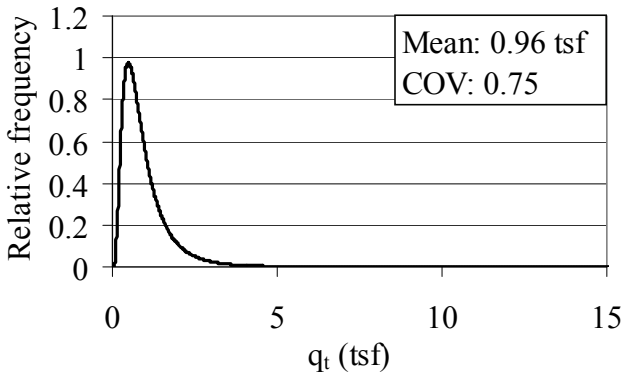

Figure B.18 Limestone split tensile strength (q_t) frequency plot for John Ringling Causeway Bridge

Given the lack of site-specific correlation between q_u and E_i for the RNG-OFF case, the correlation proposed by Jacobs (2003) was employed:

$$E_i = 6.410 \cdot (q_u \cdot 13.889)^{0.7549} \quad \text{(B.3)}$$

where E_i is in units of ksi, and q_u is in units of tsf.. This expression was formed based on hundreds of measured data points for sixteen bridge sites located throughout the state of Florida.

B.6.4 Substructure-Superstructure interface shear capacity

For all cases except RNG-OFF and SRB-CHA, either cast-in-place shear pins or cast-in-place anchor bolts are present at the bridge pier substructure-superstructure interfaces. For cases where shear pins (or anchor bolts) are present, shear capacities at the substructure-superstructure interface are determined using the ACI (2005) Appendix D provisions, which pertain to anchorage in structural concrete. More specifically, the ACI provisions facilitate

calculation of the bearing capacity of shear pins (or anchor bolts) and in addition, shear pin resistance to rupture due to direct shearing.

The pier in the RNG-OFF case contains pot bearings, where the unfactored shearing capacities of the pot bearings are taken directly from the structural plans. The pier in the SRB-CHA case contains only elastomeric bearing pads, and so, in accordance with common design practice, failure is taken as the shear force necessary to impose a pad shear strain, γ, equal to 1.0 (corresponding to an angle change of 45° in the pad.

APPENDIX C
CASE-SPECIFIC BARGE FORCE-DEFORMATION MODELS

C.1 Introduction

The probabilistic simulations carried out as part of this study include the use of coupled vessel impact analysis (CVIA) (details of the CVIA algorithm are given in Consolazio and Cowan 2005). An integral component of the CVIA technique—which has been implemented in a research version of the finite element (FE) software package FB-MultiPier (2009)—is the modeling of a barge as a single-degree-of-freedom (SDF) system with a nonlinear spring (or barge force-deformation relationship), mass, and initial (impact) velocity. Barge crushing behavior has been shown to be sensitive to the impacted (pier) surface geometry, and shape-specific force-deformation relationships have been developed for multiple surface types (Consolazio et al. 2009a). However, for two bridge cases considered in the current study (SR-20 at Blountstown, Pier 58, or BLT-CHA; John Ringling Causeway, Pier 9, or RNG-OFF), the applicable range of impact scenarios and pier geometries necessitated the development of specialized barge force-deformation relationships. Presented in this appendix are barge force-deformation relationships that were developed for use, when applicable, with the CVIA technique in the BLT-CHA and RNG-OFF probabilistic simulations.

C.2 State Road 20 (SR-20) at Blountstown, Pier 58 (BLT-CHA)

The Blountstown Bridge—formally known as the New Trammell Bridge—was constructed in 1998 to span the Apalachicola River in northwestern Florida. The Pier 58 structural model (BLT-CHA) is shown in Fig. C.1. The channel pier structure consists of two round (5.5 ft diameter, 37 ft tall) pier columns spaced 30 ft apart. The pier columns are axially collinear with two 9 ft diameter drilled shafts. The pier columns and drilled shafts are integrated with a 30.5 ft tall shear wall, which is rounded (10.5 ft in diameter) at the front and rear pier faces.

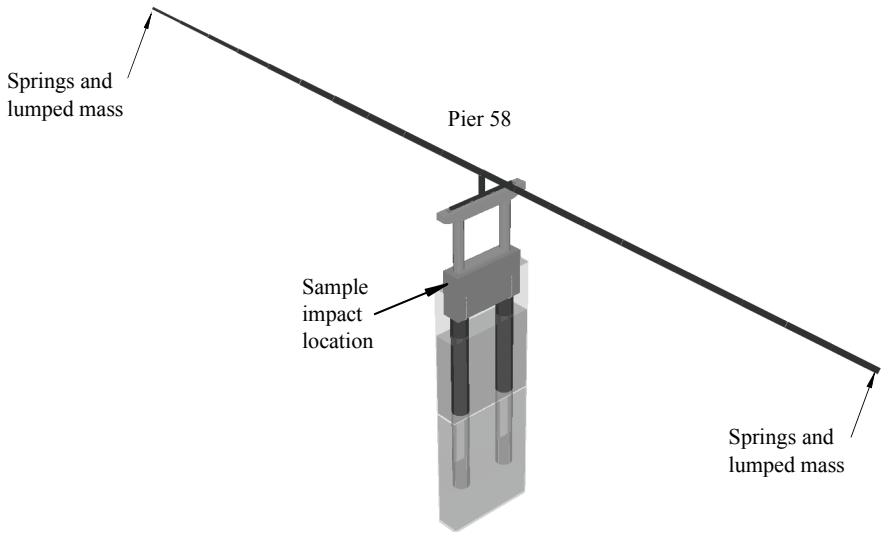

Figure C.1 SR 20 at Blountstown, Pier 58 OPTS (BLT-CHA) model

The range of impact scenarios applicable to the BLT-CHA case is such that either the 30.5 ft tall shear wall or one of the two 5.5 ft diameter pier columns is susceptible to direct impact during a collision. Schematics of the impact scenarios associated with collision of the BLT-CHA shear wall are shown in Fig. C.2. For a given impact angle, θ_o, three types of impact are considered: oblique impact on the flat portion of the shear wall (Fig. C.2a); impact on the rounded front pier face (Fig. C.2b); and, impact on the rounded rear pier face (Fig. C.2c). Barge force-deformation relationships for oblique impacts on flat surfaces were developed previously (Consolazio et al. 2009b). Furthermore, previous studies have led to the development of barge force-deformation for impacts on fully engaged, round impact surfaces (Consolazio et al. 2009a). However, the impact scenarios applicable to the BLT-CHA case include the condition where only a portion of the round impact surface is engaged during collision.

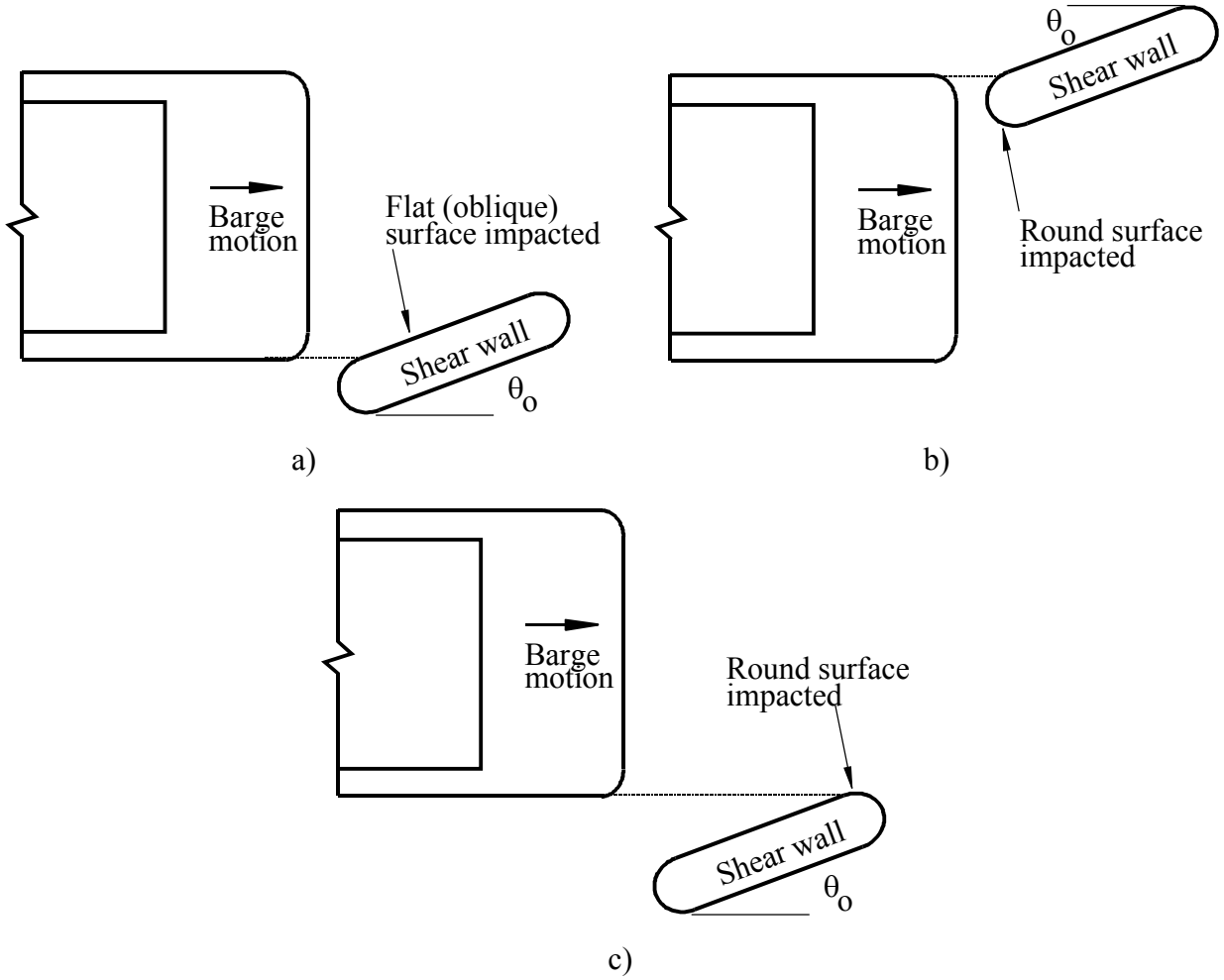

Figure C.2 Impact scenarios applicable to BLT-CHA shear wall. a) Flat, oblique impact on shear wall; b) Round-surface impact on front of shear wall; c) Round-surface impact on rear of shear wall

The concept of a partially engaged, round impact surface is illustrated for the impact scenarios associated with the BLT-CHA pier columns (Fig. C.3). In the Fig. C.3a schematic, the

entire width of the pier column is engaged. However, in the Fig. C.3b–C.3d schematics, the relative barge and pier column positions are such that reduced-width portions (0.25 to 0.75) of the pier column are engaged during impact. Barge force-deformation relationships for partially engaged, round impact surfaces (discussed below) have been developed, and have been incorporated into the probabilistic simulations conducted for the BLT-CHA case.

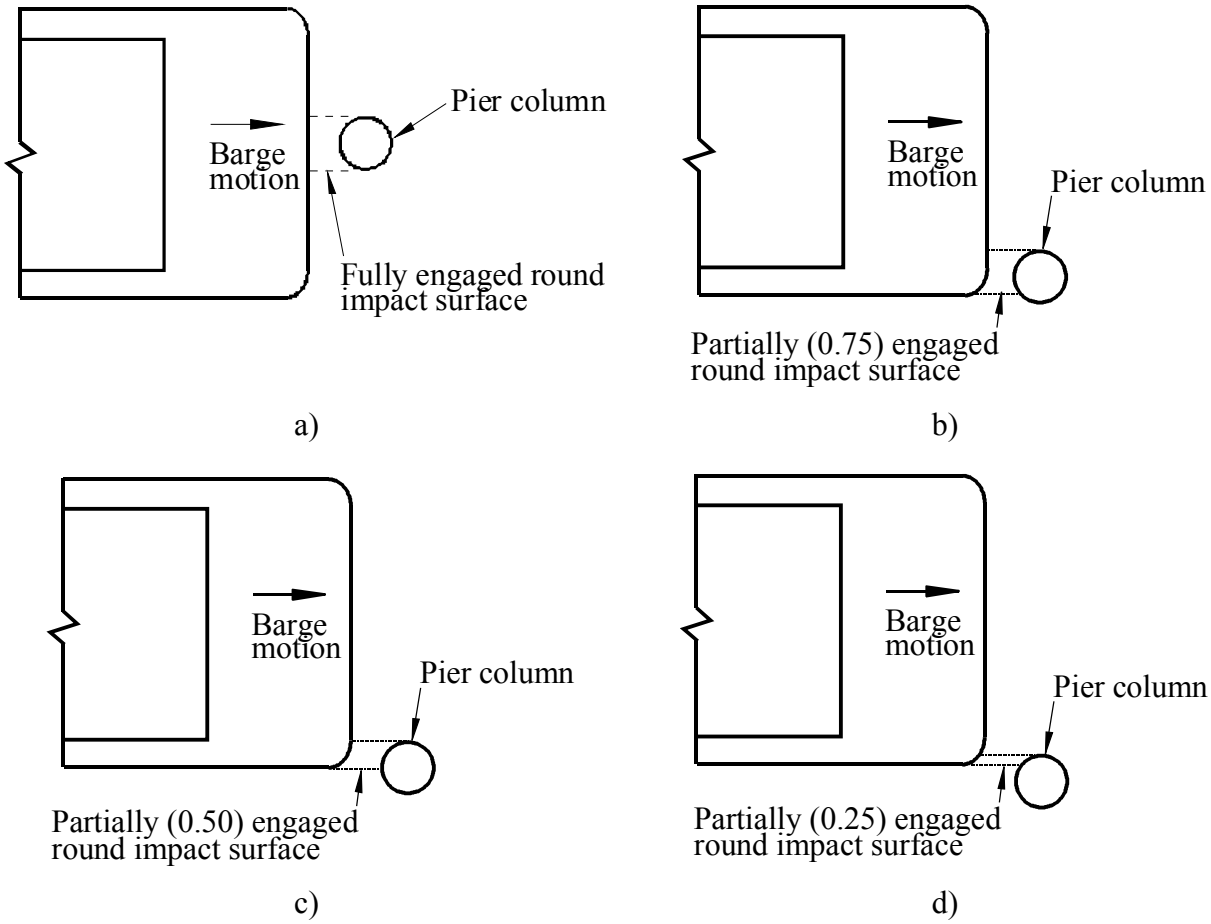

Figure C.3 Impact scenarios applicable to BLT-CHA pier columns. a) Fully engaged impact; b) Partially (0.75) engaged impact; c) Partially (0.50) engaged impact; d) Partially (0.25) engaged impact

C.3 Barge force-deformation relationships for impacts on partially engaged round surfaces

In a recent study, design-based barge force-deformation relationships were formed for direct (i.e., head-on, fully engaged) impacts with flat and round impact (pier) surfaces (Consolazio et al. 2009a). More specifically, Consolazio et al. (2009a) conducted quasi-static FE barge bow crushing simulations using LS-DYNA (LSTC 2009). In these simulations, either flat or round impact surfaces of varying widths (or diameters) were pressed into high-resolution barge bow models. Then, for each simulation, the crushing force was paired with the crushing deformation of the barge to form a barge bow force-deformation relationship (additional details are given in Consolazio et al. 2009a).

Barge force-deformation relationships for impacts on partially engaged, round surfaces have been developed in a similar manner for use, as applicable, in the CVIA simulations. Using the previously developed high-resolution FE barge bow model (from Consolazio et al. 2009a), barge bow crushing simulations were carried out in LS-DYNA for the configurations shown in Fig. C.4. Specifically, for 6 ft, 9 ft, and 12 ft diameter round surfaces, each of the crushing simulations depicted in Fig. C.4 were carried out so as to achieve a barge (crush) deformation of 12 ft. The results from the simulations are shown in Figs. C.5–C.7 and summarized in Fig. C.8.

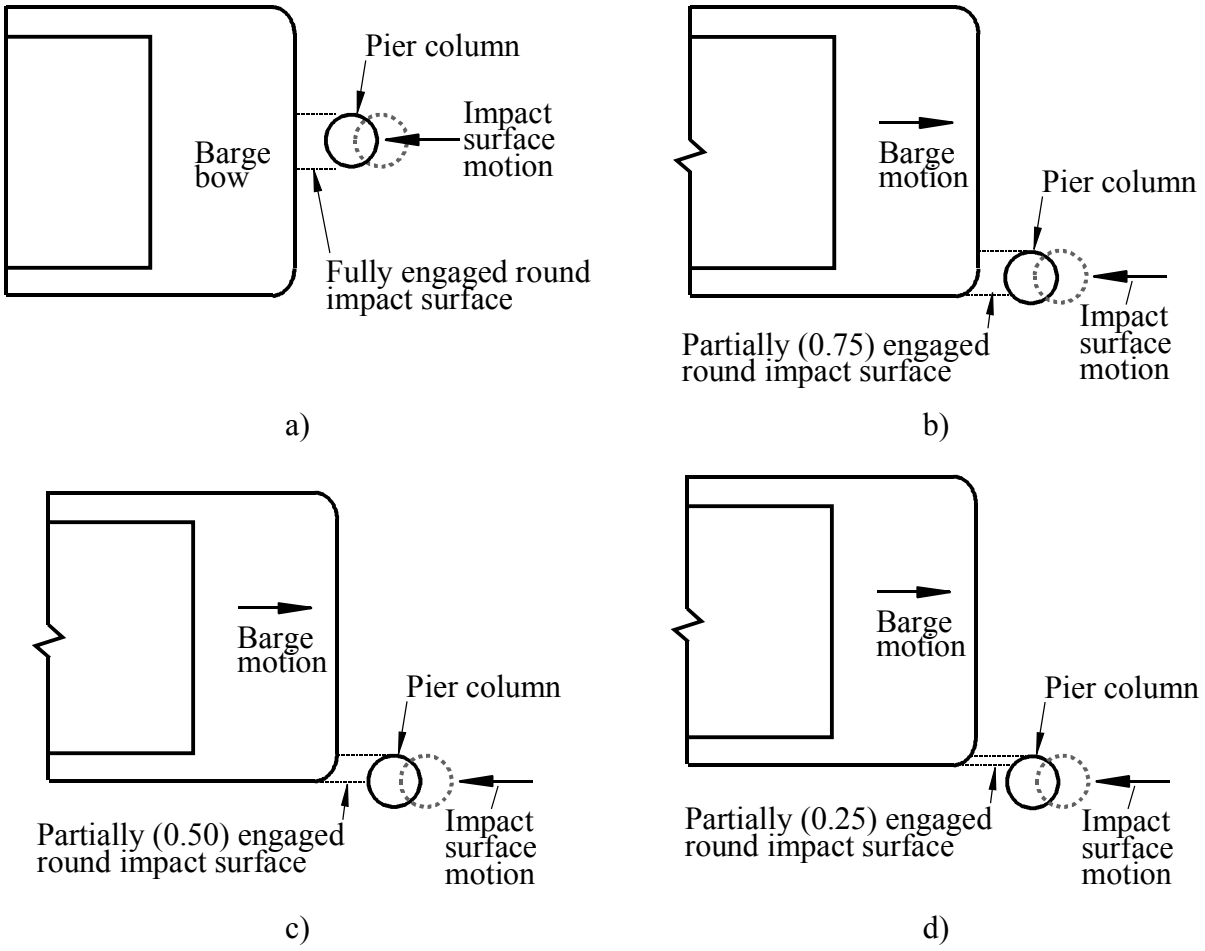

Figure C.4 Barge bow crushing simulations conducted. a) Fully engaged impact; b) Partially (0.75) engaged impact; c) Partially (0.50) engaged impact; d) Partially (0.25) engaged impact

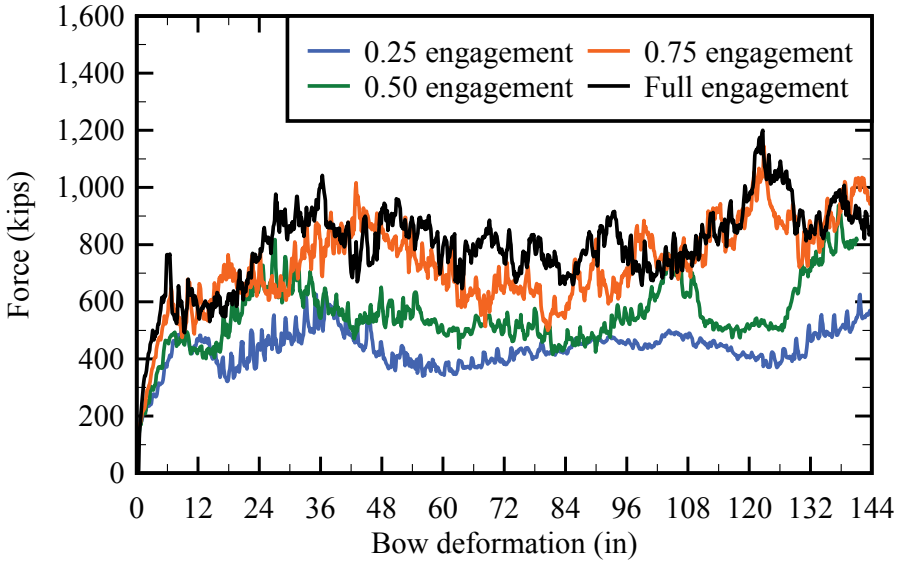

Figure C.5 LS-DYNA barge bow crushing simulations for a 6 ft round impact surface

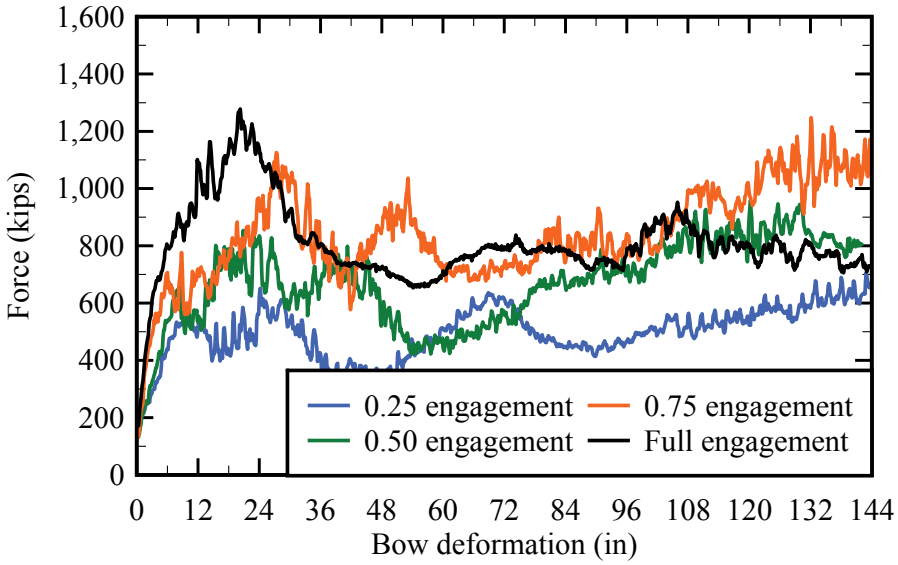

Figure C.6 LS-DYNA barge bow crushing simulations for a 9 ft round impact surface

During the crushing simulations, complex interactions between round impact surfaces and the as-modeled internal barge structure (which consists of a network of longitudinal and transverse stiffening members) can lead to maximum impact forces that are relatively larger than those corresponding to the fully engaged results (e.g., the 12 ft series, 0.75 engaged simulation, shown in Fig. C.8). Additionally, the barge crushing simulation results indicate that (even at severely reduced widths of impact surface engagement) significant relative maximum force levels are sustained. For example, for the simulations in which only 0.25 of the impact surface width is engaged, the maximum force magnitude is maintained at a ratio of nearly one-half the

fully engaged maximum force magnitude (Fig. C.8). This latter phenomenon corresponds to a conservative approach to maximum impact force prediction given that—at reduced levels of round impact surface engagement (i.e., for engagement width ratios less than 0.5)—the barge and impacted round surface may undergo a relative sliding (or glancing) type of impact motion that results in only nominal levels of barge crushing deformation, which tends to lead to reduced impact force magnitudes.

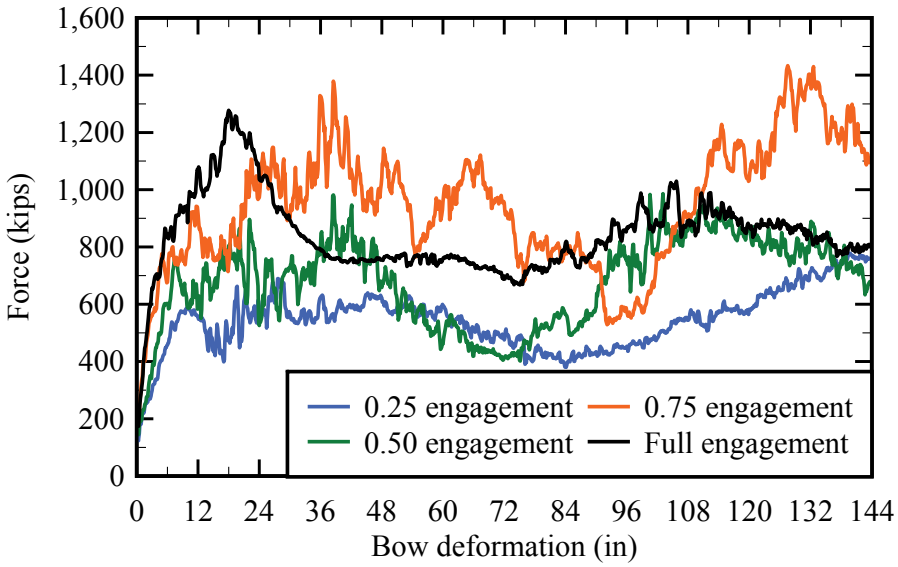

Figure C.7 LS-DYNA barge bow crushing simulations for a 12 ft round impact surface

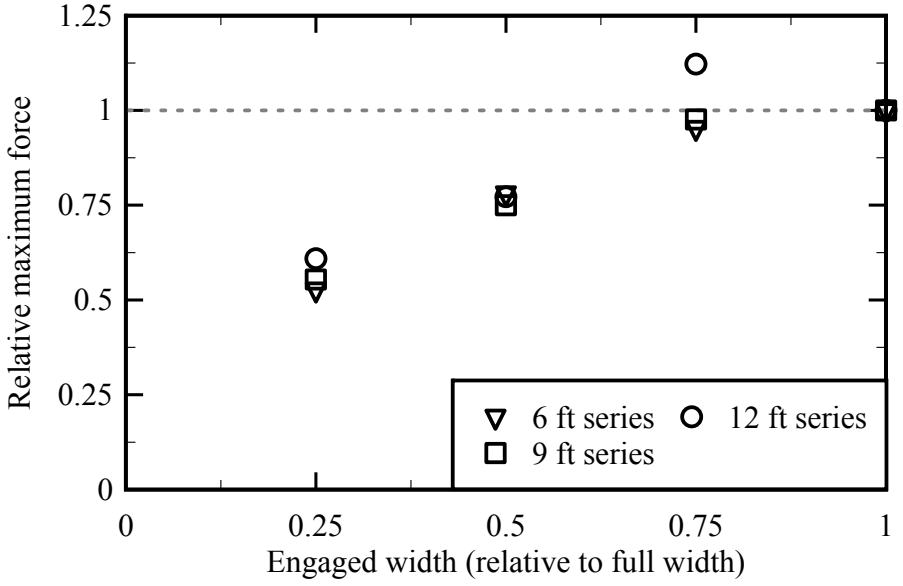

Figure C.8 Relative maximum forces for partial width impacts on round surfaces

Using the high-resolution FE barge bow crushing simulation results (filtered with a 100 Hz low-pass filter), an empirical expression was formed (Fig. C.9) that correlates engaged (round) impact surface width—relative to full impact surface width—to maximum barge impact force—relative to full impact surface width:

$$F_{rat} = 0.3 + 0.9 \cdot E_{rat}, F_{rat} \leq 1 \quad \text{(C.1)}$$

where F_{rat} is the maximum impact force ratio (with a maximum value of 1), and E_{rat} is the engaged impact width ratio. However, given the phenomena described above, Eq. C.1 has been paired with a previously developed, maximum impact force prediction equation for round surfaces that accounts for collision-related variability (e.g., barge structural configuration), where such variability could potentially have a significant effect on the above-described phenomena. Details of how these uncertainties factor into the expression are discussed in Consolazio et al. (2008). Specifically, the maximum impact force prediction equation is expressed as:

$$P_{BY} = 1500 + 30 \cdot w_P \quad \text{(C.2)}$$

where P_{BY} is the maximum barge impact force (kips), and w_P is the round impact surface width (ft).

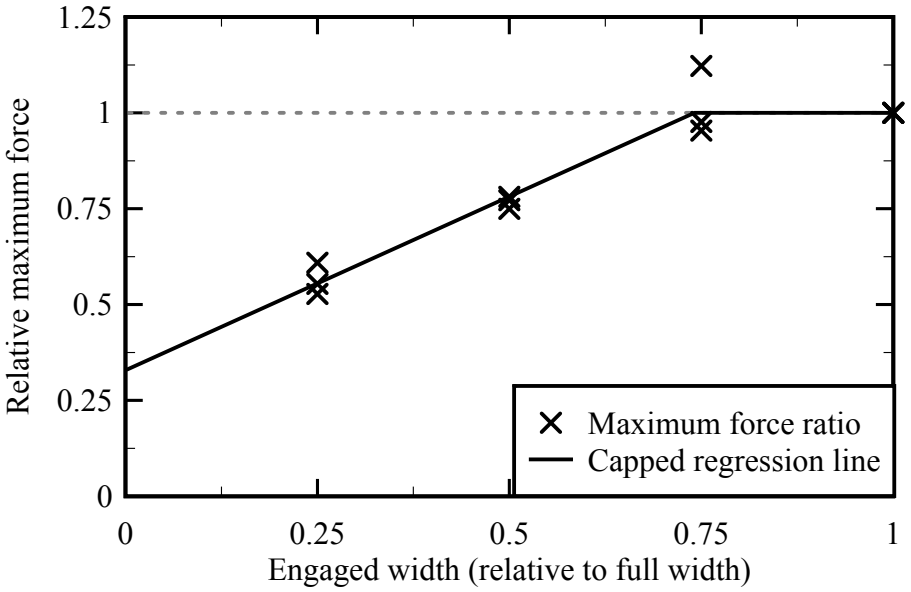

Figure C.9 Relative maximum force regression line for partial width impacts on round surfaces

In accordance with the findings of Consolazio et al. (2009a), Eq. C.2 can be used to form an elastic-perfectly plastic force-deformation relationship with a yield crush depth of 2 in. Furthermore, using Eq. C.1 in conjunction with Eq. C.2, a barge force-deformation relationship can be formed for a given round impact surface (and engaged width). For example, for a round impact surface with w_P equal to 5.5 ft that is partially engaged (where E_{rat} is equal to 0.6), F_{rat} equals 0.84 per Eq. C.1 and P_{BY} equals 1665 kips per Eq. C.2. Then, the product of F_{rat} and P_{BY}, 1399 kips, can be used to form an elastic perfectly-plastic barge force-deformation relationship (Fig. C.10) that, in turn, can be used in conjunction with the CVIA method to conduct the corresponding collision simulation. Note that the barge force-deformation unloading behavior is assumed to follow the initial slope.

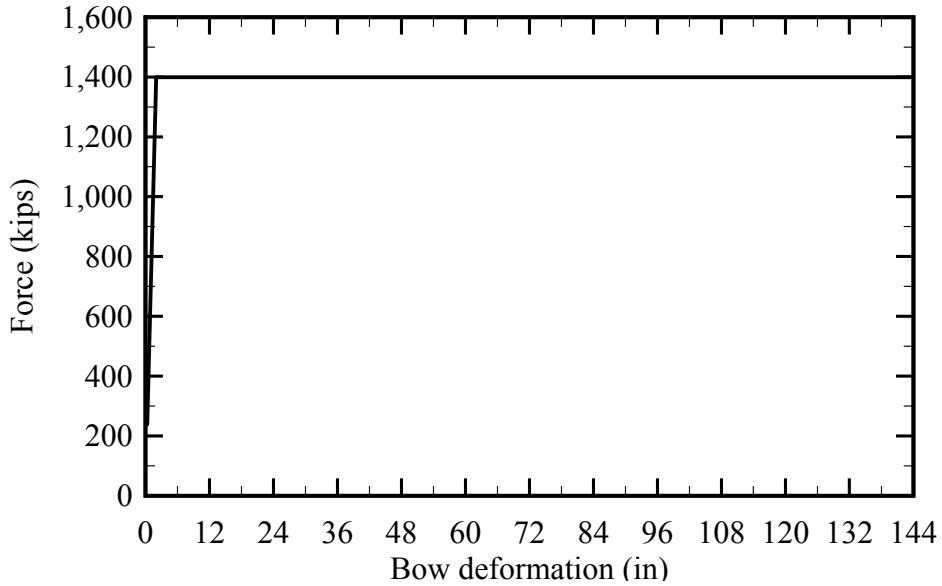

Figure C.10 Barge force-deformation relationship for a 5.5 ft diameter round impact surface with a 0.6 width engagement ratio

C.4 John Ringling Causeway, Pier 9 (RNG-OFF)

The John Ringling Causeway Bridge, constructed in 2003, spans the southern portion of Sarasota Bay in southwestern Florida. The structural model for Pier 9 (RNG-OFF) is shown in Fig. C.11. The pier contains a 25 ft tall, hollow bullet-shaped reinforced concrete cross-section, which is 13 ft in diameter at the narrow ends. Also, the bullet cross-section has a constant 2.7 ft wall thickness. The pier rests on an 8.8 ft thick, bullet-shaped pile cap overlying two round, solid reinforced-concrete drilled shafts of 9 ft diameter. The thick, concrete filled, bullet-shaped pile cap for RNG-OFF is positioned (vertically) near the mean high water (MHW) elevation for Sarasota Bay. Consequently, the pile cap is generally the only member susceptible to direct contact during barge collision events. However, barge force-deformation relationships have not previously been formed for impacts on bullet-shaped structural members. The development of barge force-generation relationships for the RNG-OFF case is discussed below.

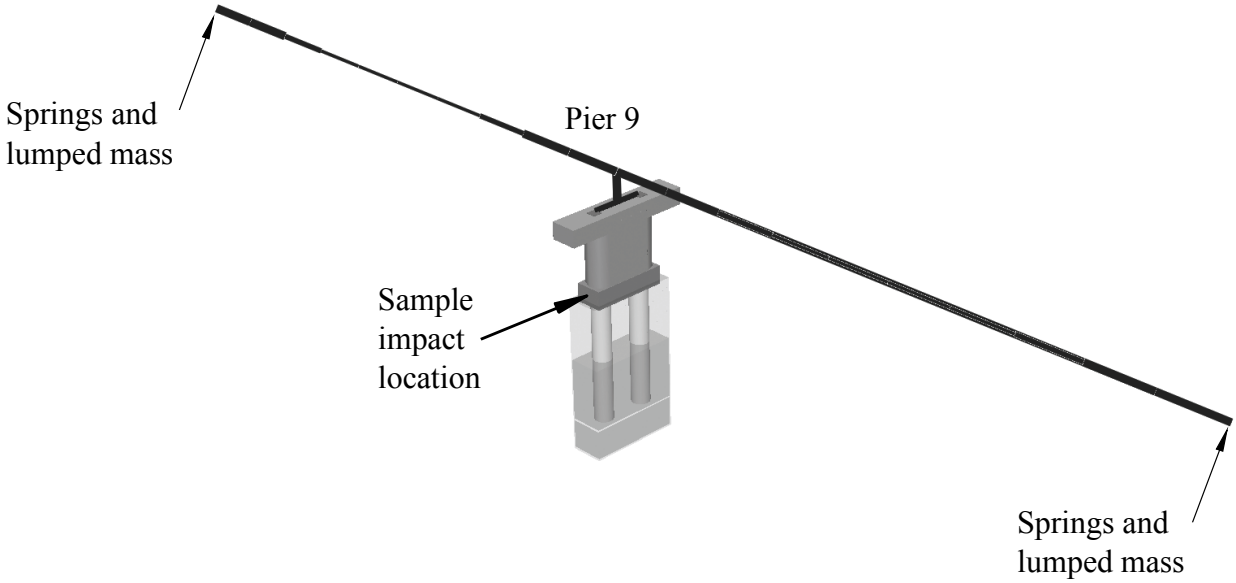

Figure C.11 John Ringling Causeway, Pier 9 (RNG-OFF) OPTS model

C.4.1 Use of force-displacement relationships for RNG-OFF simulations

For both the set of simulations conducted by Consolazio et al. (2009a) and those pertaining to the partially engaged round surface impacts (described above), one-to-one matching was approximately achieved between the motion of the impact surface and the magnitude of barge crushing deformation generated by the advancing flat or round impact surface shapes. Consequently, design force-deformation relationships were readily formed from the simulation results. Accordingly, for collision scenarios in which the front portion of the bullet-shaped surface is engaged by the barge (Fig. C.12), the barge tends to deform around the impacted surface. Therefore, the previously developed force-deformation relationships can be employed.

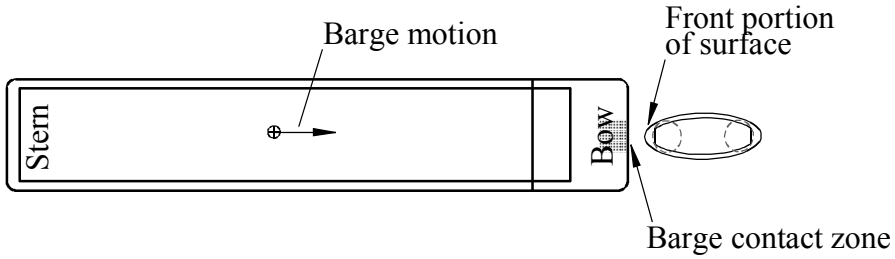

Figure C.12 Collision between a barge and the front portion of bullet-shape impact surface

However, for barge collision simulations involving other portions of the bullet-shaped surface, the impacting barge generally demonstrates a tendency to slide across the impacted surface portion (rather than deform around the impacted surface). For example, consider the collision between a loaded Jumbo Hopper barge (weighing 1645 tons) and the RNG-OFF pile cap (Fig. C.13).

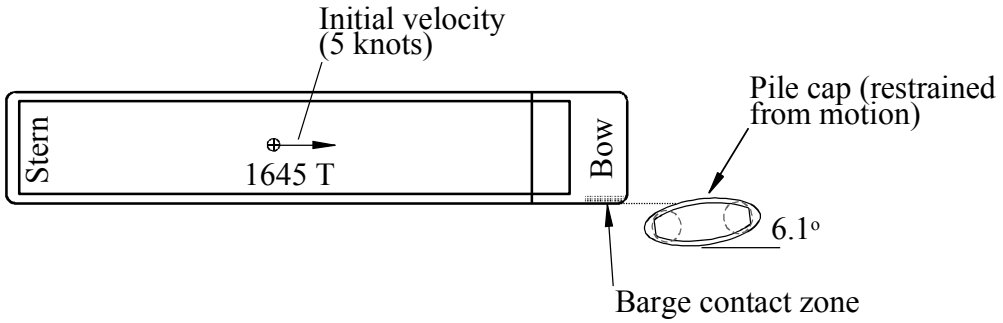

Figure C.13 Collision between a loaded Jumbo Hopper barge and the RNG-OFF pile cap

The collision scenario shown in Fig. C.13 is possible given the John Ringling Causeway (RNG) structural layout and associated waterway traffic conditions. The relative barge-pier orientation shown is based on the intended vessel transit path (which is 6.1° skew) for waterway traffic that passes under the John Ringling Causeway (RNG). Furthermore, the initial velocity, prescribed at 5 knots, is consistent with known vessel-bridge collision design parameters given in the RNG structural plans (Consolazio et al. 2008). The impact scenario, when simulated using the finite element analysis (FEA) software LS-DYNA (LSTC 2009) and a previously developed high-resolution FE barge model (barge model development is detailed in Consolazio et al. 2010), produces only nominal barge crushing deformation. Instead, the barge slides across more than 5 ft of the pier surface (Fig. C.14); note that the force-displacement history has been filtered with a 100 Hz low-pass filter. Due to the predominant sliding behavior of the barge (relative to the impacted pier surface), the direct generation of barge force-deformation (i.e., barge force-crushing) relationships for use with CVIA is precluded.

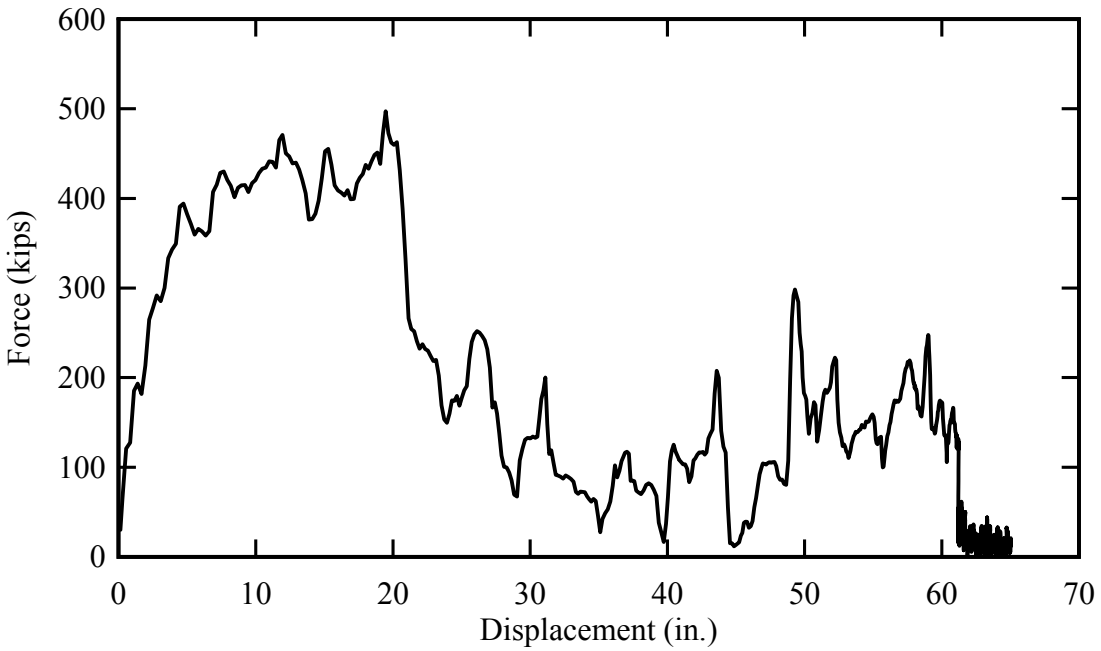

Figure C.14 LS-DYNA barge force-displacement history

Although, generally, the CVIA technique is intended for use with force-deformation relationships, force-displacement relationships are employed as part of the CVIA technique for the RNG-OFF simulations. In this context, force-displacement indicates the pairing of resultant collision force and resultant barge motion (as opposed to barge crushing deformation). For the applicable RNG-OFF collision scenarios, the approximation of barge force-generation behavior as a force-displacement relationship—in conjunction with use of the CVIA method—has been found to produce reasonable predictions of collision force-histories. For example, for the impact scenario discussed above, the impact force-history predicted by the high-resolution LS-DYNA simulation shows reasonable agreement with that predicted by the corresponding FB-MultiPier simulation (with use of CVIA and the force-displacement history, shown in Fig. C.14, as a description of the SDF barge model).

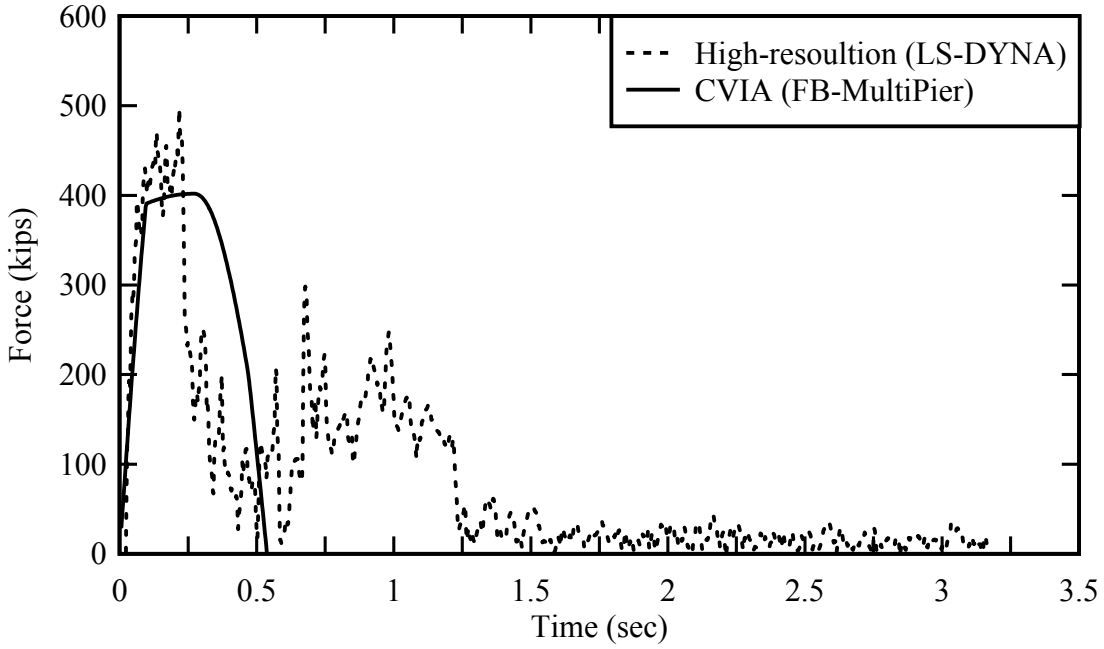

Figure C.15 Collision simulation force-history comparison

C.4.2 Barge force-deformation relationships specific to the RNG-OFF simulations

The bullet-shaped pile cap of RNG-OFF has been divided into three impact zones (Fig. C.16), where the initial contact point between the barge and the impacted surface is used to determine the applicable barge force-generation relationships. For impact (initial contact) in Zone 1, the previously developed (and above described) barge force-deformation relationships for round impact surfaces are employed. In contrast, for impact (initial contact) in Zone 2 or Zone 3, the approximation of barge force-generation relationships using force-displacement relationships is necessitated. The relative barge-surface orientations considered are representative of the practical range of impact scenarios (see Appendix B for vessel transit path characteristics specific to RNG-OFF)

Given the reasonable level of success associated with the use of force-displacement relationships (in conjunction with the CVIA method), an inventory of barge force-displacement relationships specific to the RNG-OFF pile cap shape have been formed. Specifically, for each of the impact scenarios shown in Figs. C.17–C.24, a collision simulation was carried out using LS-DYNA and a previously developed high-resolution barge FE model with a prescribed initial velocity of 5 knots (model development is described in Consolazio et al. 2010). Note that, to facilitate incorporation of the Zone 2 and Zone 3 simulation results into the CVIA technique, the results obtained from each simulation have been filtered with a 100 Hz low-pass filter and post-processed using a kernel smoothing technique. More specifically, the impact force and barge displacement filtered history data were each resampled using a point-by-point local weighted average (based on a Gaussian kernel with a bandwidth of 0.1 sec). Then, the filtered-smoothed force and displacement histories were paired through time to form a corresponding force-displacement history. Subsequently, the force-displacement history ordinates were scaled by 1.33 to account for collision-related uncertainties (in accordance with Consolazio et al. 2009a).

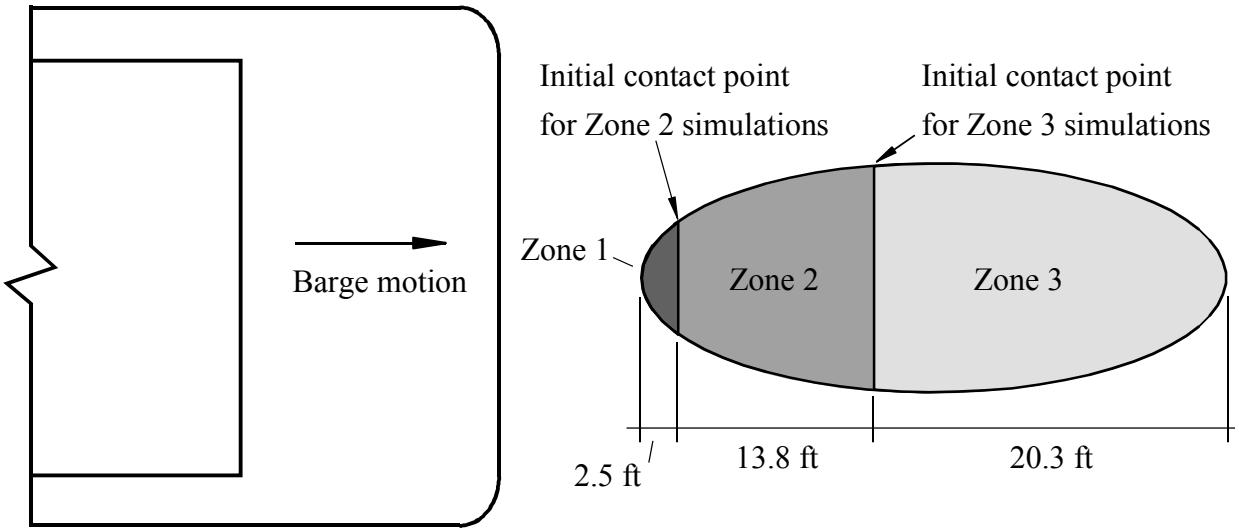

Figure C.16 RNG-OFF pile cap impact zones

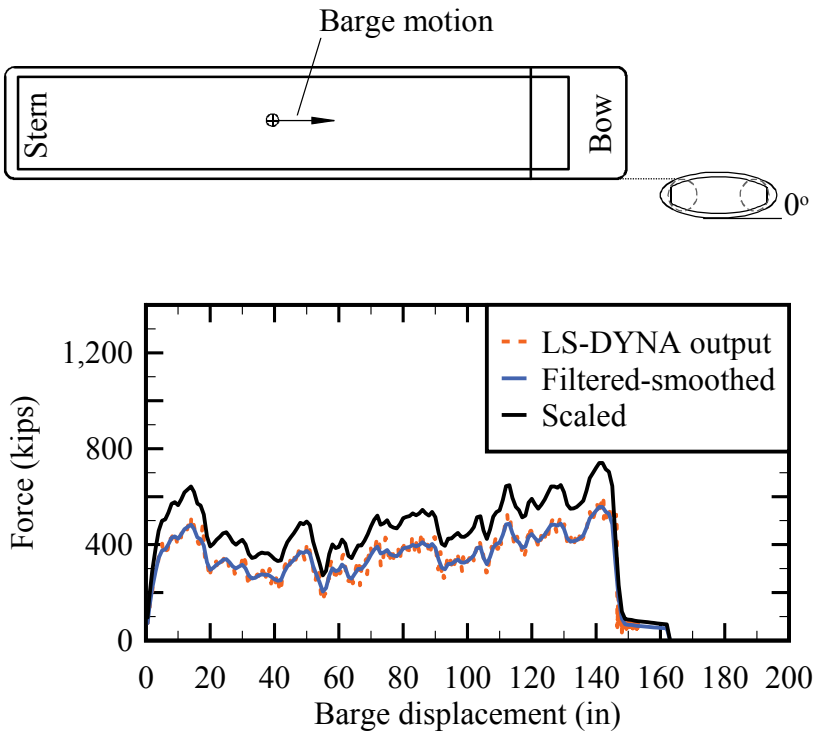

Figure C.17 Force-displacement relationship for 0° impact in zone 2

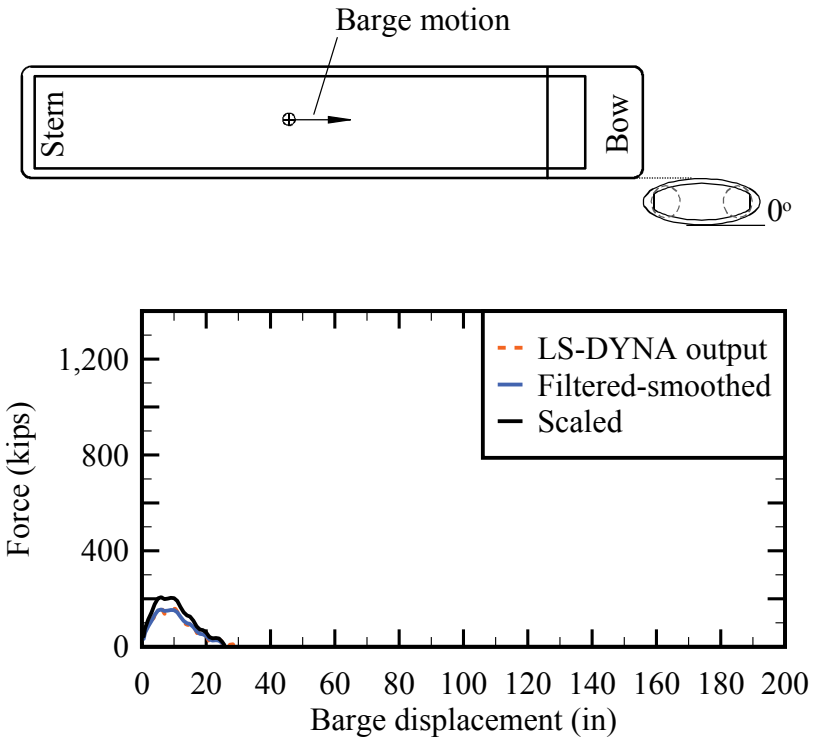

Figure C.18 Force-displacement relationship for 0° impact in zone 3

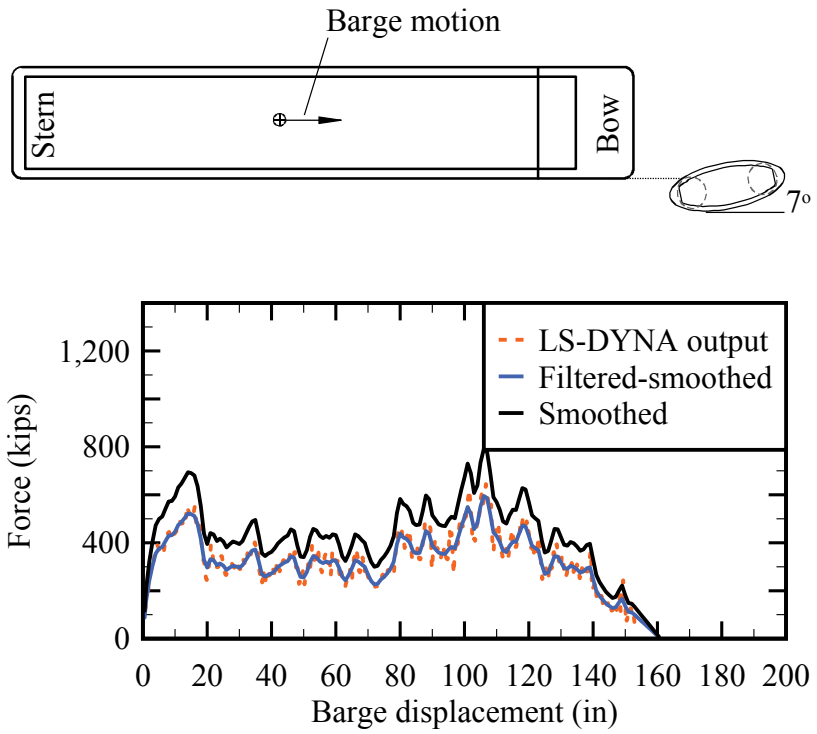

Figure C.19 Force-displacement relationship for 7° impact in zone 2

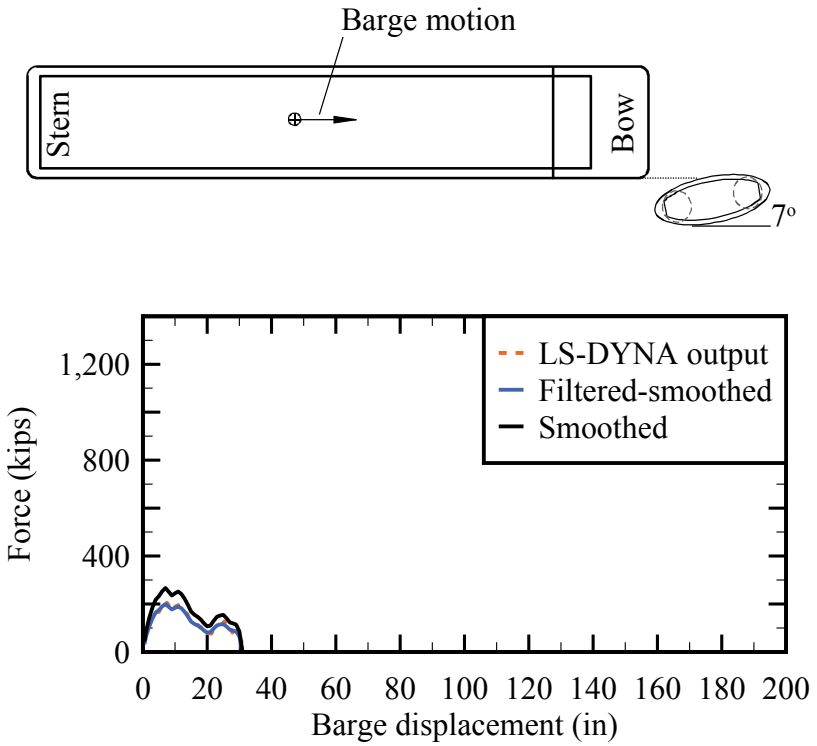

Figure C.20 Force-displacement relationship for 7° impact in zone 3

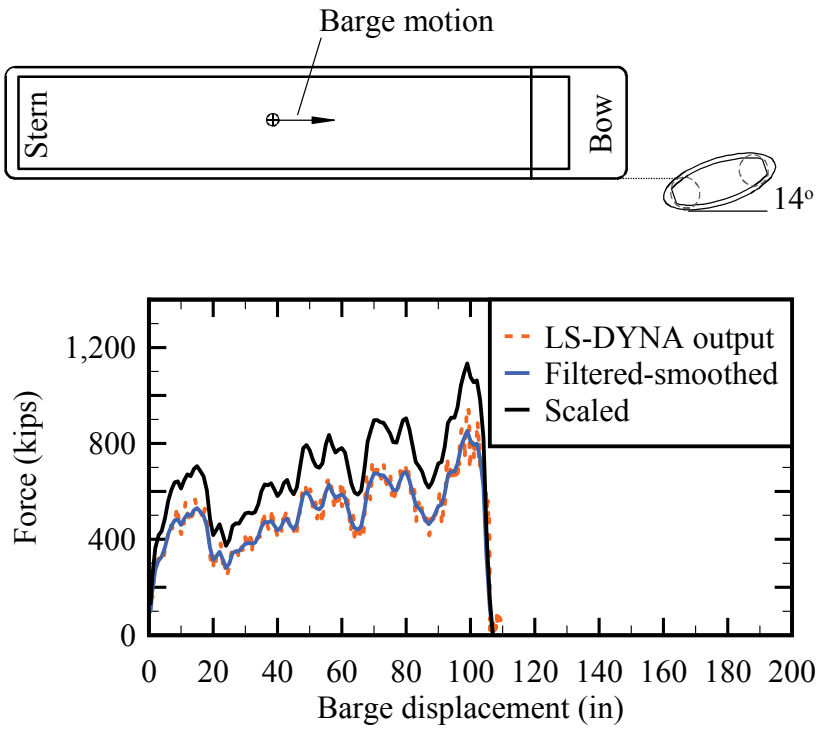

Figure C.21 Force-displacement relationship for 14° impact in zone 2

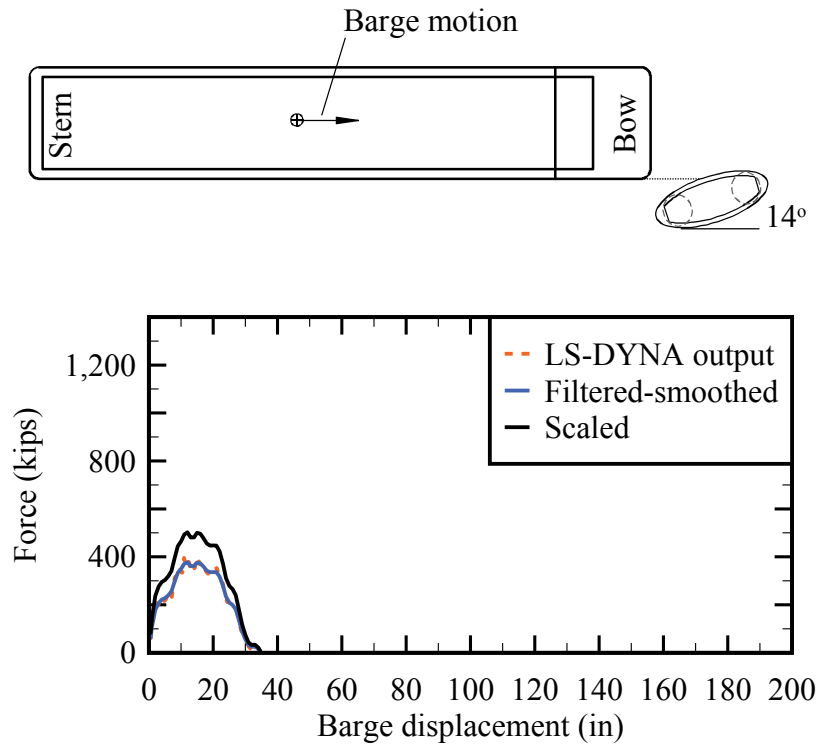

Figure C.22 Force-displacement relationship for 14° impact in zone 3

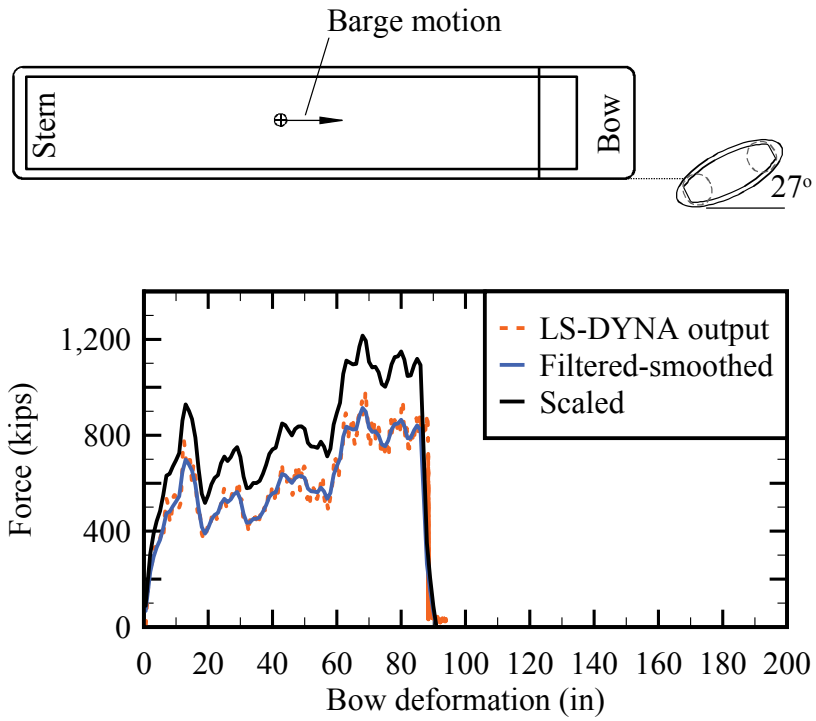

Figure C.23 Force-displacement relationship for 27° impact in zone 2

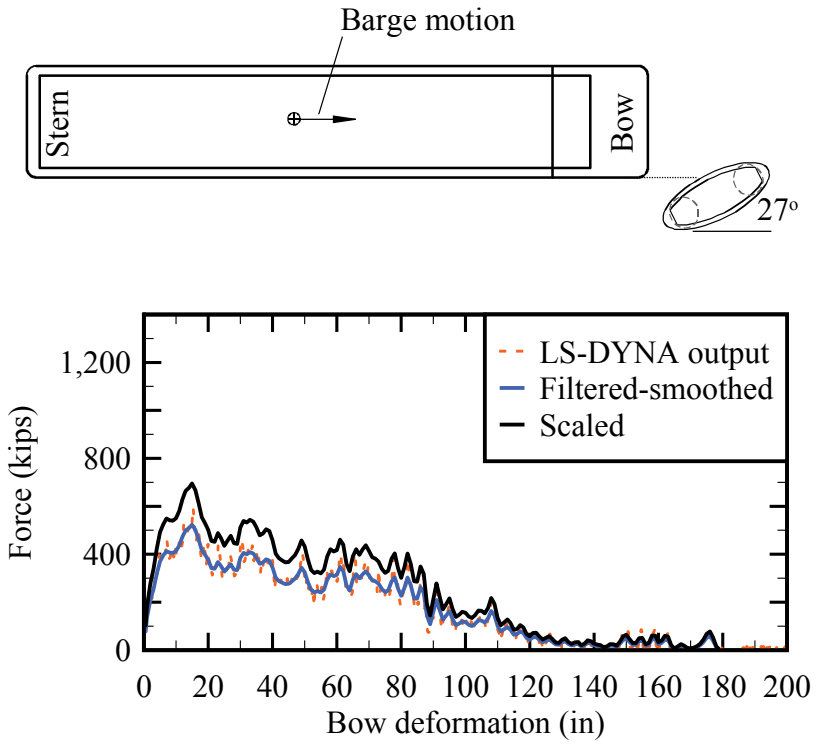

Figure C.24 Force-displacement relationship for 27° impact in zone 3

The process of forming barge force-displacement relationships for use in the CVIA simulations of RNG-OFF is illustrated for the impact scenario shown in Fig. C.25. Since impact occurs in Zone 2 and at an angle of 10°, point-by-point linear interpolation between the force-displacement curves shown in Fig. C.19 and Fig. C.21 are used to approximate the applicable force-displacement relationship (Fig. C.26). Then, the force-displacement relationship can be used in conjunction with the CVIA method to conduct the corresponding collision simulation. Note that unloading behavior is assumed to follow the initial slope of the interpolated force-displacement relationship.

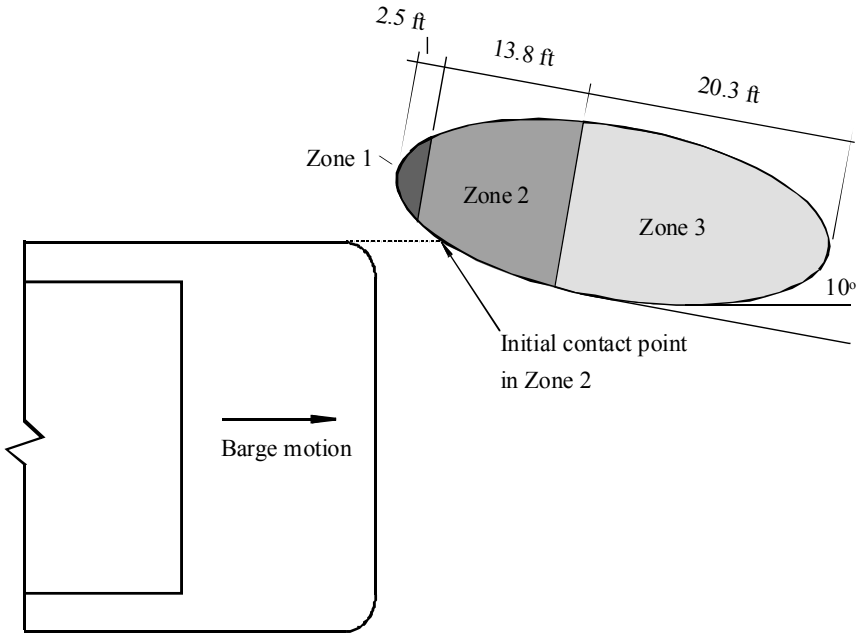

Figure C.25 Schematic for 10° barge impact in Zone 2 of the RNG-OFF pile cap

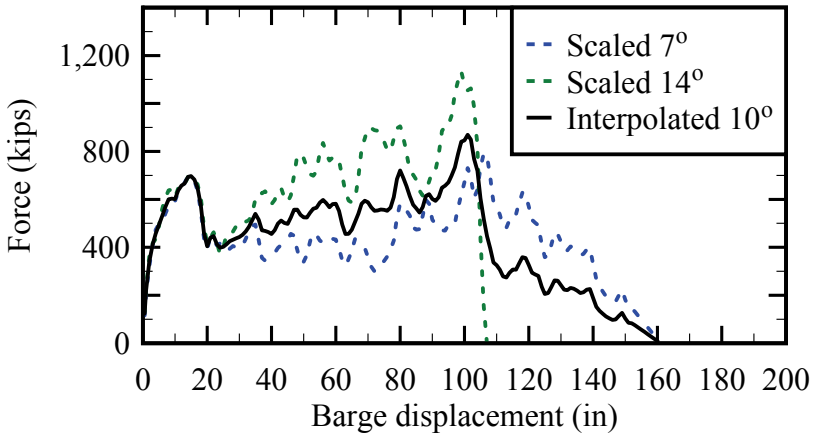

Figure C.26 Force-displacement relationship for 10° impact in zone 2

APPENDIX D
DETAILED BARGE BOW FORCE-DEFORMATION DATA FROM HIGH-RESOLUTION FINITE ELEMENT ANALYSES OF OBLIQUE CRUSHING

A parametric study of high-resolution finite element barge bow crushing simulations has been conducted to assess the influence of oblique crushing scenarios on barge bow force-deformation characteristics and peak forces generated during crushing (see Chapter 9). The parametric study consists of more than fifty (50) bow crushing simulations involving pier surfaces (with widths of 6 – 35 ft) being crushed quasi-statically into a jumbo hopper barge bow model at various oblique angles (ranging from 0° – 45°). Throughout each simulation, contact forces between the barge and pier models are monitored and paired with the specified crushing rate to form force-deformation curves for each simulation. Detailed force-deformation data resulting from the parametric study are presented in this appendix.

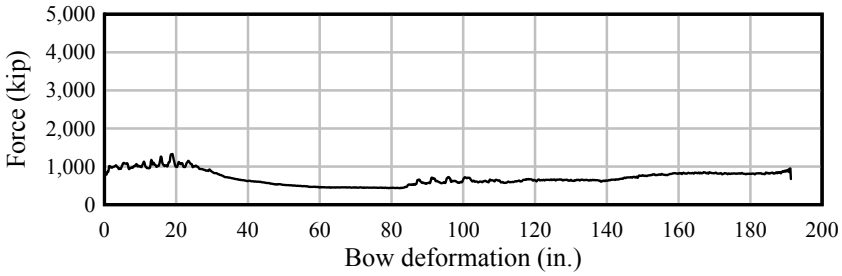

Figure D.1 Barge bow force-deformation data. 6-ft flat-faced pier surface at 0°

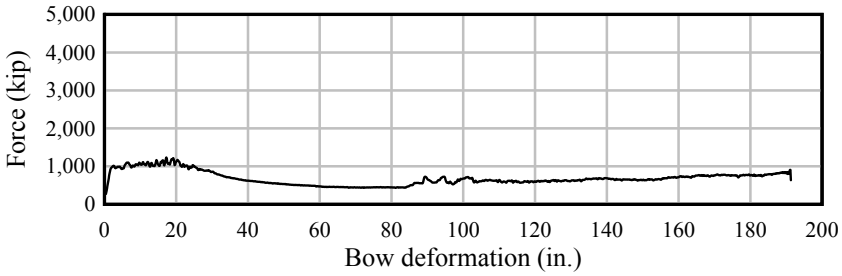

Figure D.2 Barge bow force-deformation data. 6-ft flat-faced pier surface at 1°

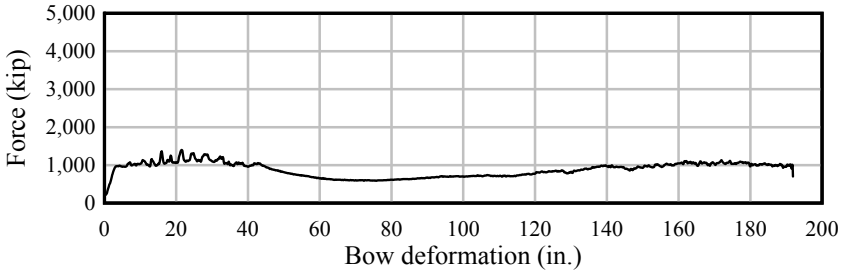

Figure D.3 Barge bow force-deformation data. 6-ft flat-faced pier surface at 2°

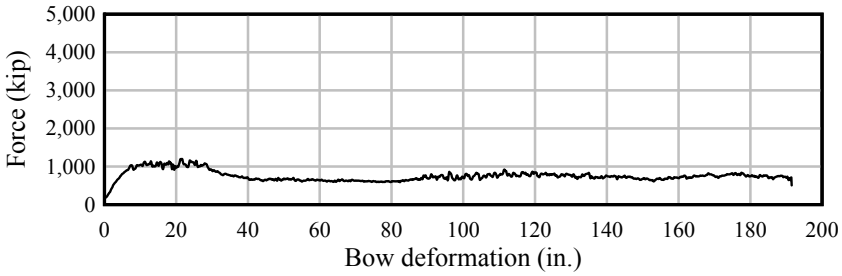

Figure D.4 Barge bow force-deformation data. 6-ft flat-faced pier surface at 5°

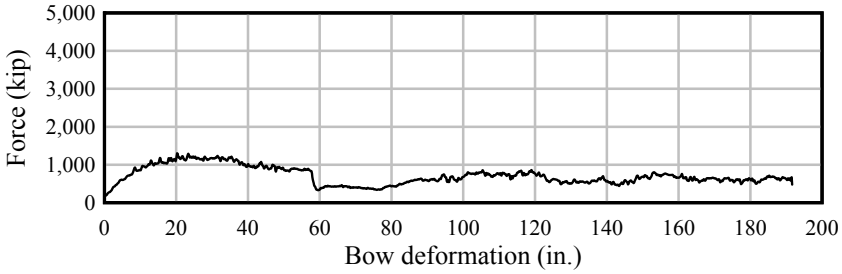

Figure D.5 Barge bow force-deformation data. 6-ft flat-faced pier surface at 10°

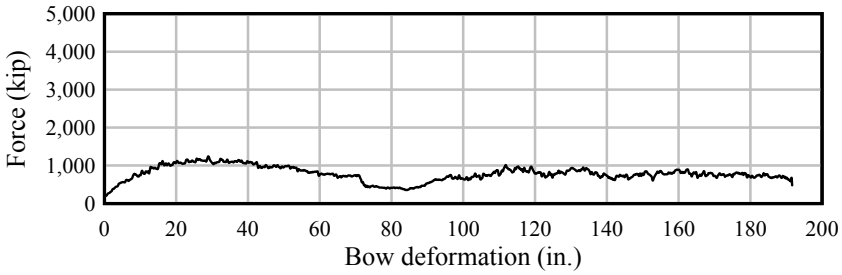

Figure D.6 Barge bow force-deformation data. 6-ft flat-faced pier surface at 15°

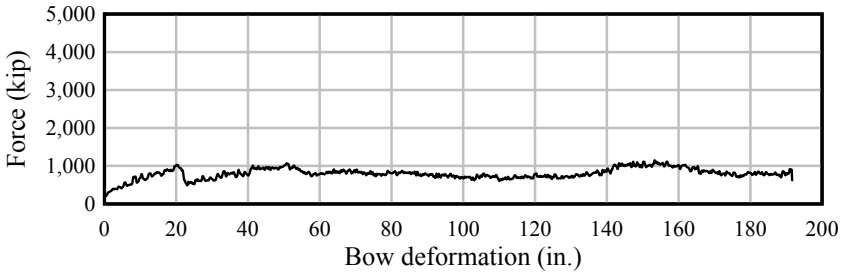

Figure D.7 Barge bow force-deformation data. 6-ft flat-faced pier surface at 30°

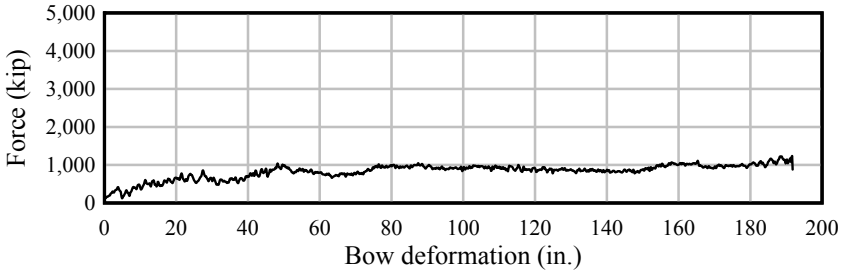

Figure D.8 Barge bow force-deformation data. 6-ft flat-faced pier surface at 45°

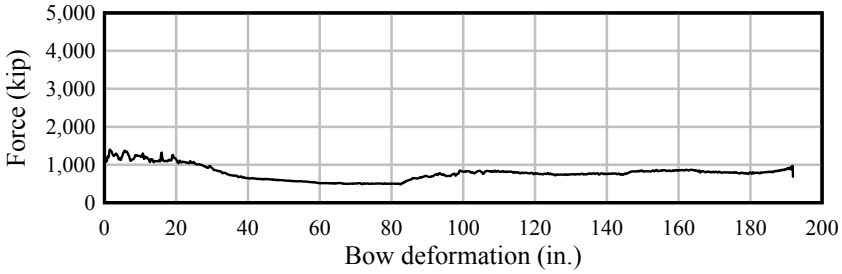

Figure D.9 Barge bow force-deformation data. 9-ft flat-faced pier surface at 0°

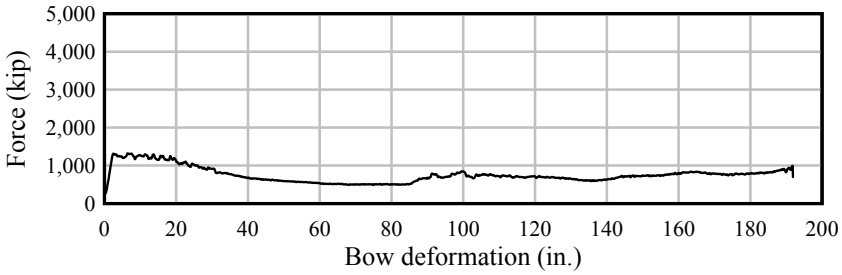

Figure D.10 Barge bow force-deformation data. 9-ft flat-faced pier surface at 1°

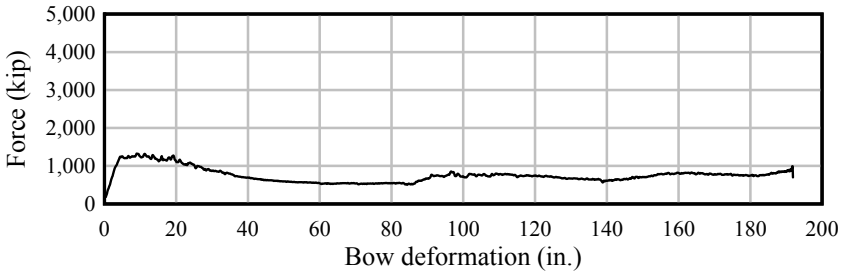

Figure D.11 Barge bow force-deformation data. 9-ft flat-faced pier surface at 2°

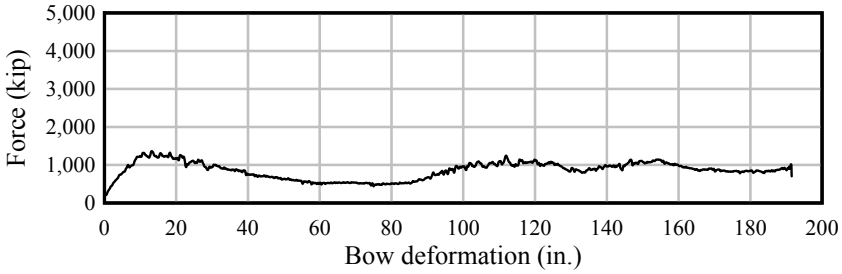

Figure D.12 Barge bow force-deformation data. 9-ft flat-faced pier surface at 5°

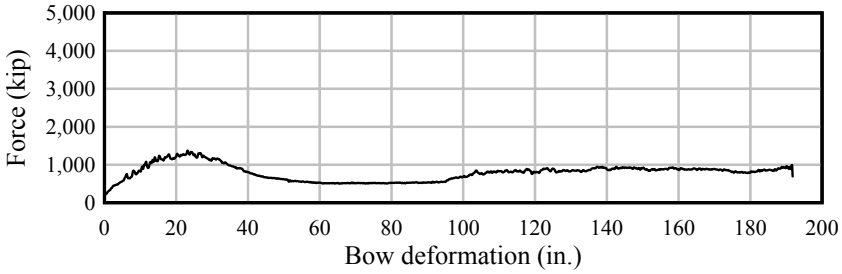

Figure D.13 Barge bow force-deformation data. 9-ft flat-faced pier surface at 10°

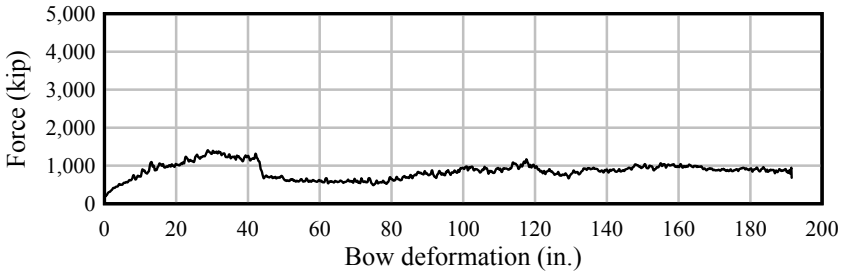

Figure D.14 Barge bow force-deformation data. 9-ft flat-faced pier surface at 15°

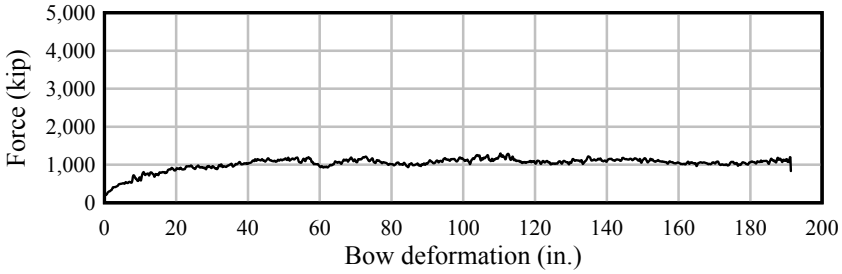

Figure D.15 Barge bow force-deformation data. 9-ft flat-faced pier surface at 30°

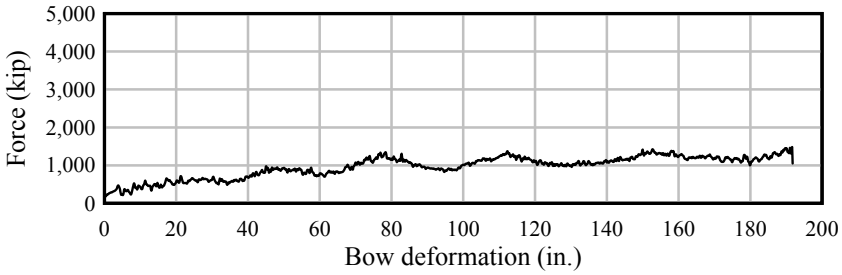

Figure D.16 Barge bow force-deformation data. 9-ft flat-faced pier surface at 45°

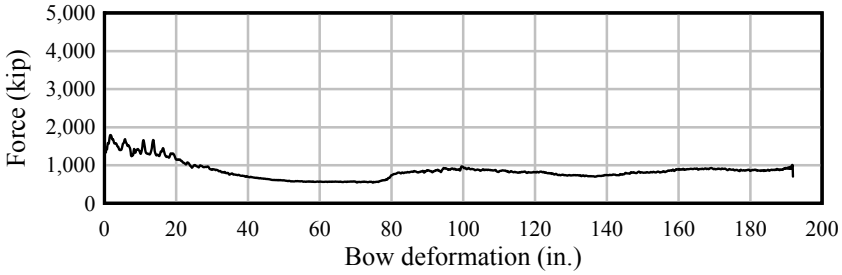

Figure D.17 Barge bow force-deformation data. 12-ft flat-faced pier surface at 0°

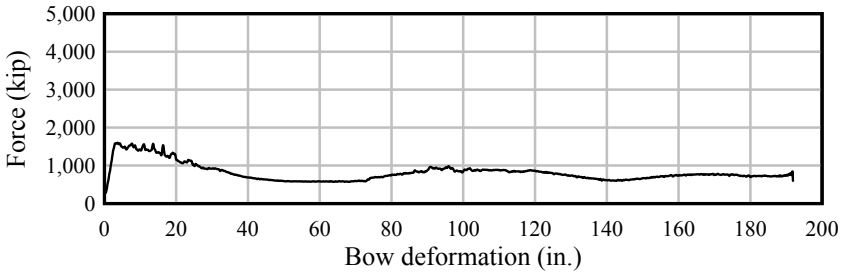

Figure D.18 Barge bow force-deformation data. 12-ft flat-faced pier surface at 1°

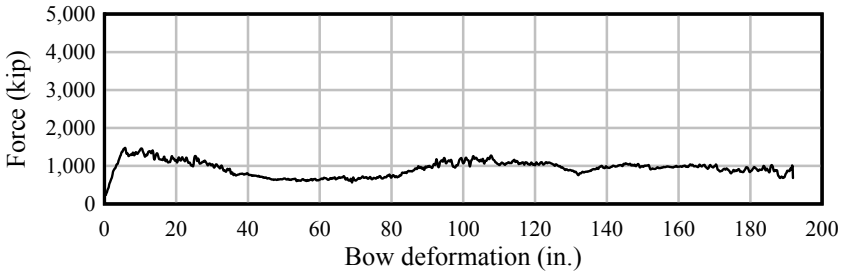

Figure D.19 Barge bow force-deformation data. 12-ft flat-faced pier surface at 2°

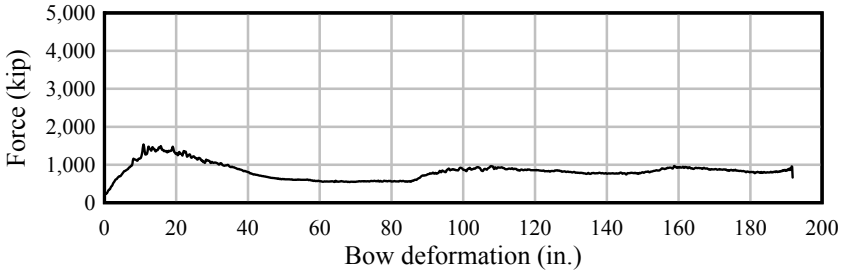

Figure D.20 Barge bow force-deformation data. 12-ft flat-faced pier surface at 5°

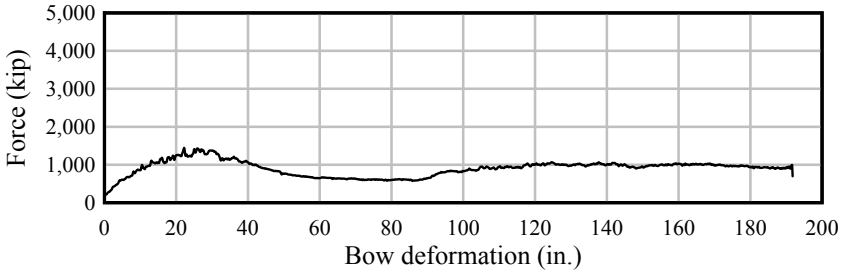

Figure D.21 Barge bow force-deformation data. 12-ft flat-faced pier surface at 10°

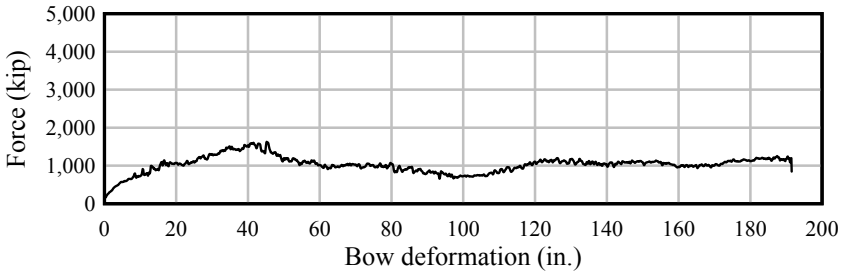

Figure D.22 Barge bow force-deformation data. 12-ft flat-faced pier surface at 15°

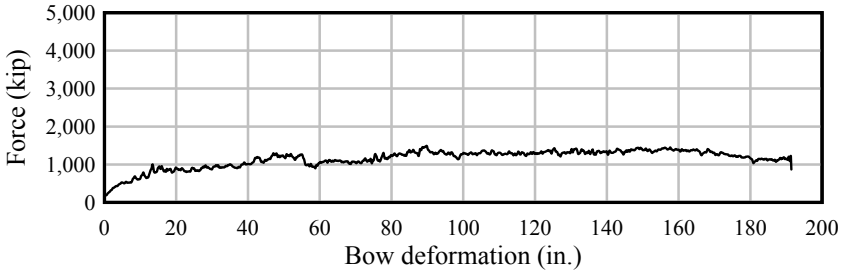

Figure D.23 Barge bow force-deformation data. 12-ft flat-faced pier surface at 30°

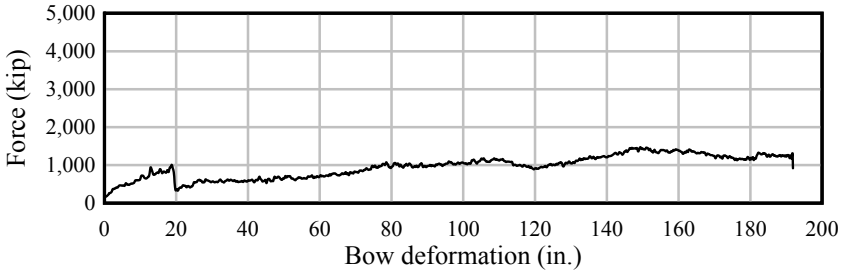

Figure D.24 Barge bow force-deformation data. 12-ft flat-faced pier surface at 45°

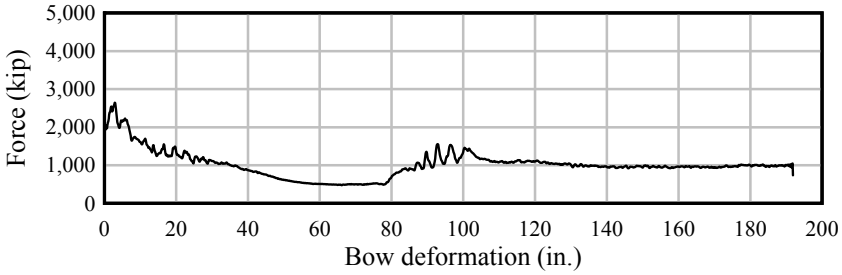

Figure D.25 Barge bow force-deformation data. 18-ft flat-faced pier surface at 0°

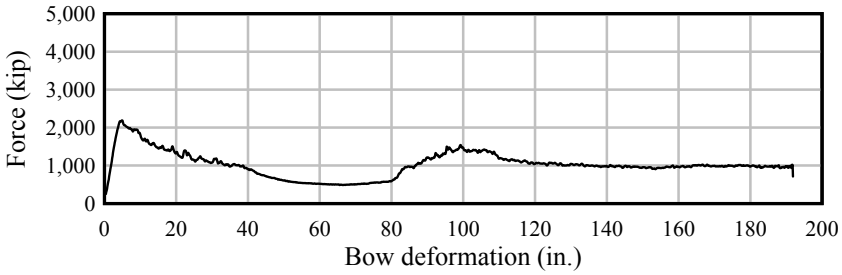

Figure D.26 Barge bow force-deformation data. 18-ft flat-faced pier surface at 1°

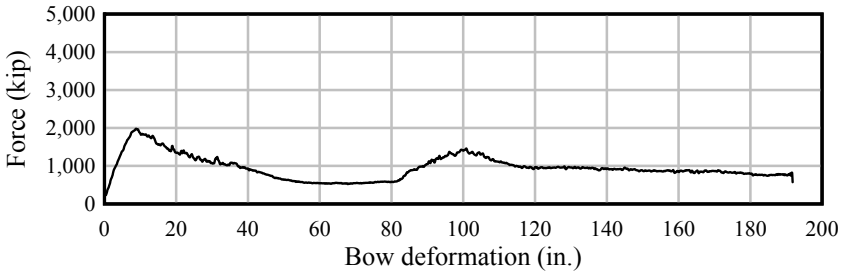

Figure D.27 Barge bow force-deformation data. 18-ft flat-faced pier surface at 2°

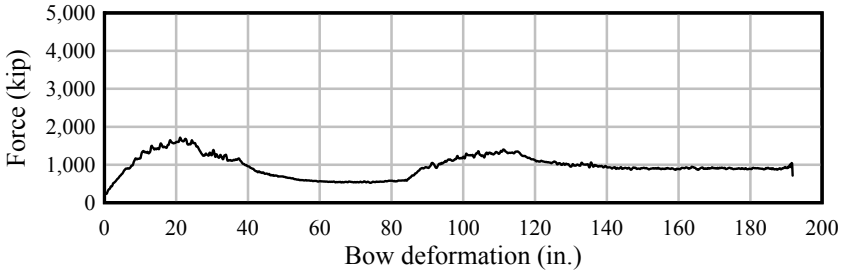

Figure D.28 Barge bow force-deformation data. 18-ft flat-faced pier surface at 5°

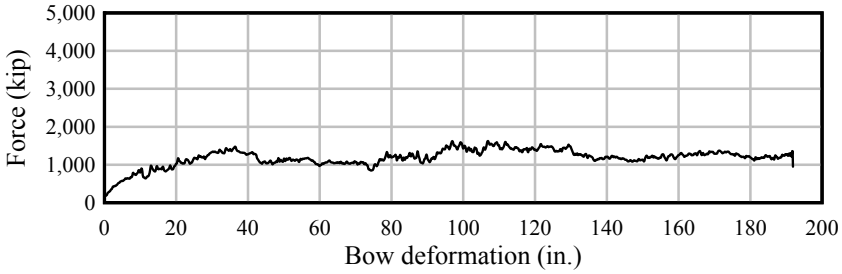

Figure D.29 Barge bow force-deformation data. 18-ft flat-faced pier surface at 10°

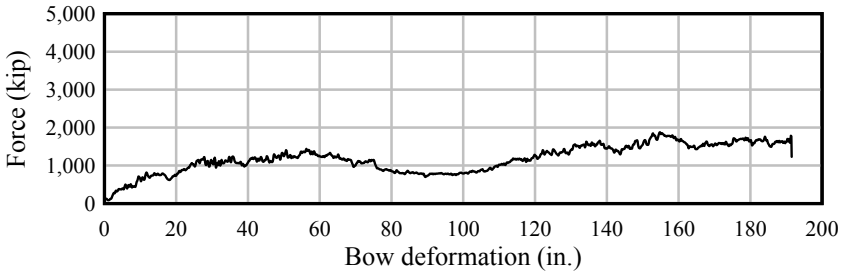

Figure D.30 Barge bow force-deformation data. 18-ft flat-faced pier surface at 15°

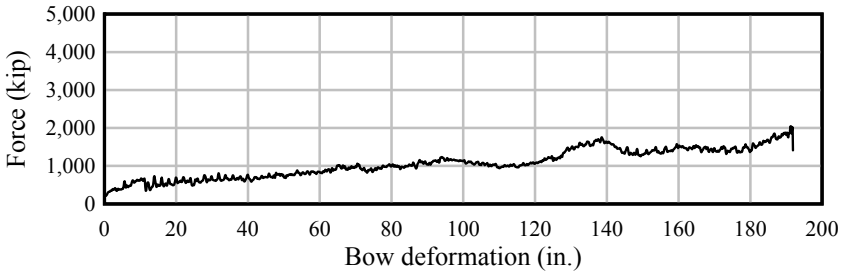

Figure D.31 Barge bow force-deformation data. 18-ft flat-faced pier surface at 30°

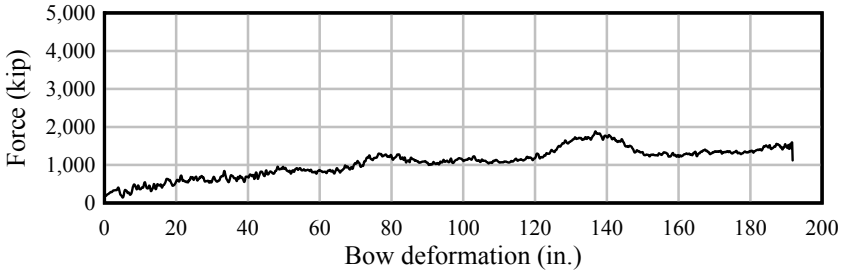

Figure D.32 Barge bow force-deformation data. 18-ft flat-faced pier surface at 45°

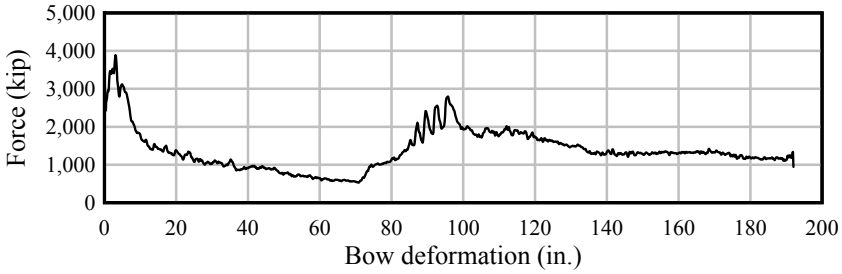

Figure D.33 Barge bow force-deformation data. 26-ft flat-faced pier surface at 0°

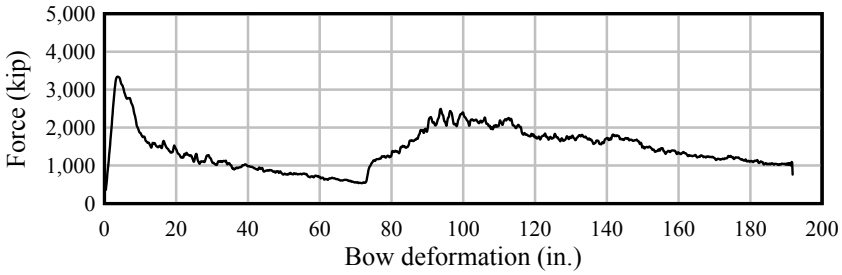

Figure D.34 Barge bow force-deformation data. 26-ft flat-faced pier surface at 0.5°

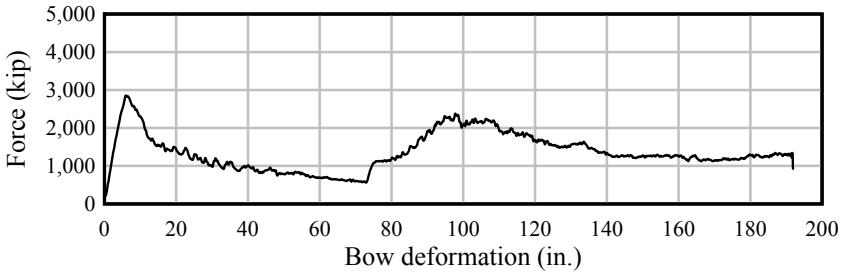

Figure D.35 Barge bow force-deformation data. 26-ft flat-faced pier surface at 1°

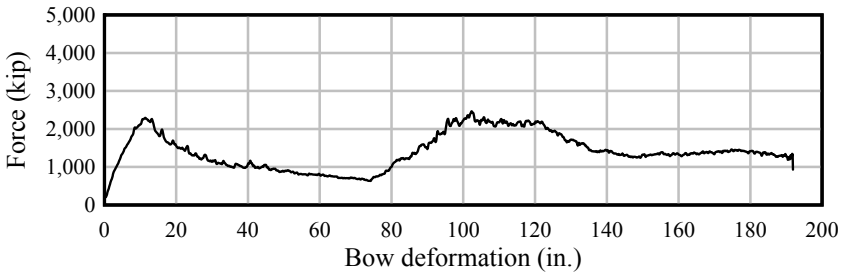

Figure D.36 Barge bow force-deformation data. 26-ft flat-faced pier surface at 2°

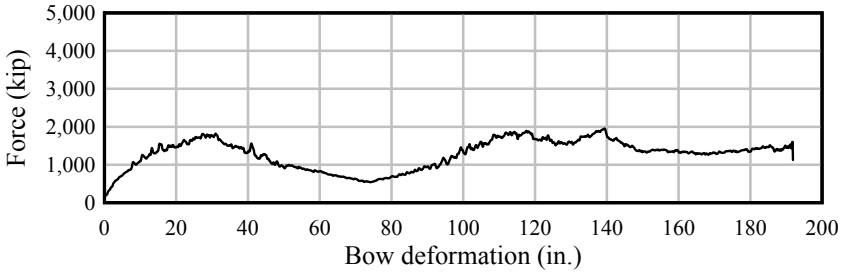

Figure D.37 Barge bow force-deformation data. 26-ft flat-faced pier surface at 5°

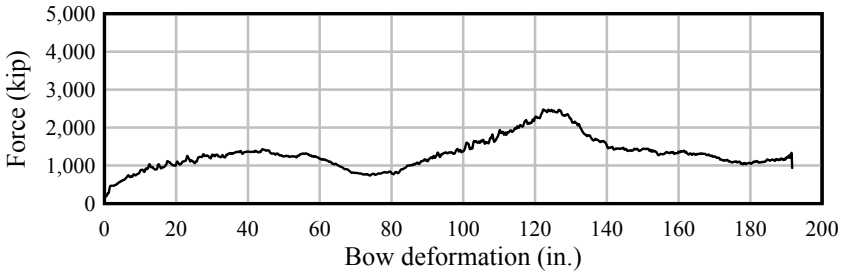

Figure D.38 Barge bow force-deformation data. 26-ft flat-faced pier surface at 10°

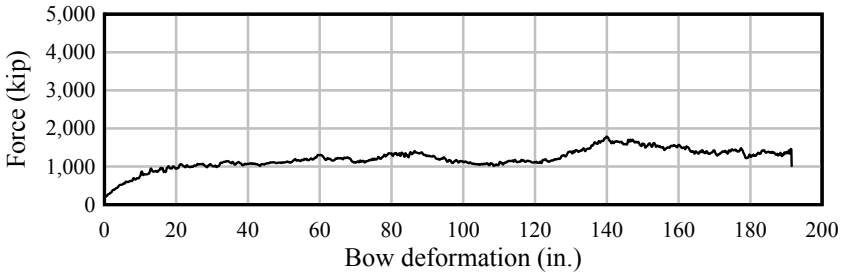

Figure D.39 Barge bow force-deformation data. 26-ft flat-faced pier surface at 15°

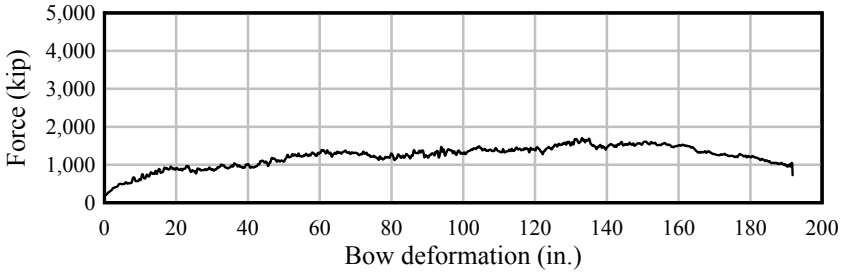

Figure D.40 Barge bow force-deformation data. 26-ft flat-faced pier surface at 30°

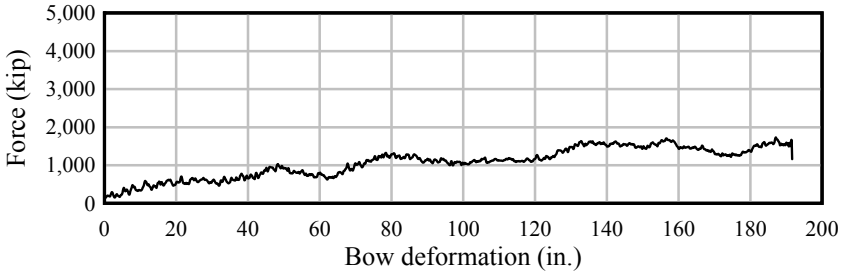

Figure D.41 Barge bow force-deformation data. 26-ft flat-faced pier surface at 45°

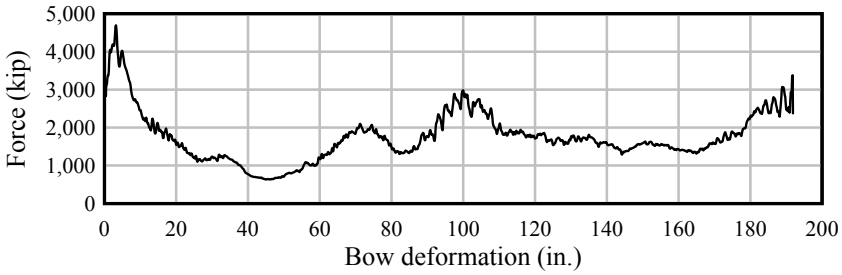

Figure D.42 Barge bow force-deformation data. 35-ft flat-faced pier surface at 0°

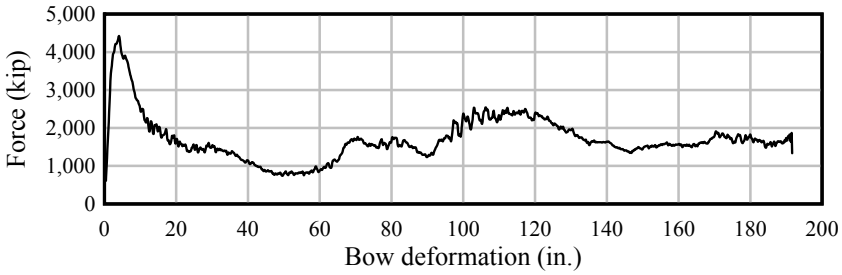

Figure D.43 Barge bow force-deformation data. 35-ft flat-faced pier surface at 0.25°

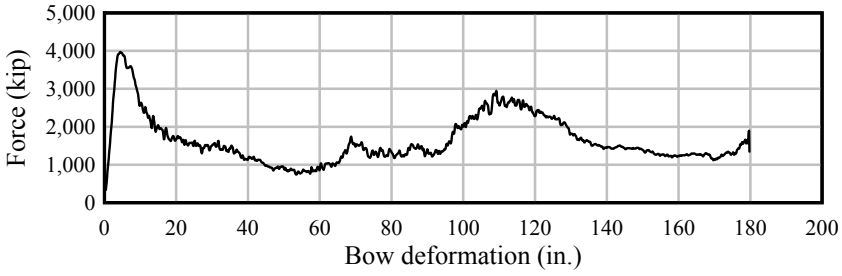

Figure D.44 Barge bow force-deformation data. 35-ft flat-faced pier surface at 0.5°

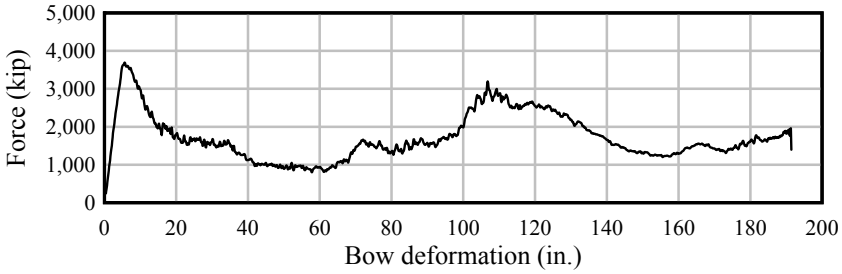

Figure D.45 Barge bow force-deformation data. 35-ft flat-faced pier surface at 0.75°

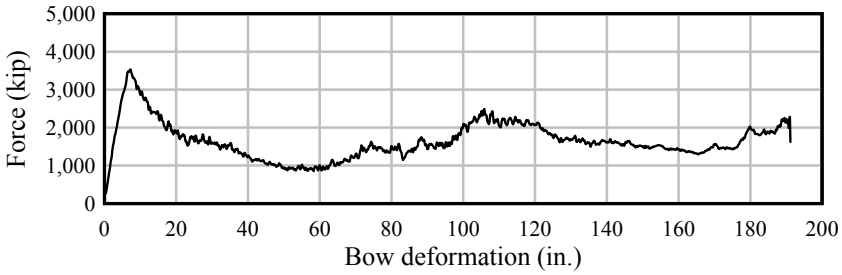

Figure D.46 Barge bow force-deformation data. 35-ft flat-faced pier surface at 1°

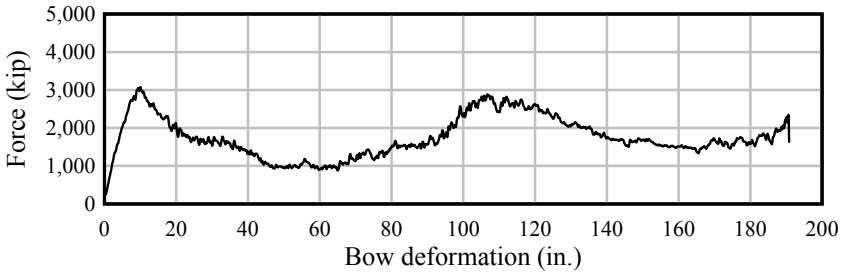

Figure D.47 Barge bow force-deformation data. 35-ft flat-faced pier surface at 1.5°

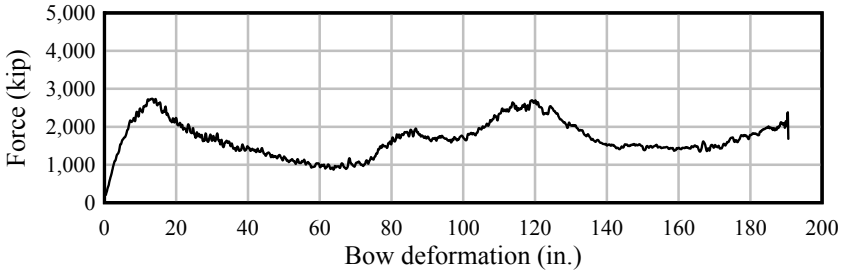

Figure A.48 Barge bow force-deformation data. 35-ft flat-faced pier surface at 2°

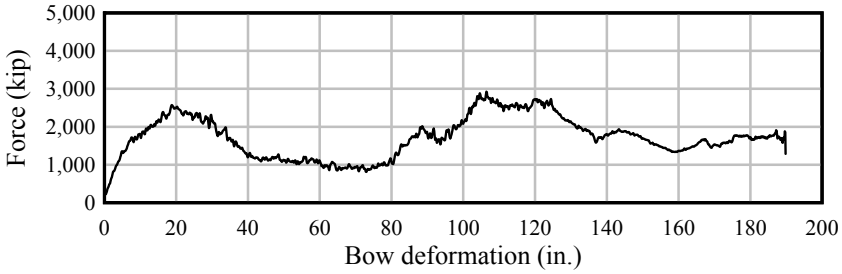

Figure D.49 Barge bow force-deformation data. 35-ft flat-faced pier surface at 3°

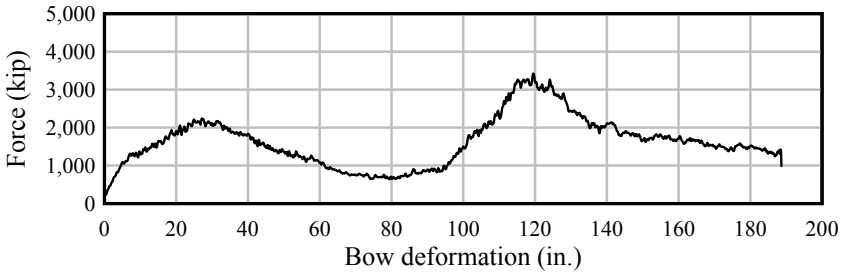

Figure D.50 Barge bow force-deformation data. 35-ft flat-faced pier surface at 5°

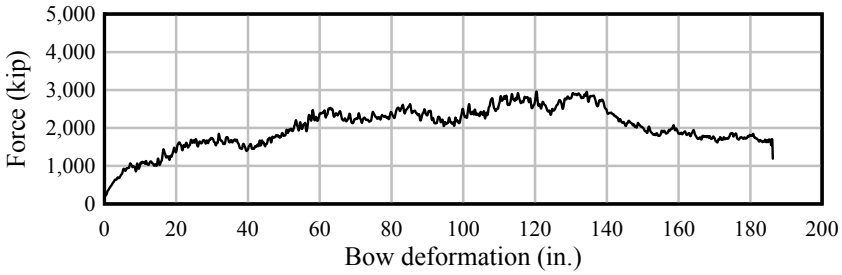

Figure D.51 Barge bow force-deformation data. 35-ft flat-faced pier surface at 10°

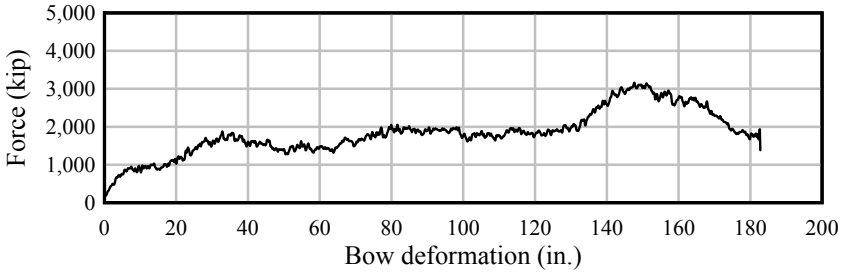

Figure D.52 Barge bow force-deformation data. 35-ft flat-faced pier surface at 15°

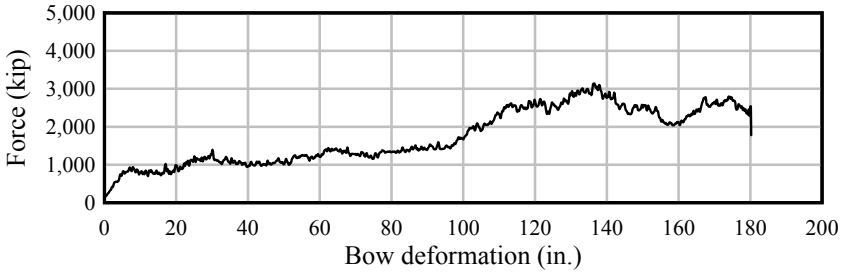

Figure D.53 Barge bow force-deformation data. 35-ft flat-faced pier surface at 20°

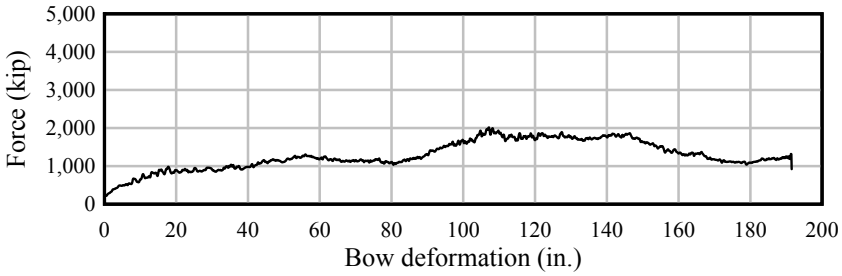

Figure D.54 Barge bow force-deformation data. 35-ft flat-faced pier surface at 30°

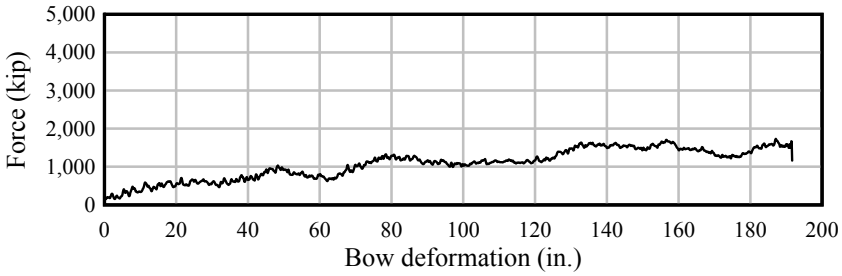

Figure D.55 Barge bow force-deformation data. 35-ft flat-faced pier surface at 45°